Numerical Investigation of the Turbulent ISM

DISSERTATION

zur Erlangung des Grades eines
Doktors der Naturwissenschaften
der
Fakultät für Physik und Astronomie
der Ruhr-Universität Bochum

von

Ralf Kissmann

Bochum 2006

Abgabe der Dissertation: 1. Dezember 2006
Datum der Disputation: 9. Februar 2007
Erstgutachter: PD Dr. Horst Fichtner
Zweitgutachter: Prof. Dr. Rainer Grauer

Contents

Für Doro

Preface

The notion of turbulence is known to us from everyday life. Mostly it is known with regard to the atmosphere (from weather charts and air travel), but there is also a quite indeterminate use of the word turbulence for actions which do not have anything to do with turbulence in the classical sense. Also interstellar space is known to most of us. Already the notion that there is a gas between the stars is, however, not common knowledge anymore. In this work we will, thus, combine these fields to discuss the interstellar turbulence.

What is the motivation for studying interstellar turbulence? There are many answers to that question. One of them is that interstellar space with the low collision rates in this dilute plasma is the only known system, where turbulence with extremely high Reynolds numbers (the ratio of inertial to the viscous forces at work) actually occurs. This, however, can not be and is not the reason for the existence of this work. The reason is rather the impression that there exist many distinct approaches to understand interstellar turbulence. Each scientific community seems to have its own way of handling this matter, without much interaction between the various groups. On can at least distinguish between two principal approaches.

On the one hand there are those who extend basic turbulence theory into the domain of interstellar plasmas. That is methods and simulations borne to investigate scaling laws for isothermal turbulence are applied to the interstellar medium. These applications are usually to phases of the interstellar matter, for which the basic methods of numerical turbulence research can be applied without change. That is research on structure functions and similar statistical aspects of turbulence has so far been performed mainly for isothermal molecular cloud turbulence.

On the other hand there is the astrophysical approach. Coming from the astrophysical side scientists usually intend to capture the spatial structure of the ISM without special regard for the turbulent fluctuations. Such simulations are usually more focused on the density and temperature distribution than on the local dynamics and are very accurate regarding the spatial structure of the ISM, because the multi-phase structure of the ISM is explicitly taken into account. Another important point is that such simulations are mostly global simulations describing a major fraction of the ISM in our Galaxy. Thus, they are in general not suited for turbulence research on more local scales.

Here we present a way to investigate interstellar turbulence with the tools stemming from turbulence theory, while at the same time retaining an interstellar medium as realistic as possible. To achieve this goal, we especially take care to model the physics and the external influences on the medium as accurately as possible. For example, we investigate the question if it is realistic to describe the plasma of molecular cloud in an isothermal fashion. Moreover we show that the driving of the turbulent fluctuations is an important issue to be addressed carefully if the resulting medium is desired to be related to what is observed.

Finally, we should mention those theorists who usually regard interstellar turbulence as some variety of the classical hydrodynamical Kolmogorov turbulence. What remains of turbulence in their studies is basically the slope and the extent of the turbulence spectrum due to the fact that in an analytical model it is not possible to include the full richness of the statistics of a turbulent field. One particular example for this is the analytical estimate for the heating rate of the warm interstellar medium. For this investigation the turbulence spectrum is modelled as a set of adjustable parameters, which are subject to the resulting heating rate. For such an analytical estimate, the spectrum is determined by the external influences instead of being in self-consistent interaction with those influences. Therefore, we supplement these analytical estimates by self-consistent numerical simulations. We would like to cross check these estimates for the heating rate using a self-consistent model for the turbulence.

Already the discussion of the heating rate shows the impact of turbulence on interstellar space. Apart from this there are scientists, who even think turbulence to be responsible for a major part of the spatial structures in the interstellar medium. In particular the star formation seems to be partly determined by the turbulence in the surrounding medium. This is because the fluctuating velocity field is not only able to prevent dense interstellar clouds from collapsing, but also because the fluctuations themselves can produce densities so high that star formation can be triggered in the resulting density clumps. Furthermore there are also the influences of turbulence, which are not that easily accessible to observations. The transport and acceleration of charged, energetic particles is mainly determined by the fluctuations of the magnetic field. Due to their high energy densities they probable have a significant influence on the turbulence itself.

Turbulence is one of the most important ingredients of the plasma in interstellar space. Up to now it is, however, not even fully understood in its most basic incompressible form, not to mention the compressible, magnetised turbulence pervading interstellar space. Here we do not try to gain any insight into these basic processes. We rather try to investigate the turbulent interstellar medium using a model that yields information on the turbulence statistics which is as close to reality as possible at the same time. In this work we mainly concentrate on the development of the necessary tools to achieve this task. After introducing the concept of interstellar turbulence in more detail in the first chapter, we develop the necessary analytical tools for the investigation of interstellar turbulence. A numerical code to be used for the corresponding computations has to yield correct results at discontinuities without producing spurious oscillations, while at the same time being of high order away from these discontinuities. Moreover, the code also has to handle the heating and cooling and other source terms correctly. In this work we develop a numerical code, which is capable of fulfilling all these demands. After ensuring its capability we finally apply the newly developed code to the simulation of ISM turbulence. This work should not be regarded as an exhaustive work on interstellar turbulence. Our aim is rather to develop the appropriate analytical and numerical tools to permit a consistent study of this research field. Therefore, the supplied example computations have rather to be regarded as a way to show the applicability of the newly developed numerical code.

Bochum, 2006 Ralf Kissmann

Chapter 1

Introduction

> *I noticed …tracts of palely glowing gas, shining sometimes by their own light, sometimes by the reflected light of stars. Often these nacrous cloud-continents had secreted within them a number of vague pearls of light, the embryos of future stars.*
>
> Olaf Stapledon, *Star Maker* ***1937***

This work deals with the turbulence of the interstellar medium. As such it can be viewed as a work about a certain kind of turbulence or about a certain state of the interstellar matter. Whatever view is taken, we are concerned with the combination of two important basic fields of physics and astronomy: turbulence and the interstellar medium. In view of this we feel the necessity to start with three introductions: One for the interstellar matter, one for turbulence, and one for the combination of those fields.

1.1 Matter in Interstellar Space

When people look at the sky in a clear dark night, what they essentially see – apart from the objects in our solar system – are numerous stars. Even the cloud-like band of the Milky Way is merely the diffuse luminosity of many stars, which can not be resolved by our naked eyes. Already small telescopes, however, reveal extended gas structures either reflecting stellar light or radiating by themselves. One famous example for such an extended gas cloud is the *Horsehead Nebula* depicted in Fig. 1.1 which was discovered in 1889 on an astrophysical photography of the Orion region. In the beginning of the area of the observation by telescopes only these denser gas clouds were known to astronomers. Today, however, it is clear that the interstellar medium (ISM), as this gaseous phase is called, is ubiquitous. Even though in some regions the gas is more dilute than any so-called vacuum available in laboratories it is nonetheless observable due to the enormous column densities.

Nowadays there are many different astrophysical plasmas under investigation by a huge number of scientists. The corresponding different environments are best visualised by a journey outward from our home planet. Starting from there after leaving the planet's atmosphere we initially encounter the Earth's ionosphere – the highly ionised part of our atmosphere – and thereafter we find ourselves in the magnetosphere. From there we cross the magnetopause to cross from the region influenced by the Earth into the interplanetary plasma of the solar wind. Following its flow direction to the outer regions of the heliosphere, we, eventually, leave the region dominated by our Sun to cross over into the interstellar plasma.

Heaving left behind the interplanetary plasma we find ourselves in a region of very dilute plasma, which is commonly known as the local bubble. Here the temperatures are very high – about a million degrees – whereas the plasma density is as low as 70000 atoms per cubic meter (in a volume of the size of the Earth one would not find one kilogram of matter). This region is on the one hand not a good example

Fig. 1.1: High resolution image of the *Horsehead Nebula* (IC 434) in Orion as observed with the VLT KUEYEN telescope of the European Southern Observatory (ESO) on Paranal (Chile). For further information see `http://www.eso.org/outreach/press-rel/pr-2002/phot-02-02.html`.

for the average properties of the interstellar medium. On the other hand it already shows that the idea of an average interstellar medium is not what is realised in reality.

As we continue our journey outwards from our solar system we encounter a huge variety of plasmas. From the dense dark cores of molecular clouds where new stars are continuously born to the hot coronal gas left behind after hot giant stars turned into supernovae after a short lifespan of greedy consumption of their hydrogen fuel. In between these two extremes we encounter many different phases of interstellar matter. Whereas the discussion on how many phases there are to be found in the ISM is still ongoing, it is clear that the plasma encountered between the stars is mainly made up of different forms of hydrogen. While helium still contributes a few percent of the interstellar matter all other elements have to be viewed as trace elements for the ISM plasma and are commonly referred to as *metals* by most astrophysicists. This, however, does not mean that these elements can be neglected – many of these have to be used to gain knowledge about interstellar matter at all. One famous example is the CO line, by which the gas mass in molecular clouds is usually deduced, since CO is thought to trace the amount of molecular hydrogen H_2, which is not easily observed directly.

If we would intend to go still further away from our Sun we would eventually end up in the very thin gas filling the vast space between the individual galaxies. Since, however, we are not interested in this, we stop our journey before we reach the outer halo of our Galaxy. We rather turn back to the matter filling our Galaxy itself – to try to grasp some numbers for what is so appealing to the eye.

1.1.1 Quantitative View of the ISM

When summing up the entire gas mass of our Milky Way and dividing this by the volume it occupies, one arrives at the average density of the ISM. On average there are about 10^6 atoms in one cubic meter. This corresponds to an overall mass of fifteen percent of the visible mass of our Galaxy. Apart from that 99% of the mass of the ISM is in the form of gas with the remaining 1% being bound in dust particles.

When talking about global properties it is also interesting to discuss the average energy densities. Early estimates gave the easily memorisable number of one electronvolt per cubic centimetre for each

Names	Main constituent	Detected by	Volume of interstellar medium	Fraction by mass	N (m^{-3})	Temp (K)
‘Molecular clouds’	H_2, CO CS, etc.	Molecular lines; dust emission	$\sim$ 0.5%	40%	$\geq 10^9$	10-30
‘Diffuse clouds’; ‘HI clouds’; ‘cold neutral medium’	H,C,O with some ions, C^+, Ca^+	21-cm emission & absorption	5%	40 %	$10^6 - 10^8$	80
‘Intercloud medium’	H, H^+, e^-; ionisation fraction 10-20 %	21-cm emission & absorption; Hα emission	40 %	20 %	$10^5 - 10^6$	8000
‘Coronal gas’	H^+, e^-; highly ionised species, O^{5+}, C^{+3}, etc.	OVI; soft X-rays 0.1-2 keV	~50%	0.1%	$\sim 10^3$	$\sim 10^6$

Table 1.1. Properties of the different phases of the ISM taken from Longair (1994).

of the energy densities of cosmic rays, of the magnetic field and of the dynamic pressure. Nowadays this value has been refined to about $9 \cdot 10^{-14}$ J/m^3 $= 0.56$ eV cm^{-3} (see e.g. Cox 2005). Moreover the thermal pressure has been estimated to be about one tenth of the dynamic pressure. From this one can easily estimate an average temperature for the interstellar medium. This is, however, a futile measure, because the local temperature depends on the local density – typically the average values are untypical for any local structure in the ISM.

According to the classical view the interstellar medium is made up of distinct phases. The typical properties of these are given in Table 1.1. Classically these phases are thought to be in thermal pressure equilibrium. Such a phase structure of the ISM is obtained via the computation of the self-consistent balance between heating and radiative cooling of the interstellar gas. One of the first analyses of a two-phase structure of the ISM, where the heating is based only on cosmic rays, is found in Field et al. (1969). As a result one finds an equilibrium temperature depending on the density and in turn the thermal pressure. From this it is possible to identify stable and unstable phases in a diagram giving the thermal pressure as a function of density basically by the local slope by application of the stability criteria from Field (1965). This can be understood by the example curves shown in Fig. 1.2: For a negative slope a slight disturbance of the equilibrium to higher temperatures makes the gas cool. At constant thermal pressure, however, this makes the gas move to the right in the diagram, thereby pushing it further from the equilibrium and, thus, causing even stronger cooling. This leads to a runaway effect until a stable branch of the diagram is reached.

With this analysis at hand the stable phases are identified as the phases actually observed and the unstable phases being merely unstable transients. One important assumption, however, in the above discussion is the thermal pressure equilibrium. In this picture the energy input of supernova explosions and other highly dynamic events has not been taken into account. With this in mind a pressure equilibrium will not establish itself everywhere in the ISM, thus, yielding a rather dynamic picture. Moreover the fact, that the dynamical pressure is much higher than the thermal pressure is a strong hint for the dynamical nature of the ISM. Whereas such investigation is definitely worthwhile to get an impression

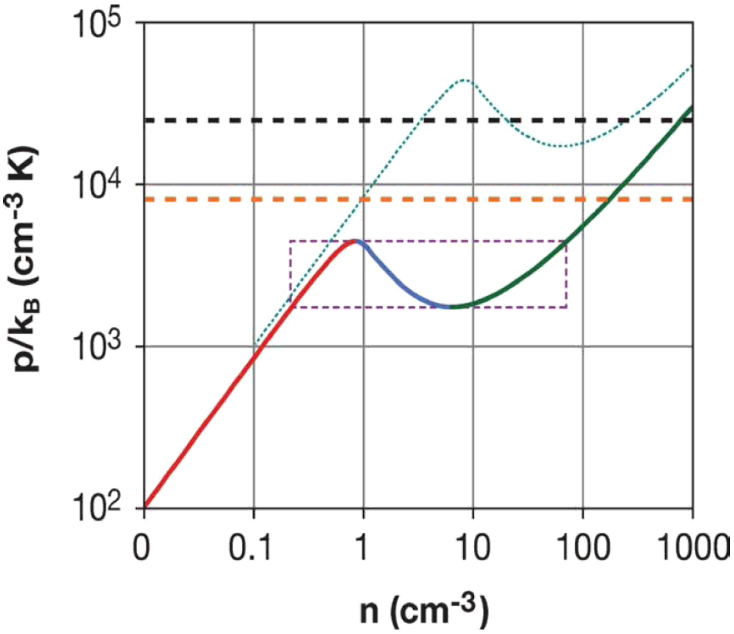

Fig. 1.2: Example pressure curve for a two phase ISM, taken from Cox (2005). Shown is the thermal pressure as a function of number density. Indicated as red and green are the stable phases with the unstable phase marked blue.

of the possible phase structure of the ISM, its dynamical nature has to be investigated, whenever being interested in the real structure of the ISM.

1.1.2 Turbulence in the ISM

Returning to the fact that supernovae appear to be the dominant source for dynamical pressure in the ISM it is clear that the energy input occurs at large spatial scales (as compared to the scales where kinetic energy is usually dissipated). This, however, is just the typical paradigm for turbulent flow. For the latter it is assumed that there is a source of fluctuation energy at large spatial scales much larger than the dissipation scales. Another important aspect of the interstellar plasma is the fact that particle collisions are, due to the low densities, very rare. This leads to very high Reynolds numbers for the major part of the ISM. With high Reynolds numbers being the basic ingredient for turbulence (classically, it is thought that they have to exceed a value of $Re = 10^3$) it is, thus, to be expected that the ISM is highly turbulent.

This turbulence, again, has a strong impact on the propagation of cosmic rays. These are scattered at the inhomogeneities of the interstellar magnetic field. Due to this scattering their propagation can essentially be described by a convection-diffusion equation, where the diffusive part depends strongly on the form of the turbulence.

Before making the direct connection between turbulence and interstellar medium, it is necessary to introduce the basic ideas about turbulence. This will be done in the next section section, where the discussion will be started with the historical Kolmogorov turbulence. At the end I will introduce intermittency and show recent ideas about MHD turbulence.

1.2 Turbulence

Since in this work we analyse the properties of turbulence in interstellar space, it is sensible to start out with the ideas of turbulence in this context. In a way a large part of the astrophysical community is still stuck in 1941 when Kolmogorov published his famous paper in which he introduced the Kolmogorov spectrum (see Kolmogorov 1941b). This is due to the fact that people only use this omnidirectional spectrum for the description of turbulent fluctuations in interstellar space (see e.g. Spangler 1991). Turbulence research, however, made clear that there is more information available in the velocity field than just this spectrum. For this the so-called *structure functions* are analysed. These also contain information about the *intermittency* of the fluctuations.

Very important is the fact that changes with respect to, e.g., the intermittency of the fluctuations cause only very marginal effects for the omnidirectional spectrum (even for turbulence in a magnetised medium), whereas the higher order structure functions strongly depend on the intermittency. Therefore, a plain description of the turbulent field via the omnidirectional spectrum is not sufficient to include all aspects of the turbulence. In particular it will not be possible to obtain all the physics in an experiment, when just investigating the omnidirectional spectrum.

Terms like *structure functions* and *intermittency* will become more clear for the reader when discussing the evolution from the Kolmogorov model to more recent ideas for turbulence. First we will discuss the former of these terms in order to get a little different view of the Kolmogorov model. These discussions will concentrate on incompressible, hydrodynamic turbulence – not until the end of the section will we get to the transition to general MHD turbulence.

1.2.1 The Navier-Stokes Equation

In the following sections we will show that despite the fact that the spectrum is the aspect of turbulence that is usually referred to it is connected to just one of a whole hierarchy of structure functions. It will also be shown that the spectrum is easily derived from an evaluation of the structure functions. While this was not the way it happened historically, it shows the assumptions required for this result very clearly and will therefore be used in this work.

The first step on the road from structure functions to the spectrum was actually accomplished by Kolmogorov himself in his third 1941 turbulence paper (Kolmogorov 1941a). This first step is the derivation of the so-called *four-fifth law*. For this Kolmogorov started out from the Navier-Stokes equation:

$$\begin{aligned} \partial_t \mathbf{v} + \mathbf{v}\cdot\nabla\mathbf{v} &= -\nabla p + \nu\nabla^2\mathbf{v} + \boldsymbol{f} \\ \nabla\cdot\mathbf{v} &= 0 \end{aligned} \tag{1.1}$$

This form of the Navier-Stokes equation has a forcing term $\boldsymbol{f}(t, \boldsymbol{r})$ included, which has to be present in stationary turbulence in order to replenish the energy dissipated by viscosity. Apart from that here we consider an incompressible fluid. The equation itself possesses many symmetries of which four are of major interest for turbulence research. Disregarding the forcing term (or rather assuming, that it will behave in the same way as the rest of the equation) one can easily find these to be:

- Symmetry under spatial translations
- Symmetry under time translations
- Rotational symmetry
- Scaling symmetry

These are clearly only valid, whenever no fixed spatial or temporal boundaries are present. The last of these symmetries is of utmost importance when calculating the hierarchy of structure functions in the Kolmogorov picture as will become clear later. Disregarding the forcing term again, the Navier-Stokes equation is invariant under the scaling:

$$\boldsymbol{r} \mapsto \lambda\boldsymbol{r} \qquad \mathbf{v} \mapsto \lambda^h\mathbf{v} \qquad t \mapsto \lambda^{1-h}t \tag{1.2}$$

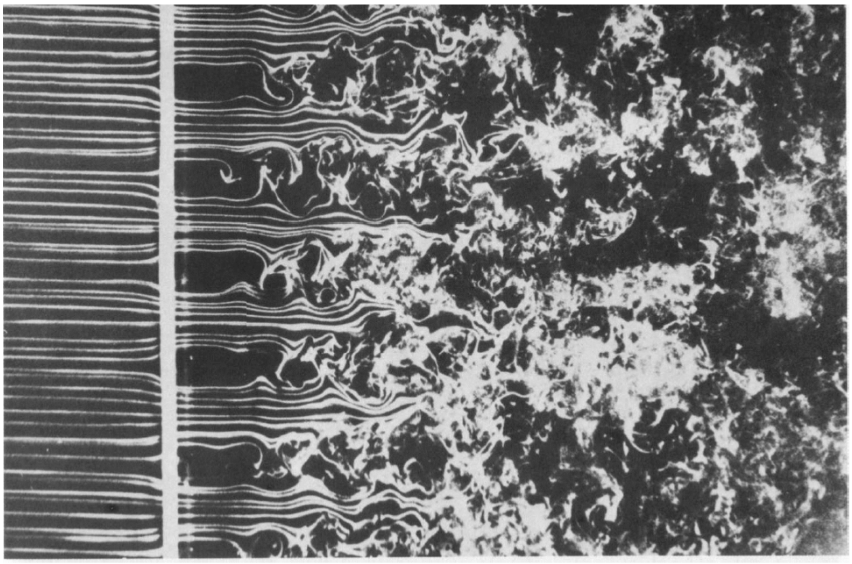

Fig. 1.3: Homogeneous turbulence produced by flow through a grid (Photograph T. Corke and H. Nagib – see also in van Dyke (1982)).

only in the case $h = -1$. If, however, the Reynolds number is very high, the viscous term tends to zero and the Navier-Stokes equation becomes symmetric under the above scaling law for an arbitrary value of h.

All these symmetries only hold if the initial conditions and the boundaries also correspond to the given symmetries, which is generally not the case. Therefore one has to introduce different assumptions in order to regain some of the above symmetries:

1.2.2 Assumptions

Apart from the *recovery* of the symmetries in a statistical sense there are some important hypotheses which are used in the derivation of the structure functions. Before proceeding any further we, therefore, first discuss these assumptions. As stated above, the first assumption is that the symmetries in the Navier-Stokes equation are restored in a statistical sense for high Reynolds numbers and far away from any boundaries.

As an example for this assumption one can examine grid-generated turbulence. Regarding Fig. 1.3 where such a turbulent system is shown, it is apparent that the influence of the boundaries vanishes far away from these. It also seems justified to say that the turbulence has become homogeneous and isotropic in a statistical sense at that point.

In the same sense (far away from boundaries, at small spatial scales, . . .) we will later on use the assumption that the turbulence behaves self-similar in a statistical sense. With the definition:

$$\delta \mathbf{v}(\boldsymbol{r}, \boldsymbol{l}) = \mathbf{v}(\boldsymbol{r} + \boldsymbol{l}) - \mathbf{v}(\boldsymbol{r}) \tag{1.3}$$

for the velocity increments, the postulated small-scale homogeneity then corresponds to the independence of $\delta \mathbf{v}(\boldsymbol{r}, \boldsymbol{l})$ from $\boldsymbol{r}$ over a small volume.

The assumption of self-similarity, then, corresponds to the proposal of a scaling law for these velocity increments like the one holding for the Navier-Stokes equation. Namely, we assume:

$$\delta \mathbf{v}(\boldsymbol{r}, \lambda \boldsymbol{l}) = \lambda^h \delta \mathbf{v}(\boldsymbol{r}, \boldsymbol{l}) \tag{1.4}$$

This assumption is made under the same conditions as the assumption about the reappearance of the symmetries – i.e. $\boldsymbol{r}$ and $\boldsymbol{l}$ have to be small.

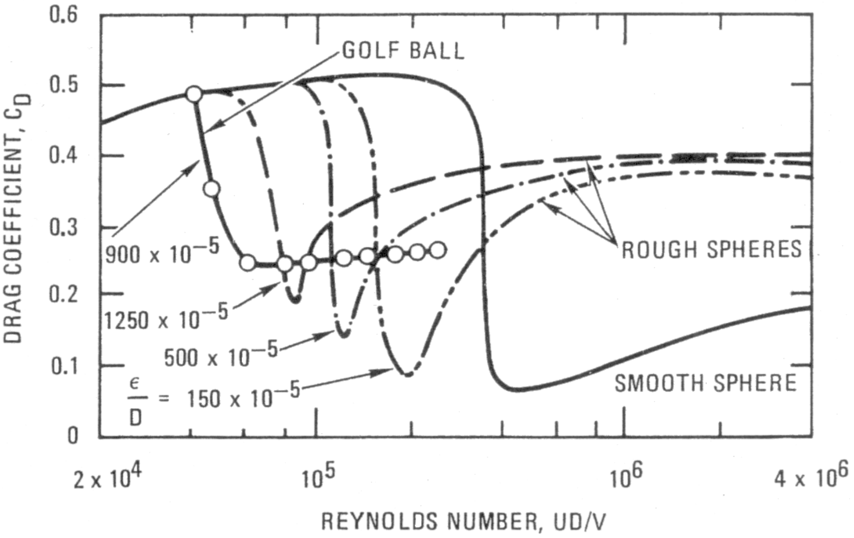

Fig. 1.4: Drag coefficient C_D for the flow around different kinds of spheres as indicated in the figure taken from Blevins (1984).

The next hypothesis is strongly based on observations. From experiments on the drag force on different kinds of bodies (see e.g. Fig. 1.4) it is found that the drag force at high Reynolds numbers becomes constant. To discuss this assumption in general one has to look at the equation for the dissipation of kinetic energy:

$$\varepsilon \propto \frac{1}{2}\frac{U^3}{L} = \frac{U^2/2}{L/U} \tag{1.5}$$

where U is the velocity at the large spatial scale L. If this relation is to be constant for the high Reynolds numbers, which are encountered in turbulent flow in general (and in astrophysical fluids in particular) it is clear that in one circulation time, which would be about L/U, a finite fraction of the kinetic energy of the fluid has to be transferred (by nonlinear interactions) to scales sufficiently small for this energy to be dissipated. This gives us some idea about the speed of this process.

Apart from this we assume that the force $\boldsymbol{f}$ driving the fluctuations is active only at large scales far away from the dissipation range. Moreover we assume that the system reaches a statistically stationary state for $t \to \infty$. Using these assumption we can get an idea about the structure functions and the spectrum of isotropic, incompressible, hydrodynamical turbulence. The first stage on the way to these results, however, is the so-called four-fifth law by Kolmogorov himself.

1.2.3 The Four-Fifth Law

As will become clear along the way, the four-fifth law is one of the most important laws in turbulence at all. This is because it is an exact, non-trivial law, which can be derived from the Navier-Stokes equation directly. To be able, however, to understand the derivation of this law we first have to go back to the Navier-Stokes equation.

For this there are several known conservation laws, the most important of which – for our purpose – is the energy conservation. First we introduce the notation:

$$E \equiv \left\langle \frac{1}{2}|\mathbf{v}|^2 \right\rangle \qquad \text{and} \qquad \Omega \equiv \left\langle \frac{1}{2}|\omega|^2 \right\rangle \tag{1.6}$$

for the *mean energy* per mass and the *mean enstrophy*, respectively, where ω indicates the vorticity. With this the energy balance equation for the Navier-Stokes equation can be found to be:

$$\frac{d}{dt}E = -2\nu\Omega \equiv \varepsilon \tag{1.7}$$

where the quantity:

$$-\frac{d}{dt}E \tag{1.8}$$

is referred to as the mean energy dissipation ε.

Another conservation law relevant for discussions on turbulence is the energy budget for different scales. For this wavenumber space is subdivided into two domains. This means that for each quantity $f(\boldsymbol{r})$ we distinguish the two parts:

$$f_K^< \equiv \sum_{k\leq K} \hat{f}_{\boldsymbol{k}} e^{\imath \boldsymbol{k}\cdot\boldsymbol{r}} \qquad \text{and} \qquad f_K^> \equiv \sum_{k>K} \hat{f}_{\boldsymbol{k}} e^{\imath \boldsymbol{k}\cdot\boldsymbol{r}} \tag{1.9}$$

where k is the wavenumber. Here K is some wavenumber dividing wavenumber space in two parts. Beware that these functions are not Fourier transforms of the original functions but rather the high-pass and low-pass filtered versions of these.

Now such functions can be defined for all relevant quantities included in the Navier-Stokes equation. Apart from the velocity itself we will decompose the following quantities according to the above prescription:

$$\begin{aligned}
\mathcal{E}_K &\equiv \frac{1}{2}\left\langle |\boldsymbol{U}|^2 \right\rangle = \frac{1}{2}\sum_{k\leq K} |\hat{\mathbf{v}}_k|^2 && \text{kinetic energy at large scales} \\
\Omega_K &\equiv \frac{1}{2}\left\langle |\omega|^2 \right\rangle = \frac{1}{2}\sum_{k\leq K} k^2|\hat{\mathbf{v}}_k|^2 && \text{Cumulative enstrophy up to K} \\
\mathcal{F}_K &\equiv \frac{1}{2}\left\langle |\boldsymbol{f}_K^< \cdot \mathbf{v}_K^<|^2 \right\rangle = \sum_{k\leq K} \hat{\boldsymbol{f}}_{\boldsymbol{k}} \cdot \hat{\mathbf{v}}_{-\boldsymbol{k}}^2 && \text{Energy injection up to K} \\
\Pi_K &\equiv \left\langle \mathbf{v}_K^< \cdot \left(\mathbf{v}_K^< \cdot \nabla \mathbf{v}_K^>\right)\right\rangle + \left\langle \mathbf{v}_K^< \cdot \left(\mathbf{v}_K^> \cdot \nabla \mathbf{v}_K^>\right)\right\rangle && \text{Cumulative enstrophy up to K}
\end{aligned} \tag{1.10}$$

For the above definitions keep in mind that we are talking about an incompressible medium – therefore we do not have to take variations for the density into account. Using these definitions one can find (Frisch 1995, see e.g.) an energy budget equation which shows the evolution of the cumulative kinetic energy between the lowest wavenumber and wavenumber K:

$$\partial_t \mathcal{E}_K + \Pi_K = -2\nu\Omega_K + \mathcal{F}_K \tag{1.11}$$

In this equation also the nonlinear interactions become important: the rate of change of the cumulative energy of wavenumbers up to K is equal to the energy injected up to this wavenumber minus the energy dissipated in this regime minus the flux of energy Π_K.

If we now use the assumptions from section 1.2.2 we can greatly simplify the above equations. For a statistically stationary state we first neglect time derivatives. Moreover, we assume the energy injection to be confined to scales with $k < K$. With the further assumption of an infinite Reynolds number the above conservation equations can be combined to give:

$$\lim_{\nu\to 0} \Pi_K = \varepsilon \tag{1.12}$$

leading to the result that the energy which is transported from the large to the small scales is equivalent to the energy dissipated at the small spatial scales. This does, however, tell us nothing about how the energy is transported trough wavenumber space – we did not use any assumption on the locality or non-locality of energy transport in wavenumber space.

From Eq. (1.12) one can finally deduce (for the actual derivation see Frisch 1995) the probably most important results about incompressible hydrodynamic turbulence. This result is Kolmogorov's four-fifth law which states that the third order longitudinal *structure function* is given by the mean energy dissipation per unit mass as:

$$S_3(l) = \left\langle \left(\delta v_{||}(\boldsymbol{r}, \boldsymbol{l})\right)^3 \right\rangle = -\frac{4}{5}\varepsilon l \tag{1.13}$$

This result is exact and very general as compared to many other results in turbulence theory. All theories considering incompressible turbulence with driving at large spatial scales have to fulfil this equation. Note also that, observations, e.g., in wind tunnels demonstrate that this result is obviously reproduced in nature. A result of this form is so far only deducible for the third order structure function. It even gives a convenient handle for measuring higher order structure function to great accuracy, when they are expressed as a ratio compared to the third order structure function.

1.2.4 Structure Functions for Kolmogorov Turbulence

Many of the additional results derived by Kolmogorov and others, while based on the exact four-fifth law usually need more assumptions to be satisfied (not all of which are justified as we will see later).

One such result is the scaling exponent for the presumably self-similar velocity field. When applying Eq. (1.4) to the four-fifth law, one finds the scaling exponent to be:

$$h = \frac{1}{3} \tag{1.14}$$

when a self-similar flow can safely be assumed. This assumption also leads to a scaling law for the *longitudinal structure functions* of order p:

$$S_p(l) \propto l^{p/3} = l^{\zeta_p} \tag{1.15}$$

where:

$$S_p(l) \equiv \left\langle [(\mathbf{v}(\boldsymbol{r} + l\boldsymbol{n}) - \mathbf{v}(\boldsymbol{r})) \cdot \boldsymbol{n}]^p \right\rangle = \left\langle |\delta \mathrm{v}_{||}(\boldsymbol{r}, \boldsymbol{l})|^p \right\rangle \tag{1.16}$$

is defined as the spatial average of the p-th power of the velocity difference over the distance l with n indicating a unit vector. One important result concerning the structure functions is the power law for the energy spectrum of the fluctuations. It can be shown (see e.g. Frisch 1995) that the energy spectrum is directly connected to the second-order structure function. Whenever the second-order structure function scales as a power law with exponent q the spectrum can be shown to have a power law with exponent $-(q + 1)$. Thus, we find with $q = 2/3$ according to Eq. (1.15) in this context for the energy spectrum of the fluctuations:

$$E(k) \equiv \frac{d\mathcal{E}}{dk} \propto k^{-5/3} \tag{1.17}$$

Be aware that the connection between the energy spectrum of the fluctuations and the second order structure function holds irrespective of the assumption about the self-similarity of the turbulence. Therefore, the point we have to stress about the energy spectrum is that the information contained in this is equivalent to the information contained in the second order structure function. For more accurate knowledge about the velocity fluctuations one has to consult the higher order structure functions. Whereas the spectrum found in experiments is consistent with the Kolmogorov spectrum, these higher order structure functions do pose a problem with regard to the Kolmogorov model. This is illustrated in Fig. 1.5, where the first structure function exponents obtained using the extended self-similarity (see Benzi et al. 1993) are compared to the predictions from the Kolmogorov model. Clearly the deviation becomes more and more severe with the increasing order of the structure function. It is also evident that the second order structure function yielding the spectral slope does not contradict the Kolmogorov model whereas the higher order structure functions do so. Nowadays it is thought that the reason for this discrepancy is the neglect of intermittency in the Kolmogorov model. This will be elaborated in the next paragraph where we will introduce some important aspects of the more recent turbulence theory.

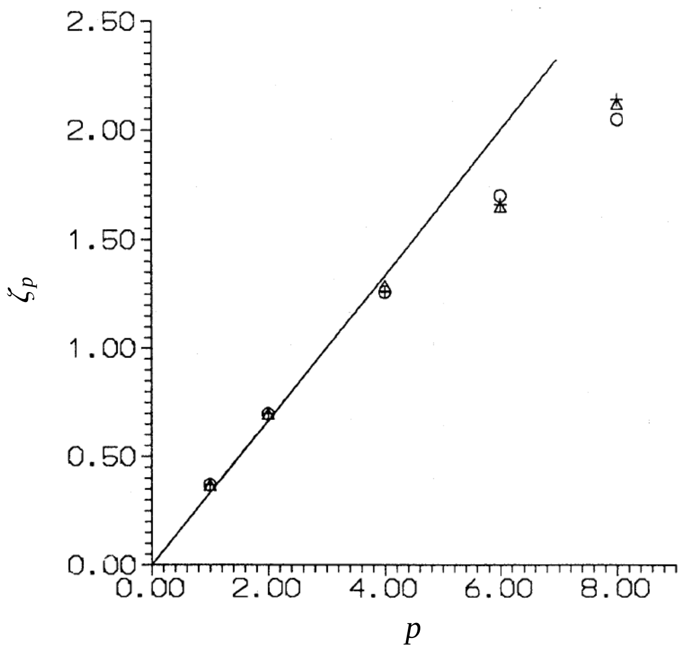

Fig. 1.5: Exponents $\zeta_p$for the structure functions for high Reynolds number flow past a cylinder taken from Benzi et al. (1993) given as a function of the order p. The data points show values for the exponents computed from the observations using different methods. The solid line shows the Kolmogorov scaling.

1.2.5 From Kolmogorov to the Present

The results given in the preceding sections can mainly be found in Kolmogorov's works in 1941 (see Kolmogorov 1941a,b). Since then there was a huge development in turbulence theory. Not all aspects of turbulence are understood today, but there were issues neglected in his theory from 1941, which have meanwhile been found to be important. The most important aspect, which was taken into account only later, is the so-called *intermittency* .

Thus, the question arises: what is intermittency and how does it change the behaviour of a turbulent system?

Basically in an intermittent fluid system there are large patches of space with a quiescent behaviour, which are interrupted by patches of chaotic, irregular flow. From this definition it becomes clear that an intermittent system cannot be self-similar and vice versa (at least not in the sense discussed above) – this is due to the fact, that the small scales in a quiet region are very different from those in the irregular flow.

1.2.6 The β Model

We can catch a first glimpse of intermittency in turbulence by the β model introduced in Frisch et al. (1978). In the Kolmogorov picture the cascade is assumed to be self-similar and, thus, has to be space filling. Landau, however, pointed out, that if dissipation is intermittent – as later on became clear in laboratory experiments – one would have to reconsider this picture. Therefore, a space filling cascade was not likely anymore.

A simple method to realise an intermittent form of the Kolmogorov picture is the so-called β model. In this model the cascade is assumed to be not space filling anymore, but otherwise the model closely sticks to the cascade idea of Kolmogorov. To get an idea of the new features of the model we included Fig. 1.6 and Fig. 1.7 to illustrate the difference between the two cascade models. In Fig. 1.6 the cascade (going from top to bottom) is space filling. Each individual eddy decays into several smaller eddies (four

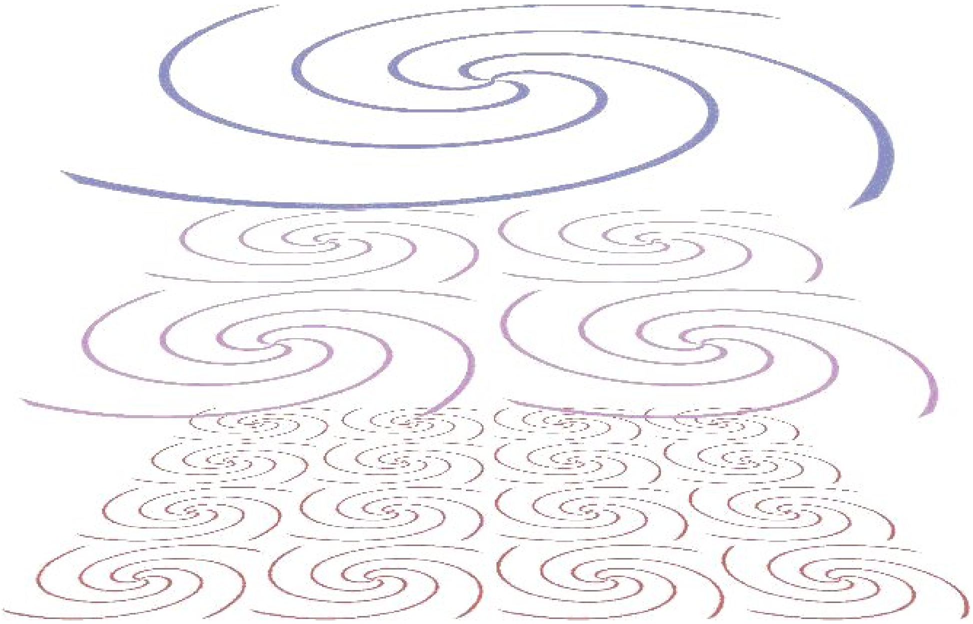

Fig. 1.6: Visualisation of the Kolmogorov cascade. Here we show three steps of the classical cascade. We start with one large-scale eddy (top). This decays into four smaller eddies filling up the same space as the initial eddy (middle). Finally these eddies again decay into smaller ones (bottom).

in this case), which fill up the space previously filled by the larger eddy.

In the β model, in contrast to that, each large eddy decays into smaller ones, which do not fill the entire space formerly occupied by the larger eddy anymore. Therefore, the energy contained in the large eddies is restricted to smaller and smaller fractions of the available space, thus, yielding a very intermittent signal.

The name of this model is closely connected to the idea that the smaller eddies resulting from the larger ones do not fill up the entire available space: This is because the space filling factor of the resulting eddies is designated as β (with $0 \leq \beta < 1$).

When the eddies on the largest scales have sizes l_0 then the n-th *daughter*-eddy has – in the simplified picture that all eddies decay in the same way – a size of $l = r^n l_0$, where r is the ratio of the sizes of the *daughter*-eddy to the *mother*-eddy. From this we find, that $n = \ln(l/l_0)/\ln(r)$. Therefore, the fraction of space, p_l, containing n-th generation eddies as compared to the space filled with eddies of size l_0 is:

$$p_l = \beta^n = \beta^{\frac{ln(l/l_0)}{\ln r}} \tag{1.18}$$

In this context Frisch et al. introduce the so-called codimension $3 - D$ given by:

$$p_l \overset{!}{=} \left(\frac{l}{l_0}\right)^{3-D} \qquad \Longrightarrow \qquad 3 - D = \frac{\ln\beta}{\ln r} \tag{1.19}$$

where D is the *fractal* dimension of space occupied by the eddies of size l. Thus, the probability to find an eddy of size l is connected to a fractal dimension, where $D = 3$ regains the Kolmogorov picture of the *daughter* eddies to fill all the available space. The structure functions obtained in this extension of the Kolmogorov model naturally differ from those in the former picture:

In the β model the fluctuation energy at scale l becomes:

$$E_l \propto \mathrm{v}_l^2 p_l = \mathrm{v}_l^2 \left(\frac{l}{l_0}\right)^{3-D} \tag{1.20}$$

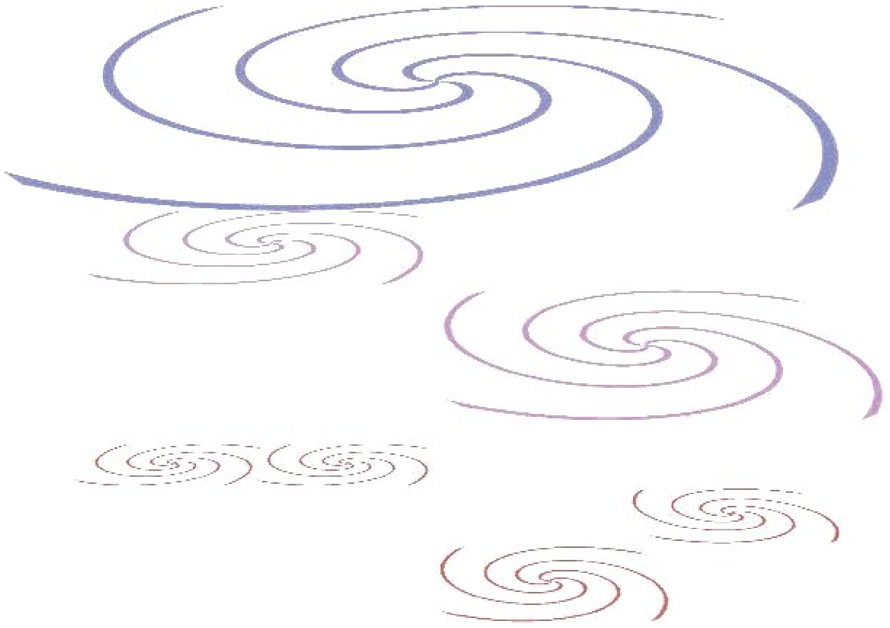

Fig. 1.7: Visualisation of the intermittent cascade in the β model. As in the classical cascade we start with one large-scale eddy (top). This decays into smaller eddies, which are not space filling anymore (middle). After another step of the cascade we end with again smaller eddies, which fill even less of the available space (bottom).

Then the spectral flux becomes by dimensional arguments:

$$\pi_l = \frac{E_l}{t_l} = \frac{\mathrm{v}_l^3}{l}\left(\frac{l}{l_0}\right)^{3-D} \tag{1.21}$$

This has, according to Eq. (1.12), to be the same as the energy dissipation at the smallest scales $\varepsilon \propto \mathrm{v}_0^3/l_0$. The scale independence of the spectral flux π_l thus, leads to:

$$v_l \propto v_0\left(\frac{l}{l_0}\right)^h \qquad \text{with} \qquad h = \frac{1}{3} + \frac{3-D}{3} \tag{1.22}$$

This may be viewed as a scaling exponent for the velocity field, which obviously differs from the one found for the Kolmogorov picture – but for $D = 3$ the Kolmogorov exponents is again restored. From this one finds the structure functions to be:

$$S_p(l) = \left\langle \delta\mathrm{v}_{\|}^p(\boldsymbol{r}, l)\right\rangle \propto \mathrm{v}_0^p\left(\frac{l}{l_0}\right)^{\zeta_p} \qquad \text{mit} \qquad \zeta_p = \frac{p}{3} + (3-D)\left(1 - \frac{p}{3}\right) \tag{1.23}$$

This also means that the spectral index becomes different from the one in the Kolmogorov picture. From the second order structure function the spectrum becomes:

$$E(k) \propto k^{-\left(\frac{5}{3}+\frac{3-D}{3}\right)} \tag{1.24}$$

This means, that in the β model the classical Kolmogorov spectrum is the shallowest spectrum possible. For a more intermittent model, however, the spectrum becomes steeper than that. The β-model represents intermittency in a quite simplified fashion. Especially the fact that intermittency is essentially only detected in the dissipation range is not taken care of in this model. There are many more elaborate models available (see Frisch 1995, for further reading), which e.g. use multifractals to gain a better fit to the observed (or numerically computed) structure functions. Here, we will only introduce one additional model, which predicts the structure functions surprisingly well. This seems not only to be the case for incompressible hydrodynamic turbulence, but also in compressible MHD turbulence there is so far no contradiction to the She-Leveque model discussed in the following paragraph.

1.2.7 The She-Leveque Model

The She-Leveque model introduced by She and Leveque (1994) is a model based on the connection of the dissipative structures (vortex tubes in incompressible turbulence and shocks for the compressible equations) to the scaling in the inertial range. In the Kolmogorov (1941a) model the mean value of the energy dissipation ε (see above) is a central quantity in deriving the turbulence models. However, a footnote-remark in the first edition of Landau's book on fluid mechanics together with Lifshitz about the lack of intermittency in the Kolmogorov theory was aiming especially at the fact that the dissipation seemed to be intermittent, which was clearly not attributed for in that model. In later editions the remark found its way into the main text (see e.g. Landau and Lifshitz 1987) – it is popularly known as *Landau's remark*.

This issue was tackled by Kolmogorov himself in his 1962 paper (Kolmogorov 1962), where he introduced the so-called refined similarity hypothesis. In his 1941 work he used the assumption that the average energy dissipation was constant to obtain the relation:

$$\varepsilon = const. \propto \frac{\mathrm{v}_l^3}{l} \qquad \Longrightarrow \qquad \mathrm{v}_l \propto (\varepsilon l\,)^{\frac{1}{3}}$$

The same formula was then used not for the constant average energy dissipation but for the energy dissipation ε_l at scale l. This can be viewed as the energy dissipation averaged over a ball of radius l. When we also allow for scaling of the energy dissipation instead of taking the mean as in the Kolmogorov (1941a) model we arrive at:

$$\mathrm{v}_l \propto (\varepsilon_l l\,)^{\frac{1}{3}} \qquad \longrightarrow \qquad S_p(l) = \left\langle \delta \mathrm{v}^p(\boldsymbol{r}, l) \right\rangle \propto l^{\zeta_p} \tag{1.25}$$

with some unknown scaling exponent ζ_p. What is essentially named the *refined similarity hypothesis* is the assumption that the velocity and the dissipation ε_l are statistically independent. With the assumption of some so far unknown scaling behaviour of the local energy dissipation ε_l given as:

$$\left\langle \varepsilon_l^p \right\rangle \propto l^{\tau_p} \tag{1.26}$$

we find for the scaling of the velocity differences over a distance l:

$$\left\langle \delta \mathrm{v}_l^p \right\rangle \propto l^{\zeta_p} \qquad \text{with} \qquad \zeta_p = \frac{p}{3} + \frac{\tau_p}{3} \tag{1.27}$$

where the exponent is complemented by $\tau_p/3$ as compared to the results of the Kolmogorov (1941a) model. When all statistically averaged quantities at scale l depend only on the mean dissipation we regain the classical picture, where $\tau_p = 0$.

Whereas it soon became clear that the latter was supported neither by experimental nor numerical studies, the models prior to She and Leveque (1994) had to use adjustable parameters to determine ζ_p and τ_p. She and Leveque (1994) were the first to give a physical meaning to the parameters introduced to obtain these variables. The main assumption in their work is that there exists a *hierarchy of fluctuation structures* $\varepsilon_l^{(p)}$ being defined by the moments of the dissipation as:

$$\varepsilon_l^{(p)} = \frac{\left\langle \varepsilon_l^{p+1} \right\rangle}{\left\langle \varepsilon_l^p \right\rangle} \tag{1.28}$$

Here $\varepsilon_l^{(0)}$ is the mean energy dissipation. This is naturally scale-independent as was also used in the Kolmogorov (1941a) model. The other *extreme characteristic structure* of the hierarchy is:

$$\varepsilon_l^{(\infty)} \equiv \lim_{p\to\infty} \frac{\varepsilon_l^{p+1}}{\varepsilon_l^{p}} \tag{1.29}$$

This is associated to the filamentary structure of the dissipation. It is the intensity of the most intermittent structures of the dissipation. For incompressible Navier-Stokes turbulence as discussed in She and Leveque (1994) these structures are vortex tubes – one-dimensional structures in three-dimensional space. By dimensional arguments this is just: $\varepsilon_l^{(\infty)} \propto \delta E^\infty / t_l$ where δE^∞ represents the kinetic energy to be dissipated and t_l is the time scale for this dissipation. Being interested in the scaling behaviour of the velocity increments one has to discuss the scaling behaviour of $\varepsilon_l^{(\infty)}$. She and Leveque (1994) assume normal scaling for t_l, thus, setting a uniform time scale for the dissipation of various intensities. This time scale can then be estimated as in the Kolmogorov model:

$$t_l = \frac{l}{\mathrm{v}_l} \overset{\varepsilon\propto \mathrm{v}_l^3/l}{\propto} l(\varepsilon l\,)^{-\frac{1}{3}} = \varepsilon^{-\frac{1}{3}} l^{\frac{2}{3}} \tag{1.30}$$

where the average dissipation was used for the definition of the time scale t_l. With this we can discuss $\varepsilon_l^{(\infty)}$. For the most intermittent structures we assume that the energy to be dissipated is δv_0^2. This means that the most dissipative structures are connected to discontinuities in the velocity field. From Eq. (1.30) and the above arguments we find:

$$\varepsilon_l^{(\infty)} \propto \varepsilon \left(\frac{l}{l_0}\right)^{-\frac{2}{3}} \propto l^{\,-\frac{2}{3}} \tag{1.31}$$

By the definition of $\varepsilon_l^{(\infty)}$ this directly translates into:

$$\varepsilon_l^{(\infty)} = \lim_{p\to\infty} \frac{\left\langle \varepsilon_l^{p+1} \right\rangle}{\left\langle \varepsilon_l^{p} \right\rangle} = \lim_{p\to\infty} \frac{l^{\,\tau_{p+1}}}{l^{\,\tau_p}} \propto l^{\,-\frac{2}{3}} \tag{1.32}$$

Concentrating on the exponents, one has for the scaling of the dissipation:

$$\lim_{p\to\infty} \left(\tau_{p+1} - \tau_p\right) = -\frac{2}{3} \qquad \Longrightarrow \qquad \tau_p = -\frac{2}{3} p + C_0 \quad (p \to \infty) \tag{1.33}$$

Here C_0 indicates the codimension of the intermittent dissipative structures. This can be found by the application of a Legendre transform and is for incompressible Navier-Stokes turbulence set to $C_0 = 2$ by the authors. This choice becomes clear, when taking into account that the most dissipative structures in this case are vortex tubes of dimension 1.

The next important step in the derivation by She and Leveque (1994) is the assumption that there exists a relation like:

$$\frac{\left\langle \varepsilon_l^{p+1} \right\rangle}{\varepsilon_l^{(\infty)} \left\langle \varepsilon_l^{p} \right\rangle} = A_p \left(\frac{\left\langle \varepsilon_l^{p} \right\rangle}{\varepsilon_l^{(\infty)} \left\langle \varepsilon_l^{p-1} \right\rangle} \right)^{\beta}, \quad 0 < \beta < 1 \tag{1.34}$$

Here the constants A_p are independent of the scale l, but there is no need for them to be universal. The authors motivate the above relation with the expectation that $\varepsilon_l^{(p+1)}$ and $\varepsilon_l^{(p)}$ are somehow connected to each other. However, the symmetry yielding this relation is not yet known. From this assumption we directly arrive at:

$$l^{\,\tau_{p+1}-\tau_p+\frac{2}{3}} \propto l^{\,\beta(\tau_p-\tau_{p-1}+\frac{2}{3})} \tag{1.35}$$

yielding:

$$\tau_{p+1} - \tau_p + \frac{2}{3} = \beta(\tau_p - \tau_{p-1} + \frac{2}{3}) \tag{1.36}$$

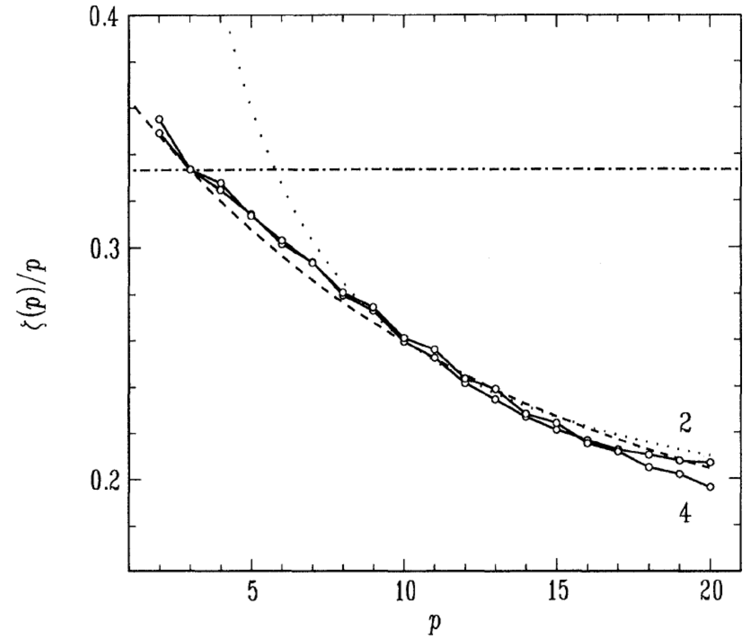

Fig. 1.8: Structure functions in two different turbulent flows taken from Herweijer and van de Water (1995) – the numbers 2 and 4 indicate the flow conditions given in Table 1 in their manuscript. The dash-dotted line shows the prediction by the Kolmogorov model. The dotted line shows the results by a multifractal model and the dashed line represents the She-Leveque model.

This is for $p \rightarrow \infty$ identical to the asymptotic law given in Eq. (1.33) and allows us to write for the general scaling of the dissipation:

$$\tau_p = -\frac{2}{3} + 2 + f(p) \tag{1.37}$$

Using this in Eq. (1.36) yields a difference equation for $f(p)$:

$$f(p+1) - (1+\beta)f(p) + \beta f(p-1) = 0 \tag{1.38}$$

the only nontrivial solution of which is $f(p) = \alpha\beta^p$. The constants in this equation are fully determined by the conditions $\tau_0 = 0$ and $\tau_1 = 0$. The former of these, according to the authors, holds, when a finite support of the dissipation is assumed for the limit of zero viscosity. The latter condition follows in turn from the fact that $\varepsilon_l^{(0)}$ is scale independent as was discussed above. With the resulting constants $\alpha = -2$ and $\beta = 2/3$ the final result for the scaling exponent of the dissipation reads:

$$\tau_p = -\frac{2}{3}p + 2\left(1 - \left(\frac{2}{3}\right)^p\right) \tag{1.39}$$

from which the velocity structure functions can be derived to be:

$$\left\langle \delta v_l^p \right\rangle \propto l^{\,\zeta_p} \qquad \text{with} \qquad \zeta_p = \frac{p}{9} + 2\left(1 - \left(\frac{2}{3}\right)^{p/3}\right) \tag{1.40}$$

The excellent fit of this result to experimental data of turbulence is illustrated in Fig. 1.8. The given data were observed by Herweijer and van de Water (1995) in laboratory turbulence. They are compared to the predictions by Kolmogorov, a multifractale and the She-Leveque models. Clearly the She-Leveque model gives the best fit to the data of all these models.

In summary, the above She and Leveque (1994) model nicely describes the features of incompressible turbulence even for structure functions of high order. A major benefit of this model is that all parameters used in the model are physical parameters, which are known ab initio for the system under consideration.

The model and its physical interpretation was further extended by Dubrulle (1994), who gave a more general form for the exponent of the structure functions:

$$\frac{\zeta_p}{\zeta_3} = (1-\Delta)\frac{p}{3} + \frac{\Delta}{1-\beta}(1-\beta^{p/3}) \tag{1.41}$$

where the factors Δ and β depend on the codimension of the dissipative structures and their characteristic of intermittency. From this Boldyrev et al. (2002) deduce for the exponent of the structure function for supersonic compressible MHD turbulence:

$$\frac{\zeta_p}{\zeta_3} = \frac{p}{9} + 1 - \left(\frac{1}{3}\right)^{p/3} \tag{1.42}$$

which they find to be consistent with their numerical simulations. This corresponds to a fluctuation spectrum of the form: $E(k) \propto k^{-1.74}$ which is a little steeper than the famous Kolmogorov spectrum.

Apart from the She and Leveque (1994) model there are many more models for the structure functions which are also introduced in Frisch (1995). These are, however, not introduced here, because we only intended to give a brief overview of what has changed since 1941.

The most important remark to be kept in mind is that it is not possible to distinguish between the different models via a comparison of the omnidirectional spectra. A discrimination between the different models is, however, most easily done on the basis of the higher order structure functions – for measurements with sufficiently small error bars the fifth order or higher structure function can be expected to discriminate one or the other of the models. It is, however, not easy to obtain such high order structure functions, since very good statistics is necessary to be able to obtain these. This posed a major problem in the past, which was finally solved by Benzi et al. (1993), where they introduced the *extended self-similarity*. They claim that the ratio of the slopes of the structure functions remains the same as in the inertial range also in the dissipation range. Thus, with the unity slope of the third-order structure function, the ratio of the other structure functions with the third order structure function nicely yields their exponents even for low Reynolds number turbulence. This is also widely used when evaluating structure functions for numerical simulations.

With this we conclude the discussion of the most important aspects of homogeneous turbulence. Now we will discuss the other field important for this work – the interstellar matter.

1.3 Interstellar Turbulence

After the detailed discussion about turbulence and structure functions we are left to combine the classical picture of the interstellar medium with what was introduced in the preceding section. There we learnt that in MHD turbulence one can expect that the energy injected at large scales is transmitted to the damping scales in an intermittent cascade. For the ISM this means that the kinetic energy injected into the ISM by supernova explosions and other dynamical processes is eventually transformed into small-scale fluctuations, which are dissipated in shock waves, in current sheets or in vortex tubes. These dissipative structures are not space filling but show some degree of intermittency.

This can, interestingly, be connected to actual observations. When discussing the phase structure of the ISM we did not yet include the star forming regions in our considerations. These can be said to exhibit an intermittent behaviour: The densest clouds in interstellar space, which are the regions where new stars are born, show a filamentary structure.

This fact helps to illuminate one of the mysteries concerning the star formation rate. In the classical analyses the star formation rate was usually determined by considering gravitationally collapsing clouds.

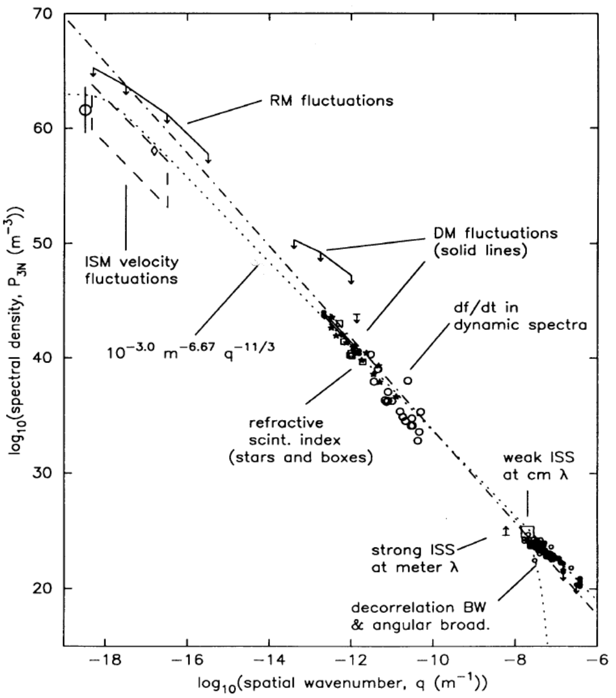

Fig. 1.9: Electron density power spectrum as a function of wavenumber, taken from Armstrong et al. (1995).

Without taking turbulence into account one can compute the Jeans limit giving the minimum mass of a gas cloud that would collapse in a characteristic time. This time, however, implies star formation rates much higher than the one actually encountered in nature.

This contradiction was first resolved by the introduction of a turbulent pressure, which was used to inhibit the rapid gravitational collapse of a dense cloud (see e.g. Lizano and Shu 1989). Recently, this indirect contribution of turbulence to the star formation process was changed to a more active role for the turbulence (see e.g. Elmegreen 1991): The idea that the small star forming clumps of matter are intermittent structures of the ISM turbulence rather than freely decaying clouds in thermal equilibrium with their environments seems to spread in the astrophysical community.

All in all turbulence seems to become more and more important after the initial discussions on a turbulent ISM initiated by von Weizsäcker (1951) was soon abandoned. This abandonment is understandable, when taking into account that the discussion of intermittency in turbulence had not yet been started at that time. With regard to the picture of homogeneous turbulence preferred at that time the observations clearly did not correspond to the picture of global turbulence: instead of a homogeneous distribution of small vortices observations showed what would nowadays be known as an intermittent distribution of molecular clouds. Therefore, a more or less static model of the ISM became quite popular at that time. In that picture the contribution of supernovae was mainly in heating and ionising the diffuse ISM. Even in the 70s the observation of supersonic linewidth was not initially connected to turbulence.

This changed at the end of the seventies, when observation techniques became better. At that time power law correlations were found for different structures in the ISM. Moreover, the smallest scales were already accepted to be turbulent because correlations were found at these scales in radio observations. With the availability of infrared observations astronomers also found filamentary structure in clouds thought so far to belong to the diffuse type. Therefore, turbulence in the ISM became apparent at more and more spatial scales. In 1995, there was for the first time a fluctuation spectrum available for many spatial scales. This spectrum was compiled by Armstrong et al. (1995) for the density fluctuations and is shown in Fig. 1.9. For a more detailed account of the observation of interstellar turbulence see e.g.

Elmegreen and Scalo (2004).

All in all the fact that the interstellar medium is highly turbulent seems to be accepted nowadays by most astronomers. With this acceptance also a different view of the influence of supernova explosions for the ISM started to spread, namely that a major part of the energy of a supernova explosion is transferred into kinetic energy at large spatial scales. This is 'transported' to the damping scales via nonlinear interactions. Remembering that the dynamical energy density is much higher than the thermal energy density it is clear that the energy budget of the ISM is strongly influenced by the turbulence.

Taking all this into account, it is clear that turbulence can not be neglected when discussing the spatial structure of the interstellar medium. It is especially interesting, how strong the intermittency actually is in that environment. Together with that, the study of the turbulence statistics is of great importance to supplement models for particle transport in the Galaxy.

There is, however, a major difference between laboratory turbulence and ISM turbulence since in the latter case there are many additional influences to be taken into account. Therefore, modellers have to ask themselves which are the most important of these influences and how to describe the interstellar plasma correctly. This aspect is investigated in this work.

Chapter 2

The Physical Model

As we learned in the preceding introduction there are many different kinds of plasmas in interstellar space. They reach from those small systems like planetary magnetospheres to the dilute warm gas filling most of the space between the stars of our Milky Way[1] Therefore, it is clear that there is no general physical model, by which all these phases can be described in the same way. We rather have to find the model scenario, which is best suited for the scientific purpose at hand. Here we are interested in modelling the turbulence of the ISM with special regard to the statistics and the spatial structure. Moreover, all the investigations will be done for limited spatial regions. This implies the use of a periodic box for the simulations, since we do not know appropriate boundary conditions for such a region. Furthermore, a periodic box is best suited for the evaluation of the turbulence statistics, keeping in mind that many quantities have to be evaluated in Fourier space.

2.1 Mathematical Description of the ISM Plasma

Before actually discussing the mathematical description of the ISM we first have to check, whether it is justified to speak of the plasma state of the ISM. For this there are several conditions to be checked. A first characteristic of a plasma is the so-called Debye shielding effect. This is related to the fact that charges in a plasma arrange themselves in such a way as to shield any electrostatic field originating from other charges. A measure for the corresponding distance over which the shielded charge can still be felt by other charged particles is the Debye length λ_D:

$$\lambda_D = \sqrt{\frac{\varepsilon_0 k_B}{n_e e^2}} \tag{2.1}$$

For this shielding effect to be of any significance we have to demand even the smallest length scale l under consideration to exceed the Debye length:

$$l \gg \lambda_D \tag{2.2}$$

This relation is fulfilled for all the interstellar environments under consideration in this work. Even for the hottest and at the same time must dilute phase of the ISM – namely the hot coronal gas – the Debye length can be estimated using the numbers from table 1.1 to be of the order of $\lambda_D \simeq 4 \cdot 10^6$ m. This length has to be compared to the smallest spatial scale to be resolved in the simulation, which is about $l \simeq 0.08$ parsecs for the simulations with the highest spatial resolution. Therefore, Eq. (2.2) is clearly fulfilled for the ISM.

For the Debye shielding to be effective in a plasma, however, there also has to be a sufficiently high number of electrons inside a Debye sphere. This condition amounts to:

$$n_e \lambda_D^3 \gg 1 \tag{2.3}$$

---

[1] Further out there are even larger structures, but here we are only interested in the ISM of our own Galaxy.

which is also nicely fulfilled for all phases of the ISM taken into account – all of these have more than 10^5 electrons inside a Debye sphere. Therefore, from the point of view of the possibility of Debye shielding, all phases of the ISM have to be regarded as a plasma.

Another important aspect of plasmas is the possibility for the electron gas to oscillate with respect to the heavier particles. The angular frequency of this collective oscillation of the electrons is known as the electron plasma frequency:

$$\omega_{pe} = \sqrt{\frac{n_e e^2}{m_e \varepsilon_0}} \simeq 56\,\sqrt{n_e}\mathrm{Hz} \tag{2.4}$$

with n_e given in particles per cubic meter. For this independent motion of the electrons to be possible at all it is necessary that the damping of these oscillations by with neutrals is sufficiently weak. Therefore, we have to fulfil the additional constraint:

$$\frac{\omega_{pe}}{2\pi} > \nu_{en} \tag{2.5}$$

where ν_{en} is the electron-neutral collision frequency, which can approximately be given as:

$$\nu_{en} \simeq n_n |\boldsymbol{u}_e - \boldsymbol{u}_n| \sigma_{en} \tag{2.6}$$

Due to the high number density in these regions the collisions frequency can be expected to be highest in molecular clouds. Moreover, the interaction cross section σ_{en} is highest for the lowest temperatures. These also occur in molecular clouds. Therefore, we can be sure that if the above condition holds for molecular clouds it will also be satisfied for other phases of the ISM. Even though the authors discuss interaction of protons and neutrons, from Glassgold et al. (2005) the cross section can be estimated never to exceed a value of $3 \cdot 10^{-17}$ m^2. With this in mind it is clear that the collision frequency is much smaller than the electrons plasma frequency, which even for the low electron densities in molecular clouds will never fall below $\omega_{pe} = 10^3$ Hz, thus, allowing for collective electron fluctuations.

Since we are now sure to be dealing with an actual plasma environment, the next question is how to model this plasma mathematically. There is a whole range of possibilities for the mathematical description of a plasma ranging from kinetic approaches to overall fluid pictures. For numerical turbulence research with the available computer hardware, however, some kind of fluid description is necessary, because a fully kinetic description does not yield sufficiently high Reynolds numbers to gain any statistical information on the turbulence. For such a description to be valid, however, one important condition is that the typical scale for spatial variations is large as compared to the kinetic scales of the fluid.

A good proxy to check this condition is the collisional mean free path, which is generally given as:

$$l_c = (n\sigma_c)^{-1} \tag{2.7}$$

This length scale is signifying the typical distance traversed by a particle in the plasma before it is scattered by a collision. For a fluid description of the medium to be valid this length has to be shorter than the smallest spatial scales over which any significant gradient can be expected in our simulations. As will be seen in the later discussions the strongest shocks even show gradients from one cell to the other. Therefore, it is the size of the numerical cells, which has to exceed the collisional mean free path for a fluid description to be sensible in the case of ISM turbulence.

When taking into account that, e.g., the H^+-H scattering cross section, σ_c, typically decreases for higher energies (see Glassgold et al. 2005) – corresponding to higher temperatures – the dilute ISM will be the phase with the longest collisional mean free path. Thus, as long as the dilute ISM can be described as a fluid, this will also be the case for the denser phases of the ISM. This is especially true when taking into account that in the denser phases molecules determine the actual scattering rate, which are much more efficient with respect to the scattering process. Taking into account that the lowest densities considered in this work never drop below 10^4 particles per cubic metre, with the scattering cross section already for H^+-H scattering always in excess of $3 \cdot 10^{-19}$ m^2, the collisional mean free path will never exceed $3.3 \cdot 10^{14}$ m. This value is still an order of magnitude below the smallest spatial scale of 0.08 pc resolved in our numerical simulations. For the coronal gas, however, things might be different. With the very low number densities and the extremely high temperatures of the gas a fluid description would be questionable at such small scales as investigated in this work. This phase, however, will not be considered here.

Another condition for the validity of the fluid description is connected to the fact that charged particles gyrate around the magnetic field lines. For a fluid description to be valid the radius of these orbits has to be much shorter than the smallest scales over which a gradient occurs in the numerical simulations. The corresponding quantity to be compared to the spatial scales in the numerical simulations is the so-called gyroradius, which can be given in the form:

$$r = \sqrt{\frac{m\beta}{2\mu_0 e^2 n}} \tag{2.8}$$

where $\beta = 2\mu_0 p/B^2$ which is estimated to be 0.3 for the equilibrium ISM. Clearly the gyroradius for the ions will be highest for the more dilute phases of the ISM. But even for the coronal gas the gyroradius does not exceed values of 10^7 m, which is still considerably shorter than the smallest spatial scales resolved in the numerical model. With the fact being established that we can safely use a fluid description for our plasma, we now have to discuss how this model would exactly look like.

2.1.1 The General Fluid Description

Even within the framework of a fluid description for plasmas, however, there are many different realisations available for this description. What becomes available when the conditions for a fluid description are given, is an infinite hierarchy of fluid equations for each particle species α present. The foundation for this hierarchy is the fundamental transport equation:

$$\frac{\partial f_\alpha}{\partial t} + \mathbf{v} \cdot \nabla f_\alpha + \frac{1}{m_\alpha} \boldsymbol{F}_\alpha \cdot \nabla_{\mathbf{v}} f_\alpha = \left(\frac{\delta f_\alpha}{\delta t} \right) \tag{2.9}$$

known as the Boltzmann equation. Here f_α is the particle distribution function in six-dimensional phase space for particle species α. Additionally $\boldsymbol{F}_\alpha$ indicates the forces acting on the particles. This *kinetic* equation describes the evolution of the particle distribution function for each individual species. It contains the full information about the distribution of an ensemble of particles in six-dimensional phase space consisting of the independent spatial ($\boldsymbol{r}$) and velocity ($\mathbf{v}$) coordinates. The right-hand side of the Boltzmann equation contains the collisional interactions between the different particle species.

From the Boltzmann equation the full set of fluid equation for the individual particle species α are obtained by computing *all* its velocity moments. The resulting infinite hierarchy of balance equations still contains the same information as the Boltzmann equation. These equations are coupled to each other by the fact that the balance equation corresponding to the kth velocity moment also contains a $k + 1$th moment term. For actual application to a scientific problem, therefore, this hierarchy has to be truncated by means of a physical assumption for one of the moments of f_α. The equations usually taken into account in a fluid description are the mass, momentum and energy balance equations, representing the first three moments of the Boltzmann equation:

$$\frac{\partial \rho_\alpha}{\partial t} + \nabla \cdot (\rho_\alpha \boldsymbol{u}_\alpha) = S_\alpha \tag{2.10}$$

$$\frac{\partial (\rho_\alpha \boldsymbol{u}_\alpha)}{\partial t} + \nabla \cdot (\rho_\alpha \boldsymbol{u}_\alpha \boldsymbol{u}_\alpha) + \nabla \cdot \mathsf{P}_\alpha - n_\alpha < \boldsymbol{F} >_\alpha = \boldsymbol{M}_\alpha \tag{2.11}$$

$$\frac{1}{\gamma - 1} \frac{\partial p_\alpha}{\partial t} + \frac{1}{\gamma - 1} \nabla \cdot p_\alpha \boldsymbol{u}_\alpha + (\mathsf{P}_\alpha \cdot \nabla) \cdot \boldsymbol{u}_\alpha + \nabla \cdot \boldsymbol{q}_\alpha = E_\alpha \tag{2.12}$$

With only these fluid equations taken into account the hierarchy is truncated by means of a physical assumption for the heat flow vector $\boldsymbol{q}_\alpha$. This we will assume to vanish for the ISM. As for the Boltzmann equation $\boldsymbol{F}_\alpha$ indicates external forces acting on the fluid, of which only the electromagnetic forces will be taken into account. This will be discussed later on, when the MHD equations are derived. The parameters used in the above fluid equations are defined as follows:

$$n_\alpha(\boldsymbol{r}) \equiv \int_v f_\alpha(\boldsymbol{r},\mathbf{v}) d^3\mathrm{v} \qquad \text{Number density} \tag{2.13}$$

$$\rho_\alpha(\boldsymbol{r}) \equiv m_\alpha n_\alpha(\boldsymbol{r}) = m_\alpha \int_v f_\alpha(\boldsymbol{r},\mathbf{v}) d^3\mathrm{v} \qquad \text{Mass density} \tag{2.14}$$

$$\boldsymbol{u}_\alpha(\boldsymbol{r}) \equiv \frac{1}{n_\alpha(\boldsymbol{r})} \int_v \mathbf{v} f_\alpha(\boldsymbol{r},\mathbf{v}) d^3\mathrm{v} \qquad \text{Flow velocity} \tag{2.15}$$

$$\mathsf{P}_\alpha(\boldsymbol{r}) \equiv \rho_\alpha(\boldsymbol{r}) \int_v (\mathbf{v} - \boldsymbol{u}_\alpha(\boldsymbol{r}))(\mathbf{v} - \boldsymbol{u}_\alpha(\boldsymbol{r})) f_\alpha(\boldsymbol{r},\mathbf{v}) d^3\mathrm{v} \qquad \text{Pressure tensor} \tag{2.16}$$

$$p_\alpha(\boldsymbol{r}) \equiv \frac{1}{3} \sum_i \mathsf{P}_{\alpha ii}(\boldsymbol{r}) = \frac{1}{3}\rho_\alpha(\boldsymbol{r}) \int_v |\mathbf{v} - \boldsymbol{u}_\alpha|^2 f_\alpha(\boldsymbol{r},\mathbf{v}) d^3\mathrm{v} \qquad \text{Scalar pressure} \tag{2.17}$$

$$\boldsymbol{q}_\alpha(\boldsymbol{r}) \equiv \frac{1}{2}\rho_\alpha(\boldsymbol{r}) \int_v |\mathbf{v} - \boldsymbol{u}_\alpha(\boldsymbol{r})|^2 (\mathbf{v} - \boldsymbol{u}_\alpha(\boldsymbol{r})) f_\alpha(\boldsymbol{r},\mathbf{v}) d^3\mathrm{v} \qquad \text{Heat flow} \tag{2.18}$$

Here $(\mathbf{v} - \boldsymbol{u}_\alpha(\boldsymbol{r}))$ is the difference between the velocity $\mathbf{v}$ of a particle of type α and the average velocity $\boldsymbol{u}_\alpha$ of the corresponding species. Apart from these fluid quantities there are also the source terms to be specified. These are defined as:

$$\begin{aligned} S_\alpha &\equiv m_\alpha \int_v \left(\frac{\delta f_\alpha(\boldsymbol{r},\mathbf{v})}{\delta t}\right)_{coll} d^3\mathrm{v} \notag \\ \boldsymbol{M}_\alpha &\equiv m_\alpha \int_v \mathbf{v} \left(\frac{\delta f_\alpha(\boldsymbol{r},\mathbf{v})}{\delta t}\right)_{coll} d^3\mathrm{v} \tag{2.19} \\ E_\alpha &\equiv \frac{1}{2} m_\alpha \int_v |\mathbf{v} - \boldsymbol{u}_\alpha|^2 \left(\frac{\delta f_\alpha(\boldsymbol{r},\mathbf{v})}{\delta t}\right)_{coll} d^3\mathrm{v} \tag{2.20} \end{aligned}$$

These terms describe sources or sinks of density, momentum and energy due to collisions and processes like ionisation and recombination. Thus, the only missing quantities for the description of astrophysical fluids are the external forces for the momentum equation. Disregarding gravitational interactions and radiation pressure the only remaining external forces relevant in astrophysical contexts are the electromagnetic ones.

2.1.2 Forces

The term $\boldsymbol{F}_\alpha$ describes the forces acting on the fluid of species α. These can be of internal or external nature – either forces effected by other fluid elements or forces acting on the system from the outside. A typical example for an external force is the gravitation acting on the system from a large mass like the Sun or the galactic centre. This, however, will not be taken into account in the following, since it is only of minor influence for the local structure of most phases of the interstellar medium. Only for molecular clouds gravitational interaction in the form of self-gravity of the plasma might become important. As will be discussed in chapter 4, however, this would only become important for dense cloud cores, which, however, are not investigated in this work. Apart from that self-gravity is – like the kinetic equation – numerically very expensive to handle. Investigation of self-gravitating turbulence has to be left as a task for a future generation of supercomputers.

The only remaining forces being of interest for the interstellar matter are, therefore, the electromagnetic forces. These are described via the *Lorentz-force* acting on the individual particles:

$$\boldsymbol{F}_L = q(\boldsymbol{E} + \mathbf{v} \times \boldsymbol{B}) \tag{2.21}$$

The two additional unknowns – namely the electric (**E**) and the magnetic field (**B**) – can be deduced from the Maxwell equations:

2.1.3 Maxwell Equations

The equations governing electromagnetic phenomena are the famous Maxwell equations. For the case of a vacuum these are:

$$\nabla \cdot \boldsymbol{E} = \frac{\rho^c}{\varepsilon_0} \qquad \text{Coulomb's law} \tag{2.22}$$

$$\nabla \times \boldsymbol{B} - \frac{1}{c^2}\frac{\partial \boldsymbol{E}}{\partial t} = \mu_0 \boldsymbol{J} \qquad \text{Ampère's law} \tag{2.23}$$

$$\nabla \times \boldsymbol{E} + \frac{\partial \boldsymbol{B}}{\partial t} = 0 \qquad \text{Faraday's law} \tag{2.24}$$

$$\nabla \cdot \boldsymbol{B} = 0 \qquad \text{No magnetic monopoles} \tag{2.25}$$

Here $\boldsymbol{J}$ and ρ^c are the electromagnetic current density and the charge density, respectively. In a highly conductive medium like the ISM the term commonly known as the *displacement current* $\frac{\partial \boldsymbol{E}}{c^2 \partial t}$ can be omitted whenever the typical velocities are much lower than the speed of light. Because this is always the case in all the phases of the ISM to be taken into account in this work this assumption is used henceforth for the remainder of this work.

Whereas it is possible to solve the coupled set of the fluid and the Maxwell equations this is neither necessary nor desirable for the ISM. One important disadvantage of the full Maxwell equations is the fact that electromagnetic waves have to be taken into account. Just by arguments of computational cost these have to be left out of our considerations. Generally, however, we are rather interested in plasma waves than in electromagnetic waves. Therefore, we will use a reduced system to describe electromagnetic phenomena as will be introduced later on. Before this, however, we will discuss how to merge the system of fluid equations for the different species into a reduced system of equations.

2.2 Macroscopic Equations

In principle it is possible just to take the derived fluid equations and integrate them for each species separately. This, however, is simply not necessary for most parts of the ISM since many species are so rare, that they are of no importance for the global dynamics and can, therefore, be left out of the considerations. Regarding their abundance it is definitely electrons, hydrogen atoms and protons, which are the most important species for the major parts of the ISM – in the colder parts of the ISM also hydrogen molecules can become important.

With the number of species reduced to those relevant for the problem under consideration it is still possible to simplify the system of equations even further. For the MHD equations, for example, the idea is to describe the plasma as one conducting fluid instead of describing the behaviour of the individual species separately. For this description adding the contributions of each individual species results in variables like the total mass and the total momentum. This means that by computing the sums of the single species equations introduced above we will arrive at the MHD equations.

Unfortunately, it is not a priori clear whether this is a good approximation for all phases of the ISM since the coupling between neutrals and charged particles might be too weak to justify the usage of the MHD equations for the more dilute phases. This problem can easily be visualised by the discussion of the typical speeds. For a neutral fluid signals are propagated typically with the speed of sound. For a charged fluid there are several wave propagation speeds. For example the *Alfvén* speed describes an additional wave propagation mode being possible due to the presence of a magnetic field:

$$\mathrm{v}_A = \frac{B_0}{\sqrt{\mu_0 \rho}} \tag{2.26}$$

Obviously the value for the Alfvén speed depends on some mass density ρ. However, depending on the strength of the coupling this is either the overall density in the case of strong coupling or the density of the charged particles, when the coupling is weak. Therefore, it can be expected that describing a medium with weak coupling between ions and neutrals via the MHD equations will yield unphysical results. It is, however, not initially clear what *weak coupling* means in this context.

To solve this problem, the easiest thing is to consider two distinct fluids instead of one: one fluid for the neutral particles and one for the charged particles connected by the appropriate interaction terms. In such an approach, however, the major difficulty lies in finding the appropriate source terms – and in a correct numerical implementation. In this work we intend to compare the results obtained via the two different approaches. Therefore, we introduce a two-fluid description – summing up charged and neutral fluids respectively – for the investigation of interstellar turbulence.

In the subsequent paragraphs we will derive the corresponding equations for the two-fluid approach. The MHD equations are easily found from these by the sum of the resulting equations. We start our discussion by defining averaged quantities, which will be described by the macroscopic equations.

2.2.1 Macroscopic Variables

Instead of considering each plasma species itself it is very convenient to use macroscopic quantities. In the case of the two-fluid approach this means that we will only investigate the sums of the quantities for the neutral particles and the charged particles via their corresponding equations. For the species to be averaged, we will now define the important average quantities.

First, for each of the examined fluids the mass density is just the sum of all individual mass densities:

$$\rho = \sum_\alpha \rho_\alpha = \sum_\alpha m_\alpha n_\alpha \qquad \rho_n = \sum_\beta \rho_\beta = \sum_\beta m_\beta n_\beta \tag{2.27}$$

where ρ is the mass density of the charged particle fluid and ρ_n correspondingly designates the mass density of the neutral particles. Thus, α and β indicate the charged and the neutral species respectively. For the charged particle species the same is done for the electric charge density, which is referred to as ρ^c (see also Eq. (2.22) to distinguish it from the mass density:

$$\rho^c = \sum_\alpha \rho^c_\alpha = \sum_\alpha q_\alpha n_\alpha \tag{2.28}$$

where each particle of species α carries the charge q_α. The next quantity to define are the mean convection velocities for the two fluids, which are given as:

$$\rho \boldsymbol{u} = \sum_\alpha \rho_\alpha \boldsymbol{u}_\alpha \qquad \rho_n \boldsymbol{u}_n = \sum_\beta \rho_\beta \boldsymbol{u}_\beta \tag{2.29}$$

These velocities are actually the mass-weighted mean of the individual species velocities. From these definitions we find the expression for the electric current density to be:

$$\boldsymbol{J} = \sum_\alpha q_\alpha n_\alpha \boldsymbol{u}_\alpha \tag{2.30}$$

For the charged particle species these general relations can be simplified due to the high conductivity in interstellar space:

2.2.2 The Charged Particle Fluid

Whenever being interested only in the fluid of the charged particles – either in the case where no neutral particles are present[2] or in the case where they are considered separately – the above quantities are

---

[2] Which is a good assumption, e.g., for the solar wind in the inner heliosphere or for the coronal gas in the ISM.

modified in the following way:

$\rho = m_e n_e + m_i n_i$	Mass density	(2.31)
$\rho^c = e n_e - e n_i$	Charge density	(2.32)
$\boldsymbol{u} = \dfrac{\rho_e \boldsymbol{u}_e + \rho_i \boldsymbol{u}_i}{\rho_e + \rho_i}$	Mean fluid velocity	(2.33)
$\boldsymbol{J} = e n_i \boldsymbol{u}_i - e n_e \boldsymbol{u}_e$	Electric current density	(2.34)

where we only took electrons and one singly charged positive ion species into account. From the definition of the electric current density it is possible to obtain an expression for the velocities of the individual species. A brief manipulation of Eq. (2.34) yields for those:

$$\boldsymbol{u}_i = \frac{\mu}{m_e}\frac{\rho}{\rho_i}\boldsymbol{u} + \frac{\mu}{e\rho_i}\boldsymbol{J} \tag{2.35}$$

$$\boldsymbol{u}_e = \frac{\mu}{m_i}\frac{\rho}{\rho_e}\boldsymbol{u} - \frac{\mu}{e\rho_e}\boldsymbol{J} \tag{2.36}$$

where $\mu = m_e m_i/(m_e + m_i)$ is the reduced mass.

One important point about interstellar matter is the high conductivity of the plasma in interstellar space. That means that local charge increases on spatial scales larger than the Debye-length are quickly removed by high currents. Therefore, electrons and ions can safely be assumed to have the same number density on such scales:

$$\frac{n_e - n_i}{n_e + n_i} \ll 1 \tag{2.37}$$

Thus, for the remainder of this work the resulting equations will by simplified by usage of:

$$n = n_e = n_i \tag{2.38}$$

By this we also find a more simple form for the current density:

$$\boldsymbol{J} = en(\boldsymbol{u}_i - \boldsymbol{u}_e) \tag{2.39}$$

This equation can now be used to rewrite the equation for the average velocity of electrons and ions. We start by writing:

$$\boldsymbol{u} = \boldsymbol{u}_i - \frac{\rho_e}{\rho}(\boldsymbol{u}_i - \boldsymbol{u}_e) = \boldsymbol{u}_e + \frac{\rho_i}{\rho}(\boldsymbol{u}_i - \boldsymbol{u}_e) \tag{2.40}$$

Then we get, using Eq. (2.39):

$$\boldsymbol{u} = \boldsymbol{u}_i - \frac{\rho_e}{\rho}\left(\frac{\boldsymbol{J}}{en}\right) = \boldsymbol{u}_e + \frac{\rho_i}{\rho}\left(\frac{\boldsymbol{J}}{en}\right) \tag{2.41}$$

Thus, we find for the individual velocities of ion and electron fluids using the assumption of high conductivity:

$$\boldsymbol{u}_i = \boldsymbol{u} + \frac{m_e}{e\rho}\boldsymbol{J} \tag{2.42}$$

$$\boldsymbol{u}_e = \boldsymbol{u} - \frac{m_i}{e\rho}\boldsymbol{J} \tag{2.43}$$

With all this in mind we will now derive the equations describing the newly introduced variables.

2.3 Continuity Equation

To get an idea of how the individual fluid equations are obtained, we will briefly show the corresponding procedure using the example of the continuity equation. As stated above this is done via adding the equations describing the mass density of all species to be described by a single fluid equation (that is either the neutral or the charged fluid). For the example of a charged particle fluid consisting of electrons and one ion species this sum reads:

$$\frac{\partial(\rho_i + \rho_e)}{\partial t} + \nabla \cdot (\rho_i \boldsymbol{u}_i + \rho_e \boldsymbol{u}_e) = S_i + S_e \tag{2.44}$$

Despite the fact that ionisation processes become important in the dilute phases of the ISM, this task is left for the future. Because the main focus is on molecular clouds here, it appears to be a well-justified assumption (see Tóth 1994; Hosking and Whitworth 2004). Therefore the corresponding sources and sinks of mass density can be set to zero in this context. With the above definitions of the macroscopic fluid variables, we therefore find for both fluids:

$$\frac{\partial\rho}{\partial t} + \nabla \cdot (\rho \boldsymbol{u}) = 0 \tag{2.45}$$

$$\frac{\partial\rho_n}{\partial t} + \nabla \cdot (\rho_n \boldsymbol{u}_n) = 0 \tag{2.46}$$

In general the fluid equations corresponding to the higher order moments of the Boltzmann equation are derived in the same way. The derivations become, however, increasingly complicated with the growing order and are, therefore, given in appendix B. The results of these considerations are stated in the following paragraphs.

2.4 Momentum Balance

As in the case of the continuity equation that for the momentum balance for the charged particle fluid basically results from an addition of the corresponding equations for the individual species. In the case of the momentum balance and the balance equations of higher order, however, this is complicated by the fact that in general the sum of the individual pressure tensors does not correspond to the overall pressure tensor. While this is less critical when the individual species velocities are very similar to the average fluid velocities the derivation is performed in a form as general as possible.

Fortunately, we do not have to include any external forces for the neutral fluid, since gravitation will have no major impact on the system (and self-gravity is omitted from the discussion). As discussed above, the remaining forces for the charged particle fluid are, thus, merely the electromagnetic ones.

The only additional obstacle in this derivation are the source terms connecting the individual species momentum equations. For these we will only take elastic scattering and charge exchange reactions into account, both being described by interaction terms of the same form.

Taking all this into account, we find for both momentum equations:

$$\frac{\partial\left(\rho_n \boldsymbol{u}_n\right)}{\partial t} + \nabla \cdot (\rho_n \boldsymbol{u}_n \boldsymbol{u}_n) + \nabla \cdot \mathsf{P}_n = \nu_n \rho (\boldsymbol{u} - \boldsymbol{u}_n) + \frac{\mu}{e}\left(\nu_{in} - \nu_{en}\right) \boldsymbol{J} \qquad \text{neutral fluid} \tag{2.47}$$

$$\frac{\partial\left(\rho \boldsymbol{u}\right)}{\partial t} + \nabla \cdot (\rho \boldsymbol{u} \boldsymbol{u}) + \nabla \cdot \mathsf{P} + \frac{1}{\mu_0} \boldsymbol{B} \times (\nabla \times \boldsymbol{B}) = -\nu_n \rho (\boldsymbol{u} - \boldsymbol{u}_n) - \frac{\mu}{e}\left(\nu_{in} - \nu_{en}\right) \boldsymbol{J} \qquad \text{charged fluid} \tag{2.48}$$

For the momentum balance of the charged fluid we used the additional assumption that the displacement current can be neglected for ISM plasmas.

Comparing the two equations it becomes clear that the source terms on the right-hand sides balance each other as expected with the source terms stemming from mutual interactions. The last of the source terms given in Eqs. (2.48) and (2.47) is a frictional force aligned to the electric current. It is of the order of the frequency of neutral-charged particle collisions divided by the electron gyrofrequency (see Song et al. 2001) and can generally be neglected for ISM plasmas: with the typical magnetic field strength of $5 \cdot 10^{-10}$ T for the ISM we find an electron gyrofrequency of $\omega_e \simeq 88$ Hz which is orders of magnitude higher than typical collision frequencies.

Equation (2.48) still contains the magnetic field. Therefore we also have to find an equation describing the evolution of the magnetic induction. For this we consider the generalised form of Ohm's law in the next section.

2.5 The Induction Equation

As was already stated above, the magnetic field is described in its most general form by usage of Maxwell's equations (2.22) - (2.25). Of these Faraday's law (2.24) describes the temporal evolution of the magnetic field.

$$\frac{\partial \boldsymbol{B}}{\partial t} = -\nabla \times \boldsymbol{E} \tag{2.49}$$

Thus, next we need an equation either describing the time evolution of the electric field or one linking the electric field with the magnetic induction. At this point it is customary to decide for the latter. Thus, we use *Ohm's law*, which relates the electric field to the current density, instead of solving the complete set of Maxwell's equations.

In its usual form, that is when neglecting the temporal evolution of the current density and the pressure terms, Ohm's law takes the form (see e.g. Bittencourt 2004):

$$\eta \boldsymbol{J} = \boldsymbol{E} + \boldsymbol{u} \times \boldsymbol{B} \tag{2.50}$$

with η indicating the resistivity. In appendix B.2 this relation is shown to apply also to a multi-fluid description of the system. Solving Ohm's law for the electric field and inserting the result in the above equation yields:

$$\frac{\partial \boldsymbol{B}}{\partial t} = \nabla \times (\boldsymbol{u} \times \boldsymbol{B}) - \nabla \times (\eta \boldsymbol{J}) \tag{2.51}$$

Again making use of the fact that for interstellar plasmas the displacement current is negligible yields a simplified version of Ampère's law. Using this in the above equation we end up with an induction equation describing the temporal evolution of the magnetic field depending only on the fluid velocity (of the charged particle fluid) and the magnetic induction:

$$\frac{\partial \boldsymbol{B}}{\partial t} = \nabla \times (\boldsymbol{u} \times \boldsymbol{B}) - \frac{1}{\mu_0} \underbrace{\nabla \times \eta(\nabla \times \boldsymbol{B})}_{(\nabla\eta) \times \nabla \times \boldsymbol{B} + \eta \underbrace{\nabla \times (\nabla \times \boldsymbol{B})}_{\nabla^2 \boldsymbol{B}}} \tag{2.52}$$

$$= \nabla \times (\boldsymbol{u} \times \boldsymbol{B}) + \frac{1}{\mu_0} \left[\eta \nabla^2 \boldsymbol{B} - (\nabla\eta) \times (\nabla \times \boldsymbol{B}) \right] \tag{2.53}$$

For the interstellar medium the terms containing the resistivity $\eta \propto 1/\sigma$ are negligible due to the extraordinary high conductivity σ. Apart from that the first term on the RHS can be transformed into a conservative form:

$$\nabla \times (\boldsymbol{u} \times \boldsymbol{B}) = -\nabla \cdot (\boldsymbol{uB} - \boldsymbol{Bu}) \tag{2.54}$$

Thus, we arrive at a hyperbolic equation for the magnetic induction:

$$\frac{\partial \boldsymbol{B}}{\partial t} = -\nabla \cdot (\boldsymbol{uB} - \boldsymbol{Bu}) \tag{2.55}$$

So far we derived seven equations to describe eight quantities – the mass density, the three components of the momentum density, the three components of the magnetic induction and the pressure. Therefore, to close the system we need at least one additional equation. This equation has to couple the pressure to the system of equations derived so far.

2.6 Closure of the System

To couple the pressure to the system of equations derived so far there are, in principle, several methods at hand. Either we use an equation of state connecting the pressure directly to the other variables or we have to use an equation describing the temporal evolution of the pressure. The latter is the natural choice, because the equations of state should be somehow contained in such an evolution equation.

2.6.1 Internal Energy

As for the other evolution equations it is also possible to derive an evolution equation for the pressure of the neutral and the charged fluid by adding the respective evolution equations. As is shown in appendix B.3.2 the evolution of the pressure of the charged particle fluid is determined by the following somewhat lengthy equation that takes interactions between the charged fluid and the neutral fluid into account:

$$\begin{aligned} &\frac{1}{\gamma-1}\frac{\partial p}{\partial t}+\frac{1}{2}\frac{\partial}{\partial t}\left(\rho u^2\right)+\nabla\cdot\left(\left(\frac{1}{\gamma-1}p+\frac{1}{2}\rho u^2+\mathsf{P}\right)\boldsymbol{u}\right)+\nabla\cdot\boldsymbol{q} \\ &\qquad=-\eta\boldsymbol{J}^2-\nu_n\rho\boldsymbol{u}\cdot(\boldsymbol{u}-\boldsymbol{u}_n)-\frac{\mu}{e}\left(\nu_{in}-\nu_{en}\right)\boldsymbol{J}\cdot(2\boldsymbol{u}-\boldsymbol{u}_n)-\left(\frac{\mu^2}{e^2n}\left(\frac{\nu_{in}}{m_i}+\frac{\nu_{en}}{m_e}\right)\right)J^2+\boldsymbol{J}\cdot\boldsymbol{E}+E_i+E_e \end{aligned} \tag{2.56}$$

Here we already included the source terms stemming from the momentum equation explicitly; the source terms for the single species pressure equations E_i and E_e still have to be specified. This equation describes the evolution of the thermal energy density of the system. This can be seen as follows. The internal energy in its most general form for ν mols of a polyatomic gas is given as:

$$e_{Int}=\nu c_V T \tag{2.57}$$

where T is the corresponding temperature and c_V is the specific heat for constant volume. The latter depends on the structure of the molecules or atoms which the gas under consideration is comprised of. The most general form is:

$$c_V=\frac{3}{2}R+\frac{1}{2}RN_{Rot}+RN_{Vib} \tag{2.58}$$

where N_{Rot} and N_{Vib} indicate the number of rotational and vibrational degrees of freedom. Only the first term describing the kinetic degrees of freedom is present for all gases. The others only occur for gases comprised of molecules. All this information is usually shifted into the adiabatic exponent γ. This is connected to the specific heat in the following way:

$$\gamma=\frac{c_v+R}{c_v}\qquad\Longrightarrow\qquad c_v=\frac{R}{\gamma-1} \tag{2.59}$$

With this, we finally find for the internal energy:

$$e_{Int}=\frac{1}{\gamma-1}(n_e+n_i)k_BT=\frac{1}{\gamma-1}p \tag{2.60}$$

where on one hand we made use of the relations

$$R=N_ak_B,\qquad\text{and}\qquad \nu N_a=n \tag{2.61}$$

together with ideal gas law:

$$p=(n_e+n_i)k_BT \tag{2.62}$$

Deviations from the latter are known to occur only for denser gases and can, thus, be safely neglected for applications to interstellar space. Unfortunately the above pressure equation is not of conservative form. Apart from the fact that pressure is not a conserved quantity, this also becomes clear from the source terms of the above equation. There, the Ohmic heating term $\eta \boldsymbol{J}^2$ results from a conversion of kinetic energy of the individual charged fluids into heat and, thus, pressure. Therefore, even for a system without external energy sources the pressure is not conserved.

For the correct representation of a shock in a numerical scheme it is, however, necessary for all evolution equations to be conservative. This is illustrated in Leveque (1992), where it is shown that for a non-conservative form of the equations a numerical scheme yields erroneous results for the case of Burgers' equation. This is also connected to the fact that the entropy must not decrease with time.

2.6.2 Total Energy Density

The conservative equation, which contains the above evolution equation for the thermal energy density, is the equation for the temporal evolution of the total energy density. Whereas the pressure equation in the form given above describes the time evolution of the thermal energy density, for the total energy density also the kinetic and magnetic energy have to be taken into account. With these energies being defined as:

$$e_{fluid} = \frac{\rho|\boldsymbol{u}|^2}{2} \qquad \text{and} \qquad e_{mag} = \frac{|\boldsymbol{B}|^2}{2\mu_0} \tag{2.63}$$

we have to find an equation for the overall energy density:

$$e = \frac{\rho|\boldsymbol{u}|^2}{2} + \frac{|\boldsymbol{B}|^2}{2\mu_0} + \frac{p}{\gamma - 1} \qquad \text{charged fluid} \tag{2.64}$$

$$e_n = \frac{\rho|\boldsymbol{u}_n|^2}{2} + \frac{p_n}{\gamma - 1} \qquad \text{neutral fluid} \tag{2.65}$$

This equation is obtained in much the same way as the other macroscopic equations. By summing of the individual equations we obtain an equation for the global fluid under consideration. For this we have to make use of the equations obtained so far. All in all the computation is straightforward but quite tedious. This is especially so due to the large number of interaction terms. With the actual computation given in appendix B.3 we finally arrive at:

$$\frac{\partial e}{\partial t} + \nabla \cdot \left(\left(e + \frac{B^2}{2\mu_0} + \mathsf{P}\cdot \right) \boldsymbol{u} + \boldsymbol{q} - \frac{1}{\mu_0}(\boldsymbol{u}\cdot\boldsymbol{B})\boldsymbol{B} + \eta \boldsymbol{J} \times \frac{\boldsymbol{B}}{\mu_0} \right) = -S_{ien} \qquad \text{(ionised fluid)} \tag{2.66}$$

$$\frac{\partial e_n}{\partial t} + \nabla \cdot (e_n + \mathsf{P}\cdot)\boldsymbol{u}_n + \nabla \cdot \boldsymbol{q}_n = S_{ien} \qquad \text{(neutral fluid)} \tag{2.67}$$

where the interaction terms are given as:

$$\begin{aligned} S_{ien} =& \nu_n \rho \boldsymbol{u}_n \cdot (\boldsymbol{u} - \boldsymbol{u}_n) + \frac{\mu}{e}(\nu_{in} - \nu_{en})\, \boldsymbol{J} \cdot \boldsymbol{u}_n \\ &+ 2\frac{k_B}{\gamma - 1}\rho_i \frac{\nu_{in}}{m_i + m_n}(T_i - T_n) + 2\frac{k_B}{\gamma - 1}\rho_e \frac{\nu_{en}}{m_e + m_n}(T_e - T_n) \\ &+ \left(\frac{\nu_{in}}{m_i + m_n}\right)\frac{1}{n}\left(\rho_i(\boldsymbol{u} - \boldsymbol{u}_n) - \frac{\mu}{e}\boldsymbol{J}\right)^2 + \left(\frac{\nu_{en}}{m_e + m_n}\right)\frac{1}{n}\left(\rho_e(\boldsymbol{u} - \boldsymbol{u}_n) + \frac{\mu}{e}\boldsymbol{J}\right)^2 \end{aligned} \tag{2.68}$$

These equations together with the definitions of the overall energy densities finally closes the system of equations. When summing up the equations for the two-fluid system one arrives again at the classical MHD equations. Before continuing with the discussion of the numerical implementation of these equations, however, we first will address additional issues concerning the physical model.

2.7 External Influences

What we will discuss in this section are the external influences on the plasma analysed in this work. As was already mentioned we will neglect any gravitational forces in order to be able to concentrate on the influence of turbulence itself.

For this, one has to include one important external influence onto the system namely the energy inherent in the turbulent fluctuations:

2.7.1 Turbulence Driving

As was discussed in the introduction what is generally known as turbulence is the decay of large-scale eddies into successively smaller ones. This means that the kinetic energy has to be transferred to such large scales in the first place. As was also explained in the introduction it is generally thought, that supernova explosions and other such forceful events supply the energy for the fluctuations observed in interstellar space. There are different approaches to capture this energy input in a numerical model.

The approach nearest to what is apparently realised in nature is to use Sedov explosions (see Sedov 1959) to model individual supernova events. This is done in several works with the aim to simulate the global galactic structure (see e.g. de Avillez 2000). This approach is suited for such large-scale models, but it would not be sensible to use when examining small-scale structures like molecular clouds.

In the latter case the scale on which supernova release their energy into the plasma is often larger than the extent of the computational domain. Therefore, the energy input has to be modelled indirectly in these cases. For this the considerations about turbulence can be taken into account. Within the scenario that the fluctuation energy is transported to successively smaller scales, the idea for the energy input into the computational domain would be to put in some fluctuations on large scales stemming from the energy input at even larger scales.

Ultimately, the energy input is applied in a wavenumber space representation with energy being put into the system only at the smallest wavenumbers corresponding to the largest spatial scales available for the computation. Considering that it is found that fluctuations in the inertial range are mainly incompressible only solenoidal velocity fluctuations are put into the system. This is to mimic the fact that the fluctuations occurring on the scales under consideration are being transported by the turbulence from even larger scales.

The numerical implementation of this driving force will be discussed in the next chapter. Here it was only important to introduce the idea of a continuous forcing of the fluctuations at large spatial scales.

Together with this input of energy into the computational domain we also have to consider dissipation. Otherwise the energy content of the system would not be limited at large times. This means, that some way to dissipate the energy has to be introduced. Whereas the ideal MHD equations do not contain any dissipation, it already becomes important when using a two-fluid description for the plasma. Moreover, the numerical scheme used in this work introduces additional dissipation. Both types of dissipation essentially convert kinetic energy into thermal energy. In this case, the problem is how to get rid of the thermal energy.

2.7.2 Heating and Cooling Processes

Due to the continuous input of kinetic energy, which is converted into thermal energy we have to find means to get rid of the unphysical, excessive heat. In the interstellar medium, heat, generated e.g. by dissipation near interstellar shocks, is usually radiated away by line radiation. Especially at temperatures up to $\sim 10^4$K the cooling of interstellar plasma mainly occurs due to line radiation of different neutral atoms or molecules. The most important of these coolants are discussed in Penston (1970) and Dalgarno and McCray (1972). According to these authors the cooling function for interstellar matter can in its most general form be given as:

$$\Lambda(x,T) = \sum_i \frac{n_{x_i}}{n_H} \left[\frac{n_e}{n_H} \lambda_e(x_i,T) + \lambda_H(x_i,T) \right] \tag{2.69}$$

where the sum is over all relevant species. Here the ratio n_{x_i}/n_H gives the relative abundance of the species under consideration, which is kept constant for the computations (nucleosynthesis by stars and

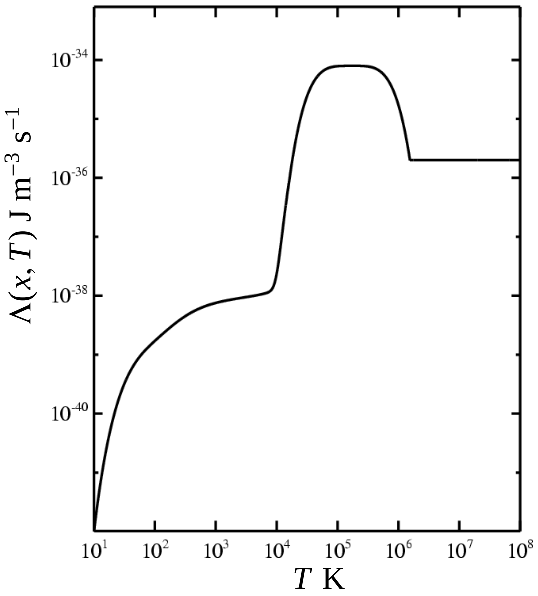

Fig. 2.1: Cooling function as used in this work. For temperatures up to $10^{4.2}$K values as given in Penston (1970) are used. The cooling curve for higher temperatures is approximated as suggested in Gerritsen and Icke (1997).

release of, thus, enriched plasma into the interstellar medium is disregarded here). The factor x represents the ratio of the electron number density to the number density of hydrogen nuclei. For our purpose this will also be kept constant. In this work we will use the individual cooling functions $\lambda_H(x_i, T)$ and $\lambda_e(x_i, T)$ given in Penston (1970). Above some $10^{4.2}$ K, however, most elements become ionised. The corresponding equilibrium ionisation for the various elements in interstellar matter is computed, e.g., in Cox and Tucker (1969) from which these authors also deduce the cooling function for temperatures above $10^{4.2}$ K. Connecting both regimes gives the cooling rates for a broad range of temperatures, the result of which is the classical cooling curve depicted, e.g., in Dalgarno and McCray (1972).

For the temperature range up to $10^{4.2}$ K we use the explicit values tabulated in Penston (1970). The cooling function for higher temperature is then approximated by the parameterisation given in Gerritsen and Icke (1997). This yields the final form of the cooling function given in Fig. 2.1.

Similar to the line cooling processes interstellar matter is also heated via external radiation absorbed in the gas. Dominant in that respect is the absorption of ultraviolet radiation absorbed by dust grains present in the ISM. Other processes like heating due to cosmic rays and X-rays is negligible for the major part of the interstellar matter (see Wolfire et al. 1995).

The energy absorbed by the dust grains is then transfered to the gas by collisions with the dust particles. Bakes and Tielens (1994) give for the corresponding heating rate of the interstellar gas:

$$n_H\Gamma = 1.0 \cdot 10^{-25} n\varepsilon G_0 \text{ J m}^{-3} \text{ s}^{-1} \tag{2.70}$$

Here ε is the fraction of FUV radiation absorbed by the dust grains, that is converted to the heating of the gas and is mainly determined by the neutral fraction of the gas under consideration. This fraction is estimated by Bakes and Tielens as:

$$\varepsilon = \frac{4.9 \cdot 10^{-2}}{1 + 96 \left(G_0 T^{1/2}/n_e\right)^{0.73}} + \frac{3.7 \cdot 10^{-2} (T/10^4)^{0.7}}{1 + 2 \cdot 10^2 \left(G_0 T^{1/2}/n_e\right)} \tag{2.71}$$

where n_e is the electron density. The variable G_0 occurring in both equations is the incident FUV field normalised to the estimate of the local interstellar value of $f_\gamma = 1.6 \cdot 10^{-6}$J m^{-2} s^{-1} (see Habing 1968) which is assumed to be about 1.7.

The above formula has, however, to be used with care, since it is, according to the authors, only valid for a restricted range of parameters – i.e. it should not be applied to temperatures above 10^4 K. This also becomes clear from the fact that not only ε increases without bounds for increasing temperature, but also by the fact that it becomes greater than unity, which is in conflict with its interpretation as an efficiency.

2.7.3 The Equation of State

When it is safe to assume an isothermal medium, which would exist for very efficient cooling, the treatment becomes much simpler. In such a case the energy equation can be shown to be reduced to an equation of state of the form:

$$p = c_s \rho \tag{2.72}$$

where c_s is the isothermal speed of sound. While this would reduce the numerical cost of the method, since the integration of the energy equation together with any cooling terms can be omitted, the medium has to be initialised very careful. Without an energy equation the system can not self-consistently converge to the correct pressure values. This is discussed in more detail in chapter 4, where we describe the molecular cloud medium using an equation of state.

2.7.4 Simulation Time Scale

Regardless if the system of equations is closed by an equation of state or an evolution equation for the total energy density, we can expect the system to advance eventually to an equilibrium. In the case of radiative cooling there will exist a balance between the input of kinetic, external heating and the heat output by radiative cooling. For the isothermal case it is rather an equilibrium between the input of kinetic energy and natural as well as numerical dissipation.

Thus, one can expect that the system will eventually advance to a balance between energy losses (either radiative losses or just losses of kinetic energy) and kinetic energy input. At that stage there will be a finite amount of kinetic energy stored in the system. This balance yields one of the most important time scales for turbulence. According to Frisch (1995) the so-called *large-eddy turnover time* is given as:

$$\tau = \frac{L}{\mathrm{v}_0} \qquad \text{with} \qquad L = \frac{(\mathrm{v}_0)^3}{\varepsilon} \qquad \text{and} \qquad \mathrm{v}_0 = \left(\frac{2}{3}E\right)^{1/2} \tag{2.73}$$

where E is the overall energy contained in the numerical domain and ε is the corresponding overall dissipation rate. This time scale describes the characteristic interaction time of eddies at the largest scales. Dimensionally it is obvious that this classical estimate was adopted for incompressible turbulence. For compressible turbulence one has to find another estimate. Sticking to the idea to use some ratio of a characteristic scale to a characteristic velocity, we will use the same argument as it is given in Padoan et al. (2004). With the turbulence driving being applied for wavenumbers up to $kL/2\pi =$, the largest turbulent scale is approximately $L/3$, where L is the length scale of the numerical domain. Using additionally the average velocity $\overline{u}$ as the characteristic velocity, we find:

$$\tau_D = \frac{L}{3\overline{u}} \tag{2.74}$$

In high Mach number turbulence any of these time scales can be much shorter than the sound crossing time for a sound wave to traverse the computational domain. This is due to the fact that the interaction of the large eddies determines the dynamics of turbulence. For a turbulence simulation it is essential for the simulations to run for several of these time scales.

Variable				with	normalisation constant		
Length	x	$=$	$L\,\tilde{x}$	L	[m]		
Mass	m	$=$	$m_0\,\tilde{m}$	m_0	[kg]		
Number density	n	$=$	$n_0\,\tilde{n}$	n_0	[m^{-3}]		
Temperature	T	$=$	$T_0\,\tilde{T}$	T_0	[K]		
Density	ρ	$=$	$\rho_0\,\tilde{\rho}$	ρ_0	[kg m^{-3}]	$=$	$m_0 n_0$
Gas pressure	P	$=$	$P_0\,\tilde{P}$	P_0	[Pa]	$=$	$n_0 k_B T_0$
Velocity	u	$=$	$u_0\,\tilde{u}$	u_0	[m s^{-1}]	$=$	$c_s = \sqrt{k_B T_0/m_p}$
Time	t	$=$	$\tau\,\tilde{t}$	τ	[s]	$=$	$L/u_0 = L/c_s$
Magnetic induction	B	$=$	$B_0\,\tilde{B}$	B_0	[T]	$=$	$\sqrt{\mu_0\rho_0}c_s$
Current density	J	$=$	$J_0\,\tilde{J}$	J_0	[C m^{-2} s^{-1}]	$=$	$B_0/(L\mu_0) = c_s/L\,\sqrt{\mu_0/\rho_0}$
Energy density	e	$=$	$e_0\,\tilde{e}$	e_0	[J m^{-3}]	$=$	$\rho_0 c_s^2$
Energy sources	S^e	$=$	$S_0^e\,\tilde{S}^e$	S_0^e	[J m^{-3} s^{-1}]	$=$	$e_0/\tau = \rho_0 c_s^3/L$

Table 2.1. Normalisation factors for the evolution equations.

2.8 The Numerical Model

When implementing a physical model as described in the preceding sections into a numerical program, there are several issues to consider. Naturally the evolution equations derived above cannot be solved in a general way using continuous variables when using a numerical solver. Rather all variables have to be computed on a spatial and a temporal grid. Other issues to be taken into account are the boundary and initial conditions. Finally as many numerical quantities as possible should be close to unity. This issue stems from the time when float precision was quite low, but still quantities of the order unity might help to improve the precision of the numerical solution. In this section we will handle the above points starting with the derivation of a normalised form of the equations.

2.8.1 Normalised Form of the Equations

The equations introduced in the previous chapter are being normalised in order to obtain quantities of order unity for the numerical computation. This means that all variables are split into a dimensionless variable of order unity and a normalisation constant. In our case there are only four independent variables with respect to this normalisation procedure. These, however, can be chosen at will as long as they correspond to the environment under consideration. The base units used for the normalisation in this work are the mass of the hydrogen atom, a typical number density n_0 of the environment under consideration, the length of the computational domain and some typical speed. A typical choice for the latter is either the speed of sound or the Alfvén speed. These correspond to choosing the temperature or the magnetic field as base units, respectively. In this work we will use the speed of sound as the base unit for the velocity. This is a justified choice when taking into account that in molecular clouds the plasma is mainly neutral. Apart from that the temperature is usually much better known than the magnitude of the magnetic induction.

Both types of normalisation constants are given in table 2.8.1 with the independent normalisation constants at the top. Table 2.8.1 also shows how the other variables depend on the independent four base units.

It might seem surprising at first sight that such a basic unit as time will not be chosen as an independent normalisation constant. Spatial scales and typical velocities are, however, more easily supplied –

therefore, a typical time scale is found by dimensional analysis to be:

$$\tau_0 = \frac{L}{\mathrm{v}_0} \tag{2.75}$$

As mentioned above it is under different circumstances also sensible to use the Alfvén speed as the base unit for the velocity. This choice, however, does not change the normalised form of the equations at all. The only difference is that the dimensionless variables have to be initialised differently. This will clarified when discussing the initial conditions. Before, however, we will first discuss the corresponding set of normalised, dimensionless evolution equations.

The Dimensionless Form of the Equations

With the normalisation of the individual variables introduced above we also have to normalise the equations describing the temporal evolution of these variables. The actual derivation of these normalised evolution equations is again shifted to the appendix – the interested reader will find it in appendix C. Here we will only discuss the results, which will be the equations used in the numerical scheme. Starting with the continuity equations these are:

$$\frac{\partial \rho}{\partial t} = -\nabla \cdot \boldsymbol{s} \qquad \text{(ionised fluid)} \tag{2.76}$$

$$\frac{\partial \rho_n}{\partial t} = -\nabla \cdot \boldsymbol{s}_n \qquad \text{(neutral fluid)} \tag{2.77}$$

$$\frac{\partial \boldsymbol{s}}{\partial t} = -\nabla \cdot \left(\frac{\boldsymbol{ss}}{\rho} + \left(p + \frac{B^2}{2} \right) \mathbb{1} - \boldsymbol{BB} \right) + \boldsymbol{F} \qquad \text{(ionised fluid)} \tag{2.78}$$

$$\frac{\partial \boldsymbol{s}_n}{\partial t} = -\nabla \cdot \left(\frac{\boldsymbol{s}_n \boldsymbol{s}_n}{\rho_n} + p_n \mathbb{1} \right) + \boldsymbol{F}_n \qquad \text{(neutral fluid)} \tag{2.79}$$

$$\frac{\partial \boldsymbol{B}}{\partial t} = -\nabla \cdot \left(\frac{\boldsymbol{sB} - \boldsymbol{Bs}}{\rho} \right) \tag{2.80}$$

where we left out the tilde for these normalised quantities. Here $\mathbb{1}$ is the unit matrix and the abbreviation $\boldsymbol{s}_k = \rho_k \mathbf{v}_k$ is the momentum density used for both fluid species.

This system of equations has to be closed by either an energy equation or an equation of state. For the former the normalised form is found in appendix C to be:

$$\frac{\partial e}{\partial t} = -\nabla \cdot \left(\left(e + p + \frac{B^2}{2} \right) \boldsymbol{s} - (\boldsymbol{s} \cdot \boldsymbol{B}) \boldsymbol{B} \right) \frac{1}{\rho} + S \qquad \text{(ionised fluid)} \tag{2.81}$$

$$\frac{\partial e_n}{\partial t} = -\nabla \cdot (e_n + p_n) \frac{\boldsymbol{s}_n}{\rho} + S_n \qquad \text{(neutral fluid)} \tag{2.82}$$

which together with the definition of the normalised total energy density:

$$e = \frac{s^2}{2\rho} + \frac{B^2}{2} + \frac{1}{\gamma - 1} p \tag{2.83}$$

closes the above system of equations. For the cases of vanishing external heating or an isothermal medium, however, it is not necessary to supply an energy equation at all. In the former case Eqs. (2.81) and (2.82) become equivalent to an adiabatic equation of state:

$$p \sim \rho^\gamma \tag{2.84}$$

which also holds in the same form for dimensionless quantities. For the case of an isothermal medium it is sufficient to use:

$$p = \frac{c_s^2}{u_0^2} \rho \overset{\text{here}}{=} \rho \tag{2.85}$$

which allows to directly replace the pressure by the mass density, when the speed of sound is chosen as the base velocity. What is still missing now is the explicit normalised form for the different source terms $\boldsymbol{F}$ and S used in the above equations.

2.8.2 Normalised Source Terms

The source terms given in the general not yet normalised form in the momentum and energy equations are:

$$\boldsymbol{F} = -\boldsymbol{F}_{ien} + \boldsymbol{F}_{ext} \qquad \boldsymbol{F}_n = \boldsymbol{F}_{ien} + \boldsymbol{F}_{ext} \tag{2.86}$$

$$S = -S_{ien} + S_{ext} \qquad S_n = S_{ien} + S_{ext} \tag{2.87}$$

Here $\boldsymbol{F}_{ien}$ and S_{ien} are the interaction terms arising from elastic collisions and charge exchange reactions. Here S_{ext} contains the external heating and cooling terms introduced above, which naturally only arise in the energy equation. External forces $\boldsymbol{F}_{ext}$ will not be taken into account in this work. Moreover, we have to mention that external heating and cooling will only be used in for the single fluid description. Therefore, we will discuss collisional and external source terms separately.

External Sources

The normalised forms of the external heating and cooling terms can be found quite easily. As described in detail in appendix C the dimensionless form of the source terms is found to be (beware that we will designate the normalised source terms in the same way as the dimensional ones):

$$S_{ext} = (n_H^2\Lambda - n_H\Gamma)\frac{\tau_0}{e_0} = (n_H^2\Lambda - n_H\Gamma)\frac{L}{m_0 n_0 u_0^3} \tag{2.88}$$

By this we find the normalisation factors for Λ and Γ:

$$S_{ext} = \rho^2\Lambda\frac{L}{m_0 u_0^3} - \rho\Gamma\frac{L n_0}{m_0 u_0^3} \tag{2.89}$$

where ρ indicates the normalised mass density. This shows that whenever external source terms play a role the normalisation has to be fixed. This is very similar with regard to the internal sources as will be seen in the following.

Internal Sources

The interaction terms for the two-fluid description are given in section B.5 of the appendix as:

$$\boldsymbol{F}_{ien} = \nu_n\rho(\boldsymbol{u} - \boldsymbol{u}_n) + \frac{\mu}{e}(\nu_{in} - \nu_{en})\boldsymbol{J} \tag{2.90}$$

$$\begin{aligned} S_{ien} =& \nu_n\rho\boldsymbol{u}_n \cdot (\boldsymbol{u} - \boldsymbol{u}_n) + \frac{\mu}{e}(\nu_{in} - \nu_{en})\boldsymbol{J}\cdot\boldsymbol{u}_n \\ &+ 2\frac{k_B}{\gamma-1}\rho_i\frac{\nu_{in}}{m_i + m_n}(T_i - T_n) + 2\frac{k_B}{\gamma-1}\rho_e\frac{\nu_{en}}{m_e + m_n}(T_e - T_n) \\ &+ \left(\frac{\nu_{in}}{m_i + m_n}\right)\frac{1}{n}\left(\rho_i(\boldsymbol{u} - \boldsymbol{u}_n) - \frac{\mu}{e}\boldsymbol{J}\right)^2 + \left(\frac{\nu_{en}}{m_e + m_n}\right)\frac{1}{n}\left(\rho_e(\boldsymbol{u} - \boldsymbol{u}_n) + \frac{\mu}{e}\boldsymbol{J}\right)^2 \end{aligned} \tag{2.91}$$

with ν_n given according to Eq (B.13) and the individual scattering frequencies given as:

$$\nu_{xn} = \frac{\rho_n}{m_x + m_n}|\boldsymbol{u}_x - \boldsymbol{u}_n|\sigma_{xn} \tag{2.92}$$

with x representing either electrons or ions. This representation nicely applies for single particle interactions, but can not be easily applied to the fluid picture. This is because the interaction cross section depends on the relative velocities of the colliding particles. This velocity, however, does not directly correspond to the velocity of a fluid element. It is rather somehow connected to this and the temperature of the fluid. Hence the scattering frequency for a fluid is usually rather given as:

$$\nu_{xn} = \rho_n \frac{\langle \sigma_{xn} \mathrm{v}_{xn} \rangle}{m_x + m_n} \tag{2.93}$$

where an average value of $\sigma_{xn}\mathrm{v}_{xn}$ is used, instead of any velocity and temperature dependence. For molecular clouds this constant can according to Hosking and Whitworth (2004) be estimated as $\langle \sigma_{xn}\mathrm{v}_{xn} \rangle = 1.69 \cdot 10^{-15}\ \mathrm{m}^3\ \mathrm{s}^{-1}$. Taking all this into account we find for the normalised form of the momentum source term:

$$\begin{aligned}
\tilde{\mathbf{F}}_{ien} &= \left(\nu_n \rho (\boldsymbol{u} - \boldsymbol{u}_n) + \frac{\mu}{e} (\nu_{in} - \nu_{en}) \boldsymbol{J} \right) \frac{L}{\rho_0 u_0^2} \\
&= \nu_n \frac{L}{u_0} \frac{\rho}{\rho_0} \frac{(\boldsymbol{u} - \boldsymbol{u}_n)}{u_0} + \frac{\mu}{e} (\nu_{in} - \nu_{en}) \frac{L}{u_0} \boldsymbol{J} \frac{1}{\rho_0 u_0} \\
&= \tilde{\nu}_n \tilde{\rho} (\tilde{\boldsymbol{u}} - \tilde{\boldsymbol{u}}_n) + (\tilde{\nu}_{in} - \tilde{\nu}_{en}) \frac{\mu}{e} \frac{1}{\rho_0 u_0} \frac{u_0}{L} \sqrt{\frac{\rho_0}{\mu_0}} \tilde{\boldsymbol{J}} \\
&= \tilde{\nu}_n \tilde{\rho} (\tilde{\boldsymbol{u}} - \tilde{\boldsymbol{u}}_n) + (\tilde{\nu}_{in} - \tilde{\nu}_{en}) \frac{\mu}{eL\sqrt{\mu_0 \rho_0}} \tilde{\boldsymbol{J}}
\end{aligned} \tag{2.94}$$

Here the first term can be expressed by the normalised quantities introduced above and a normalise scattering frequency $\tilde{\nu}_n$. The second term, however, already introduces some additional normalisation factors.

The normalised scattering frequency can be found from Eq. (2.93) which has just to be multiplied by L/v_0 as shown in the above equation:

$$\tilde{\nu}_{xn} = \nu_{xn} \frac{L}{u_0} = \frac{\rho_n}{m_x + m_n} \langle \sigma_{xn} \mathrm{v}_{xn} \rangle \frac{L}{u_0} = \tilde{\rho}_n \frac{\langle \sigma_{xn} \mathrm{v}_{xn} \rangle L m_n n_0 / u_0}{m_x + m_n} = \tilde{\rho}_n \langle \sigma_{xn} \mathrm{v}_{xn} \rangle \frac{L n_0}{u_0} \frac{\mu_{nx}}{m_x}$$

Thus, we find, that the normalised form of the collision frequency depends on our normalisation factors, i.e. the importance of the collisions for the system not only depends on the collision cross section and the density but also e.g. on the global length scale taken into account.

Analogous consideration are also necessary for the source terms of the energy equations. In this case we find:

$$S_e \rightarrow S_e \frac{L}{\rho_0 u_0^3} \tag{2.95}$$

Since we will use the two-fluid model only for molecular clouds all variables will be normalised to the neutral medium, which is by far the most abundant fluid in this phase of the ISM. With this consideration we find:

$$\begin{aligned}
S_e =& \tilde{\nu}_n \tilde{\rho} \tilde{\boldsymbol{u}}_n \cdot (\tilde{\boldsymbol{u}} - \tilde{\boldsymbol{u}}_n) + \frac{\mu}{eL\sqrt{\mu_0 \rho_0}} (\tilde{\nu}_{in} - \tilde{\nu}_{en}) \tilde{\boldsymbol{J}} \cdot \tilde{\boldsymbol{u}}_n \\
&+ \frac{2}{\gamma - 1} \frac{\mu_{ni}}{m_n} \tilde{\nu}_{in} \tilde{\rho} (\tilde{T} - \tilde{T}_n) + \frac{2}{\gamma - 1} \frac{\mu_{ne}}{m_n} \tilde{\nu}_{en} \tilde{\rho} (\tilde{T} - \tilde{T}_n) \\
&+ \left(\frac{\mu_{ni}}{m_n} \frac{\mu}{m_e} \right) \tilde{\nu}_{in} \frac{1}{\tilde{\rho}} \left(\tilde{\rho} (\tilde{\boldsymbol{u}} - \tilde{\boldsymbol{u}}_n) - \frac{\mu}{eL\sqrt{\mu_0 \rho_0}} \tilde{\boldsymbol{J}} \right)^2 + \left(\frac{\mu_{ne}}{m_n} \frac{\mu}{m_i} \right) \tilde{\nu}_{en} \frac{1}{\tilde{\rho}} \left(\tilde{\rho} (\tilde{\boldsymbol{u}} - \tilde{\boldsymbol{u}}_n) + \frac{\mu}{eL\sqrt{\mu_0 \rho_0}} \tilde{\boldsymbol{J}} \right)^2
\end{aligned} \tag{2.96}$$

where we assumed the temperatures of ions and electrons to be the same. This normalised form now can be used in the numerical method which will be described later in this work. To conclude the discussion of the numerical model the last issues are the discussion of the boundary conditions and the initialisation of the system of equations.

2.8.3 Initialisation and Boundary Conditions

The choice of the boundary conditions for simulations of interstellar plasma poses a far more severe problem than is thought in the beginning. In principle the best way would be to describe the whole ISM of the Galaxy at once. This, however, will not be possible for the near future due to the limited computing power. Therefore, we will be able only to describe a small volume of the ISM in the numerical model. For such a volume it is, however, not easily possible to dynamically prescribe values on the boundary of the numerical domain. Therefore, it is most sensible is to use periodic boundary conditions for a small volume of the ISM. This also solves the problem that many numerical methods are only well defined for such boundaries.

However, one has to be careful with regard to the physical processes when using such boundary conditions, due to the fact that no matter can be transported out of or into the numerical domain. Therefore, one has to make sure that the initial conditions used for the problem correspond to the real physical system. This can be visualised by the example of a more global picture: the density and the pressure distribution of the ISM in the Galaxy is determined by the equilibrium of pressure forces and gravitational fields. Whenever the pressure is increased – e.g. by heat disposed by the decay of turbulent fluctuations – this equilibrium is disturbed and the matter will be shifted further away from the galactic plane. This could result in a quite global decrease of density. Such structures can naturally not be observed when using periodic boundaries.

This leads us directly to the question of the initial conditions. Here, we will discuss different systems for which the turbulent ISM will be investigated. Mainly, we will concentrate on molecular clouds and on the more diffuse part of the ISM, for which typical parameters are given in table 1.1. Basically the correct initialisation is automatically assured by the choice of the base variables when normalising the evolution equations. Then most variables just have to be initialised as unity. When no sources are present, one might expect this to be sufficient since the dimensionless equations do not depend on the base units anymore. Already, however, when the Alfvén speed and the speed of sound differ things get a little more complicated.

There are, however, further issues to be taken into account regarding the initialisation of the system. When using the temperature and, thus, the speed of sound as the base unit for the velocity, the normalisation of the magnetic field will equate the magnetic energy to the thermal energy. In interstellar space, these energy densities are usually not identical, however. Therefore, the dimensionless magnetic field has to be initialised with a value different from unity. This matter is taken care of by the so-called plasma β. This quantity is defined as the ratio of the thermal energy density to the magnetic energy density:

$$\beta = \frac{p_{therm}}{p_{mag}} = \frac{p}{B^2/2\mu_0} = \frac{\rho_0 u_0^2}{\rho_0 u_0^2} \frac{\tilde{p}}{\tilde{B}^2/2} = \frac{\tilde{p}}{\tilde{B}^2/2} \tag{2.97}$$

When aiming to quantify this dimensionless measure the phase structure is of not so much importance as it would be when investigating, e.g., temperatures instead of thermal energy densities. This is due to the fact that for the simple two-phase models of the ISM these are thought to be in thermal pressure equilibrium. Thus, the thermal energy can be approximated to be constant even when investigating different phases of the ISM. Therefore, we will estimate the plasma β just using the average values of the ISM. On average the thermal energy density is according to Cox (2005) about one tenth of the total pressure of $0.3 \cdot 10^{-12}$ Pa for the galactic plain. The non-thermal part, in contrast to that, is supposedly distributed equally among the magnetic field, cosmic ray and dynamical pressure (the latter of these might also contain the thermal pressure of the hot component of the ISM). Therefore, each of these is attributed a pressure of about $0.09 \cdot 10^{-12}$ Pa. For the magnetic field this value corresponds nicely to the value of $5 \cdot 10^{-10}$ T, which is used as the average mid-plane value stated by Cox (2005). With these estimates we find the typical value of the plasma β for the equilibrium ISM to be about $\beta \simeq 0.3$, which is used for the rest of this work. Therefore, the initial value for the dimensionless magnetic field is fixed by Eqn. (2.97) when the plasma β is set and the pressure is given as unity.

When, as is done in this work, dealing with driven turbulence another ratio of the normalisation constants has to be specified, because the energy input rate has to correspond to the physical rate observed in the ISM, which will be estimated below. What is thought to drive the turbulent fluctuations in interstellar space are large-scale energetic events like supernova explosions or galactic superwinds. Here, we stick to the usual approach concentrating on the supernova explosions with regard to the driving of the fluctuations.

For the simulation results to conform to reality we, therefore, have to make sure that the energy input rate used for the numerical calculations represents the input rate encountered in nature. At first this seems to be as easily achieved as the normalisation of the cooling and heating terms. Whereas the latter are simple source terms, however, the input of the velocity fluctuations is a bit more complicated – that is we decided to choose a fixed amount of energy as input at equally spaced time steps.

What is needed is an estimate for the value of the energy input rate of supernova explosions and similar processes. For supernova explosions we will obtain a crude estimate based on estimates for the kinetic energy of the ejected material, the explosion frequency and the volume of the galactic disk. The kinetic energy of the ejected material of a single supernova explosion is supposedly about $E \simeq 10^{43} - 10^{44}$ J (see e.g. Dyson and Williams 1997). Numerical simulations by Thornton et al. (1998), however, indicate that the lower end of this scale is more appropriate, since a major part of the kinetic energy is dissipated as heat in shock waves. For the dense matter in molecular clouds a value of 10^{43} J is appropriate, whereas for the diffuse gas a somewhat higher value of $3 \cdot 10^{43}$ J can be adopted.

For the volume of the galactic disk and the supernova explosion rate we use values by de Avillez (2000), from which we estimate the frequency τ_{SN} for the whole galactic disk to be about one supernova per century. The volume V_{Disc} of the regions, for which the supernova explosions are taken to be homogeneously distributed can be estimated to be $1.4 \cdot 10^{11}$ pc^3. This leaves us with an estimate for the global average energy input rate S_e by supernova explosions as:

$$S_e \simeq E\, \tau_{SN}/V_{Disc} \tag{2.98}$$

For the global average this leads us to an input rate of kinetic energy of:

$$S_e \simeq (0.77 - 2.3) \cdot 10^{-27}\ \mathrm{J\ m^{-3} s^{-1}} \tag{2.99}$$

where the lower value would be the one used for molecular clouds and the higher for the diffuse gas. For molecular clouds, however, we have then again to take into account that these are star forming regions, where supernova explosions and winds by young giant stars are far more frequent than for the average ISM. Therefore, we will use higher value for our numerical studies of these regions. Conforming to Vestuto et al. (2003) we will also use an energy input of $1 \cdot 10^{-26}$ J m^{-3} s^{-1}.

The physical input energy computed above usually does not initially correspond to the numerical one, with the latter naturally depending on the normalisation. The normalisation constant for the input power is:

$$S_e = S_{e0}\tilde{S}_e \qquad \text{with} \qquad S_{e0} = \frac{e_0}{\tau_0} = \frac{\rho_0 u_0^2}{L_0/u_0} = \frac{\rho_0 u_0^3}{L_0} \tag{2.100}$$

The normalised source term $\tilde{S}_e$, therefore, has to be adjusted so that the actual sources correctly represent the supernova input rate. Thus, the simulations are not independent of the normalisation anymore – at least S_{e0} has to be the same for all system to be addressed by a numerical simulation.

Similar arguments also apply when normalising the quantities of the charged particle fluid for a weakly ionised plasma. With the base units being the units of the neutral fluid most variables for the charged fluid have to be initialised by the degree of ionisation.

With this paragraph we conclude the discussion on the physical model and turn to the numerical aspects of the simulations. Before continuing on the numerical implementation we, therefore, would first like to introduce the basic method to solve the system of equations numerically.

Chapter 3

Numerical Simulations

In this chapter we discuss the important numerical issues in the context of ISM turbulence simulations. Naturally, we start with the description of the numerical method used to solve the set of hyperbolic equations. Unfortunately, source terms present in the equations are not directly covered by the scheme. Therefore, we will also introduce a way to include an appropriate solver for the source terms. Additionally, the implementation of the driving of the turbulence is an important issue as is the solenoidality of the magnetic field whenever such a field is present. First, however, we start with the discussion of the scheme itself.

3.1 CWENO

The numerical scheme used for the computations presented in this work is the so-called CWENO (Centrally Weighted Essentially Non-Oscillatory) algorithm (see e.g. Kurganov and Levy 2000). This name already implies a lot about the method: the important point is that CWENO is a central method on the one hand and uses a reconstruction suppressing spurious oscillations on the other. This scheme has to be seen in contrast to the much more complex Godunov schemes (see Godunov 1959), which solve the Riemann problem for each cell boundary for every time step. The idea behind the CWENO scheme is to abandon the necessity to use a Riemann solver by averaging over the appropriate fraction of every cell. The resulting scheme, therefore, enjoys the major advantage of simplicity over the upwind schemes like the Godunov scheme. Although central schemes are more dissipative than Godunov schemes, this problem can be solved by using a higher order version of the central scheme. Apart from that they are very efficient and applicable to a wide field of problems due to their simplicity.

In the following paragraphs we try to give an idea what this method is about and how it can easily be derived.

3.1.1 Basic Idea

The basic idea behind the CWENO scheme is to utilise the conservative structure of systems of equations of the form:

$$\partial_t \boldsymbol{u} + \nabla \cdot \mathsf{F}(\boldsymbol{u}) = 0 \tag{3.1}$$

where $\mathsf{F}(\boldsymbol{u})$ is some flux function depending on the vector of variables $\boldsymbol{u}$ to be investigated. Integrating this equation over one cell and one time step yields a scheme, which computes the values at the next time step using an estimate of the flux-integrals $\boldsymbol{F}(\boldsymbol{u})$ on the cell boundaries. Additionally a correction due to the estimate for the Riemann-fans at these boundaries has to be taken into account. This will become clear, when the scheme is explained in more detail in the next section. In this work we will only describe the multi-dimensional version of the CWENO scheme, because we are only using the 3-D version of the scheme anyway and the one-dimensional description can be found in Kurganov and Levy

(2000). Moreover, the transition from the two-dimensional scheme as described in the next paragraph to the three-dimensional scheme is much more straightforward than it would be for the one-dimensional scheme.

3.1.2 The Two-Dimensional CWENO Scheme

The multi-dimensional CWENO scheme is best illustrated via the example of the two-dimensional scheme. The only step in the scheme sometimes not easily extended to higher dimensions is the reconstruction of point values from the cell averages. This, however, will be the issue of the next section. The two-dimensional scheme will be applied to hyperbolic differential equations of the form:

$$\partial_t \boldsymbol{u} + \partial_x \boldsymbol{f}(\boldsymbol{u}) + \partial_y \boldsymbol{g}(\boldsymbol{u}) = 0 \tag{3.2}$$

This equation is examined on a discrete spatial grid with cells given by:

$$\left(x_i - \frac{\Delta x}{2} \ldots x_i + \frac{\Delta x}{2}\right) \times \left(y_j - \frac{\Delta y}{2} \ldots y_j + \frac{\Delta y}{2}\right) \tag{3.3}$$

For these individual cell the scheme will compute the average values of $\boldsymbol{u}$, which will from now on be termed as *cell-averages* of $\boldsymbol{u}$. Since the scheme has to deal with point values on the cell boundaries, too, these point values are evaluated from the cell averages by the application of a piecewise polynomial reconstruction – that is the spatial variation of $\boldsymbol{u}$ is approximated by a polynomial of the desired order. For the second-order version of the scheme one can, e.g., assume this reconstruction in the cell $C_{i,j}$ at time t^n to be of the form:

$$\boldsymbol{p}_{i,j}(\boldsymbol{x}, t^n) = \boldsymbol{p}^n_{i,j}(x, y) = \boldsymbol{u}_{0i,j} + \boldsymbol{u}_{xi,j}(x - x_i) + \boldsymbol{u}_{yi,j}(y - y_j) \tag{3.4}$$

While a cross-term containing both linear parts may also be added, it is not of any importance, because it cancels out due to the evaluation of these polynomials on the middle of the cell faces in the final form of the second order scheme (see below). One has to bear in mind that these polynomials are given for just one cell. Thus, there is an ambiguity at the cell boundaries as to which of these reconstructions is to be used. For this we introduce the notation $p^{\pm}$, where, e.g., $p^{+}_{i+\frac{1}{2},j}$ is the point value at the upper x-boundary of cell $C_{i,j}$ with the reconstruction stemming from the next cell $C_{i+1,j}$.

From this one obtains the cell-averages via integration as:

$$\bar{\boldsymbol{u}}_{i,j} := \frac{1}{\Delta x \Delta y} \int_{y_{j-\frac{1}{2}}}^{y_{j+\frac{1}{2}}} \int_{x_{i-\frac{1}{2}}}^{x_{i+\frac{1}{2}}} \boldsymbol{p}^n_{i,j}(x, y) dx dy \tag{3.5}$$

where $x_{i\pm\frac{1}{2}}$ and $y_{j\pm\frac{1}{2}}$ signify the cell boundaries in the corresponding directions. For further reference the point values evaluated using such a reconstruction at some specific points are getting labelled:

$$\begin{aligned}
\boldsymbol{u}_{i,j} &:= \boldsymbol{p}^n_{i,j}(x_i, y_j), & \boldsymbol{u}^N_{i,j} &:= \boldsymbol{p}^n_{i,j}(x_i, y_{j+\frac{1}{2}}), & \boldsymbol{u}^{NE}_{i,j} &:= \boldsymbol{p}^n_{i,j}(x_{i+\frac{1}{2}}, y_{j+\frac{1}{2}}), \\
\boldsymbol{u}^E_{i,j} &:= \boldsymbol{p}^n_{i,j}(x_{i+\frac{1}{2}}, y_j), & \boldsymbol{u}^{SE}_{i,j} &:= \boldsymbol{p}^n_{i,j}(x_{i+\frac{1}{2}}, y_{j-\frac{1}{2}}), & \boldsymbol{u}^S_{i,j} &:= \boldsymbol{p}^n_{i,j}(x_i, y_{j-\frac{1}{2}}), \\
\boldsymbol{u}^{SW}_{i,j} &:= \boldsymbol{p}^n_{i,j}(x_{i-\frac{1}{2}}, y_{j-\frac{1}{2}}), & \boldsymbol{u}^W_{i,j} &:= \boldsymbol{p}^n_{i,j}(x_{i-\frac{1}{2}}, y_j), & \boldsymbol{u}^{NW}_{i,j} &:= \boldsymbol{p}^n_{i,j}(x_{i-\frac{1}{2}}, y_{j+\frac{1}{2}})
\end{aligned} \tag{3.6}$$

With all this in mind the equations are basically solved by a spatial integration of the system in Eq. (3.2) over each cell and an integration in time from the actual to the next time step. There is, however, a problem inherent in this integration directly connected to the reconstruction. With every cell having in general an individual reconstruction polynomial there may occur a jump in the different polynomial reconstructions from one cell to another. The integration of Eq. (3.2) over each cell and over one time step results in:

$$\bar{\boldsymbol{u}}^{n+1}_{i,j} = \bar{\boldsymbol{u}}^n_{i,j} - dx \int_{t^n}^{t^n+\Delta t} \Big(\boldsymbol{f}(\boldsymbol{u}(x_{i+\frac{1}{2}}, y_j, \tau)) - \boldsymbol{f}(\boldsymbol{u}(x_{i-\frac{1}{2}}, y_j, \tau)) + \boldsymbol{g}(\boldsymbol{u}(x_i, y_{j+\frac{1}{2}}, \tau)) - \boldsymbol{g}(\boldsymbol{u}(x_i, y_{j-\frac{1}{2}}, \tau)) \Big) d\tau \tag{3.7}$$

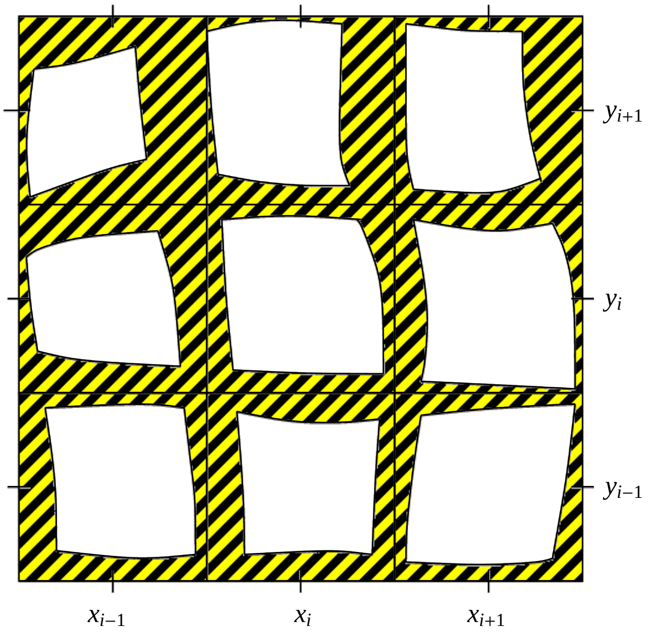

Fig. 3.1: The area around the cell x_i, y_j with the non-smooth regions hatched.

This equation does not look too bad but due to the discontinuities where the fluxes are to be evaluated, one would have to solve a generalised Riemann problem at these positions to obtain the temporal evolutions of the fluxes, which is a numerically very expensive task.

We can, however, make use of the fact that such a jump can only propagate with a finite velocity depending on the system of equations to be solved with the scheme. In general this maximum propagation velocity will change with space and time. Therefore, when we would like to integrate the system in Eq. (3.2) over one cell and over the time-interval $[t^n, t^{n+1}]$ only the data near the cell boundaries as, e.g., illustrated in Fig. 3.1 might be non-smooth at any time between t^n and t^{n+1}. Thus, instead of integrating each entire cell we treat the smooth and non-smooth domains individually. This leads to a scheme, which does not have to utilise Riemann solvers, while still producing high-order results, since we average the non-smooth parts of the solutions over a domain as small as possible. This has to be seen in contrast to the Nessyahu-Tadmor scheme (Nessyahu and Tadmor 1990) where an integration is performed over a complete staggered cell.

To perform the integration over the smooth and the non-smooth regions separately one needs an estimate for the form of these areas which also has to be able to reflect the order of the scheme. It will, however, become evident that the transfer into the *semidiscrete* framework simplifies things again. A semidiscrete scheme is one, which was derived utilising the fact that the time step dt is small as compared to any characteristic time scale of the system of hyperbolic equations with regard to a single numerical cell. The use of the semidiscrete limit is motivated by the fact that a fully discrete scheme suffers from higher numerical dissipation. This results from an accumulation of excessive dissipation due to the small time steps needed in a fully discrete scheme. The size of these time steps is mainly determined by the CFL condition first introduced in one of the first papers on finite difference methods for partial differential equations by Courant et al. (1928). This is a necessary condition for the stability of a numerical scheme. It essentially states that a numerical method can only be convergent if its numerical domain of dependence contains the true domain of dependence of the actual partial differential equation. With respect to this condition a fully discrete scheme has to fulfil the restricted condition $\Delta t \propto (\Delta x)^2$ for the time step, whereas for the semidiscrete scheme it is possible to use the convective CFL condition see also Kurganov and Levy (2000). Apart from that we enjoy the fact that a semidiscrete scheme is much simpler than a fully discrete one.

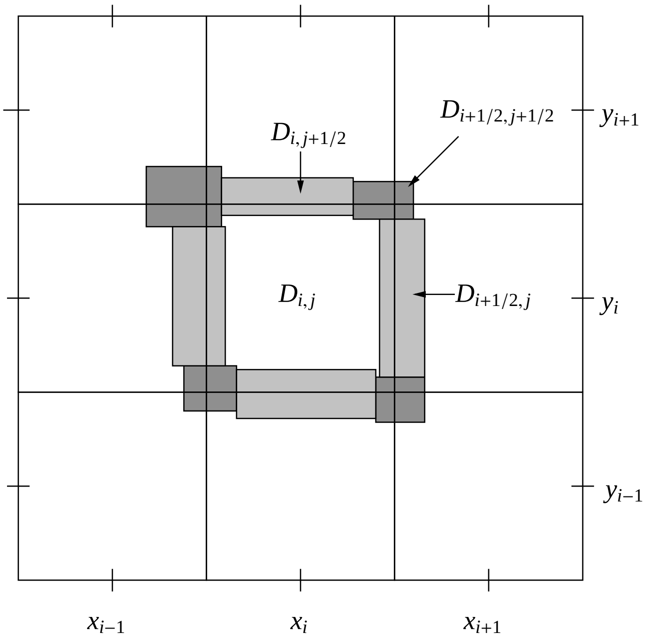

Fig. 3.2: High-order approximation for the non-smooth regions in the individual cells for the CWENO scheme.

An example for a high order estimation for the form of those regions of non-smooth data is illustrated in Fig. 3.2. In this figure we distinguish three types of regions. First there is the smooth region in the inner part of each cell. Secondly the light gray and the dark grey regions indicate regions possibly holding non-smooth data. The dark grey regions can, however, safely be neglected. This is due to the fact that we are using the semidiscrete form of the scheme, which says that we are solving the system of equations in the limit $dt \to 0$.

In the semidiscrete limit the size of the dark-grey regions can be estimated to be:

$$D_{i+\frac{1}{2},j+\frac{1}{2}} = (a^+_{i+\frac{1}{2},j+\frac{1}{2}} + a^-_{i+\frac{1}{2},j+\frac{1}{2}})(b^+_{i+\frac{1}{2},j+\frac{1}{2}} + b^-_{i+\frac{1}{2},j+\frac{1}{2}})dt^2 + O(dt^3) \tag{3.8}$$

where $D_{i+\frac{1}{2},j+\frac{1}{2}}$ indicates the corresponding region in Fig. 3.2. Additionally, $a^{\pm}$ are the right- and left-handed maximum propagation velocities for discontinuities for the upper right corner in the x-direction respectively. In the same way $b^{\pm}$ corresponds to the signal propagation velocities in the y-direction. Like the equations describing the problem under consideration these velocities have to be specified corresponding to the problem. They are obtained from the Jacobian for each direction as will be discussed in section 3.3. The size of this region is of second order in time and can, therefore, safely be neglected in the semidiscrete limit.

As compared to this the light-grey areas can be estimated to have the size:

$$D_{i+\frac{1}{2},j} = (a^+_{i+\frac{1}{2},j} + a^-_{i+\frac{1}{2},j})dt\left(\Delta y - (b^+_{i+\frac{1}{2},j-\frac{1}{2}} + b^-_{i+\frac{1}{2},j+\frac{1}{2}})dt\right) + O(dt^3) \tag{3.9}$$

which is of order dt, thus, showing that the dark-grey areas can indeed be neglected as compared to these. So, it is clear that we only have to discuss the light-grey areas and the undisturbed area in the centre of the cell.

As mentioned above, we have to integrate the system over the individual areas separately in order to avoid Riemann-solvers and to obtain the highest possible order. In turn we have to use some procedure to get from this distributed framework back to the original grid. The overall method can be split in three major steps:

1. Integration of the system over the light-grey and the undisturbed domains indicated in Fig. 3.2 utilising a local polynomial reconstructions to obtain averages for all domains for the next time step.
2. These averages are then used to obtain a reconstruction of all necessary point values at the next time step.
3. This is then projected to the original grid, thus, finally yielding cell averages at time t^{n+1}.

For step 1 the cell averages over the domains indicated in Fig. 3.2 are designated as:

$$\int_{D_{i,j}} \longrightarrow \bar{\boldsymbol{\omega}}_{i,j}, \qquad \int_{D_{i+\frac{1}{2},j}} \longrightarrow \bar{\boldsymbol{\omega}}_{i+\frac{1}{2},j}, \qquad \int_{D_{i,j+\frac{1}{2}}} \longrightarrow \bar{\boldsymbol{\omega}}_{i,j+\frac{1}{2}} \tag{3.10}$$

From these cell averages given at time t^n we compute local averages at time t^{n+1}. From these local averages $\boldsymbol{\omega}^{n+1}$ we compute a local piecewise polynomial reconstruction $\tilde{\boldsymbol{\omega}}^{n+1}$. The global piecewise polynomial reconstruction needed for the second step of the above procedure is then written as:

$$\tilde{\omega}^{n+1}(x,y) := \sum_{i,j} \left(\omega^{n+1}_{i,j} \chi_{i,j} + \tilde{\boldsymbol{\omega}}^{n+1}_{i+\frac{1}{2},j} \chi_{i+\frac{1}{2},j} + \tilde{\boldsymbol{\omega}}^{n+1}_{i,j+\frac{1}{2}} \chi_{i,j+\frac{1}{2}} \right) \tag{3.11}$$

Here the $\tilde{\chi}$'s are the characteristic functions of the corresponding domains D – that is the χ's restrict the local polynomial reconstructions to the appropriate domains.

The third step consists of the projection of this interpolant onto the original grid according to:

$$\bar{\boldsymbol{u}}^{n+1}_{i,j} = \frac{1}{\Delta x \Delta y} \int_{y_{j-\frac{1}{2}}}^{y_{j+\frac{1}{2}}} \int_{x_{i-\frac{1}{2}}}^{x_{i+\frac{1}{2}}} \tilde{\boldsymbol{\omega}}^{n+1}(x,y) dx\, dy \tag{3.12}$$

According to Eq. (3.11) this results in:

$$\begin{aligned} \bar{\boldsymbol{u}}^{n+1}_{i,j} = \frac{1}{\Delta x \Delta y} \Bigg(& \iint_{D_{i,j}} \tilde{\boldsymbol{\omega}}^{n+1}_{i,j}(x,y) dx\, dy \\ & + \iint_{D_{i-\frac{1}{2},j} \cap C_{i,j}} \tilde{\boldsymbol{\omega}}^{n+1}_{i-\frac{1}{2},j}(x,y) dx\, dy + \iint_{D_{i+\frac{1}{2},j} \cap C_{i,j}} \tilde{\boldsymbol{\omega}}^{n+1}_{i+\frac{1}{2},j}(x,y) dx\, dy \\ & + \iint_{D_{i,j-\frac{1}{2}} \cap C_{i,j}} \tilde{\boldsymbol{\omega}}^{n+1}_{i,j-\frac{1}{2}}(x,y) dx\, dy + \iint_{D_{i,j+\frac{1}{2}} \cap C_{i,j}} \tilde{\boldsymbol{\omega}}^{n+1}_{i,j+\frac{1}{2}}(x,y) dx\, dy \Bigg) \end{aligned} \tag{3.13}$$

Here terms like $D_{i-\frac{1}{2},j} \cap C_{i,j}$ indicate that we only integrate the part of the domains D, which extend into the cell $C_{i,j}$ under consideration. In the semidiscrete limit these integrals become:

$$\iint_{D_{i\pm\frac{1}{2},j} \cap C_{i,j}} \tilde{\boldsymbol{\omega}}^{n+1}_{i\pm\frac{1}{2},j} dx\, dy = (D_{i\pm\frac{1}{2},j} \cap C_{i,j})\, \bar{\boldsymbol{\omega}}^{n+1}_{i\pm\frac{1}{2},j} + O(dt^2) \tag{3.14}$$

$$\iint_{D_{i,j\pm\frac{1}{2}} \cap C_{i,j}} \tilde{\boldsymbol{\omega}}^{n+1}_{i,j\pm\frac{1}{2}} dx\, dy = (D_{i,j\pm\frac{1}{2}} \cap C_{i,j})\, \bar{\boldsymbol{\omega}}^{n+1}_{i,j\pm\frac{1}{2}} + O(dt^2) \tag{3.15}$$

for the non-smooth areas and:

$$\iint_{D_{i,j} \cap C_{i,j}} \tilde{\boldsymbol{\omega}}^{n+1}_{i,j} dx\, dy = D_{i,j}\, \bar{\boldsymbol{\omega}}^{n+1}_{i,j} \tag{3.16}$$

for the smooth area inside the cell, where the latter is obtained due to the conservation property of the reconstruction. Here $C_{i,j}$ is again the cell under consideration.

With these results we find when neglecting terms of order $\mathcal{O}(dt^2)$:

$$\begin{aligned}\frac{d}{dt}\bar{u}_{i,j}(t) &= \lim_{\Delta t\to 0}\frac{\bar{\boldsymbol{u}}^{n+1}_{i,j}-\bar{\boldsymbol{u}}^{n}_{i,j}}{\Delta t} \\ &= \lim_{\Delta t\to 0}\left(\sum_{\pm}\frac{|D_{i\pm\frac{1}{2},j}\ \cap\ C_{i,j}|}{\Delta t\Delta x\Delta y}\bar{\boldsymbol{\omega}}^{n+1}_{i\pm\frac{1}{2},j}+\sum_{\pm}\frac{|D_{i,j\pm\frac{1}{2}}\ \cap\ C_{i,j}|}{\Delta t\Delta x\Delta y}\bar{\boldsymbol{\omega}}^{n+1}_{i,j\pm\frac{1}{2}}+\frac{|D_{i,j}\ \cap\ C_{i,j}|}{\Delta x\Delta y}\bar{\boldsymbol{\omega}}^{n+1}_{i,j}-\bar{\boldsymbol{u}}_{i,j}\right)\end{aligned} \tag{3.17}$$

What is needed to analyse this expression is the result for the local averages and additionally an estimate for the size of the different domains. When computing the local cell averages it will become clear that we will need the size for those domains containing the non-smooth data for this computation. This was, however, already given in Eq. (3.9) and can be approximated as:

$$D_{i\pm\frac{1}{2},j}\ \cap\ C_{i,j} = a^{\mp}_{i\pm\frac{1}{2},j}\Delta t\Delta y \qquad D_{i,j\pm\frac{1}{2}}\ \cap\ C_{i,j} = b^{\mp}_{i,j\pm\frac{1}{2}}\Delta t\Delta y \tag{3.18}$$

Now what is left to be computed are the local cell averages – that is we have to revert to the first step to obtain these averages by a local integration of the hyperbolic system to be solved.

Local Cell Averages

As an example we will explicitly derive the expression for the local cell average of the left/right-handed non-smooth region ($D_{i\pm\frac{1}{2},j}$ in Fig 3.2). This is obtained by integrating Eq. (3.2) over the domain:

$$D_{i\pm\frac{1}{2},j}\times[t^n,t^{n+1}]$$

We start by integrating in time obtaining:

$$\int_{t^n}^{t^{n+1}}\frac{\partial\boldsymbol{u}}{\partial t}dt = \boldsymbol{u}^{n+1}-\boldsymbol{u}^{n} = -\int_{t^n}^{t^{n+1}}\boldsymbol{f}(\boldsymbol{u})_x dt-\int_{t^n}^{t^{n+1}}\boldsymbol{g}(\boldsymbol{u})_y dt \tag{3.19}$$

Assuming, that $\boldsymbol{u}$ is represented by a polynomial reconstruction $P^n_{i,j}$ we additionally integrate over the spatial domain:

$$\int_{D_{i\pm\frac{1}{2},j}}(\boldsymbol{u}^{n+1}-\boldsymbol{u}^{n})dx\,dy = -\int_{t^n}^{t^{n+1}}\left(\int_{D_{i\pm\frac{1}{2},j}}\boldsymbol{f}(\boldsymbol{u})_x dx\,dy+\int_{D_{i\pm\frac{1}{2},j}}\boldsymbol{g}(\boldsymbol{u})_y dx\,dy\right)dt \tag{3.20}$$

Using the polynomial representation for $\boldsymbol{u}$ and utilising the conservation property of the reconstruction for step t^{n+1} leaves us with:

$$D_{i\pm\frac{1}{2},j}\bar{\omega}^{n+1}_{i\pm\frac{1}{2},j}-\int_{D_{i\pm\frac{1}{2},j}}\boldsymbol{p}^n_{i,j}(x,y)dx\,dy = -\int_{t^n}^{t^{n+1}}\left(\int_{D_{i\pm\frac{1}{2},j}}\boldsymbol{f}(\boldsymbol{u})_x dx\,dy+\int_{D_{i\pm\frac{1}{2},j}}\boldsymbol{g}(\boldsymbol{u})_y dx\,dy\right) \tag{3.21}$$

Here we could also use the conservation property of the reconstruction for $\boldsymbol{p}^n_{i,j}$. This, however, would not help us at all, since we do not know the local cell averages $\bar{\omega}^n_{i\pm\frac{1}{2},j}$ for $t = t^n$. Therefore, we will rather evaluate the corresponding integral yielding the dependence on the local cell average and the local reconstruction.

In the above equation $|D_{i\pm\frac{1}{2},j}|$ is the area used in the integrals, which can be approximated as $|D_{i\pm\frac{1}{2},j}| \simeq (a^{+}_{i+\frac{1}{2},j}+a^{-}_{i+\frac{1}{2},j})\Delta t\Delta y$. Due to the fact that some of the integrals cancel with the spatial derivatives we can compute the flux integrals:

$$\begin{aligned}\int_{D_{i\pm\frac{1}{2},j}}\boldsymbol{f}(\boldsymbol{u})_x dx\,dy &= \int_{y_{j-\frac{1}{2}}+\Delta tb^{+}_{i\pm\frac{1}{2},j-\frac{1}{2}}}^{y_{j+\frac{1}{2}}-\Delta tb^{-}_{i\pm\frac{1}{2},j+\frac{1}{2}}}\boldsymbol{f}(\boldsymbol{u}(x,y,t))dy\Big|_{x_{i\pm\frac{1}{2}}-\Delta ta^{-}_{i\pm\frac{1}{2},j}}^{x_{i\pm\frac{1}{2}}+\Delta ta^{+}_{i\pm\frac{1}{2},j}} \\ \int_{D_{i\pm\frac{1}{2},j}}\boldsymbol{g}(\boldsymbol{u})_y dx\,dy &= \int_{x_{i\pm\frac{1}{2}}-\Delta ta^{-}_{i\pm\frac{1}{2},j}}^{x_{i\pm\frac{1}{2}}+\Delta ta^{+}_{i\pm\frac{1}{2},j}}\boldsymbol{g}(\boldsymbol{u}(x,y,t))dx\Big|_{y_{j-\frac{1}{2}}+\Delta tb^{+}_{i\pm\frac{1}{2},j-\frac{1}{2}}}^{y_{j+\frac{1}{2}}-\Delta tb^{-}_{i\pm\frac{1}{2},j+\frac{1}{2}}}\end{aligned} \tag{3.22}$$

In the semidiscrete limit the integrals in the second line vanish since the integration area $[x_{i\pm\frac{1}{2}} - a^-_{i\pm\frac{1}{2},j}\Delta t \dots x_{i\pm\frac{1}{2}} + a^+_{i\pm\frac{1}{2},j}\Delta t]$ vanishes for $\Delta t \to 0$ while the integrand remains nearly constant. Thus, we find in this limit:

$$
\begin{aligned}
D_{i\pm\frac{1}{2},j}\overline{\omega}^{n+1}_{i\pm\frac{1}{2},j} &\simeq \int_{D_{i\pm\frac{1}{2},j}} \boldsymbol{p}^n_{i,j}(x,y)dx\,dy - \int_{t^n}^{t^{n+1}} \int_{y_{j-\frac{1}{2}}+b^+_{i\pm\frac{1}{2},j-\frac{1}{2}}\Delta t}^{y_{j+\frac{1}{2}}-b^-_{i\pm\frac{1}{2},j+\frac{1}{2}}\Delta t} \boldsymbol{f}(\boldsymbol{u}(x,y,t))dy\Big|_{x_{i\pm\frac{1}{2}}-a^-_{i\pm\frac{1}{2},j}\Delta t}^{x_{i\pm\frac{1}{2}}+a^+_{i\pm\frac{1}{2},j}\Delta t} dt \\
&\xrightarrow{\Delta t\to 0} \int_{y_{j-\frac{1}{2}}}^{y_{j+\frac{1}{2}}} \left(a^+_{i\pm\frac{1}{2},j}\Delta t\boldsymbol{p}^+_{i\pm\frac{1}{2},j} - a^-_{i\pm\frac{1}{2},j}\Delta t\boldsymbol{p}^-_{i\pm\frac{1}{2},j}\right) dy \\
&\quad - \int_{t^n}^{t^{n+1}} \int_{y_{j-\frac{1}{2}}}^{y_{j+\frac{1}{2}}} \left(\boldsymbol{f}(\boldsymbol{u}^+(x,y,t^n)) - \boldsymbol{f}(\boldsymbol{u}^-(x,y,t^n))\right) dy\,dt
\end{aligned}
\tag{3.23}
$$

At this point one has to decide about the order of the scheme. This is due to the fact that we have to evaluate the spatial integrals using a method of the same order as the order of the scheme. This should also fit the order of the reconstruction since it usually is the lowest order the component of the lowest order which determines the order of the resulting scheme. Therefore, it is not sensible to use higher order components, since they are usually more expensive to compute. For a second-order reconstruction it is sufficient to use a midpoint rule for the estimation of the integrals, since this is of second order. Then the above result can be approximated as:

$$
\begin{aligned}
D_{i+\frac{1}{2},j}\overline{\omega}^{n+1}_{i+\frac{1}{2},j} &\simeq \left(a^+_{i+\frac{1}{2},j}\boldsymbol{u}^W_{i+1,j} - a^-_{i+\frac{1}{2},j}\boldsymbol{u}^E_{i,j}\right)\Delta t - \left(\boldsymbol{f}(\boldsymbol{u}^W_{i+1,j})) - \boldsymbol{f}(\boldsymbol{u}^E_{i,j})\right)\Delta t \\
D_{i-\frac{1}{2},j}\overline{\omega}^{n+1}_{i-\frac{1}{2},j} &\simeq \left(a^+_{i-\frac{1}{2},j}\boldsymbol{u}^W_{i,j} - a^-_{i-\frac{1}{2},j}\boldsymbol{u}^E_{i-1,j}\right)\Delta t - \left(\boldsymbol{f}(\boldsymbol{u}^W_{i,j})) - \boldsymbol{f}(\boldsymbol{u}^E_{i-1,j})\right)\Delta t
\end{aligned}
\tag{3.24}
$$

which can be combined into:

$$
\overline{\omega}^{n+1}_{i\pm\frac{1}{2},j} \simeq \frac{1}{(a^+_{i\pm\frac{1}{2},j} + a^-_{i\pm\frac{1}{2},j})\Delta y\Delta t}\left(\left(\pm a^\pm_{i\pm\frac{1}{2},j}\boldsymbol{u}^{W(E)}_{i\pm1,j} \mp a^\mp_{i\pm\frac{1}{2},j}\boldsymbol{u}^{E(W)}_{i,j}\right)\Delta t - \left(\pm\boldsymbol{f}(\boldsymbol{u}^{W(E)}_{i\pm1,j})) \mp \boldsymbol{f}(\boldsymbol{u}^{E(W)}_{i,j})\Delta t\right)\right)
\tag{3.25}
$$

Now, we can come back to the expressions needed in Eq. (3.17). The term needed there for $\omega^{n+1}_{i\pm\frac{1}{2},j}$ can now explicitly be given as:

$$
\begin{aligned}
\frac{(D_{i\pm\frac{1}{2},j}\ \cap\ C_{i,j})}{\Delta t\Delta x\Delta y}\overline{\omega}^{n+1}_{i\pm\frac{1}{2},j} &\simeq \frac{a^\pm_{i\pm\frac{1}{2},j}\Delta t\Delta y}{\Delta t\Delta x\Delta y}\frac{1}{(a^+_{i\pm\frac{1}{2},j} + a^-_{i\pm\frac{1}{2},j})\Delta y\Delta t}\left(\left(\pm a^\pm_{i\pm\frac{1}{2},j}\boldsymbol{u}^{W(E)}_{i\pm1,j} \mp a^\mp_{i\pm\frac{1}{2},j}\boldsymbol{u}^{E(W)}_{i,j}\right)\Delta t\right. \\
&\qquad \left. - \left(\pm\boldsymbol{f}(\boldsymbol{u}^{W(E)}_{i\pm1,j}) \mp \boldsymbol{f}(\boldsymbol{u}^{E(W)}_{i,j})\right)\Delta t\right) \\
&= \frac{a^\pm_{i\pm\frac{1}{2},j}}{(a^+_{i\pm\frac{1}{2},j} + a^-_{i\pm\frac{1}{2},j})\Delta x}\left(\left(\pm a^\pm_{i+\frac{1}{2},j}\boldsymbol{u}^{W(E)}_{i\pm1,j} \mp a^\mp_{i\pm\frac{1}{2},j}\boldsymbol{u}^{E(W)}_{i,j}\right) - \left(\pm\boldsymbol{f}(\boldsymbol{u}^{W(E)}_{i\pm1,j})) \mp \boldsymbol{f}(\boldsymbol{u}^{E(W)}_{i,j})\right)\right)
\end{aligned}
\tag{3.26}
$$

The results for the other terms needed in Eq. (3.17) can be found in a similar way and are just given here without further derivation. For the y direction we find:

$$
\begin{aligned}
\frac{|D_{i,j\pm\frac{1}{2}}\ \cap\ C_{i,j}|}{\Delta t\Delta x\Delta y}\overline{\omega}^{n+1}_{i,j\pm\frac{1}{2}} &\simeq \frac{b^\pm_{i,j\pm\frac{1}{2}}}{(b^+_{i,j\pm\frac{1}{2}} + b^-_{i,j\pm\frac{1}{2}})\Delta y}\left(\left(\pm b^\pm_{i,j\pm\frac{1}{2}}\boldsymbol{u}^{S(N)}_{i,j\pm1} \mp b^\mp_{i,j\pm\frac{1}{2}}\boldsymbol{u}^{N(S)}_{i,j}\right)\right. \\
&\qquad \left. - \left(\pm\boldsymbol{f}(\boldsymbol{u}^{S(N)}_{i,j\pm1})) \mp \boldsymbol{f}(\boldsymbol{u}^{N(S)}_{i,j})\right)\right)
\end{aligned}
\tag{3.27}
$$

And, finally, for the central part of the cell:

$$
\begin{aligned}
\left[\frac{|D_{i,j}\ \cap\ C_{i,j}|}{\Delta t\Delta x\Delta y}\overline{\omega}^{n+1}_{i,j} - \overline{\boldsymbol{u}}^n_{i,j}\right] &\simeq \frac{1}{\Delta x}\left(\left(-a^-_{i+\frac{1}{2},j}\boldsymbol{u}^E_{i,j} - a^+_{i-\frac{1}{2},j}\boldsymbol{u}^W_{i,j}\right) - \left(\boldsymbol{f}(\boldsymbol{u}^E_{i,j}) + \boldsymbol{f}(\boldsymbol{u}^W_{i,j})\right)\right) \\
&\quad + \frac{1}{\Delta y}\left(\left(-b^-_{i,j+\frac{1}{2}}\boldsymbol{u}^N_{i,j} - b^+_{i,j-\frac{1}{2}}\boldsymbol{u}^S_{i,j}\right) - \left(\boldsymbol{g}(\boldsymbol{u}^N_{i,j}) + \boldsymbol{g}(\boldsymbol{u}^S_{i,j})\right)\right)
\end{aligned}
\tag{3.28}
$$

When we put all these results into Eq. (3.17) we obtain the final form for the semidiscrete scheme:

$$\frac{d}{dt}\bar{u}_{i,j}(t) = -\frac{H^x_{i+\frac{1}{2},j}(t) - H^x_{i-\frac{1}{2},j}(t)}{\Delta x} - \frac{H^y_{i,j+\frac{1}{2}}(t) - H^y_{i,j-\frac{1}{2}}(t)}{\Delta y} \tag{3.29}$$

with the numerical fluxes defined as:

$$H^x_{i+\frac{1}{2},j} = \frac{1}{a^+_{i+\frac{1}{2},j} + a^-_{i+\frac{1}{2},j}} \left(a^+_{i+\frac{1}{2},j} \boldsymbol{f}(\boldsymbol{u}^E_{i,j}) - a^-_{i+\frac{1}{2},j} \boldsymbol{f}(\boldsymbol{u}^W_{i+1,j}) - a^+_{i+\frac{1}{2},j} a^-_{i+\frac{1}{2},j} \left(\boldsymbol{u}^W_{i+1,j} - \boldsymbol{u}^E_{i,j} \right) \right) \tag{3.30}$$

and an analogous expression for the y-direction.

Remarks:

- The scheme can easily be extended to more than two dimensions just by adding the appropriate terms for the additional directions.
- For a higher order reconstruction the derivation can be re-done with a higher order approximation for the integrals. This, however, leads exactly to the results one would get when extending the above equations by intuition. That is terms like $\boldsymbol{u}^E_{i,j}$ have to be replaced by $\frac{1}{6}\left(\boldsymbol{u}^{NE}_{i,j} + 4\boldsymbol{u}^E_{i,j} + \boldsymbol{u}^{SE}_{i,j}\right)$ when applying the fourth order Simpson's quadrature formula for the integrals.

3.1.3 The Reconstruction

After having introduced the scheme itself a few words are needed about the aforementioned reconstruction. This is used to obtain point values from the cell averages to be used for the evaluation of the numerical fluxes introduced above. In principle, it is an easy task to obtain such point values from the cell averages by the application of an interpolation polynomial. This procedure, however, becomes more complicated, when we want the reconstruction to prevent spurious oscillations. This is addressed after having introduced the basic idea about the reconstruction polynomial.

The Reconstruction Polynomial

In order to be consistent with the previous approach we here describe the second order reconstruction. In $\mathbb{R}^2$ the most general form for a second order polynomial looks like this:

$$\boldsymbol{p}_2 = \boldsymbol{A}^0 + \boldsymbol{A}^x x + \boldsymbol{A}^y y + \boldsymbol{A}^{xy} xy \tag{3.31}$$

with the A^i being constants, which are different for the individual cells. If applied to the reconstruction in any of the cells of the computational domain we get:

$$\boldsymbol{p}_{i,j} = \boldsymbol{u}^n_{i,j} + \boldsymbol{u}^x_{i,j}(x - x_i) + \boldsymbol{u}^y_{i,j}(y - y_j) + \boldsymbol{A}^{xy}(x - x_i)(y - y_j) \tag{3.32}$$

Considering the scheme derived above it is, however, clear that the last term can be neglected, since it will vanish at the points where the polynomial is evaluated.

There are different possibilities for an evaluation of the individual coefficients, but it is important to require the conservation of the cell average for the cell under consideration to be fulfilled:

$$\int_{y_{j-\frac{1}{2}}}^{y_{j+\frac{1}{2}}} \int_{x_{i-\frac{1}{2}}}^{x_{i+\frac{1}{2}}} \boldsymbol{p}_{i,j} dx\, dy \overset{!}{=} \bar{\boldsymbol{u}}_{i,j} \tag{3.33}$$

Apart from that, it is also necessary for the reconstruction to be of second order wherever the solution is sufficiently smooth. Finally – and this is the most important point for high Mach number simulations – the reconstruction has to ensure a non-oscillatory behaviour of the numerical scheme.

The conservation of the cell average is most easily ensured by using $\boldsymbol{u}^n_{i,j} = \bar{\boldsymbol{u}}_{i,j}$. Additionally the required non-oscillatory behaviour is guaranteed by use of:

$$\boldsymbol{u}^x_{i,j} = \text{minmod}\left(\theta\frac{\bar{\boldsymbol{u}}^n_{i,j} - \bar{\boldsymbol{u}}^n_{i-1,j}}{\Delta x}, \frac{\bar{\boldsymbol{u}}^n_{i+1,j} - \bar{\boldsymbol{u}}^n_{i-1,j}}{2\Delta x}, \theta\frac{\bar{\boldsymbol{u}}^n_{i+1,j} - \bar{\boldsymbol{u}}^n_{i,j}}{\Delta x}\right) \tag{3.34}$$

where $\theta \in [1, 2]$ with the corresponding form for the y-direction yielding A^y. Note that larger θs correspond to less dissipative but still *non-oscillatory* limiters. Apart from that, minmod represents van-Leer's limiter (van Leer 1979). This limiter is explicitly defined by:

$$\text{minmod}(a, b, c) := \begin{cases} \text{sign}(a)\min(|a|, |b|, |c|) & \text{if} \quad \text{sign}(a) = \text{sign}(b) = \text{sign}(c) \\ 0 & \text{else} \end{cases} \tag{3.35}$$

For this limiter it can be shown that the reconstruction is not only non-oscillatory but also total-variation diminishing (TVD) (see e.g. Kurganov et al. 2001). This reconstruction guarantees oscillations to be suppressed at steep gradients as will be shown when the different tests are discussed.

3.1.4 Higher Order Schemes

The order of a numerical scheme is quite easily figured out by test simulations with increasing spatial resolution. Ideally the error for an nth order scheme decreases as 2^{-n} when the when the spatial resolution is doubled. This also is a good test to determine if the scheme converges to a solution if the analytical one is unknown. Therefore, an order as high as possible is desirable.

For the Cweno scheme introduced above there are several higher order versions available for the solution of one-dimensional hyperbolic conservation laws (see e.g. Qiu and Shu 2002). It is, however, far from trivial to extent such a scheme to more than one spatial dimension. The easiest way to do this is a dimension by dimension approach as discussed in Kurganov and Levy (2000). This approach uses the one-dimensional reconstruction for all spatial dimensions individually, where the reconstruction polynomial is slightly modified in order to take the additional dimensions into account.

Unfortunately the integrals over the cell boundaries as used, e.g., in Eq. (3.23), which have to be of the same order as the reconstruction are effectively only done via the midpoint rule in the dimension by dimension approach. This results in these integrals being only of second order. For the Cartesian directions this poses no problem. But for any structure oblique to the spatial grid the order of the scheme is strongly reduced. This is not tolerable in turbulence simulations where grid-connected numerical artifacts cannot easily be identified. Moreover, it was shown using a simple advection test that the dimension by dimension scheme for most resolutions hardly exceeded second order.

For a true third order scheme, therefore, integrals like the one in Eq. (3.23) also have to be evaluated with third order accuracy. The least expensive way to perform such an integral to third order accuracy is to use a Gaussian quadrature (see e.g. Bronstein et al. 1997, p. 837) based on using roots of the Legendre polynomials as nodes for the integration. In this case for a third order scheme in $\mathbb{R}^2$ each integral would use two nodes instead of one when applying the midpoint rule. Similar tests as for the dimension by dimension approach showed that in this case third order accuracy is readily achieved.

For numerical computations in $\mathbb{R}^3$, however, the evaluation of the integral already gets four times as expensive as for the second order scheme. Apart from that also the reconstruction becomes much more expensive than in the second order version of the scheme – also this reconstruction is not TVD anymore but rather *Essentially Non Oscillatory* (ENO). Another important issue is that near discontinuities the third order reconstruction is reduced to second order to obtain the ENO property. Therefore, for homogeneous turbulence with strong discontinuities ubiquitous in the numerical domain the best choice is a second order scheme. This scheme also proved to be more stable than higher order schemes when coming to high Mach number fluids.

3.2 Time Integration

After the Cweno scheme was introduced in the preceding paragraph we no discuss how to implement this scheme in a numerical solver. As was stated above, the Cweno scheme given in the semidiscrete form requires a very small time step. The advantage of the semidiscrete character at the same time is that there is a free choice of the method for the computation of the time evolution. Therefore, the next thing of interest is the time integration.

The simplest method for the numerical time integration is the Euler method, which uses information on the time derivative at the previous time step to advance the system to the subsequent one. Due to this use of information about one time step only, however, the Euler method is neither very accurate nor very stable. To account for these problems there are the Runge-Kutta methods of different order at hand, which use information on several *trial* steps between the previous and the subsequent time step. In this work we used a third order Runge-Kutta time integrator of the form:

$$u^{n+1} = u^n + \frac{1}{6}\Delta t \left(f'(t^n) + 4f'(t^{n+1/2}) + f'(t^{n+1}) \right) + O(\Delta t^{\,4}) \tag{3.36}$$

The time integration is explicitly given in TVD form also applied by Jiang and Shu (1996):

$$u^* = u^n + \Delta t f'(u^n) \tag{3.37}$$

$$u^{**} = \frac{3}{4}u^n + \frac{1}{4}u^* + \frac{1}{4}\Delta t f'(u^*) \tag{3.38}$$

$$u^{n+1} = \frac{1}{3}u^n + \frac{2}{3}u^{**} + \frac{2}{3}\Delta t f'(u^{**}) \tag{3.39}$$

where u^* is used as a trial step for t^{n+1} and u^{**} as a trial step for $t^{n+1/2}$. Since u^* and u^{**} only have to be used for the next intermediate time step this method is quite efficient concerning the memory consumption: All in all only the field at the previous time step u^n and the actual intermediate step have to be stored. This matter proved to be essential for being able to perform high resolution computations.

Time Step Limit

An important issue in all numerical schemes is the maximum possible value of the time integration step. This is especially an issue since with the Runge-Kutta time integrator we rely on an explicit scheme for the temporal evolution. Whereas implicit schemes often allow much larger time steps, there is no such scheme available for the direct solution of the MHD equations (even for linear differential equations implicit schemes involve inversions of huge matrices). The reason why implicit schemes usually allow larger time steps than explicit ones is that only implicit schemes are absolutely stable. Explicit schemes, in contrast to that, are stable only up to a certain time step size.

The size of the stability limit for explicit schemes is determined by the so-called Courant or CFL number introduced above. In the case of hyperbolic conservation laws the Courant number reflects the portion of a cell that is traversed by the fastest fluid element in the computational domain in a given time step *dt*:

$$c_{CFL} = \frac{u_{max} dt}{dx} \tag{3.40}$$

In the case of the Cweno scheme the CFL number clearly has to stay below 0.5. Otherwise the regions containing the Riemann fans might interact with each other. Apart from the fact that the regions containing the Riemann fans have to be small compared to the cell size, an intersection of the different Riemann fans would obviously contradict the idea of the scheme.

There is, however, also an upper limit on the time step for Runge-Kutta time integrators. The actual stability limit can be found with a so-called Von Neumann stability analysis. For central schemes applying the third order Runge-Kutta time integrator Pareschi et al. (2005) found the resulting limit to be at a Courant number of 0.42. Evidently, choosing the limit as 0.4 is a safe choice for the numerical solver used in this work.

3.3 Cweno for Numerical MHD

Even for the two-fluid system using the Cweno scheme we essentially have to solve the hyperbolic part of the equations. The source terms will be taken into account separately. This is sensible insofar as each aspect of the equations is solved with the most appropriate method. Having to solve only the hyperbolic part of the equations with the Cweno solver means that the system of equations is reduced to the MHD equations for the charged particle fluid and to the hydrodynamic equations for the neutral fluid. Here we discuss the explicit implementation of the MHD equations into the Cweno scheme, since the hydrodynamic equations are basically included therein.

As seen in the discussion of the Cweno scheme it does not need as much adaptation as, e.g., a Riemann solver. For the former it is not necessary to use different solvers for hydrodynamical or MHD simulations. The only inputs that have to be given are the system of equations to be solved and the formula for the derivation of the maximum of the characteristic speeds at the cell boundaries.

As an example we derive the characteristic speeds for the evolution equations of compressible hydrodynamical flow in appendix D. There it is shown that the characteristic speeds correspond to the eigenvalues of the Jacobian of the system for the individual directions. For the system of the normalised MHD equations this derivation is also motivated in D and can also be found in de Sterck et al. (1999). The resulting characteristic speeds are:

$$\begin{aligned} \lambda_1 &= u_x \\ \lambda_{2,3} &= u_x \pm \mathrm{v}_{A_x} \\ \lambda_{4,5} &= u_x \pm \mathrm{v}_{f_x} \\ \lambda_{6,7} &= u_x \pm \mathrm{v}_{s_x} \end{aligned} \tag{3.41}$$

for the x-direction. Here the following definitions have been used for the normalised system of equations:

$$c_s := \sqrt{\frac{\mathrm{d}p}{\mathrm{d}\rho}} = \sqrt{\gamma\frac{p}{\rho}} \qquad \text{speed of sound} \tag{3.42}$$

$$\mathrm{v}_A := \frac{B}{\sqrt{\rho}} \qquad \left(\mathrm{v}_{A_x} := \frac{B_x}{\sqrt{\rho}}\right) \qquad \text{Alfvén speed (in x-direction)} \tag{3.43}$$

$$\mathrm{v}_{f_x} := \frac{1}{\sqrt{2}}\sqrt{c_s^2 + \mathrm{v}_A^2 + \sqrt{(c_s^2 + \mathrm{v}_A^2)^2 - (2c_s\mathrm{v}_{A_x})^2}} \qquad \text{fast magnetosonic speed in x-direction} \tag{3.44}$$

$$\mathrm{v}_{s_x} := \frac{1}{\sqrt{2}}\sqrt{c_s^2 + \mathrm{v}_A^2 - \sqrt{(c_s^2 + \mathrm{v}_A^2)^2 - (2c_s\mathrm{v}_{A_x})^2}} \qquad \text{slow magnetosonic speed in x-direction} \tag{3.45}$$

Thus, we can identify four different wave types: $\lambda_{2,3}$ obviously indicates Alfvén waves and $\lambda_{4,5}$ and $\lambda_{6,7}$ represent the propagation of the fast and slow magneto-acoustic modes. Finally λ_1 indicates a wave not propagating in space, which is identified in Kalikhman (1967) as an entropy wave. All in all, the Jacobian has distinct eigenvalues, which are always real. Therefore, the system is strictly hyperbolic, which is a necessary ingredient for the numerical method.

For the Cweno method we do not have to evaluate all of the characteristic speeds. Rather it is sufficient to find the maximum possible speeds at the boundaries of the cells as was discussed in section 3.1.2. For example the velocities $a^{\pm}$ needed for the scheme are the highest possible speeds to the left and to the right, respectively.

For the MHD equations clearly $\lambda_{4,5}$ dominate all other possible speeds. Designating λ_4 as the one with the positive sign, this is usually the highest possible speed. Only for a negative flow velocity u_x greater than the fast magnetosonic speed v_{f_x} the corresponding speed has to be set to zero. The highest possible speed to the left on the other hand is λ_5. Therefore, the local speeds $a^{\pm}$ in the x-direction to be

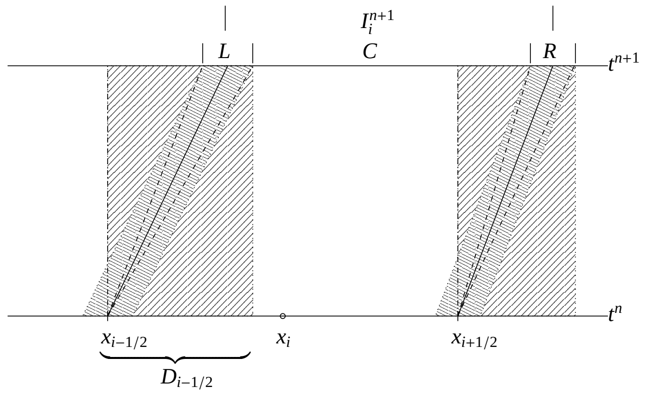

Fig. 3.3: Typical Riemann fan structure for high Mach number flow. For the discussion see the text.

used in the CWENO scheme are:

$$\begin{aligned} a^+ &= \max\left(u_x + \mathrm{v}_{f_x}, 0\right) \\ a^- &= \min\left(u_x - \mathrm{v}_{f_x}, 0\right) \end{aligned} \tag{3.46}$$

Initially this might seem as if one has to supply as much information on the system as would be necessary for a Riemann solver. Luckily, however, Eq. (3.44) can also be applied to strictly hydrodynamical simulations, for which the magnetic induction merely has to be set to zero. Moreover, one has to keep in mind that so far no exact Riemann solver for MHD problems is known, whereas the corresponding velocities necessary for the implementation of the CWENO scheme can very well be found. Finally, a Riemann solver would also have to yield the spatial dependence of all the other variables involved, which is not necessary here.

3.3.1 Improvement of the Scheme

From the above discussion it is clear that for high Mach number flows the estimate for the width of the Riemann fans given in Eq. (3.46) typically exceeds their actual width. This fact is illustrated in Fig. 3.3, where a typical Riemann fan structure is shown for high Mach number flows. Any signal propagating with any of the characteristic velocities (3.41) originating from the cell boundaries is confined to the triangular regions limited by the dashed line. In the CWENO reconstruction introduced in section 3.1 one of the major steps is the averaging performed over the regions containing the Riemann fans in order not to have to rely on a Riemann solver. In Fig. 3.3 the respective region is indicated as $D_{i-1/2}$. This region, however, clearly overestimates the actual width of the region containing the Riemann fan for flows for which the background velocity exceeds the maximum signal propagation velocity $a^\pm$ – that is the above mentioned triangular regions are much smaller than the rectangular area indicating the region over which the averaging is performed for the classical CWENO scheme.

The major reason to try to minimise the width of the Riemann fans is that the averaging over these is a major contribution to the dissipation of the scheme. From Fig. 3.3 it becomes clear that in order to minimise the region over which the averaging is performed the boundaries of this region have to be allowed to move. The best choice would, therefore, be to perform the averaging over the region L in Fig. 3.3 instead of region $D_{i-1/2}$. The resulting scheme being consistent with the ideas presented in section 3.1 is a method with a grid that moves with the local velocities v_x at the cell boundaries. If these velocities differ from cell boundary to cell boundary, as they would do in the general case, also the size of the cells changes in time. The resulting scheme for the one-dimensional case is presented in detail in Kissmann and Grauer (2006). The evolution equation derived there reads:

$$\frac{d}{dt}\bar{u}_i(t) = -\frac{(H_{i+1/2} + \mathrm{v}^0_{i+1/2}\bar{u}^n_i) - (H_{i-1/2} + \mathrm{v}^0_{i-1/2}\bar{u}^n_i)}{\Delta x} \tag{3.47}$$

with:

$$H_{i+1/2} = -\frac{\tilde{a}^{+}_{i+1/2} a^{-}_{i+1/2} u^{+}_{i+1/2} - a^{+}_{i+1/2} \tilde{a}^{-}_{i+1/2} u^{-}_{i+1/2}}{a^{+}_{i+1/2} + a^{-}_{i+1/2}} + \frac{a^{+}_{i+1/2} f(u^{-}_{i+1/2}) + a^{-}_{i+1/2} f(u^{+}_{i+1/2})}{a^{+}_{i+1/2} + a^{-}_{i+1/2}} \tag{3.48}$$

where $\Delta\tilde{x}$ is the with of the cell at the next time step. Here – similar to the case of the classical CWENO scheme – $a^{\pm}_{i\pm1/2}$ are the right- and left-handed maximum characteristic velocities at the left and right cell boundaries respectively. Here they are measured with respect to the local fluid velocities designated as $\mathrm{v}^{0}_{i\pm1/2}$. In contrast to that $\tilde{a}^{\pm}_{i\pm1/2}$ also indicates the characteristic velocities – in this case, however, defined with respect to the non-moving frame.

This scheme proved to be of very low dissipation and what is even more important yields results independent of the background flow. This is of particular importance for high Mach number flows, since the dissipation in the classical CWENO scheme is dominated by the background flow for this case. This is especially annoying since simple convection can even be solved analytically.

Unfortunately this improved scheme is so far only available for one-dimensional simulations. This is due to the fact that a co-moving grid cannot be realised in more than one dimension. The solution of this would be to project the shifted grid back onto the original one every time step. There is, however, a lot of work still to be done before arriving at such a new scheme, which will be left for future research. One particular problem in the derivation of the scheme is that for more than one dimension the definition of the co-moving Riemann-fan structure is very complicated.

All in all the CWENO scheme proves to be a very reliable scheme with the important feature of a very simple implementation for different physical problems. As we were able to show here, however, the scheme can still be improved for high Mach number flows. One thing still missing for the MHD implementation of the scheme, however, is the insurance of the solenoidality of the magnetic field.

3.3.2 Solenoidality of the Magnetic Field

There are various strategies available to ensure the absence of magnetic monopoles for numerical computations as required by the corresponding Maxwell equation (2.25):

$$\nabla \cdot \boldsymbol{B} = 0 \tag{3.49}$$

This equation has to be fulfilled at all times. Analytically this is guaranteed by the normalised evolution equation for the magnetic induction (2.80):

$$\frac{\partial \boldsymbol{B}}{\partial t} = \nabla \times (\boldsymbol{u} \times \boldsymbol{B}) \tag{3.50}$$

Therefore, analytically the divergence of the magnetic induction evolves according to:

$$\frac{\partial \nabla \cdot \boldsymbol{B}}{\partial t} = \nabla \cdot \frac{\partial \boldsymbol{B}}{\partial t} = \nabla \cdot (\nabla \times (\boldsymbol{u} \times \boldsymbol{B})) = 0 \tag{3.51}$$

Thus, an initially solenoidal magnetic induction will analytically be solenoidal for all times. Numerically, unfortunately, things look a little different. In this case we are using the hyperbolic form of the above equation:

$$\frac{\partial \boldsymbol{B}}{\partial t} = -\nabla \cdot (\boldsymbol{uB} - \boldsymbol{Bu}) = -\nabla \cdot \begin{pmatrix} 0 & u_x B_y - u_y B_x & u_x B_z - u_z B_x \\ u_y B_x - u_x B_y & 0 & u_y B_z - u_z B_y \\ u_z B_x - u_x B_z & u_z B_y - u_y B_z & 0 \end{pmatrix} \tag{3.52}$$

Analytically the two forms (3.50) and (3.52) are completely equivalent. Unfortunately, however, this is not the case anymore when using the discrete version of the equation. Additionally the truncation errors introduced by any numerical computation can accumulate during a numerical simulation. All in all it is necessary to find some method to ensure the solenoidality of the magnetic field. Otherwise *numerical monopoles* are introduced yielding physically wrong results.

To ensure the solenoidality of the magnetic field also for the numerical simulations at hand there are basically three typical methods available. These methods will here be briefly introduced one by one.

Lagrangian Multipliers

The method of Lagrangian multipliers was first implemented by Assous et al. (1993) for the numerical solution of the Maxwell equations. They introduced a Lagrangian multiplier to couple the divergence constraint to the other evolution equations. This idea was extended to the MHD equations by Dedner et al. (2002). They introduced an additional function ψ, which is integrated together with the MHD equations. Generally this variable is introduced to couple the solenoidality constraint to the other equations. This means that the system is extended to the form:

$$\frac{\partial \boldsymbol{B}}{\partial t} = -\nabla \cdot (\boldsymbol{uB} - \boldsymbol{Bu}) - \nabla\psi \tag{3.53}$$

$$\mathsf{D}(\psi) = -\nabla \cdot \boldsymbol{B} \tag{3.54}$$

with D some linear differential operator. Of the different possibilities for this operator the form:

$$\mathsf{D}(\psi) := \frac{1}{c_h^2}\frac{\partial\psi}{\partial t} + \frac{1}{c_p^2}\psi \tag{3.55}$$

could be shown to be the best choice. This results in an evolution equation of the form:

$$\partial_t\psi = -c_h^2\nabla \cdot \boldsymbol{B} - \frac{c_h^2}{c_p^2}\psi \tag{3.56}$$

This is generally denoted as the mixed generalised Lagrange multiplier (GLM) formulation. The interesting thing about this choice for the operator D is that it allows for hyperbolic (c_h) and parabolic (c_p) corrections at the same time. Especially the hyperbolic part is very interesting since it allows the transport of the divergence out of the numerical domain with the velocity c_h. Although this method proved to be very efficient for many numerical problems, it is unfortunately not very interesting for our problem. Due to the periodic boundary conditions it is not possible to transport the non-zero divergence out of the numerical domain. Moreover, the fact that the turbulence is homogeneous means that there is no place in the numerical domain where we can shift the divergence to.

Projection Schemes

An alternative way to get rid of unphysical magnetic monopoles is based on the works by Chorin. In a series of papers he introduced the so-called projection scheme to guarantee the incompressibility of the numerical solution of the Navier-Stokes equation (see Chorin 1967, 1968, 1969). This scheme was first applied to the MHD equations by Brackbill and Barnes (1980). The idea of these schemes is to evolve the MHD equations by some arbitrary numerical scheme and after each time step to project the resulting magnetic induction to a divergence free field. For doing so the magnetic induction is decomposed into the sum of a solenoidal and a divergence containing field:

$$\boldsymbol{B} = \nabla \times \boldsymbol{A} + \nabla\Phi \tag{3.57}$$

where the scalar field Φ is *responsible* for the divergence of the field. Therefore, the field $\boldsymbol{A}$ can be said to be the physically meaningful part of the magnetic induction. Thus, all that has to be done is to subtract this part from the magnetic induction in order to obtain a solenoidal magnetic field. By taking the divergence of the above equation one easily finds an equation determining the scalar field:

$$\nabla^2\Phi = \nabla \cdot \boldsymbol{B} \tag{3.58}$$

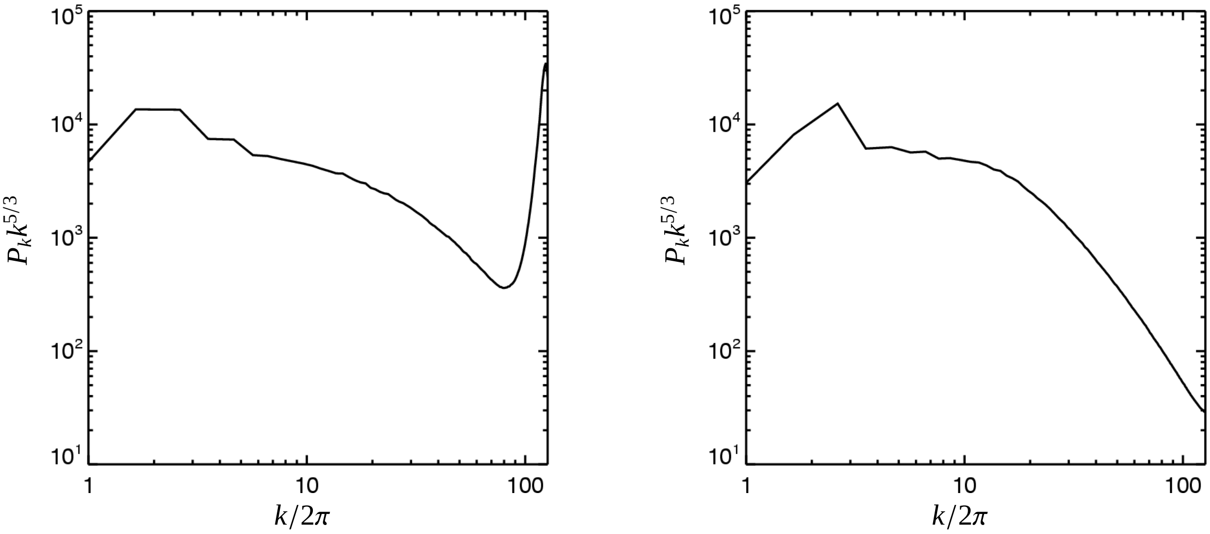

Fig. 3.4: Visualisation of the accumulation of fluctuation energy at small spatial scales for the projection schemes (left). These results are compared to those obtained with a constrained transport scheme (right). All values are normalised.

The essential step, therefore, is to solve this Poisson equation. After this the divergence free magnetic field is easily obtained by:

$$\boldsymbol{B} \to \boldsymbol{B} - \nabla\Phi \tag{3.59}$$

The actual solution of the Poisson equation can be obtained by many different methods quite easily. For this work we used a multi-grid solver or a Fourier solver (the latter was used whenever use of the fftw (see Frigo 2004) library was necessary anyhow) for the solution of this equation. For both solvers we showed the solenoidality of the magnetic field to be assured up to the round off error. For a numerical solver, however, this can only be achieved for *one kind of discretisation* i.e. we have to decide for one discretisation of the divergence of the magnetic induction – only for this discretisation we will be able to assure the solenoidality. This is also true for any other method to assure the solenoidality of the magnetic field.

Despite the fact that this method yields divergence-free fields to the round off error it proved to be not acceptable for turbulence simulations. This is due to the fact that the method introduces additional small-scale fluctuations, which produce unphysical fluctuation spectra for the highest wavenumbers. This is visualised in Fig. 3.4 where a solution obtained using a projection scheme is compared to one found by using a constrained transport scheme. There is an unphysical pile up of fluctuation energy at large wavenumbers for the former solution. This was also observed by Balsara and Kim (2004). They found that the excessive fluctuation energy at small scales is connected to the decoupling of even and odd grid points which occurs when using a centred finite difference for the representation of the divergence of the magnetic induction. The main problem, however, seems to be connected to spurious magnetic field structures produced by the projection schemes in general, which Balsara and Kim attribute to the non-locality of the projection schemes. This means that the correction does not take local shock structures into account, thus, yielding solutions not being conform to the shock solution anymore. Balsara and Kim identify the constrained transport schemes to be those best suited for turbulence simulations. Therefore, we also rely on such a scheme for our investigations.

Constrained Transport Schemes

The idea with constrained transport schemes is to formulate the equations in a way that the divergence of the magnetic induction vanishes in the desired discretisation. Originally this method was introduced

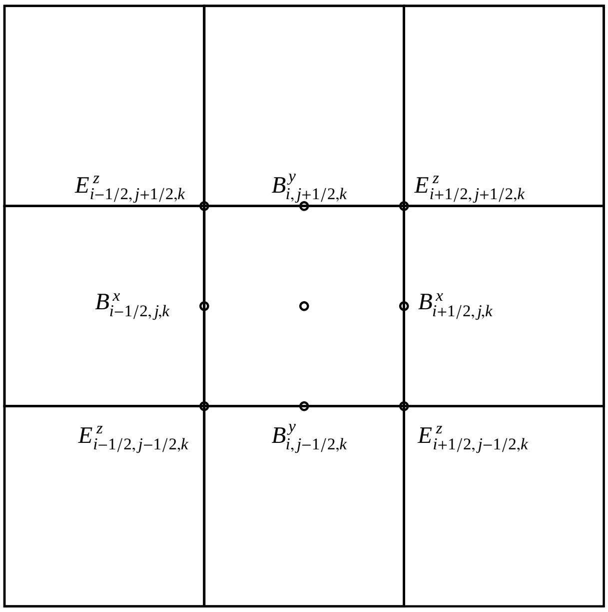

Fig. 3.5: Spatial arrangement of electromagnetic quantities for constrained transport schemes. For further discussions on the scheme cf. the text.

by Evans and Hawley (1988) where the authors introduce a staggered grid for the magnetic induction to maintain the solenoidality of the scheme for finite difference schemes. For this they write the induction equation explicitly via the curl of the electric field:

$$\frac{\partial \boldsymbol{B}}{\partial t} = -\nabla \times \boldsymbol{E} \tag{3.60}$$

Their main idea is to place – for the 2D case – the electric field at the cell corners. Numerically this is realised by writing:

$$\begin{aligned}
\frac{\partial B^x_{i-1/2,j,k}}{\partial t} &= -\frac{E^z_{i-1/2,j+1/2,k} - E^z_{i-1/2,j-1/2,k}}{\Delta y} + \frac{E^y_{i-1/2,j,k+1/2} - E^y_{i-1/2,j,k-1/2}}{\Delta z} \\
\frac{\partial B^y_{i,j-1/2,k}}{\partial t} &= -\frac{E^x_{i,j-1/2,k+1/2} - E^x_{i,j-1/2,k-1/2}}{\Delta z} + \frac{E^z_{i+1/2,j-1/2,k} - E^z_{i-1/2,j-1/2,k}}{\Delta x} \\
\frac{\partial B^z_{i,j,k-1/2}}{\partial t} &= -\frac{E^y_{i+1/2,j,k-1/2} - E^y_{i-1/2,j,k-1/2}}{\Delta x} + \frac{E^x_{i,j+1/2,k-1/2} - E^x_{i,j-1/2,k-1/2}}{\Delta y}
\end{aligned} \tag{3.61}$$

This spatial arrangement is also visualised in Fig. 3.5. This evolution equation satisfies Eq. (3.51) when the divergence is defined as:

$$(\nabla \cdot \boldsymbol{B})_{num} := \frac{B^x_{i+1/2,j,k} - B^x_{i-1/2,j,k}}{\Delta x} + \frac{B^y_{i,j+1/2,k} - B^y_{i,j-1/2,k}}{\Delta y} + \frac{B^z_{i,j,k+1/2} - B^z_{i,j,k-1/2}}{\Delta z} \tag{3.62}$$

Therefore, an initially solenoidal magnetic induction will remain so up to the truncation error of the variables used in the code. This property has been verified using the above scheme. This method can be easily implemented and very successful for finite difference schemes. When, however, dealing with fluids for which shocks might occur one has to use a method like CWENO also for the magnetic field evolution. This problem was solved by Balsara and Spicer (1999), where they combine the constrained transport idea with a Godunov type base scheme. This is done via the identification of the electrical field with the numerical fluxes.

For the special case of the Cweno scheme the constrained transport form of such schemes was derived by Ziegler (2004). By use of the numerical form of the induction equation (3.52) we identify the flux, e.g., in the x-direction for the evolution of the magnetic induction using the Cweno scheme to be:

$$\boldsymbol{H}^x_{i+\frac{1}{2},j,k} = \frac{1}{a^+_{i+\frac{1}{2},j,k} + a^-_{i+\frac{1}{2},j,k}} \left(a^+_{i+\frac{1}{2},j,k} \begin{pmatrix} 0 \\ -E_z \\ E_y \end{pmatrix}^E_{i,j,k} - a^-_{i+\frac{1}{2},j,k} \begin{pmatrix} 0 \\ -E_z \\ E_y \end{pmatrix}^W_{i+1,j,k} - a^+_{i+\frac{1}{2},j,k} a^-_{i+\frac{1}{2},j,k} \left(\boldsymbol{B}^W_{xi+1,j,k} - \boldsymbol{B}^E_{xi,j,k} \right) \right) \tag{3.63}$$

with corresponding fluxes for the other directions. From these fluxes the electric field is evaluated via interpolation as:

$$E^x_{i,j-1/2,k-1/2} = \frac{1}{4} \left(-H^y_{z\,i,j-1/2,k} - H^y_{z\,i,j-1/2,k-1} + H^z_{y\,i,j,k-1/2} + H^z_{y\,i,j-1,k-1/2} \right) \tag{3.64}$$

with corresponding interpolations for the other two components of the electric field. The only remaining issue is the discussion of the correct reconstruction of the magnetic field. Since the magnetic field is defined on a staggered grid also the reconstruction has to be a little different from the one introduced in section 3.1.3. Clearly for each component of the magnetic field the point values at the boundaries of the cells in the parallel direction do not have to be reconstructed at all. For the other directions this reconstruction is done via a mixture of interpolation and Cweno reconstruction. The details for this are also given in Ziegler (2004). There the excellent performance of the resulting scheme is shown by several one and two-dimensional test cases. The same, however, has to be done in our case to assure that the scheme has been implemented correctly.

3.4 Validity of the Scheme

In this paragraph we will discuss several tests to check the validity of the Cweno scheme for the simulations presented in this work. The validity of the basic one-dimensional scheme will be verified by different one-dimensional tests. These were performed in all three grid directions individually to ensure the homogeneity of the scheme. Moreover, we have included several multi-dimensional test cases, which were also used to check the correctness of the order of the scheme.

In most cases we have chosen tests for which an analytical solution or at least a semi-analytical one exists. For hydrodynamics (HD) and magneto-hydrodynamics (MHD) several such tests are provided in Stone et al. (1992) and Toro (1997). Here we will give a brief excerpt of the tests undertaken with our newly developed scheme. We will place special emphasis on tests containing shocks since these are on the one hand much harder to handle than smooth flow and they are on the other hand ubiquitous in high Mach number turbulence.

3.4.1 Burgers Equation

The most simple test available containing already discontinuities is the solution of the one-dimensional Burgers equation (see Burgers 1948). This prototype of a nonlinear fluid equation is named after the Dutch physicist, Johannes Martinus Burgers. Here we will investigate the solution of the *inviscid* form of the equation, which reads:

$$\frac{\partial u}{\partial t} = -\frac{1}{2}\frac{\partial u^2}{\partial x} = -u\frac{\partial u}{\partial x} \tag{3.65}$$

From this form of the equation it is clear already without any characteristic decomposition that the characteristic velocity is just u. All that is needed as input for the Cweno scheme is this characteristic velocity and the above evolution equation. For the initial condition we choose a sine wave in the numerical domain together with periodic boundary conditions. The numerical solution is obtained using a spatial

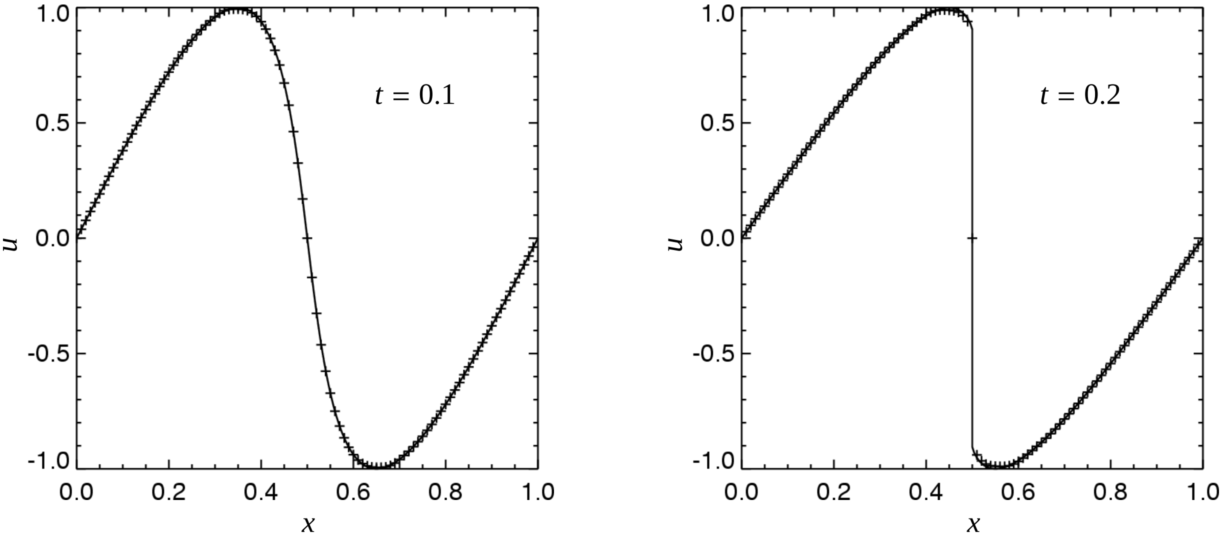

Fig. 3.6: Numerical (plus signs) and analytical (solid line) solution of the Burgers equation at two different times. Obviously the numerical solution is in very good agreement with the analytical results.

resolution of 100 grid cells for the computational domain of unit width. The time step was chosen as 0.002 so that the Courant number never exceeded 0.2. The results for the corresponding numerical solution of the Burgers equation is shown in Fig. 3.6. Obviously, the numerical solution nicely corresponds to the analytical one. The latter was found by the method of characteristics in a semi-analytical way. On the one hand the results in Fig. 3.6 show that the CWENO scheme is capable of solving hyperbolic differential equations. On the other hand it also becomes clear that discontinuities are well resolved using the CWENO scheme. There are no artificial, unphysical fluctuations near the discontinuity in the solution at time $t = 0.2$. This is a most important property of the CWENO scheme being essential for the simulation of high Mach number turbulence.

3.4.2 Euler Equations

A more complicated system of equations allowing for discontinuous solutions are the *Euler* equations. These equations being named after the Swiss physicist and mathematician, Leonhard Euler, describe the evolution of an *inviscid* fluid. They are generally given in the form:

$$\frac{\partial \rho}{\partial t} = -\nabla \cdot (\rho \mathbf{v}) \tag{3.66}$$

$$\frac{\partial (\rho \mathbf{v})}{\partial t} = -\nabla \cdot (\rho \mathbf{v}\mathbf{v} + p\mathbb{1}) \tag{3.67}$$

$$\frac{\partial e}{\partial t} = -\nabla \cdot ((e + p)\,\mathbf{v}) \tag{3.68}$$

where e is the total energy densities – that is the sum of internal and kinetic energy density. One of the most important tests of a numerical method making use of the Euler equations is the hydrodynamic shock tube problem (the classical hydrodynamical Riemann problem) first introduced by Sod (1978). The initial state of the problem is a contact discontinuity between two homogeneous domains of different density and pressure. The idea behind this problem is that the two domains are initially separated by some kind of barrier, which is removed at the start of the computation. The temporal evolution and resulting spatial structure strongly depend on the initial conditions in the two distinct domains. Luckily, however, there exists a semi-analytical solution for these kind of one-dimensional problems, see e.g. Toro (1997). Here

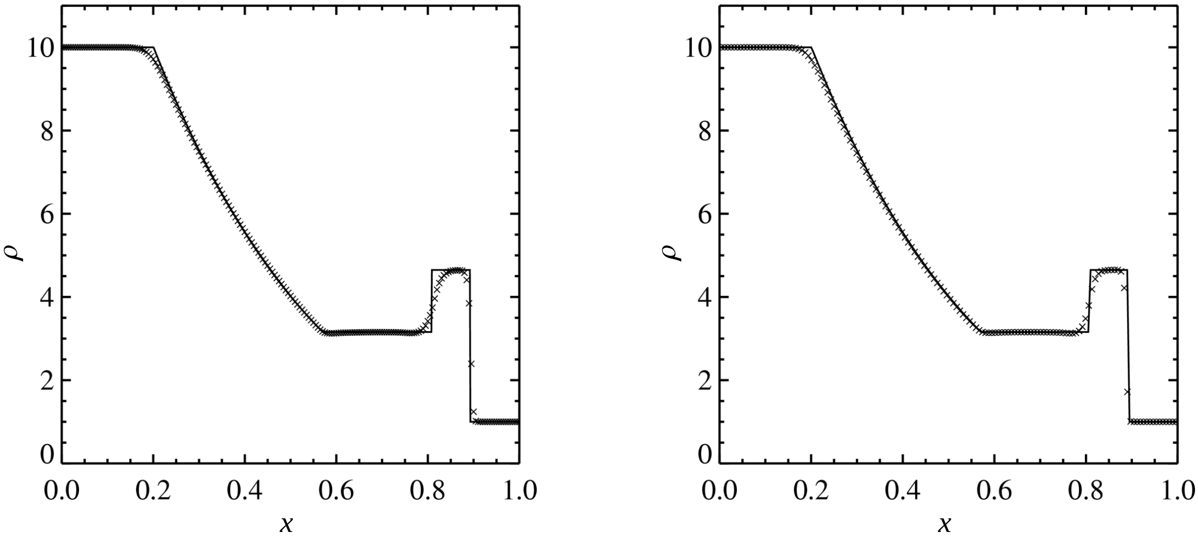

Fig. 3.7: Density distribution for the shock tube problem. Here we show a comparison of the one-dimensional (left) and the two-dimensional simulations (right). The results are obtained at time $t = 0.08$. The analytical solution is given as the solid line in both cases. Both plots show from left to right a rarefaction wave followed by a contact discontinuity and a shock wave.

we discuss a form of the problem with stronger gradients than those used by Sod in 1978. The initial conditions are chosen to be:

$$[\rho(x), p(x)] = \begin{cases} [10, 100] & \text{if} \quad x < 0.5 \\ [1, 1] & \text{if} \quad x \geq 0.5 \end{cases} \tag{3.69}$$

where we additionally decide for an adiabatic index of $\gamma = 1.4$. The resulting spatial density distribution is shown in Fig. 3.7. The left diagram reflects the solution for the strictly one-dimensional problem, that is for the gradients being present in only one of the Cartesian directions. The right diagram, however, shows the solution obtained with the gradients oblique to the Cartesian directions.

Both problems were computed with 200 grid cells along the domain shown in Fig. 3.7. The time step was chosen so that the Courant number never exceeds 0.2. The results in Fig. 3.7 are shown for the normalised time $t = 0.08$ and are directly compared to a pseudo-analytical solution.

From the comparison to the analytical solution it becomes clear that the CWENO scheme is perfectly suited to compute solutions of hydrodynamical problems. What is seen in Fig. 3.7 for any of the two problems from left to right is a rare faction wave, a contact discontinuity and finally a shock wave. All those are captured nicely by the scheme fitting quite accurately to the analytical solution. Moreover, it becomes clear that the results are quite independent of the direction with respect to the Cartesian grid: Both the strictly one-dimensional and the oblique problems are solved with similar accuracy.

The good behaviour for multi-dimensional simulations is also visualised on the right hand side of Fig. 3.8 where the spatial temperature distribution is shown. The contours are very regular and smooth without any artificial oscillations. Apart from that we also compare the temperature distribution – the temperature being the only variable besides the density showing all of the discontinuities – to the corresponding analytical solution. Again the excellent consistency becomes clear. Therefore, and also regarding other tests described, e.g., in Kleimann et al. (2004) and Kurganov et al. (2001) it is seen that CWENO is a good choice for multi-dimensional hydrodynamic problems regarding flows with shocks.

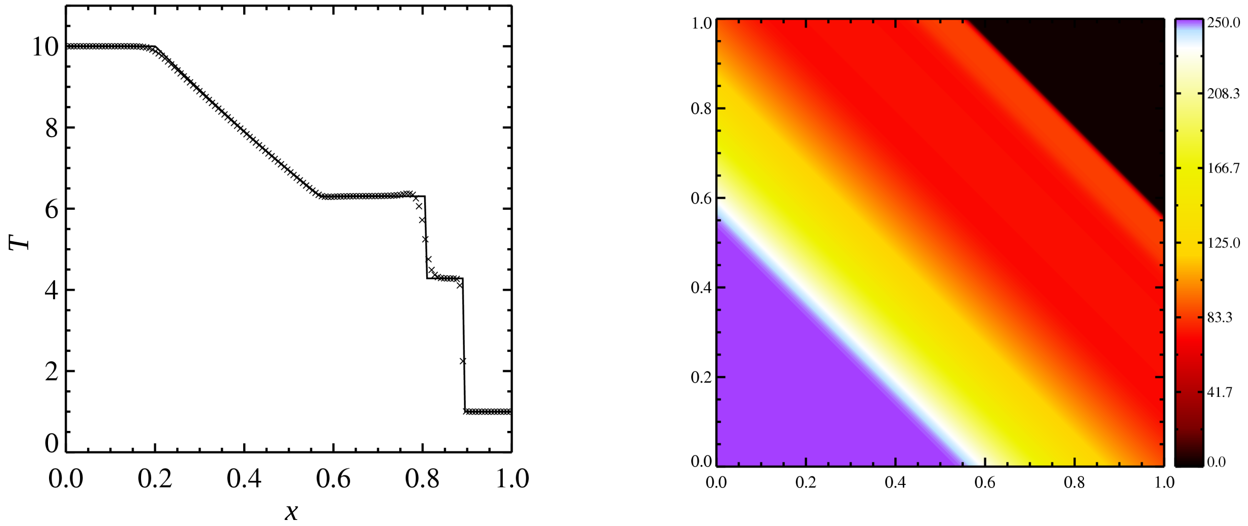

Fig. 3.8: Temperature distribution for the oblique shock tube problem. On the left the temperature profile is shown, whereas on the right the smoothness of the temperature solution for an oblique initial state is visualised.

3.4.3 MHD Equations

The next thing that has to be verified is that the MHD equations can also be solved accurately using the Cweno scheme. The corresponding equations in normalised form were already introduced in paragraph 2.8.1. We do not intend, however, to discuss the complete two-fluid system yet. We are rather interested in the ionised fluid only. Generally the two-fluid system is a combination of the hydrodynamic equations with the MHD equations via the corresponding interaction terms. These are handled via a splitting method: In one step the numerical scheme solves only the interaction terms, whereas in the next step only the hyperbolic system is solved. Therefore, it is at this point sufficient to demonstrate that the scheme can handle both the hydrodynamic and the MHD equations. It also has to be checked if the full system can be solved, but this is independent of the capability of the Cweno scheme.

The ideal MHD equations are obtained from the system of equations in paragraph 2.8.1 by neglecting the normalised fluid equations and the corresponding source terms. This leaves a system of eight equations:

$$\frac{\partial \rho}{\partial t} = -\nabla \cdot \boldsymbol{s} \qquad \text{continuity equation} \tag{3.70}$$

$$\frac{\partial \boldsymbol{s}}{\partial t} = -\nabla \cdot \left(\frac{\boldsymbol{s}\boldsymbol{s}}{\rho} + \left(p + \frac{B^2}{2} \right) 1 - \boldsymbol{B}\boldsymbol{B} \right) \qquad \text{momentum equation} \tag{3.71}$$

$$\frac{\partial \boldsymbol{B}}{\partial t} = -\nabla \cdot \left(\frac{\boldsymbol{s}\boldsymbol{B} - \boldsymbol{B}\boldsymbol{s}}{\rho} \right) \qquad \text{induction equation} \tag{3.72}$$

$$\frac{\partial e}{\partial t} = -\nabla \cdot \left(\left(e + p + \frac{B^2}{2} \right) \boldsymbol{s} - (\boldsymbol{s} \cdot \boldsymbol{B})\boldsymbol{B} \right) \frac{1}{\rho} \qquad \text{energy equation} \tag{3.73}$$

to be solved, where again e is the total energy density. The problem similar to the one discussed in the preceding section is the MHD shock tube problem introduced by Brio and Wu (1988). It is used as a standard MHD test problem despite the fact that there is no analytical solution available. With the initial conditions:

$$\left[\rho(x), p(x), B_x(x), B_y(x)\right] = \begin{cases} [1, 1, 1, 1] & \text{if} \quad x < 0.5 \\ [0.2, 0.1, 1, 0] & \text{if} \quad x \geq 0.5 \end{cases} \tag{3.74}$$

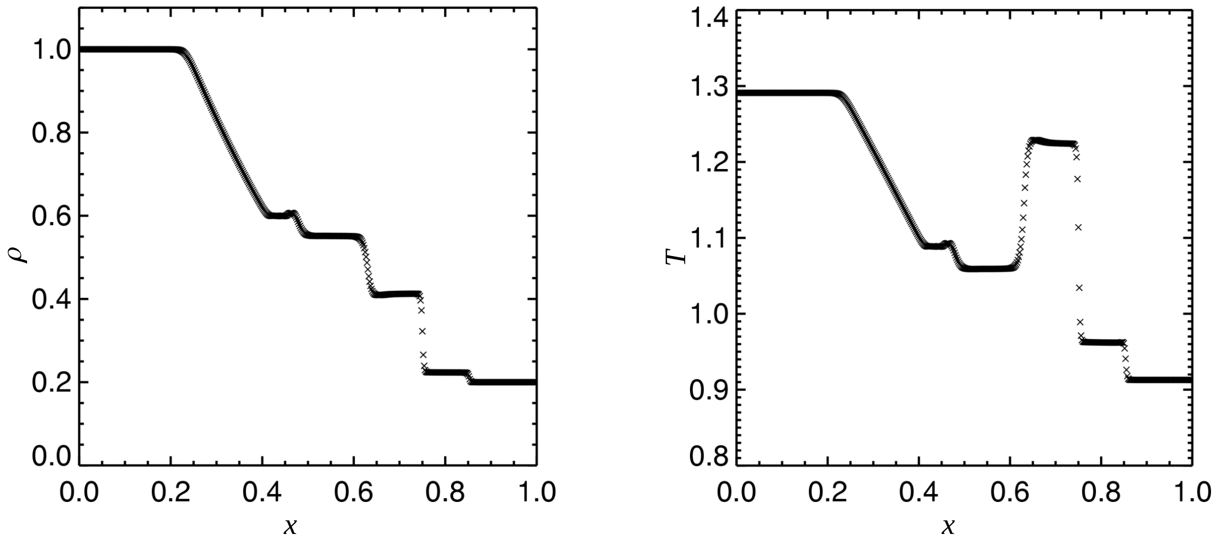

Fig. 3.9: Density (left) and temperature (right) distribution for the one-dimensional oblique Brio-Wu shock tube problem at the normalised time $t = 0.15$. Both plots show from left to right a fast rare faction wave followed by a slow rare faction wave with the subsequent contact discontinuity being followed by a slow shock and then finally by a fast shock. The solution is in excellent agreement with the corresponding simulations depicted in Fig. 4a of Ryu and Jones (1995).

and an adiabatic exponent of $\gamma = 5/3$ the initial state evolves into a rich spatial structure. The simulation results depicted in Fig. 3.9 show a multitude of shocks and rare faction waves (for details see the figure caption). These results were obtained using 512 cells in each direction with a time step size chosen so as to ensure a Courant number never exceeding 0.2.

The results shown in Fig. 3.9 are in agreement with the results for the same problem presented by Ryu and Jones (1995). As in the preceding section a simulation for the oblique problem yields very similar results as the strictly one-dimensional problem. Therefore, the scheme also is suited for multi-dimensional MHD problems. As in the hydrodynamical problems no artificial oscillations occur and, due to the constrained transport character of the scheme, also the solenoidality of the scheme poses no problem.

3.4.4 Order of the Scheme

Another important issue to be tested for the scheme is its order. That is we have to assure that the scheme really is of second order as would be expected considering its derivation. This can most easily be done by linear advection tests. Since, however, these are in no way similar to the problems we would like to solve using the scheme, we rather stick to the approach suggested in Ryu et al. (1995). These authors suggest to investigate the order of the scheme by the decay of different wave types.

Here we will briefly investigate sound waves, Alfvén waves and fast magnetosonic waves. The slow magnetosonic wave is not taken into account due to its obvious similarity to the other MHD waves. For the description of these wave types we will use the same equations of ideal MHD as discussed in the preceding section. Here we will discuss the setup of the corresponding simulations and introduce the principle ideas at the example of Alfvén waves. Despite the fact that the resulting damping rates are clearly a numerical artifact since there are no intrinsic damping processes in the ideal MHD equations, it is nonetheless possible to find a corresponding Reynolds number. This is also elaborated using the example of a decaying Alfvén wave.

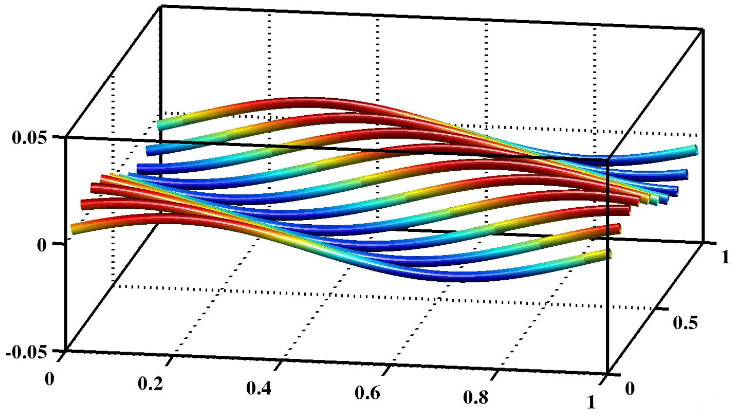

Fig. 3.10: Alfvén wave oblique to the background magnetic field with an inclination angle of 45°. Here we show the magnetic field lines bent by the wave at an instant when most of the fluctuation energy is stored as magnetic tension. The wave structure was enhanced by a factor of four for better visibility.

Alfvén Waves

One of the tests being most significant for MHD simulations is the Alfvén wave test. Alfvén waves are incompressible at least in the fluid description. This wave type propagates by the restoring force of the magnetic field lines. Therefore, they are a *reaction* to any perpendicular deflection of these field lines. A natural initialisation for a standing Alfvén waves is therefore:

$$\begin{pmatrix} \rho \\ \boldsymbol{u} \\ \boldsymbol{B} \\ T \end{pmatrix} = \begin{pmatrix} \rho_0 \\ \delta u_z \boldsymbol{e}_z \\ B_0 \boldsymbol{e}_x \\ T_0 \end{pmatrix} \qquad \text{with} \qquad \delta u_z = a_0 \mathrm{v}_A \sin(\boldsymbol{k}\cdot\boldsymbol{r}); \qquad \boldsymbol{k} = \begin{pmatrix} k_x \\ k_y \\ 0 \end{pmatrix}; \qquad \boldsymbol{r} = \begin{pmatrix} x \\ y \\ z \end{pmatrix} \tag{3.75}$$

where a_0 is just an amplitude-factor. This initial state represents a disturbance in the velocity perpendicular to the homogeneous initial magnetic field embedded in an otherwise homogeneous medium. The wave is oblique to the magnetic field with the inclination with respect to the background magnetic field chosen to be 45°. With a uniform initial magnetic field and a uniform initial density this gives an Alfvén speed of $\mathrm{v}_A = \sqrt{2}/2$.

After initialisation the magnetic field lines are bent by the shear flow in z-direction until the *tension* of the magnetic field lines gets so high that they are bent back to the initial configuration, thus, increasing δu_z again. We have consequently a continuous exchange of kinetic and magnetic energy for the fluctuations in the z-direction. The evolution of the wave is illustrated in Fig. 3.10 where the magnetic field structure is shown at a time when most of the fluctuation energy is stored in the magnetic field.

For ideal MHD Alfvén waves would not only be incompressible but also dissipation-free. The latter property is violated for numerical schemes due to numerical viscosity and resistivity of the scheme itself. This can be seen when investigating the evolution of the amplitude of the wave. Another approach to investigate this behaviour of the CWENO scheme is presented in Kleimann (2005).

This is visualised in Fig. 3.11 where the evolution of the root mean square of the velocity disturbance perpendicular to the initially homogeneous magnetic field is shown. The amplitude of the Alfvén wave decreases with time. From this and similar plots one can determine a decay rate for Alfvén waves depending on the spatial resolution.

For a plasma with finite viscosity ν and resistivity η the dissipation rate Γ_A for Alfvén waves can also be deduced analytically to be (see Ryu et al. (1995) for a derivation):

$$\Gamma_A = \frac{1}{2}\left(\frac{\nu}{\rho_0} + \eta\right) k^2 \tag{3.76}$$

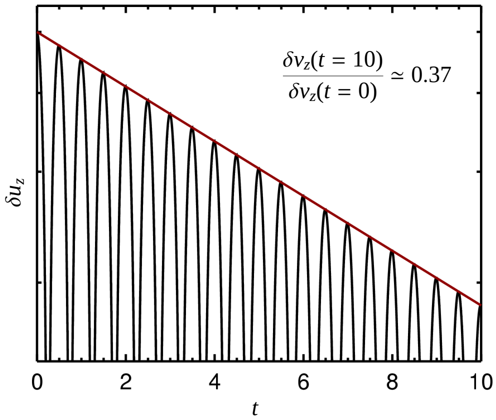

Fig. 3.11: Evolution of the root mean square of the velocity disturbance (shown in logarithmic units) perpendicular to the initially homogeneous magnetic field. The damping of the disturbance by numerical viscosity and resistivity is obvious.

where k is the wavenumber of the Alfvén wave. Here we choose a diagonally propagating Alfvén wave with $k_x = k_y = 2\pi$. Then we can define a corresponding Reynolds number as:

$$Re_A := \mathrm{v}_A L \left(\frac{1}{2} \left(\frac{\nu}{\rho_0} + \eta \right) \right) = \frac{8\pi^2 \mathrm{v}_A}{\Gamma_A L} \tag{3.77}$$

with L indicating the size of the numerical domain. The resulting Reynolds number will depend on the resolution used for the computation as the numerical dissipation will increase with decreasing resolution. This fact, however, will be discussed for all wave types together.

There is just another important issue, which can be checked from Fig. 3.11. That is, we can easily test whether the correct Alfvén speed is recovered by the scheme. For a standing Alfvén wave as discussed here this can not be done by an investigation of the motion of the spatial structure. The Alfvén speed, however, also determines the fluctuation frequency of a standing Alfvén wave. For a damping rate small compared to unity the real part of the angular frequency is $\omega_r \simeq \mathrm{v}_A k$. With our choice for the wavenumber and a unity initial magnetic field, this just yields:

$$\mathrm{v}_A = \frac{1}{\sqrt{2}} \qquad \Longrightarrow \qquad \omega_r = 2\pi \tag{3.78}$$

Thus, peaks of the velocity are expected to occur after each $\Delta t \simeq 0.5$ since also negative extremal values are seen as peaks when investigating the root mean square of the velocity. The peaks are at the correct positions in Fig. 3.11. Moreover, it is clear, that the fluctuations time scale is much shorter than the damping time scale. Therefore, the assumption that the effect of damping on the angular frequency can be neglected is justified. Thus, it is obvious that the scheme represents the Alfvén speed correctly.

All these considerations can also be performed for all possible wave types appearing in MHD. In the subsequent section, however, we will only concentrate on the typical Reynolds numbers and the order of the scheme.

Order of the Scheme

For the test of the order of the scheme we applied two additional tests apart from the decaying Alfvén wave. These were a decaying sound wave and a decaying fast magnetosonic wave. With similar arguments as above it is also possible to define corresponding Reynolds numbers for these wave types (for details see again Ryu et al. 1995). For all three wave types we performed numerical simulations with different spatial resolutions. From the derived dissipation rates Γ it is then possible to compute the

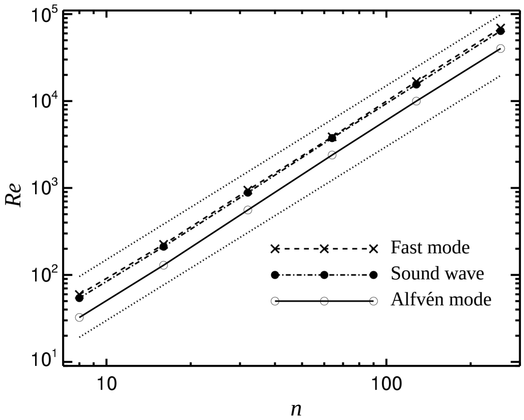

Fig. 3.12: Reynolds number dependence for the decay of different wave types on spatial resolution. With the dotted lines we additionally indicated a dependence $\propto n^2$ where n is the number of cells along any of the Cartesian directions.

Reynolds numbers for different wave types and different spatial resolutions. The results of this study are summarised in Fig. 3.12.

There the computed Reynolds numbers are shown for all wave types individually with the dotted line indicating a quadratic dependence on the number of cells in the numerical domain. Clearly the scheme is of second order even though the waves are propagating oblique to the Cartesian grid. Moreover, the dissipation rates for the different wave types are quite similar. What is interesting, however, is the fact that the incompressible mode (the Alfvén mode) is substantially more dissipative than the compressive mode. The reason for this is not entirely clarified yet, but it is clear that the scheme produces very good results for compressible wave types. Therefore, it is especially suited for the highly compressible interstellar medium. Furthermore, it is evident, that it is easily possible to reach Reynolds numbers in excess of 10^3, which is often viewed as the barrier dividing laminar from turbulent flow.

These tests conclude our little suite. With the above we were able to verify that the CWENO scheme is capable of solving multi-dimensional hyperbolic problems. It became clear that the scheme does not produce spurious oscillations at shocks or other steep gradients. Moreover, all types of MHD waves are well represented by the scheme. Due to the fact that also high Reynolds numbers can be reached the scheme is well suited for the numerical solution of the MHD equations in the context of interstellar turbulence.

3.4.5 ISM Turbulence

Obviously, the ISM turbulence discussed in this work does not qualify as a test case. If there would exist an analytical solution, the whole numerical study would be futile. We have, nonetheless, to verify that the solution obtained by the numerical procedure is a valid one. A strong hint for this is the convergence of the results with increasing spatial resolution.

Unfortunately, the dynamical nature of turbulence does not allow for a steady state at any given time. Thus, *convergence* is not that easily identified. This becomes clear when regarding the density structure at the same location for different spatial resolutions as they are depicted in Fig. 3.13. The large-scale structure is obviously the same for the different computations. While there is essentially no small-scale structure visible for the lowest resolution computation, the high resolution computations are dominated by very fine density structures whose number is increasing with increasing resolution.

A good indication of the convergence of the scheme, however, is the fact that the fine structure visible at lower resolution is still present at higher resolutions – merely even finer and frequently distorted by fluctuations whose scale was simply not present in the more weakly resolved simulations. With the above

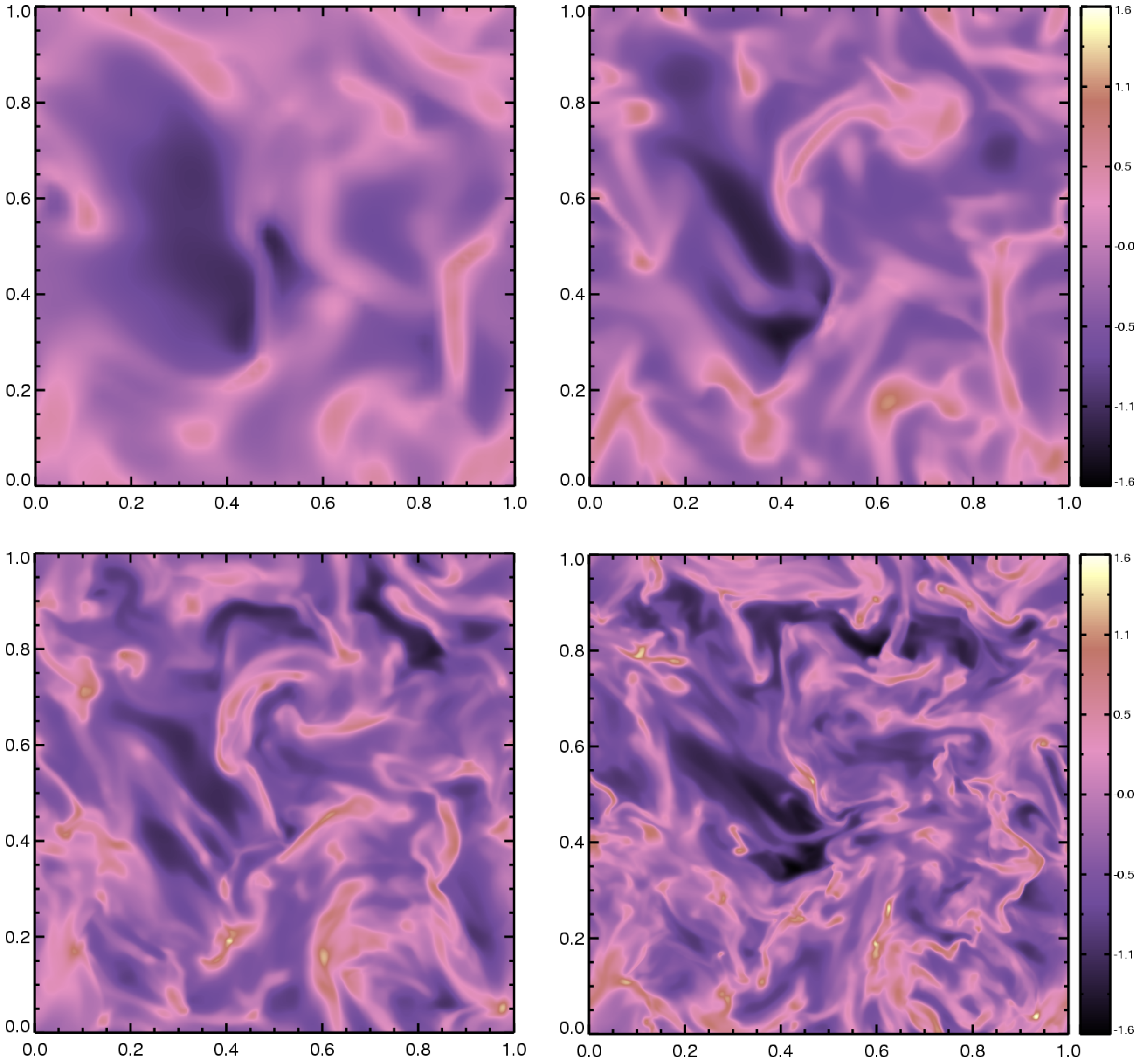

Fig. 3.13: Spatial density structure for isothermal turbulence simulations of varying spatial resolutions. The number of cells is increased from top left (64 cells in each direction) to bottom right (512 cells in each direction) with a twofold increase from image to image.

tests and the consistency shown in Fig. 3.13 we are confident that our results are indeed numerically correct and, therefore, can be interpreted physically.

Another indicator of the convergence of the scheme is usually seen in the energy content of the numerical box. For many numerical simulations one would expect the overall energy to eventually converge to some finite value. Here, however, we expect the fluctuation energies to become higher and higher for increasing resolution. This fact is visualised in Fig. 3.14, where both the energy and the enstrophy content of the simulations for various spatial resolutions are shown. The general temporal evolution is the same for each of the spatial resolutions only with differences in the absolute values. At first sight, however, there seems to be a slow trend towards convergence of the energy content of the numerical domain. One has to keep in mind, however, that the dissipation differs for all the different spatial resolutions, since it is an exclusively numerical effect. Therefore, one does not really expect a convergence towards some finite amount of energy. Thus, we have to think about the reason for the apparent convergence.

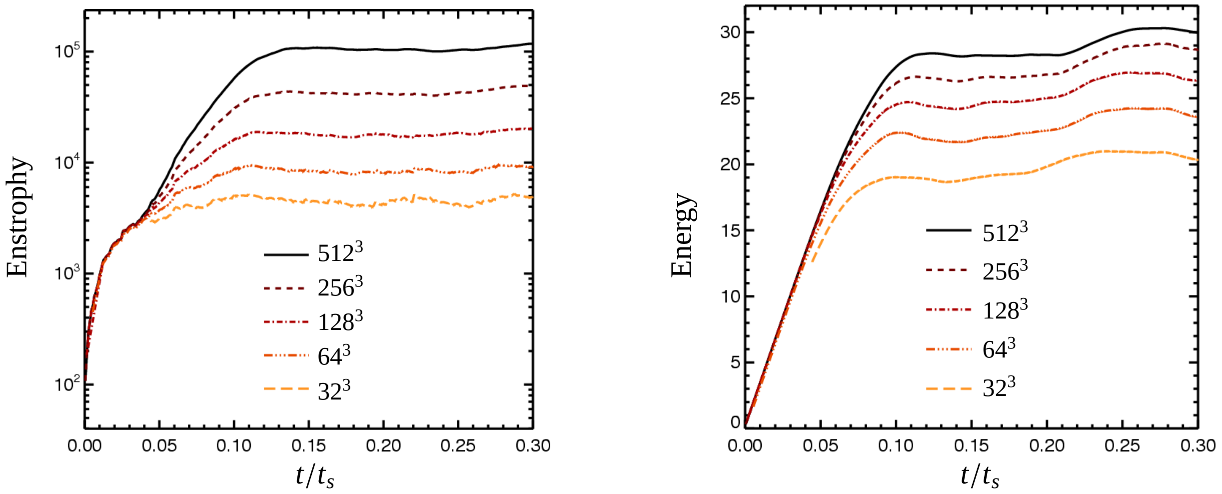

Fig. 3.14: Temporal evolution of the enstrophy (left) and energy (right) content of the numerical domain. The results are shown for different spatial resolutions as indicated in the figure.

This can be understood by investigating the nature of turbulence. Roughly speaking an increase of spatial resolution corresponds to smaller spatial scales becoming available for the turbulent fluctuations. As a first approximation the spectrum can be assumed to be fixed at the largest available wavenumber. With the spectral slope in the dissipation range being roughly the same for all the spatial resolutions the growth rate for the overall fluctuation energy for these low resolutions will be constant. As soon as the spectrum shows an inertial range, however, the spectrum at small wavenumbers becomes flatter. Therefore, an increase of spatial resolution yields a lower increase of the overall energy whenever an inertial range is present. When the inertial range is fully developed, we would, thus, expect the fluctuation energy to grow with the same rate also for all higher resolutions. Thus, we do not expect to see a convergence of the overall energy content of the numerical domain - but rather a bend in the rate of energy increase when the inertial range starts to become important. Even though at first sight Fig. 3.14 seems to show a convergence for the energy content, we rather expect the visible effect to be due to the slowly evolving inertial range. Therefore, the energy is not a good tracer to check the convergence of the scheme, when the dissipation is exclusively numerical – there is no value the fluctuation energy will converge to in contrast to what is discussed in Stone et al. (1998).

3.5 Source Terms

So far we only discussed the hyperbolic solver. This, however, in principle does not allow for the inclusion of source terms, when these – as is usual – cannot be given in hyperbolic form. Moreover, it is unclear, how the presence of source terms might change the estimate for the maximum wave speeds needed for the CWENO solver. These problems can most easily be circumvented by the application of a so-called *fractional-step method*. What we are investigating here are systems of equations of the form:

$$\frac{\partial \boldsymbol{q}}{\partial t} + \nabla \cdot \mathsf{F}(\boldsymbol{q}) = \boldsymbol{\Psi}(\boldsymbol{q}) \tag{3.79}$$

where the source terms are given on the right-hand side of the equation. In all problems considered in this work the source terms depend on $\boldsymbol{q}$ only and never on any of its derivatives. In this case the equations describing the temporal evolution of the source terms represent a system of independent ODEs for each grid point:

$$\frac{\partial \boldsymbol{q}}{\partial t} = \boldsymbol{\Psi}(\boldsymbol{q}) \tag{3.80}$$

The idea behind the fractional-step method is to split Eq. (3.79) and solve its parts separately. The concept behind the approach is to alternate between solving the two distinct problems, which in our case are the hyperbolic and the source term problem. This is well suited for problems that require different solvers. This subdivision of Eq. (3.79) then reads:

$$\text{Problem A :} \qquad \frac{\partial \boldsymbol{q}}{\partial t} + \nabla \cdot \mathsf{F}(\boldsymbol{q}) = 0 \tag{3.81}$$

$$\text{Problem B :} \qquad \frac{\partial \boldsymbol{q}}{\partial t} = \boldsymbol{\Psi}(\boldsymbol{q}) \tag{3.82}$$

Regarding the alteration we decided not for the simplest possible method, but rather for the second order *Strang splitting* introduced in Strang (1968). One solves the first subproblem over a half time step of length $\Delta t/2$. The resulting data is then used for a full time step on the second subproblem. Finally, one takes another half time step for the first subproblem. All in all we have a scheme of the form:

$$\boldsymbol{q}^n \xrightarrow{\text{A}} \boldsymbol{q}^* \xrightarrow{\text{B}} \boldsymbol{q}^{**} \xrightarrow{\text{A}} \boldsymbol{q}^{n+1} \tag{3.83}$$

This scheme can easily be shown to be of second order in time (see e.g. Leveque 1992). Furthermore, it is equivalent to a method that uses a full time step for each subproblem – only that in the case of Strang splitting the steps are not taken at the same time.

Here the use of a splitting scheme has the major advantage that we can use the methods appropriate for the individual problems. That is we can still use the shock-capturing Cweno scheme for the hyperbolic problem, while at the same time we use a Runge-Kutta time integrator for the evolution of the source terms. Additionally, whenever both problems *live* on very different time scales, the splitting allows us to use different time step sizes for the two subproblems. If, e.g., the time scale of the second problem were much shorter than the one of the first, one would just use N time steps of the second problem to advance over an overall step Δt.

There are, however, also shortcomings of splitting methods in general. On the one hand there occur some problems with so-called *singular* or *stiff* source terms. These terms denote situations when sources are very strong and concentrated in small spatial regions. Luckily this is not the case in any of our problems. On the other hand steady-state solutions do pose a problem for splitting methods. That is, the steady-state obtained using a splitting method usually depends on the time step, which should not be the case, of course. Again this poses no problem for our highly dynamic turbulence simulations that do not converge to any steady-state solution. With this we are finis the description of our basic numerical scheme. What is left is a discussion of a few specific numerical issues.

3.6 Further Numerical Issues

So far we have introduced the numerical scheme we used in order to solve the system of hyperbolic equations. There is, however, more physics to this problem than just the statement of the equations. As was already mentioned the question of the boundary conditions is most easily handled, since we are using a periodic box. The initial conditions as compared to this are much more involved. These we will only be able to discuss concisely after a section on how to obtain spectral information about the fluctuations in the numerical experiments.

3.6.1 Obtaining Turbulence Statistics

Whenever studying turbulence one is usually interested in the distribution of power over different spatial scales. This, however, can best be studied in wavenumber space. For isotropic turbulence this is done by investigating the *omnidirectional, angle integrated wavenumber spectrum*.

For MHD turbulence, however, isotropy might by broken by a sufficiently strong magnetic background field. In such a case it is common to distinguish between the spectra of fluctuations along and perpendicular to the magnetic field. In this case one obtains two different kinds of one-dimensional spectra - one along and one perpendicular to the background field. Here the latter of those is obtained as the angle averaged form of the two-dimensional fluctuation spectrum perpendicular to the magnetic field. This division in two spectra will from now on be referred to as the *anisotropy spectrum*.

The procedures of obtaining omnidirectional or anisotropy spectra will now be illustrated using the example of some kind of power law given in wavenumber space.

Velocity Spectra

The general definition for the isotropic velocity turbulence spectrum $E(k)$ was already used in the introduction of Kolmogorov turbulence and is given as the auto-correlation of the velocity field:

$$\int E(k)dk = \frac{1}{2} < \boldsymbol{u} \cdot \boldsymbol{u} > \tag{3.84}$$

Thus, the turbulence spectrum in wavenumber space represents the kinetic energy divided by the density of the fluid under consideration[1]. The above spectrum is obtained from the Fourier-transform of the individual components of the velocity field:

$$E(\boldsymbol{k}) = \frac{1}{2}(u_x^2(\boldsymbol{k}) + u_y^2(\boldsymbol{k}) + u_z^2(\boldsymbol{k})) \tag{3.85}$$

From this we still have to deduce the omnidirectional spectrum, since here we are rather interested in the energy at a particular scale without any additional directional information. Thus, to obtain $E(k)$ we still have to integrate over spherical shells of radius k in wavenumber space. Hence, the actual procedure to obtain the omnidirectional spectrum from the velocity fluctuations is as follows:

1. First we transform the velocity fluctuations into Fourier space.
2. From these we compute the $\boldsymbol{k}$-dependent fluctuation energy
3. Finally the omnidirectional spectrum is obtained through an integration over spherical shells of radius k.

This procedure is not only used to obtain the overall velocity fluctuation spectrum. In this work we will also investigate density and magnetic field spectra. Additionally, we will examine the compressive and the solenoidal part of the velocity fluctuations individually. For this we derive the spectra for:

$$u_{shear}^2(\boldsymbol{k}) = \left|\hat{\boldsymbol{k}} \times \boldsymbol{u}(\boldsymbol{k})\right|^2 \qquad u_{comp}^2(\boldsymbol{k}) = \left|\hat{\boldsymbol{k}} \cdot \boldsymbol{u}(\boldsymbol{k})\right|^2 \tag{3.86}$$

where $\boldsymbol{k}$ is the wavenumber vector and $\hat{\boldsymbol{k}}$ indicates the corresponding unit vector (see also Vestuto et al. 2003).

Since space is discrete in numerical computations this also is true for the corresponding Fourier space. Therefore, on the one hand we have to use a discrete Fourier transform (which is provided by the fftw library (see Frigo 2004)) and on the other hand also the integration over the spherical shells is a sum rather than an integral. The latter is done by binning Fourier space into shells and adding all energy contained in these shells. This procedure yields smooth power spectra for the higher wavenumbers. For small wavenumbers, however, the number of grid points covered by the shells continuously decreases, thus, leading to worse statistics for small wavenumbers. This issue can luckily, at least to some extent, be handled by a renormalisation procedure:

---

[1] This definition stems from research on incompressible turbulence where density is constant

Renormalisation

One reason for spectra to become non-smooth especially for small wavenumbers is connected to the distribution of grid points in wavenumber space. When using a Cartesian grid one runs into problems, when summing the values of the grid points on spherical shells. This is due to the fact, that in a spherical geometry grid points on a Cartesian grid are not homogeneously distributed: On the one hand the number of cells per shell can be above or below the value ($n \propto k^2$) expected for a spherical geometry. On the other hand the average wavenumber of the cells in one shell varies corresponding to the distribution of the shells. The first problem is taken care of by normalising the number of grid points in any of the shells. This is done just by counting the number of grid points in a given shell and using the inverse of this number multiplied by a factor of k^2 as a multiplier for the spectra. This already yields much smoother spectra for low wave numbers. When also taking the correct average wavenumbers for the individual shells into account the spectra will only be disturbed by physical effects and bad statistics for very low wavenumbers.

All the same procedures are also used for the computation of the anisotropy spectra. In this case the only important modification is that the integration is carried out over only two instead of three spatial dimensions. With all this in mind we are now in a position to understand the initialisation and driving of the velocity fluctuations. After this, however, we have once again to return to the discussion of available tools to investigate the statistics of the turbulence.

3.6.2 Driving and Initialisation

As mentioned in Sec. 2.7.1 we intend to mimic the kinetic energy input by supernova explosions by a continuous driving spectrum in wavenumber space. By this the initial conditions are fully determined, since we superimpose the velocity fluctuations onto an otherwise homogeneous background medium (i.e. the system is initialised with a homogeneous background density, temperature and magnetic field). Thus, we have to discuss the exact way how to implement the initially disturbed velocity field.

The velocity field has to fulfil some very important conditions: First the fluctuations have to be at large spatial scales. Then, the fluctuation have to be completely random and the energy distribution over the different scales has to satisfy some form of scale dependence. For this one also has to discuss, whether it is desired to use either compressible or solenoidal driving, because when achieving this the energy dependence in wavenumber space is also modified. Finally the energy put into the system has to be the same as would be estimated for the supernova explosions.

To clarify this matter we will discuss the procedure from the fluctuation spectrum given in Fourier space to the actual spatial fluctuations step by step. First, the spectrum in wavenumber space is initially fixed by the user as some function $f(k)$. Since we will only investigate either solenoidal or fully compressible driving, these properties have to be taken care of. From a random vector field a solenoidal field is easily found just by taking the curl of the vector field. The same is true for a scalar field and the gradient, when talking about fully compressible driving. These operations, however, have some influence on the spectral form in wavenumber space due to the fact that the differential operators are connected to operations in wavenumber space by the following relations:

$$\nabla \times \boldsymbol{A}(\boldsymbol{x}) \quad \longrightarrow \quad \boldsymbol{k} \times \boldsymbol{A}(\boldsymbol{k}) \qquad \text{and} \qquad \nabla\Phi(\boldsymbol{x}) \quad \longrightarrow \quad \boldsymbol{k}\Phi(\boldsymbol{k}) \tag{3.87}$$

This means that the spectra of the fluctuations will be modified by the above operations. This effect will depend on the type of spectrum that is eventually investigated. For most purposes this will be the omnidirectional fluctuation spectrum introduced above. For those only the absolute value of the wavenumber is of any importance. Therefore, each of the above procedures yields an additional factor of k for the slope of the velocity spectrum in wavenumber space.

As mentioned in the preceding section, the omnidirectional energy spectrum is eventually obtained from the angle-integrated form of the square of the velocity – that is the velocity spectra resulting after the above differential operation have to be squared and multiplied by k^2 (the latter resulting from the angle integration).

So far we have made clear how the spectral distribution of the initial velocity fluctuations is connected to a resulting kinetic energy fluctuation spectrum. What is still missing, however, is the randomness of the initial field. For this we worked closely along what is suggested in literature (see especially Vestuto et al. 2003; Christensson et al. 2001; Stone et al. 1998). The idea is to introduce fluctuations of random amplitude, with the amplitudes distributed according to a normal distribution on each of the input scales. The dependence of the fluctuation energy on the spatial scale is at the same time assured by including a scale dependence of the width of the normal distribution. For a normal distribution around zero this width is fully determined by the variance $\sigma^k_{\delta\boldsymbol{u}}$ of the Gaussian $G_{\delta\boldsymbol{u},k}$. For the velocity fluctuations $\delta\mathbf{v}$ this means we have:

$$\left(\sigma^k_{\delta\boldsymbol{u}}\right)^2 = \int \delta\boldsymbol{u}^2 G_{\delta\boldsymbol{u},k} d^3\delta u \equiv < \delta\boldsymbol{u}(\boldsymbol{k})^2 > \tag{3.88}$$

That is, in this case the variance is equivalent to the second order moment of the velocity fluctuations at scale k. This means that we can define the form of the initial spectrum via the variance of the amplitude distribution of velocity disturbances at scale k. With all this in mind it is possible to set the wavenumber dependence of the variance in a way as to provide any desired spectral slope. Fixing the dependence of the standard deviation on wavenumber yields a spectral slope of the form:

$$E(k)_{Init} = k^2 (k\, \sigma^k_{\delta\boldsymbol{u}})^2 \tag{3.89}$$

From the corresponding inverse relation it is clear that, if a spectrum with a power law index of $-s$ is desired, the necessary input spectrum has to have a variance of the form:

$$\sigma_{\delta\boldsymbol{u}} \propto k^{-s/2-2} \tag{3.90}$$

Thus, we are finally in the position to describe the complete initialisation procedure.

Initialisation and Driving

With the knowledge gained in the preceding paragraphs the initialisation of a turbulence simulation is quite easily done. For the density, the magnetic field and, whenever having to use the full energy equation, also for the temperature we initially prescribe constant values. These are, if possible, chosen as unity with the actual values being taken care of by the normalisation constants.

For the velocity fluctuations we prescribe some wavenumber dependence for the variance of the normally distributed amplitudes in wavenumber space. The resulting vector fields are then transformed to configuration space. There the resulting fields are projected either to their solenoidal or fully compressible part. Furthermore, any *global* momentum contained in the resulting velocity field is reduced to zero. Finally, the fluctuations are normalised to correspond to some desired energy input rate. A typical initial velocity field is shown in Fig. 3.15, where the direction and absolute value of the velocity disturbance is shown for a slice of the computational domain.

Apart from the initialisation we also include a driving of the turbulence which is very similar to the initialisation. In that case we add at regular temporal intervals a velocity fluctuation field corresponding to a fixed amount of kinetic energy to the evolved velocity field. This corresponds to the procedure:

$$\boldsymbol{u} \longrightarrow \boldsymbol{u} + A\delta\boldsymbol{u} \tag{3.91}$$

where the amplitude factor A is fixed by the desired energy input rate Δ E:

$$A = -\frac{\sum_{ijk}\rho_{ijk}\delta\boldsymbol{u}_{ijk}\boldsymbol{u}_{ijk}}{\sum_{ijk}\rho_{ijk}\delta\boldsymbol{u}^2_{ijk}} + \sqrt{\left(\frac{\sum_{ijk}\rho_{ijk}\delta\boldsymbol{u}_{ijk}\boldsymbol{u}_{ijk}}{\sum_{ijk}\rho_{ijk}\delta\boldsymbol{u}^2_{ijk}}\right)^2 + \frac{2\Delta E}{\Delta V\left(\sum_{ijk}\rho_{ijk}\delta\boldsymbol{u}^2_{ijk}\right)}} \tag{3.92}$$

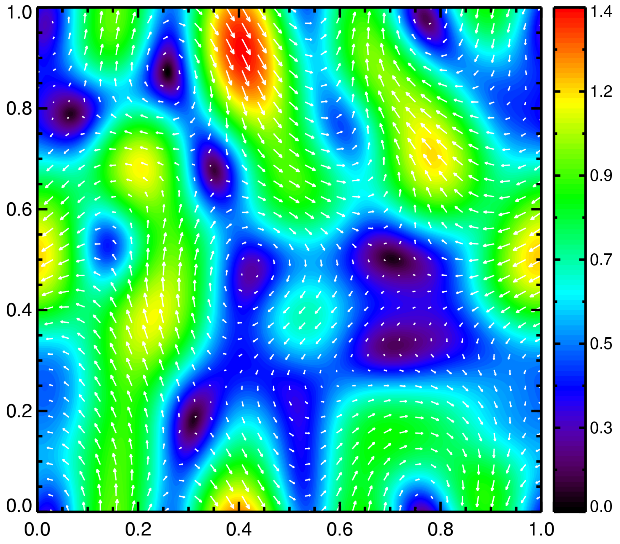

Fig. 3.15: Initial velocity field in a slice of the computational domain. The colours indicate the Mach number of the absolute value of the velocity field. At the same time the vector projections naturally give additional directional information.

where the sums are over all grid points of the computational domain. Here $\rho_{i,j,k}$ is the density in the individual grid cells. Clearly Eq. (3.92) can also be used for the initialisation with $\boldsymbol{u}_{ijk} = 0$ in that case. This concludes our discussion of the numerical setup of the physics contained in our model. Before concluding the chapter on numerics, however, we will briefly introduce another tool needed for the investigation of the turbulence statistics.

3.6.3 Structure Functions

As explained in the introduction the *structure functions* contain more information on the statistics of the fluctuations than the omnidirectional spectrum. Therefore, we briefly explain how such structure functions are evaluated for a field given on a discrete grid. In general these are defined by Eq. (1.16) as:

$$S_p(l) \equiv \left\langle |(\boldsymbol{u}(\boldsymbol{r} + l\boldsymbol{n}) - \boldsymbol{u}(\boldsymbol{r})) \cdot \boldsymbol{n}|^p \right\rangle \tag{3.93}$$

for the velocity field. To evaluate these for a vector field defined on a discrete grid there are several possibilities. For the most accurate results one would first subdivide the distance range l into several bins. Then for every single grid point the expression:

$$|(\boldsymbol{u}(\boldsymbol{r} + l\boldsymbol{n}) - \boldsymbol{u}(\boldsymbol{r})) \cdot \boldsymbol{n}|^p \tag{3.94}$$

has to be computed and added to the appropriate bin. Here $l\boldsymbol{n}$ is the vector connecting the grid point under consideration to all others. After having done this for each grid point, the optimum statistics should be achieved. This procedure, however, is very time consuming. For sufficiently high resolutions the time consumption of the procedure for computing the structure functions might even exceed the time consumption of the actual numerical computation. This is due to the fact that the numerical cost of the above method is of order N^2 where N is the number of cells in the computational domain. In contrast to that the CWENO scheme is of order N.

For our computations it soon became clear that already for a spatial resolution of 256 cells in each direction the above method was far too expensive to yield the structure functions in a sensible time. Luckily we were able to show that such a complex computation is not needed to obtain good statistics for the structure functions. It proved to be sufficient to compute the structure functions for each grid point just by using corresponding grid points in the directions of the Cartesian grid. Even in that case the statistics is still so good, that it is possible to perform this computation only for a subset of the actual grid points. By this method we were able to compute structure functions even for spatial resolutions up to 512 cells in each direction in a reasonable time.

Chapter 4

Molecular Clouds

Turbulence is most often discussed for molecular clouds. This might at first seem arbitrary, but there are good reasons to concern ourselves with these ISM structures. First, they are very important for the dynamics of the ISM, since star formation takes place in just these regions. Second, a far more trivial reason to investigate turbulence in molecular clouds is that they are of lower complexity than other regions of the ISM. This is due to the fact that typically the gas in molecular clouds is shielded from the interstellar radiation field. Therefore, dissociation by UV photons can safely be neglected for a study of molecular clouds. This means that external heating also is of no importance in these regions.

Unfortunately, as for the ISM itself, there is not just one *prototype* for the typical molecular cloud. Even for those structures one has to distinguish different kinds of clouds. The most recent classifications of molecular clouds (see Snow and McCall 2006) make a division with regard to the influence of the interstellar radiation field. The variety of clouds ranges from diffuse atomic clouds to dense molecular clouds. The former of those are essentially denser parts of the warm ISM, still fully exposed to the interstellar radiation field. Therefore, nearly no molecules can form in these surroundings, which is why chemistry can safely be neglected for these regions. The other extreme are the dense cloud cores, which are completely sealed off from the interstellar radiation field and are, therefore, rather dominated by their chemistry and also by self-gravity.

It is, however, important to note, that one will not be able to observe the different kinds of clouds individually. The above definitions are rather to be understood locally for any patch of gaseous materials. That is, a dense molecular cloud has somehow to be surrounded by dense atomic material, which will essentially be the reason for the ionising UV radiation not to reach the dense gas. A typical example of such a dense structure, most probably consisting of different dense cloud phases, is shown in Fig. 4.1. The image taken by the Very Large Telescope nicely shows the rich structure of the dense ISM.

4.1 Model Parameters

Usually, simulations for molecular clouds are carried out neglecting the interstellar radiation field and also the chemistry. Obviously, this is a quite crude approximation for most of the dense cloud categories. Before discussing this any further, we, therefore, have to ask ourselves, which type of dense cloud we will be investigating.

What would seem the most interesting phase for our purpose is formed by what Snow and McCall call the diffuse molecular clouds, which are already sufficiently isolated from the interstellar radiation field. The ionisation is, however, still sufficiently high so that the magnetic field can strongly influence the plasma and, therefore, cannot be neglected. Despite the fact, that chemistry already plays a role in these regions it is not as complex as in regions like the dense cloud cores. Moreover, the number densities being of the order of 10^8 particles per cubic meter are still low enough that self-gravity has not to be taken into account. With an ionisation fraction of 0.01 used for this section we have an initial

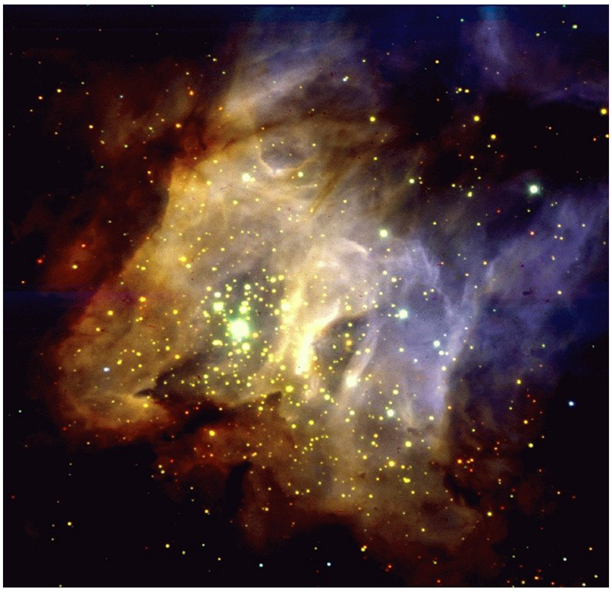

Fig. 4.1: Infrared image of the RCW38 star forming region taken with the Very Large Telescope. For further information see `http://www.eso.org/outreach/press-rel/pr-1998/pr-19-98.html`.

electron density of $n_e = 10^6$.

Thus, we can safely neglect self-gravity in this work, so that we will not be able to investigate star formation directly. Note that with the present day computational resources it is anyhow not yet possible to investigate self-gravity and turbulence at the same time. This is due to the fact that turbulence and self-gravity are both computationally expensive. The former has to be very highly resolved, whereas the latter has a basic numerical cost going as N^2, where N is the number of cells spanning the numerical domain. This does obviously not fit to the available computing resources.

With the specification of the region of interest to be the *diffuse molecular cloud* phase of the ISM we are in a position to specify the corresponding model parameters. For this phase we consider the lower limit for the number density given in Snow and McCall (2006) – that is we select $n_0 = 10^8$ m^{-3}. The corresponding value for the temperature is obtained from a model for the two-phase ISM. From the discussion in Cox (2005) with the resulting pressure curve depicted in Fig. 1.2 we find a corresponding thermal pressure of about $7.76 \cdot 10^{-14}$ Pa. This means that we are dealing with a temperature of about 56 K. From this we find a sound speed of 480 m s^{-1} when we assume an average ion mass of $m_0 = 2m_p$. The latter choice corresponds to the fact that hydrogen occurs partly in the form of neutral hydrogen molecules and that also heavier elements are present in the ISM.

For the input power by supernova explosions this choice of parameters leads, according to Eq. (2.100), to a normalisation factor of the order $S_{e0} \simeq 3 \cdot 10^{-29}$ J m^{-3} s^{-1} for a cube with side length of 40 pc. This is about 330 times smaller than what we would expect for molecular clouds. Therefore, the driving of the fluctuations for molecular clouds is introduced as a kinetic energy input of 330 in normalised units per unit time into the numerical domain. Before discussing the results of the computations, we address the numerical issues connected to these simulations.

4.1.1 Numerical Model

Naturally the normalised density is initialised as unity for the numerical computations. Furthermore the magnetic field is initially chosen to point into the x-direction with a magnitude given according to the desired plasma β as:

$$\tilde{B} = \sqrt{\frac{2}{\beta}} \tag{4.1}$$

for an initial pressure of unity. This relation can most easily be found from Eq. (2.97). As was mentioned earlier, we choose $\beta = 0.3$, because this quite nicely corresponds to the observations. The fluctuations are initialised as pure velocity fluctuations and are driven by an input of the same magnitude after every time step $\Delta t_{Drive} = 10^{-3}$. At these driving steps we put in a velocity disturbance corresponding to a kinetic energy of:

$$\Delta E_{num} = \tilde{S}_e \Delta t_{Drive} \tag{4.2}$$

These fluctuations are restricted to spatial scales with $1 \leq kL/2\pi \leq 3$, where k is the wavenumber and L indicates the length of the numerical domain, and they are put in with random phases and random amplitudes, with the latter also depending on the wavenumber. Moreover, the fluctuations are added as an incompressible velocity field to mimic the transport through wavenumber space from larger spatial scales than they are accessible in the simulations.

The simulation results presented in this section are extracted from numerical computations run up to the normalised time $t = 0.3$. This time has to be seen in contrast to the time scales relevant for turbulence as they were introduced in section 2.7.4. For the presented simulations we found a normalised energy content of the numerical domain of $E_{fluct} \simeq 30$. The normalised energy dissipation rate was chosen as $\varepsilon = 330$. Finally, we found an average normalised velocity of $\bar{u} = 6.1$. Using these values we find for the characteristic time scales values of $\tau \simeq 0.061$ and $\tau_D \simeq 0.55$ revealing that after reaching the fully turbulent state at $t \simeq 0.1$ (see Fig. 3.14) the system was evolved for more than three characteristic times.

Here we discuss mainly two different models for molecular clouds with a spatial resolution of 512 cells in each spatial direction. We concentrate on the investigation of the differences between an isothermal and an adiabatic medium – that is we do not take an energy equation into account but rather use an equation of state to close the system of equations. This might seem at first surprising, because shocks can hardly be treated without the application of an energy equation. The latter is needed to describe the heating occurring at the shock structures – for an isothermal equation of state the heating is obviously completely neglected, whereas it is suppressed when using an adiabatic equation of state. For molecular clouds, however, this is argued to be a good approximation due to the fact that cooling is very efficient in these dense regions (see e.g. Tóth 1994). As can be seen from Eq. (2.88) cooling gets very efficient for high densities as they are found in molecular clouds. Here we will investigate the changes of the structure due to the different choice for the equation of state. This will give at least a hint about the sensibility to use an isothermal equation of state. A comparison to a simulation using the full energy equation together with the appropriate cooling function for molecular clouds is left as a task for the future.

The neglect of an energy equation is, however, not all that has to be checked about the equations used to describe molecular clouds. We also have to discuss whether a description using the MHD equations is appropriate for this case. Thus, before coming to the results, we will first investigate a two-fluid model for molecular cloud turbulence.

4.1.2 The Two-Fluid Model

For molecular cloud turbulence we first have to clarify, how to model the corresponding plasma. With the preliminary work in chapter 2 we have two choices available for the numerical model – namely the MHD model and the two-fluid model. Especially, we have to check whether possible differences in the results obtained with two models can be attributed to different physics or rather different numerical errors. For the phase of the molecular clouds the obvious test is to compare the results of a magnetised shock tube tests, already introduced in Sec 3.4.3, for both models, since such shocks are expected to be the dominant structures in the high Mach number turbulence inside molecular clouds.

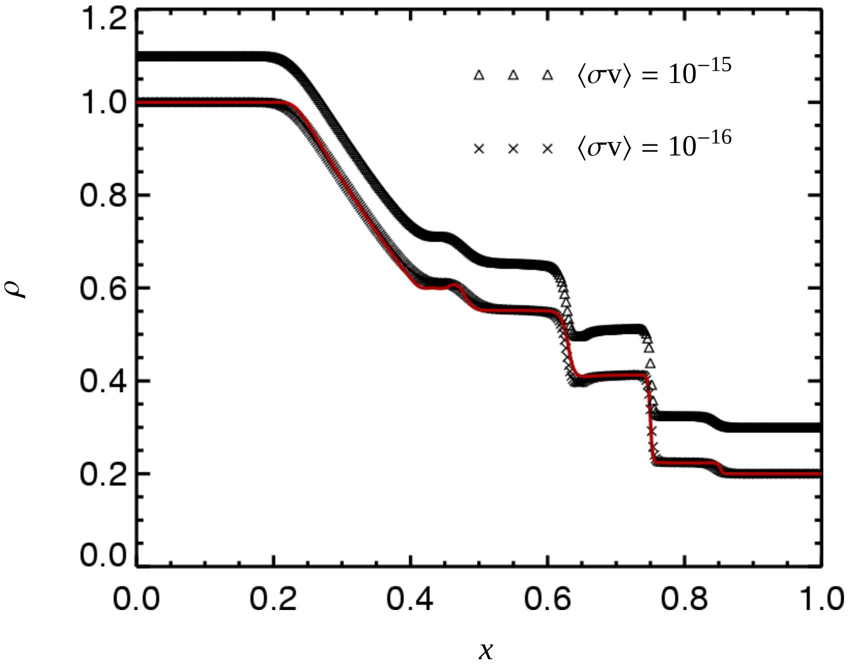

Fig. 4.2: Density distribution for the one-dimensional, non-dimensionalised Brio-Wu problem at time $t = 0.15$. Results are shown for the sum of neutral and charged fluid density for the two-fluid model with coupling strengths as indicated in the figure. To discriminate the results for $\langle\sigma \mathrm{v}\rangle = 10^{-15}$ m^3 s^{-1} are shifted upwards by $\Delta\rho = 0.1$. Additionally we show the MHD solution as the red line.

Results of the corresponding numerical computations are shown in Fig. 4.2. Here we investigate the magnetical shock tube test as it was already discussed in Sec. 3.4.3. The MHD test was set up exactly as it was done there. The two-fluid test was set up up basically in the same way apart from the fact that the mass density was split up into a part for the neutral fluid and one for the ionised fluid, with the sum yielding the same mass density as for the MHD simulation. The normalisation constants were chosen as given in the introduction to this chapter – namely we used an overall size of the computational domain of 40 parsecs, a base temperature of 56 K and a base number density of $n_0 = 10^8$ m^{-3}. For the degree of ionisation we selected $x_0 = 0.01$.

From Fig. 4.2 we can draw several important conclusions regarding the two-fluid model. While the actual interaction for molecular cloud turbulence is expected to be even stronger as discussed in Hosking and Whitworth (2004), the first important point is that the results for coupling strengths of $\langle\sigma \mathrm{v}\rangle = 10^{-16}$ m^3 s^{-1} and $\langle\sigma \mathrm{v}\rangle = 10^{-15}$ m^3 s^{-1} (see section 2.8.2 for a definition of these coupling terms) are virtually the same (note that one of the solutions is artificially shifted). This shows that the solutions for a coupling of this strength a *saturated*. That is they do not change anymore for a higher coupling strength. This can only be explained by the fact that the coupling is so strong that the velocities and the temperatures of both fluids are identical in every cell of the numerical grid. Since the evolution of the mass density is fully determined by the velocity field, the distribution of the mass density will – if initially the same – remain the same for both fluids at all times. Thus, we have the same distributions of mass and of momentum density for both fluids. With similar arguments it can be seen that this is also the case for the magnetic induction and the energy densities. This means we have total coupling in this case. This also means that for a coupling strength above a given lower limit all simulations will yield identical results – as was observed for the two different strengths here.

With this in mind one would also expect the actual two-fluid solutions to be identical to those obtained with the MHD equations. This is seen when taking into account that the evolution equation for the magnetic induction only depends on the velocity – which is identical for both fluids. Therefore, *both* fluids are directly coupled to the magnetic field, leading to the expectation that we should gain the same results as for the MHD equations.

The solutions for the sum of the densities obtained using the system of two-fluid equations are not *exactly* the same as the ones obtained from the MHD equations, which can also be seen in the same figure. The difference in the results, however, is only marginal and can be attributed to the realisation of the two-fluid model. Due to the fact that as compared to the MHD equations five additional equations have to be solved it can be expected that the dissipation is somewhat more important than for the case of the MHD equations. Stronger dissipation, however, would essentially yield smoothed out spatial structures. This nicely corresponds to the differences visible in Fig. 4.2 – most of the sharp gradients being present in the solution of the MHD equations have been smoothed out in the two-fluid simulation. The important point, however, is the fact that all waves are exactly at the same position as in the MHD equations.

This shows that the solution obtained using the two-fluid model is just the one found using the MHD equations, with the deviations being caused only by differences in the numerical procedure rather than by any physical difference. This means that for molecular cloud turbulence at the spatial scales under consideration here, there is no physical difference between the MHD and the two-fluid model. The only difference to be expected to the above test is entirely due to numerical errors. Therefore, we will stick to the MHD model alone, because the numerical cost is much lower and – as has been shown by this test – the numerical dissipation is also reduced.

There is just another important conclusion to be drawn from the above results. Clearly the nice correspondence of the two-fluid solution to the MHD solution shows that the two-fluid model is implemented correctly. It can readily be used for any system where the coupling is sufficiently weak so that the use of a two-fluid is necessary. Additionally by this discussion we have seen that the Brio-Wu shock tube test is not only to be regarded as an unphysical test case. Here we were able to use this classical test case to decide about the necessity to use a two-fluid representation for out simulations. The present results even show that the Alfvén speed in the limit of strong coupling is, indeed, determined by the sum of the density of charged and neutral particles.

In what follows we discuss the results obtained using the MHD model. We are especially interested in the differences between an isothermal medium (with an adiabatic exponent of $\gamma = 1$) and a medium to be described by an adiabatic equation of state (where we choose the adiabatic exponent as $\gamma 5/3$) – meaning a medium, where external temperature sources are neglected. For this we will start the description with what is most easily observed – the density structure.

4.2 The Density Structure

The line-of-sight integrals of the electron density n_e along a given direction is also known as *dispersion measure* and defined as:

$$D_M \equiv \int n_e dl \tag{4.3}$$

The spatial density structure resulting from the highest resolution simulations is depicted in Fig. 4.3. The following general remarks apply to both, the images showing the local density structure and the ones showing the dispersion measure.

First, it is evident that in both cases the same driving was used. The spatial structures are clearly similar and in both cases the plasma is concentrated in filamentary substructures. This is to be expected for compressible MHD simulations where the dissipative structures are shocks.

Due to the fact, however, that we used the same driving in both cases all differences have to be attributed to the difference of the equation of state. Especially the dispersion measure reveals that the density contrast is much lower for an adiabatic equation of state. Moreover, when comparing the results for the local density distributions, the shock structures are clearly much sharper for the isothermal medium. This is due to the fact that for an adiabatic medium the pressure is much higher in the vicinity of density enhancements than it would be for an isothermal medium.

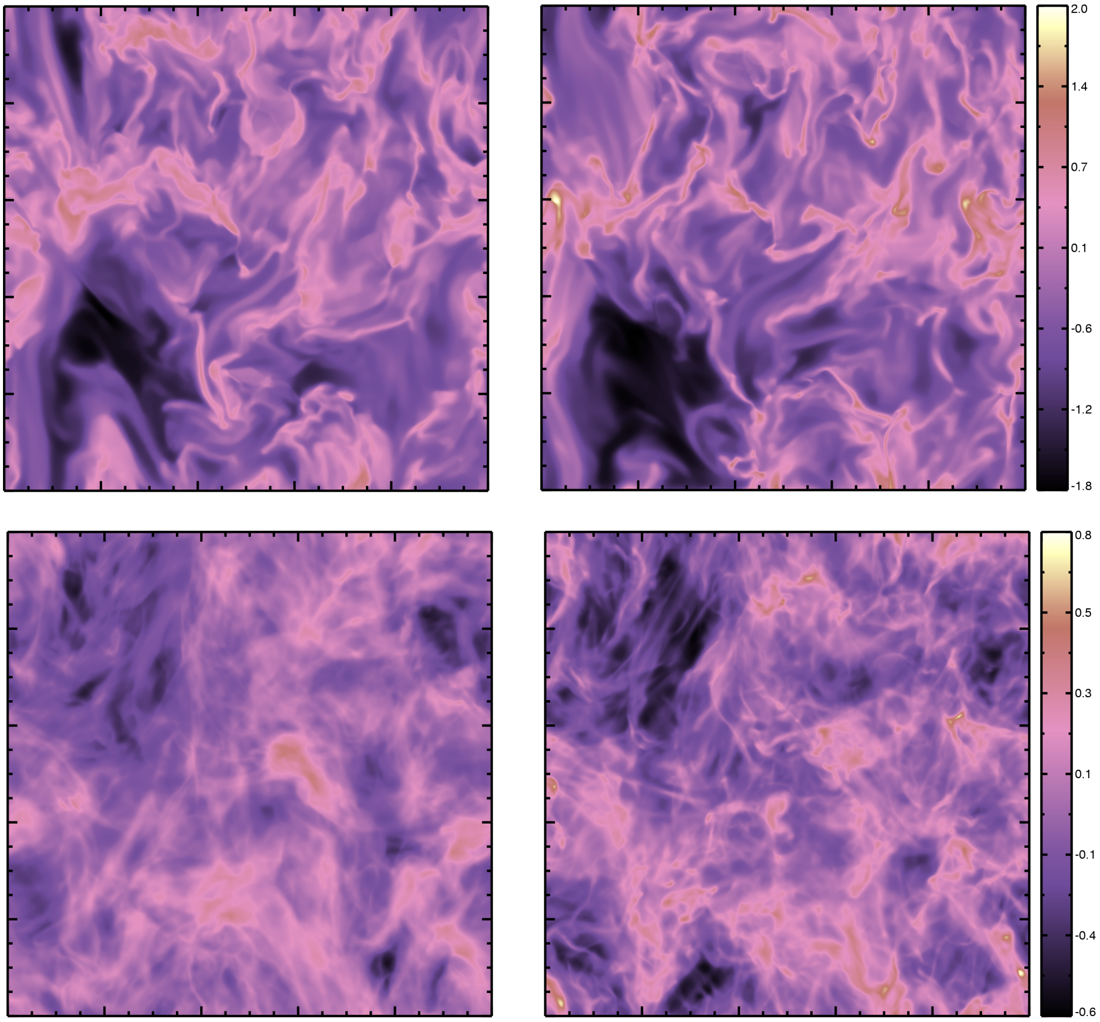

Fig. 4.3: Electron density structure resulting from MHD simulations for molecular clouds. The upper row shows local density cuts, whereas in the lower one the dispersion measure (for the definition see Eq. (4.3) is depicted. On the left the corresponding images are shown for simulations with an adiabatic equation of state whereas on the right the results for an isothermal medium are given. In each figure we show the logarithm of the number density in units of 10^6 m^{-3}.

This fact is also reflected in the density power spectra. This is shown in Fig. 4.4 as a direct comparison for both cases. For the isothermal spectrum there is apparently much more power in the high wavenumber modes corresponding to the small spatial scales. Obviously, however, not only the highest wavenumbers are influenced by the different choices for the equation of state. The fluctuations in the inertial range also differ.

Interestingly, the density power spectrum can directly be extracted from observations for the interstellar medium. So far it is the only spectrum available for comparison to numerical results. The most famous of these spectra is the one published in Armstrong et al. (1995), depicted in Fig. 1.9. Especially the fact that the spectrum is spanning about ten orders of magnitude in wavenumber space and also that it follows the Kolmogorov index is quite remarkable. There are, however, no theories available for a density fluctuation spectrum yet. The Kolmogorov theory did not predict anything on such spectra since for this the fluctuations were assumed to be incompressible. The same is true for the She-Leveque model for the structure functions to be discussed later (see e.g. section 4.3). These models were just recently extended to the case of compressible fluids without any discussion of the density fluctuations.

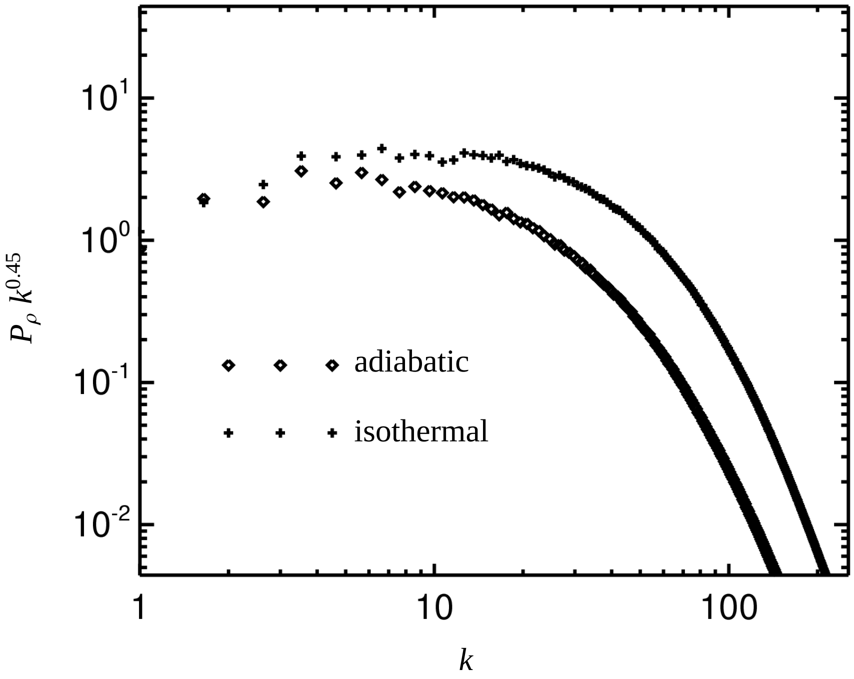

Fig. 4.4: Density power spectra for molecular cloud turbulence. Here we show the normalised density fluctuation power multiplied by $k^{0.45}$ as a function of wavenumber k for the adiabatic and the isothermal case.

When taking into account the line-of-sights along which the data for the Armstrong et al. spectrum were obtained, it becomes clear that it is related to the more dilute phase in the ISM. Therefore, it is not representative for the dense, high Mach number regions investigated here. For these a spectrum was observed by Deshpande et al. (2000), that does not correspond to the Kolmogorov scaling at all. Deshpande et al. rather find a much flatter power law with an index about 0.75. This dependence of the power law index on the Mach number is further investigated by Kim and Ryu (2005), who also found flatter spectra for increasing Mach numbers.

Our results, depicted in Fig. 4.4, are quite consistent with these models and the observations. A result, which was not discussed so far, is the fact, that the density spectrum appears to become steeper for an adiabatic medium. This can be understood when taking into account the fact that the shocks are stronger for the isothermal medium. Stronger shocks, however, also correspond to a flatter spectrum (for this also see Kim and Ryu 2005). This conclusion has to be verified by higher resolution simulations in the future, but so far it is clear that especially for the density and the density statistics there is a distinct difference between the two possible choices for the equation of state. For the classical turbulence statistics, however, the magnetic or kinetic fluctuations are of much greater importance. Especially for particle propagation it is the former of those which is needed for the evaluation of the particle trajectories. These types of fields will, therefore, be discussed in the following sections.

Here, however, we still can depict one aspect of the density field, which is thought to be closely connected to the turbulence statistics for the velocity field. As was discussed in the introduction, it is nowadays mostly accepted that the turbulence statistics is determined by the dimension of the most dissipative structures. For compressible HD these are obviously shock waves, which will also strongly contribute to the dissipation in compressible MHD turbulence. A first indication of such shocks would be a local density enhancement. As can be seen in the two-dimensional cuts and the dispersion measure in Fig. 4.3 such density enhancements are ubiquitous in the numerical domain. From those diagrams, however, the dimensionality of those structures can not be inferred. This has to be done from a three-dimensional illustration as it is given in Fig. 4.5.

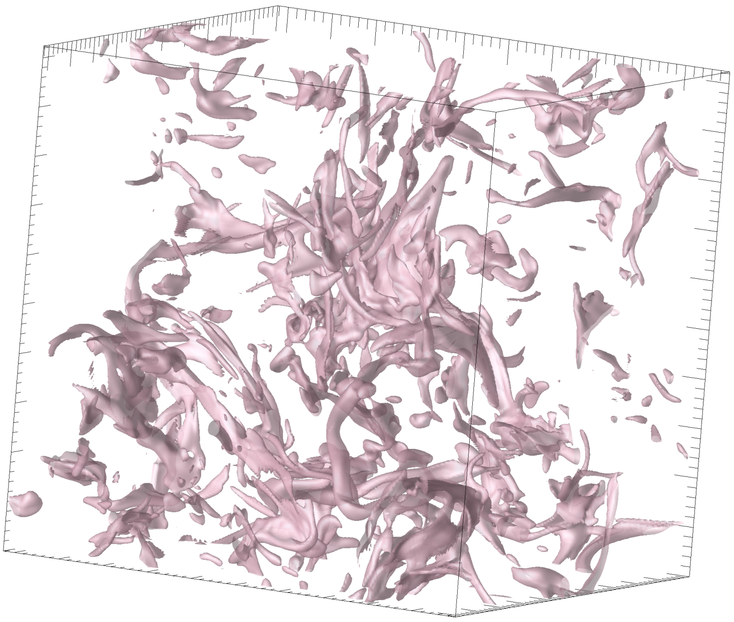

Fig. 4.5: Isosurface plot for the density for the isothermal molecular cloud turbulence computation. The isosurfaces are drawn for an electron density of $5.5 \cdot 10^6$ m^{-3}. Additionally the boundary of the numerical domain is indicated to visualise the three dimensional structure.

The picture shows an isosurface for the number density distribution for the case of the isothermal molecular clouds. The density value for which the isosurfaces were drawn was chosen as $n_e = 5.5 \cdot 10^6$ m^{-3} in order to visualise the strong density enhancements expected for shock waves. As is expected for shock waves the density enhancements are mostly located in sheet-like structures. Therefore, it can be assumed that the dissipative structures for the turbulence are two-dimensional corresponding to the ideas about compressible turbulence introduced at the beginning of this work.

The structure is also of interest in the context of star formation. The sheet-like high density structures will eventually be the ones where new stars will form. As we have seen, when discussing the dispersion measure, however, it is nearly impossible to identify actual sheet like structures from astronomical observations.

4.3 The Velocity Field

In classical turbulence theory naturally the velocity field was of most eminent interest. This is due to the fact that classically turbulence research concentrated on incompressible neutral fluids. For those, only the velocity field and the corresponding vorticity are of interest, because they contain the information about the eddy structures. Before investigating the magnetic field structure we, therefore, also analyse the statistics and the spatial distribution of the velocity field.

To continue on the discussion started at the end of the preceding section we first compare the density structure with the divergence of the velocity field. The latter shows the discontinuities in the velocity field, thus, being a good indicator for shock waves. In Fig. 4.6 we compare the local density structure with the local divergence of the velocity field. Obviously, there is a close correlation between the two. Physically a shock is a compression wave. It is, therefore, visible in Fig. 4.6 as a local minimum of the velocity divergence. Most of these dark creases in the local divergence shown in Fig. 4.6 nicely correspond to local density enhancements.

The positive divergence peaks for the velocity field are connected to rarefaction waves rather than to shocks. Indeed, peaks of the velocity divergence in Fig. 4.6 correlate with minima of the local mass

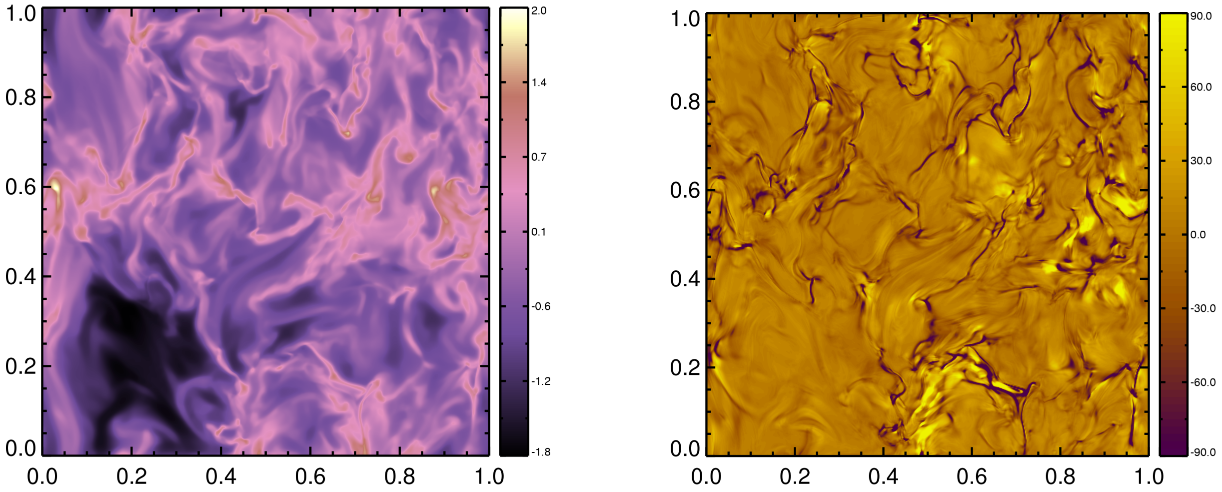

Fig. 4.6: Comparison of the local density structure (left – in normalised logarithmic units) and the local divergence of the normalised velocity field (right).

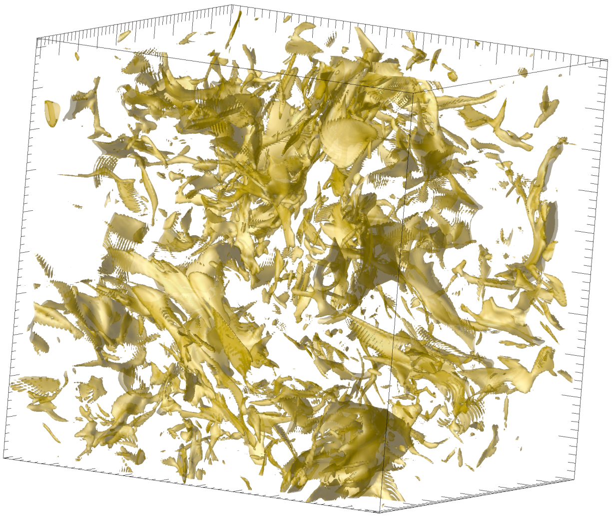

Fig. 4.7: Illustration of the dissipative velocity structures in the numerical domain. Here we show isosurface for a the velocity divergence (with an isosurface value of $\nabla \cdot \mathbf{v} = -290$).

density. This demonstrates that the density is indeed a good measure for the occurrence of shock waves in the computational domain.

As for the density we have to check for the dimensionality of the shock structures. An illustration of these for a lower resolution version of the isothermal simulation is shown in Fig. 4.7. The depicted isosurface correspond to negative values of the velocity divergence and, thus, to the dissipative shock-structures of the velocity field. As is expected for compressible simulations these dissipative structures are generally sheet-like. This is also found for the dissipative structures emerging due to the presence of a magnetic field as will be seen in the next section. The dimensionality of the dissipative structures is important for the theoretical model on the structure functions as was discussed in the introduction. Before, however, discussing the statistics of the velocity field any further, we will first conclude the analysis of the spatial velocity structure.

The actual velocity structure is depicted in Fig. 4.8 where a comparison for the adiabatic and the isothermal medium is undertaken for a cut through the computational domain. Here, the initial magnetic field points to the right in both cases. For both cases it is obvious that the velocity field shows much finer structures than the initial one shown in Fig. 3.15. This is due to the fact that the initial large-scale

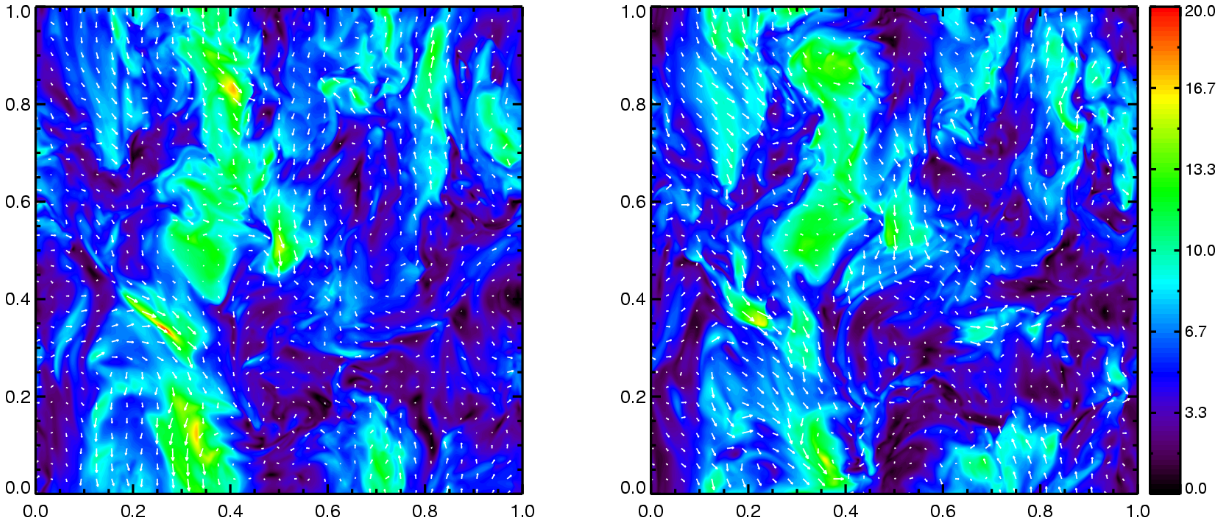

Fig. 4.8: Cut through the computational domain showing the local velocity field for the adiabatic (left) and the isothermal (right) molecular cloud medium. The absolute value is shown in units of the isothermal sound speed and is colour-coded according to the given colour bar. The vectors indicating the projection of the flow direction are normalised to the maximum velocity occurring in this subset of velocity vectors.

flow evolved into a turbulent flow with fluctuations also at the smallest spatial scales. Clearly, there is a difference between the adiabatic and the isothermal medium. This, however, cannot be as easily qualified as in the case of the density distribution. For a *quantification* of this difference with regard to turbulence it is, therefore, necessary to obtain statistical information about the velocity field.

With the velocity field in Fig. 4.8 being given in units of the isothermal speed of sound, we can easily investigate the sound Mach number M_S of the flow. In both simulations we found the average sound Mach number M_S to be $M_S \simeq 6$. This value is decidedly below what is assumed by some authors (see e.g. Boldyrev et al. 2002). This might be due to the fact that these authors take still larger scales with the corresponding large scale flows into account. Nonetheless, the environment was correctly designated as one pervaded by high Mach number turbulence. This is not true anymore with regard to the Alfvén Mach number M_A. For this we find an average Mach number as low as $M_A \simeq 1$ due to the low plasma β. Locally, however, this Mach number is much higher and can easily reach values above 10. This is also the case for the sound Mach number which reaches even higher values locally. Thus, the simulation results are in good agreement with the observations.

Before we start with the discussion on the structure functions we investigate the velocity power spectra. These are shown in Fig. 4.9 where the power spectrum for shear and compressive fluctuations are given individually (see section 3.6.1 on how turbulence spectra are obtained). Obviously, the compressive part corresponds to a Kolmogorov-like power law with an index of 5/3. At first sight the power law index for the solenoidal part of the spectrum would seem to be much flatter than one with index 5/3. This, however, can be explained by the so-called *bottleneck* effect. By this term researchers in the area of turbulence call the effect that numerical simulations often show excess power just just in front of the dissipation wavenumber k_d. This is thought to be due to the lack of smaller-scale vortices at wavenumbers $k > k_d$. It was also found that the bottleneck effect is especially relevant for the three-dimensional spectrum, which is under consideration here. This fact is elaborated in Dobler et al. (2003). There the authors show that the omnidirectional spectrum will show a bottleneck effect, whenever the drop of the spectrum in the dissipation range is quite steep. Therefore, we are not in a position to draw reliable conclusions about the spectral slope in the inertial range due to the overlying bottleneck effect. This, however, can be remedied by investigation of the second-order structure function as shown below.

When regarding Fig. 4.9 it is clear that the major part of the kinetic fluctuation energy is stored in incompressible fluctuations. This means that the inertial range is dominated by vortices rather than

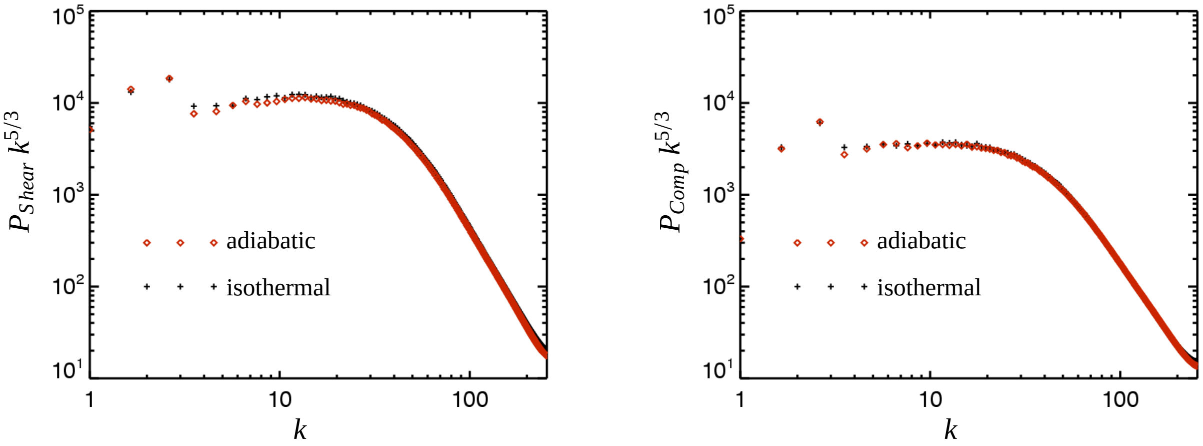

Fig. 4.9: Power spectra of the velocity fluctuations for the isothermal and the adiabatic cases as indicated in the figures. The spectra are compensated for a Kolmogorov-like power law. On the left we show only the solenoidal part of the spectrum whereas on the right the compressible part is depicted. The results are given in normalised units.

shocks or any compression waves. The compressible character of the molecular cloud medium becomes more important at the smallest spatial scales, where the fluctuations are actually dissipated. This becomes clear when comparing the spectra given in Fig. 4.9 and strongly supports the notion that turbulence in the inertial range is mainly incompressive.

As is discussed in the introduction the dissipation is assumed to have a strong influence on the scaling behaviour of the turbulence. The main idea is that the statistics is determined by the spatial dimension of the typical dissipative structures. As we saw these are mostly shocks for compressible hydrodynamics. In MHD also current sheets – obviously being of the same spatial dimension – have to be taken into account.

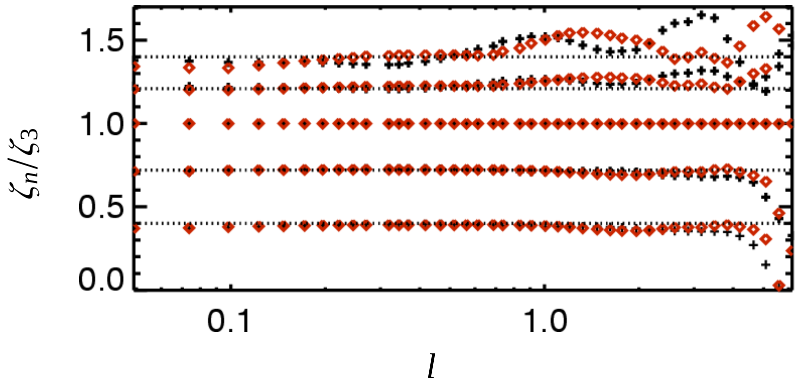

Fig. 4.10: Exponents for the structure functions up to fifth order using the extended self similarity. Here the crosses indicate the data for the isothermal medium, whereas the red diamonds show the results for the adiabatic medium. A fit to the data is indicated by the dotted lines.

The actual scaling behaviour is shown in Fig. 4.10 where the exponents of the structure functions are given using the extended self-similarity (ESS). The latter must be invoked here, since the inertial range is not visible for the structure functions themselves. The statistics is quite good for the lower order structure functions. If ESS can be trusted we have according to Fig. 4.10 the scaling exponents (see in the introduction for their definition) $\zeta_1/\zeta_3 = 0.4$, $\zeta_2/\zeta_3 = 0.72$, $\zeta_4/\zeta_3 = 1.21$ and $\zeta_5/\zeta_3 = 1.4$. These are in excellent agreement to the theoretical prediction given in Boldyrev et al. (2002) for compressible

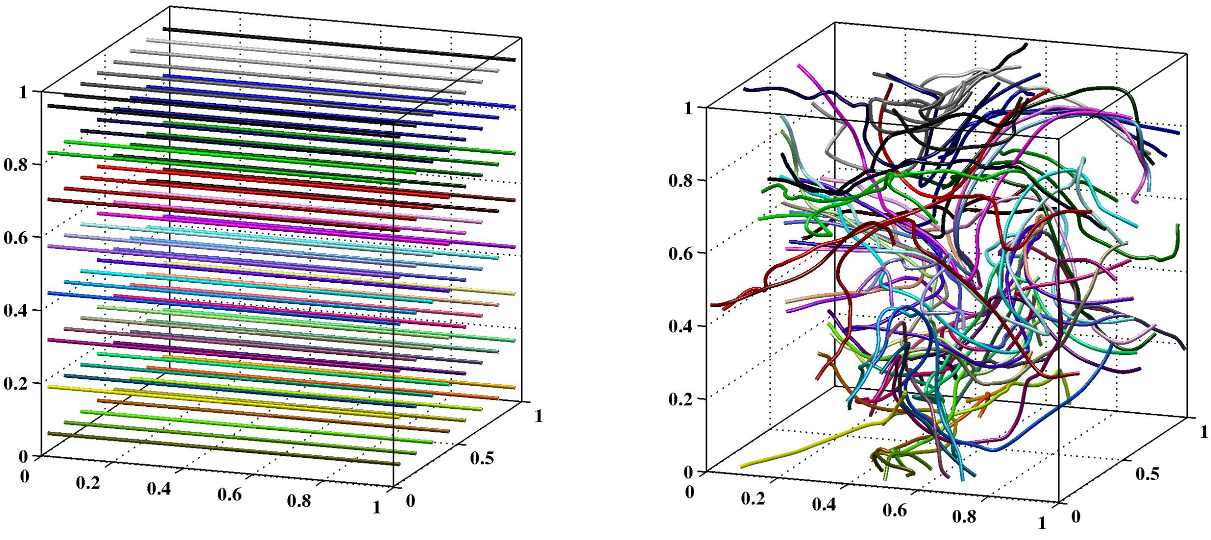

Fig. 4.11: Magnetic field lines in the numerical domain at the beginning of the computation (left) and after several eddy turnover times (right).

MHD:

$$\frac{\zeta(p)}{\zeta(3)} = \frac{p}{9} + 1 - \left(\frac{1}{3}\right)^{p/3} \tag{4.4}$$

In particular it is clear that the data do contradict the classical Kolmogorov scaling of $\zeta_n/\zeta_3 = n/3$. Therefore, the results confirm the basic She and Leveque model. For the spectral slope in the inertial range this means that we have a power law index of 1.72, which is just a little steeper than the classical Kolmogorov power law index.

Interestingly, however, there is no principal difference between the turbulence statistics of the isothermal and the adiabatic simulations. The same structure is seen in the spectra and the structure functions in both cases. While there are marginal differences, particularly the power laws are the same in both cases. This is further evidence of the basic scaling structure. Shocks themselves might look different for isothermal or adiabatic systems, but the essential aspect of the She and Leveque model is the dimensionality of the dissipative structures. This is especially the case in ideal MHD, where shocks would have no extent in the shock direction when no numerical dissipation is present.

Concluding, we can say that the statistics of the turbulence does not depend on the equation of state used for the computations. There is, however, a strong dependence of the spatial structure as was seen in the preceding paragraph. Therefore, the equation of state has to be considered carefully whenever any resemblance to actual observations is sought for.

4.4 Influence of the Magnetic Field

As mentioned repeatedly in the preceding section, we have to study the influence of the magnetic field on the spatial structure and on the turbulence statistics. The magnetic field introduces a variety of structures into the medium. Among these are the additional wave modes already discussed in Sec. 3.4.4. Additionally, the isotropy of the simulations is destroyed due to the fact that the motion of charged particles parallel and perpendicular to the magnetic field is different. On large scales, however, the system can be expected to still look isotropic, because the field lines will be bent due to the turbulence. Therefore, there is no preferred direction for these large scales anymore.

This fact is illustrated in Fig. 4.11 where the initial magnetic field lines are compared to those after several eddy turnover times. At first it might seem astonishing that the field lines are not closed through

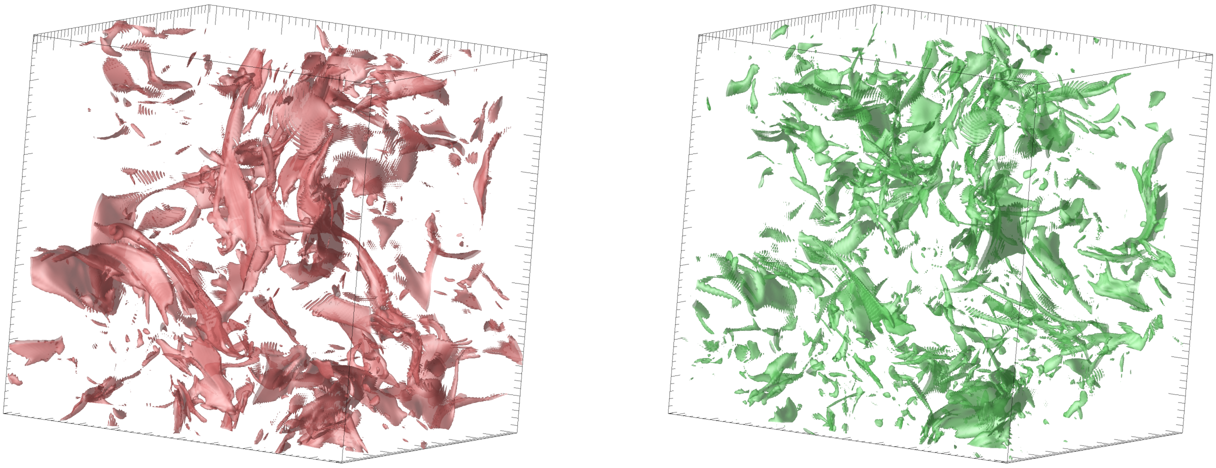

Fig. 4.12: Isosurface plots for the square of the normalised current density (left – with an isosurface value of 10^6) and the squared divergence of the normalised Elsässer variable z^+ (right – with an isosurface value of $2 \cdot 10^5$). Results are shown for the normalised time $t = 0.3$ for the isothermal case.

the periodic boundaries for fully developed turbulence. This is again due to the fact that numerically one ultimately does not solve the ideal MHD equations: the numerical errors result in some resistivity. Therefore, *numerical reconnection* can occur, so that the footpoints of the magnetic field lines on the boundaries do not have to remain connected.

When a finite magnetic induction is present we face the question which are the relevant variables for the description turbulence. For *incompressible* turbulence these are usually thought to be the *Elsässer variables*, which read in normalised form:

$$\boldsymbol{z}^{\pm} = \boldsymbol{u} \pm \frac{\boldsymbol{B}}{\sqrt{\rho}} \tag{4.5}$$

In an incompressible medium this choice is motivated by the fact that the only wave type to occur in incompressible MHD is the Alfvén wave. Unfortunately, however, there is a variety of additional wave types in compressible MHD as was already discussed in Sec. 3.4.4. One argument in favour the Elsässer variables as a nonetheless good measure is the fact that the inertial range is dominated by incompressible flow. Therefore, it would also seem sensible to investigate Elsässer variables in compressible MHD. We have to be careful, however, because incompressible eddies are not necessarily connected with Alfvén waves.

Before coming to the evaluation of the spatial structure and the statistics we will again discuss the dissipative structures. As was mentioned already in the preceding section, the dissipative structures resulting from the magnetic part of the system are thought to be current sheets. Naturally, we will, therefore, investigate the regions of high current density. These are illustrated as isosurface plots in Fig. 4.12 together with the squared divergence of the Elsässer variable z^+. The latter is also assumed to be a good tracer for the dissipation according to Merrifield et al. (2005).

As was already discussed before, these dissipative structures are clearly two-dimensional. This is even more obvious than in the case of the velocity dissipation shown in Fig. 4.7. Taking into account that we will encounter different forms of numerical dissipation in the computational domain, we find that the major fraction of these is two-dimensional. This, again, indicates that we will find the same turbulence statistics as it was discussed in Boldyrev et al. (2002). The results found for the velocity structure functions in the preceding section reveal that not only the dissipative structures but also the turbulence statistics are very well in accord with this relation.

Even though the statistics of the magnetic field is not – and probably will not be for the near future – accessible to observations it is nonetheless the main ingredient for the computation of the transport

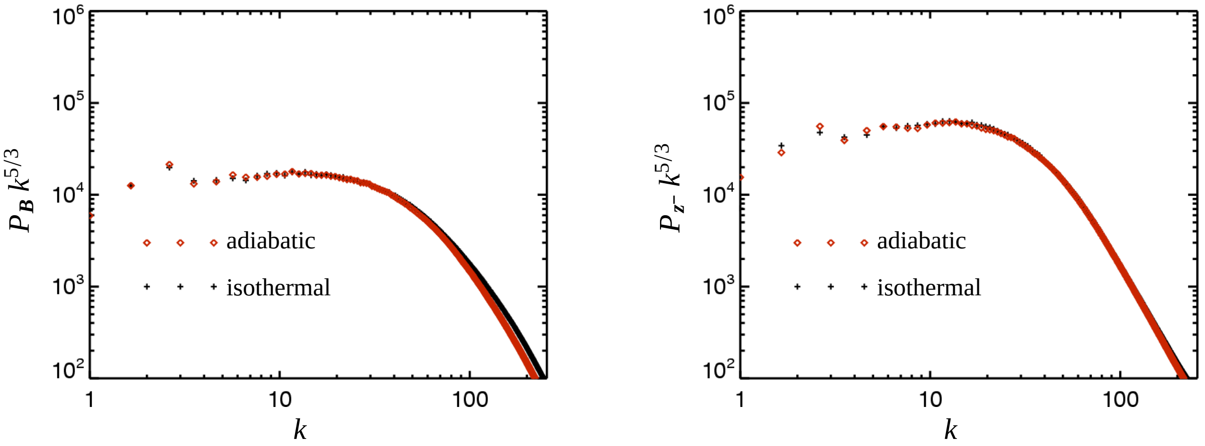

Fig. 4.13: Power spectrum for the magnetic field (left) and Elsässer variable (right) fluctuations. Both spectra are given for the isothermal and adiabatic as indicated in the figures. The spectra are multiplied by a Kolmogorov power law and are given in normalised units.

of charged energetic particles. This is because charged energetic particles are thought to be scattered at irregularities of the magnetic field (see Schlickeiser 1989). As for the velocity field, the spectral index for magnetic field fluctuation spectrum is very near to the Kolmogorov one as can be seen in Fig. 4.13.

In the same figure we also show the Elsässer variable fluctuation spectrum for z^-. For this the bottleneck effect, which was discussed for the velocity fluctuation spectrum, is again present. This implies that the information on the power law index of the spectrum should rather be obtained from the second-order structure function. The exponent of the latter is found to be $\zeta_2 = 0.7$ for both the isothermal and the adiabatic medium. This value corresponds to a power law index of 1.7, which is slightly steeper than the classical Kolmogorov spectrum as is expected for compressive turbulence. Unfortunately, the structure functions for the magnetic induction and also for the Elsässer variables show very bad scaling behaviour for higher orders, and are, therefore, not discussed here any further.

Moreover, in the spatial structure of the magnetic field itself depicted in Fig. 4.14 the two-dimensional current-sheets are indirectly visible as the abrupt changes in the magnetic field direction. For these spatial structures the difference between the isothermal and the adiabatic medium is obvious. Due to the limited observations on magnetic fields in the ISM and the fact that the simulations results look different without showing different characteristics, this result does unfortunately not help to distinguish the different cases in nature.

One especially has to keep in mind that the magnetic induction is not accessible to direct observations at all. All information on the magnetic field structure, thus, has to be obtained by indirect means. One of the methods to obtain information on the magnetic field along any line-of-sight is connected to the Faraday rotation. When plane polarised radiation of wavelength λ propagates through a plasma with a component of the magnetic field parallel to the direction of propagation, the plane of polarisation rotates with a rate depending on the local density and the magnetic induction. The overall angle of rotation when traversing a line-of-sight of length l is.

$$\delta\theta(\lambda) = R_M \lambda^2 \qquad \text{with} \qquad R_M = -\frac{e^3}{8\pi^2 \varepsilon_0 c^3 m_e^2} \int_0^l n_e(l') B_{\|}(z) dl' \tag{4.6}$$

where R_M is the so-called *rotation measure*. For example, the radiation by pulsars is significantly polarised and can, thus, be used to compute the rotation measure. The actual rotation measure can not directly be measured – what is actually measurable is the polarisation angle at some wavelength. The actual rotation measure – obviously containing information about the magnetic field along the line-of-sight – can only be deduced if the polarisation angle is measured at several different wavelengths. A fit using Eq. (4.6) will then yield the actual rotation measure.

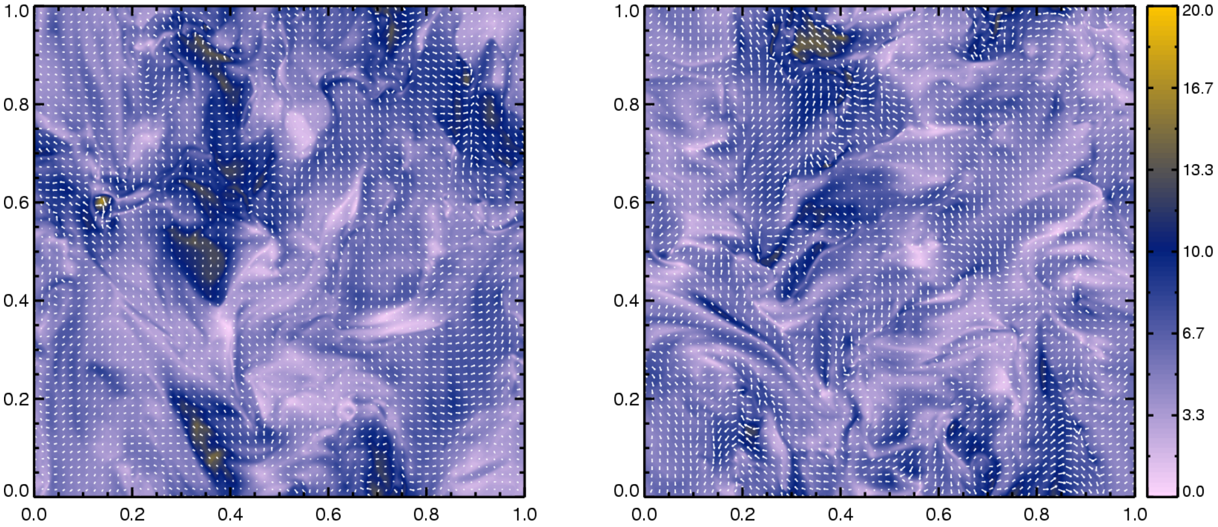

Fig. 4.14: Cut through the computational domain showing the local magnetic field structure for the adiabatic (left) and the isothermal (right) molecular cloud medium. The absolute value is shown in normalised units and is colour-coded according to the given colour bar. The vectors indicate the direction of the field onto the plane they are normalised to the maximum magnetic induction occurring in this subset of magnetic field vectors.

Here, we are in a much more comfortable situation. Knowing the spatial distribution of density and magnetic field, we can easily compute the rotation measure directly from the results of the numerical computations. In principle, we even loose a lot of the information contained in the numerical domain, but here we would like to compare the results for the adiabatic and the isothermal medium with a glance at a possible telescopic detection.

The rotation measure along the z-direction for both simulations is depicted in Fig. 4.15. Additionally we show the resulting polarisation of a homogeneously polarised radiation field behind the numerical domain for a wavelength of $\lambda = 0.21$ m as it was, e.g., observed by Wolleben and Reich (2004). Obviously, there are large regions in the numerical domain where the initial radiation field can traverse the 40 parsecs of plasma without any disturbance. Then again it is possible that in these regions the disturbances just cancel each other. All in all there are extended regions with nearly homogeneous polarisation, with rapid polarisation changes from region to region.

Evidently, however, there is not much difference between the two different cases. Again, as for the density the main difference is the smoothness of the structure in an adiabatic medium as compared to an isothermal one. For this we have to keep in mind that the spatial extent of the shock structures is largely overestimated in our numerical simulations as a consequence of the finite spatial resolution. Therefore, we can expect the real shock structures to be much narrower than found here. It will still take some time until numerical simulations will resolve these structures at all and will, thus, be able to yield results directly comparable to actual observations.

4.5 Conclusions

As was demonstrated in the preceding sections the turbulence in our molecular cloud simulations is in accord with the most recent models for compressible MHD turbulence. Not only do the resulting spectra correspond to what is expected from theory, also the structure functions do so. This theory is coupled to the assumption that the dissipative structures are mainly two-dimensional, which could be confirmed with the simulations, where shocks and current sheets make the major contribution to the damping of the turbulent fluctuations. Regarding the spectral slope we found a power law index slightly steeper than the one for incompressible, homogeneous turbulence. Despite the finite resolution it is obvious that this

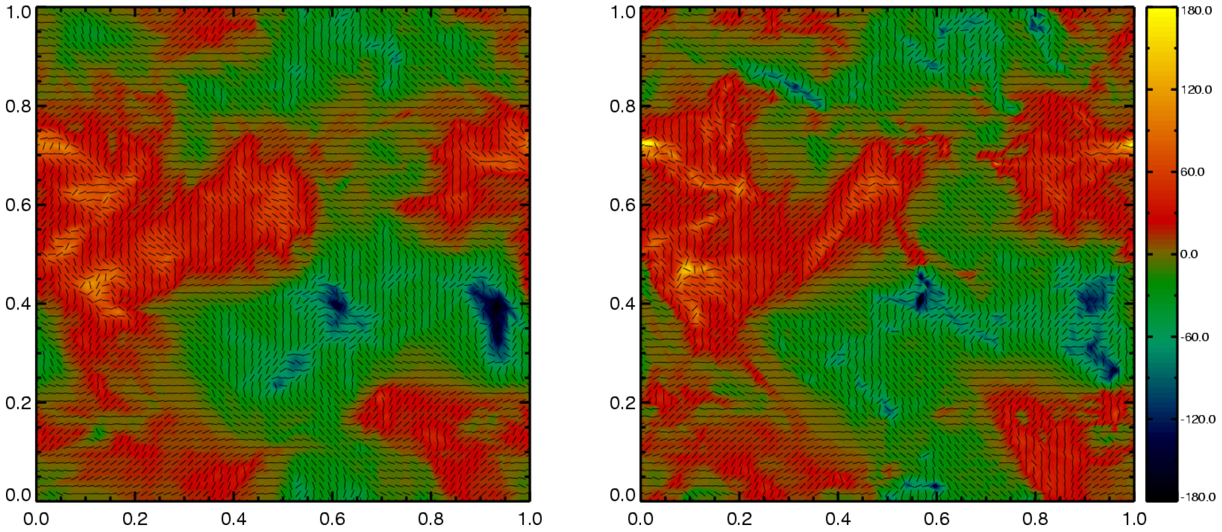

Fig. 4.15: Rotation measure for the molecular cloud medium along the z-direction for the adiabatic (left) and the isothermal (right) medium given in units of rad m^{-2}. The bars show the local polarisation of a homogeneously polarised background radiation for a wavelength of $\lambda = 0.21$ m.

power law index remains considerably below 2 for all cases. Therefore this exponent is comfortably far away from what was classically thought to be a special value for particle transport theories Schlickeiser (1988).

We investigated the difference between an isothermal and an adiabatic equation of state. While there are clear differences in the spatial structures, these do not extend to the velocity statistics of the turbulence. Only for the density spectrum there are significant differences, where, however, simulations with still higher spatial resolutions are needed to clarify more details. It might be possible that these differences result from the smoother density structures of the adiabatic medium. These would sharpen for higher spatial resolutions.

With regard to the spatial structure the main difference between the two cases is the occurrence of sharper structures in the isothermal medium. Despite the fact that shocks are not isothermal in nature, we have to take into account that the real spatial structures might be much sharper than found by our simulations, by which we can resolve spatial structures no smaller than 0.08 parsecs.

We also investigated observable quantities in particular the dispersion measure and the rotation measure for the two different cases. The main differences between those is again the sharpness of structures. When taking into account the finite resolution of the telescopes it can be doubted that these differences could be observed at all. Nonetheless, the computed structures look very similar to what is observed (see e.g. Wolleben and Reich 2004, for polarisation observations).

Chapter 5

Diffuse Interstellar Gas

As already mentioned in the previous chapter ISM turbulence is mostly discussed for molecular clouds. There are, however, also more global simulations for the interstellar medium of the Milky Way (see e.g. de Avillez and Breitschwerdt 2004; Breitschwerdt and de Avillez 2006). These are set up as a box reaching from the Galactic plane up into the halo of the Galaxy in order to investigate the stratification of the interstellar medium. Consequently, an investigation in terms of spectra and structure functions cannot be done due to the inherent inhomogeneity of the plasma. Therefore, we must be interested in a similar simulation on a more local scale. In this chapter, we will give first results on such simulations. As we will show in the next section, the simulations are computationally very expensive. Therefore, we were not able to perform computations with a spatial resolution in excess of 256 cells in each of the spatial direction, so that we will here rather concentrate on the spatial structure of the turbulence.

The most important difference between molecular gas and the diffuse phase of the ISM is that the latter is influenced by the interstellar radiation field, implying that a whole variety of new processes has to be taken into account. Despite the fact that the ongoing ionisation of the remaining atoms by the incident radiation makes a single-fluid MHD description questionable, we will nonetheless stick to the latter as it is also done by authors investigating the global ISM (see e.g. de Avillez and Breitschwerdt 2004; Breitschwerdt and de Avillez 2006). The development of a more adequate description will be left for future investigations.

In principle, a multi-fluid description of the dilute phases of the ISM would seem appropriate. This, however, would bring along several problems. One would not only have to include different interaction processes between the particles themselves, as it would seem sufficient for molecular clouds, but for the dilute gas one would also have to include ionisation by the external radiation field. This would also necessitate the use of a parameterisation of the external ionisation corresponding to the observations. A much more severe matter is the question whether the neutral gas can still be described using a fluid picture. While for charged particles due to their long range interaction scattering occurs still sufficiently frequent to justify a fluid description, this might not be the case for the neutral particles. Therefore, although it is desirable to use a multi-fluid picture for the diffuse interstellar gas, there is still a lot to be done before we are able to use such a model for turbulence research.

With all of the above in mind, when using an MHD model for the description of the dilute plasma we still have to take the fact into account that the medium is optically thin. This means that not only the interstellar radiation field can influence the individual particles but also that the radiation emitted by the particles can leave the gas. Therefore, heating and cooling processes, as discussed in section 2.7.2, have to be taken into account. In this chapter we will mainly investigate the spatial structure of the turbulence. This is due to the fact that we did not yet perform simulations with a spatial resolution of at least 512 cells in each direction, which would seem necessary to obtain good statistics for the turbulence.

5.1 Model Parameters

For the simulation of the dilute gas the parameter choice is easier than for the molecular clouds. For those finding the parameters that are consistent with observations was an intricate process due to the fact that we had to take special care to provide the correct temperature. This certainly does not pose a problem for the diffuse interstellar gas (DIG – also known as the warm interstellar medium (WIM)) due to the fact that here the energy equations is actually integrated, too. We have, however, to be careful to choose an initial condition from which the medium can evolve into a state possibly realised in nature. The hope that the initial state will independently evolve to a physically correct state is ruined, unfortunately, by the periodic boundary conditions. Due to these it is, e.g., not possible for high pressure regions to push anything out of the numerical domain – that is, we also have to deal with exactly the same number of particles in this region. Therefore, the average pressure is just determined by the temperature.

This temperature will, at least on average, not exceed the value 10^4 K due to the strongly increasing line cooling efficiency above this temperature (for this see Fig. 2.1). Thus, if we choose the initial density so low that the pressure even at an average temperature of 10^4 K is still below the value observed for the ISM, we can not expect to find simulation results, which are possibly realised in nature. The initial density has, therefore, to be at least of the value observed for the diffuse ISM. Due to the inclusion of the cooling function we will eventually end up with a dynamic equilibrium of a two-phase medium inherent in the cooling function. The initially homogeneous medium will be compressed into a dense, cold phase with a warm phase filling the space in between. The space filling factors of these phases will most probably depend on the initial density, with a lower density leading to a dominance of the warm phase, which we are essentially looking for.

By several numerical tests we arrived at a suitable initial density of $n_0 = 5 \cdot 10^5$ m^{-3}, yielding physically reasonable results for the pressure distribution. Keeping in mind that the typical density of the warm HI gas is about 10^5 m^{-3}, this allows for a fragmentation into a warm HI phase and additionally in a cold phase. The temperature in contrast to the density can be set to an arbitrary initial value, here we choose $T_0 = 1000$ K. With a side length of the cube of 40 pc we then find an energy input rate of $S_{e0} = 1.6 \cdot 10^{-29}$ J m^{-3} s^{-1}, when we introduce the same normalised driving as for the molecular clouds. This rate was deliberately chosen to be moderately lower than the rate used for the molecular cloud simulations, because for those we estimated the energy input into the turbulence to be higher than for the DIG due to the immediate presence of the sources of kinetic energy.

With the above numbers we find a value for the isothermal speed of sound of $c_s \simeq 2.9 \cdot 10^3$ m s^{-1}. Moreover, the initial pressure is, due to our choice for the velocity, lower than the pressure observed in the ISM and, thus, also lower than the value used for the molecular cloud simulations. Therefore, we have to use a lower plasma β for the DIG simulations to obtain the observed strength of the magnetic field. With the above parameters the initial magnetic induction has to be set such as to yield a value of $\beta \simeq 0.03$.

Due to the fact that the pressure for the fully developed turbulence will be much higher than the initial one and also that the initial magnetic field is much stronger than for the molecular cloud simulations, we expect a very different turbulence for this medium. With the *normalised* sound and Alfvén speeds, respectively, being much higher than for the molecular cloud simulations we will obtain a rather low Mach number turbulence. Therefore, the medium will be much less compressive than the molecular cloud medium, what is exactly what is observed in nature.

This, unfortunately, results in a much grater numerical costs than for the molecular cloud simulations, due to the fact that the time scales of the turbulent fluctuations will be longer in relation to those of wave propagation as compared to the case of the molecular clouds. This can be understood as follows: it can be expected that the normalised kinetic energy content of the numerical domain will be very similar to that for the molecular cloud simulations. The Alfvén speed as well as the speed of sound, however, are on average much higher than the corresponding normalised values for molecular clouds. Therefore, the related time scales will be shorter for the DIG. The resulting numerical costs are indeed

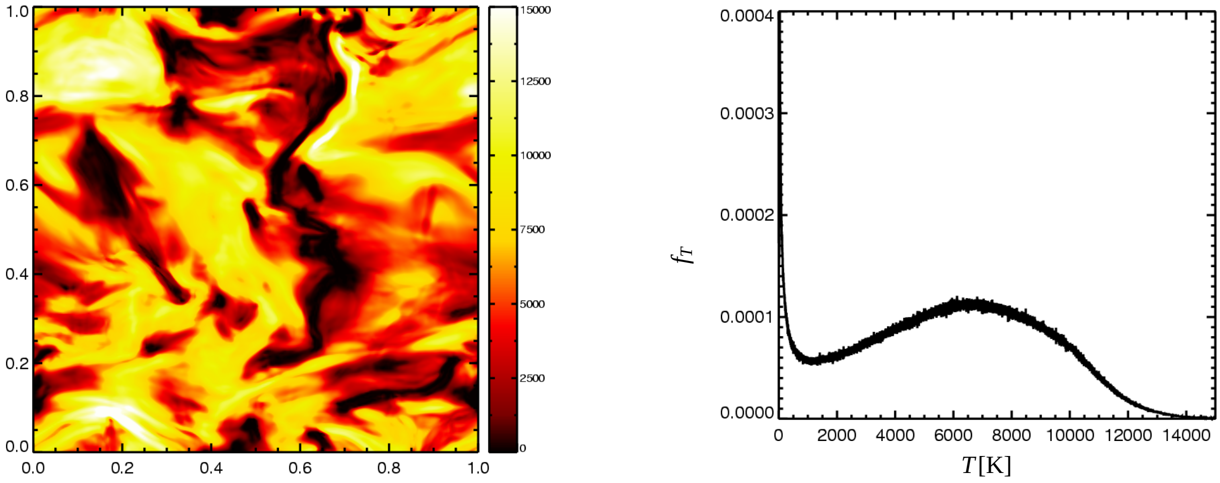

Fig. 5.1: On the left we show the temperature of the plasma in a cut through the computational domain. The temperature is given in Kelvins according to the color-coding. On the right we show the temperature distribution for the whole computational domain.

so high as to render it impossible for now to use a spatial resolution in excess of 256 grid cells. The simulations presented in this chapter have to be regarded as a first test for this model, with higher resolved simulations to be performed in the future. Here we will be especially interested in the spatial aspects of the simulations to find out if the model is consistent with measurements of the actual ISM.

The simulations were run up to the normalised time $t = 0.5$, which corresponds to an absolute time of nearly seven million years. When using the normalised fluctuation energy content of the numerical domain of $E_{fluct} \simeq 28$ at this time together with the known energy dissipation rate of $\varepsilon = 330$ we find for the large-eddy turnover time from Eq. (2.73) a value of $\tau \simeq 0.057$. From the average velocity $\bar{u} = 6.35$ we find additionally for the dynamical time a value of: $\tau_D = 0.052$. These time scales are in good agreement, although the former was introduced for incompressible turbulence. Obviously the simulations were run more than eight times longer than τ or τ_D. Even taking an initialisation phase with a duration of about $\Delta t = 0.1$ into account the fully developed turbulence was still evolved for several of these time scales.

5.2 The Temperature of the DIG

The resulting temperature for the warm phase of the diffuse interstellar gas is of special interest due to the ongoing discussion about the heating processes for this phase of the ISM. As is illustrated in Reynolds (1995) and Reynolds et al. (1999) the heating process for the dilute ionised gas known as the *diffuse interstellar gas* or the *warm ionised medium* is not entirely clear yet. One of the main problems is that the degree of ionisation is much higher than what can classically be expected at these temperatures. A possible solution of this problem was suggested in Minter and Spangler (1997) and was extended by Spanier and Schlickeiser (2005). The authors suggest the decay of interstellar plasma turbulence in the form of MHD waves as the main heating source for this environment. In their publication they compute the heating rates resulting from different wave dissipation processes and compare those to the cooling rate of the DIG. The conclusion of their work is that the dissipation of turbulence is a possible agent for the heating of the DIG resulting in temperatures compatible to the observations.

The main shortcoming of the theoretical model by Minter and Spangler is the fact that they had to use an analytical model for the turbulence spectrum. Therefore, the dissipation of the turbulence and the replenishing of the fluctuation energy in the energy range do not happen self-consistently. This could easily lead to incorrect results for the actual heating rate, for the case that there is too much energy in the model for the dissipation range. Therefore, we decided to undertake an investigation of this matter using our newly developed self-consistent MHD model. As before, fluctuation energy is injected at the largest spatial scales to be dissipated in shocks, current sheets and vortex tubes. Apart from that we do not have to impose any model on the turbulence itself – Minter and Spangler had to use different kinds of MHD waves to describe the turbulence. While it is certainly possible that the essentially incompressible fluctuations in the inertial range actually can be represented as Alfvén waves, this is not proven. The fluctuations might as well be eddies like in the classical Kolmogorov picture.

Nonetheless, the results presented have to be seen as a preliminary test for the study of the heating of the DIG. Here we used the well-documented cooling function for the warm HI gas, with a fixed degree of ionisation of 0.1, whereas major parts of the DIG have rather to be regarded as warm HII. There is, as yet however, no analytical model available for the cooling of the warm HII with a varying degree of ionisation. This is a problem, especially when keeping in mind that a cooling function for HII can not be applied to low temperatures. Therefore, one has generally to use an analytical model for the dependence of the degree of ionisation on the density and the temperature. This has to be coupled to a cooling function depending on the degree of ionisation as is at least partly realised for the cooling function introduced in section 2.7.2. Remembering that one of the main problems is the unexpectedly high degree of ionisation, we feel that this also has to be taken into account by the next generation simulations. The best choice would be the use of a multi-fluid model where ionisation and recombination are included, but such a model is not available yet for a medium possibly dominated by shocks.So far there is only the DENISIS code introduced in Schröer et al. (1998) available for this purpose, which, unfortunately is not based on a shock-capturing scheme. The results presented here can be viewed as a first hint on the possibility to heat the ISM mainly via the decay of turbulent fluctuations.

The resulting spatial temperature distribution is visualised in Fig. 5.1. The computed ISM is dominated by a warm phase with temperatures of several thousand Kelvins. Regions containing this warm gas are separated by cool clouds with temperatures below 2000 K. These can be identified as the typical molecular cloud structures. Thus, we have reproduced what is commonly known from observations – cool clouds embedded within a warm inter-cloud medium.

To be sure we identified these phases correctly, we show the temperature distribution for the whole computational domain in Fig. 5.1. Obviously there are two phases present - one cool phase with temperatures below 1000 K and a warm phase with temperatures up to 14000 K. This is the temperature range for the DIG found from observations. Especially for temperatures above 10^4 K also the cooling function used in this work assumes the medium to be fully ionised. Therefore, we confirm the result that decaying turbulence can indeed heat the inter-cloud medium to sufficiently high temperatures – even if it is highly ionised. To be sure, however, we have to get a more complete picture and look into the other variables like, e.g., the density as well.

5.3 The Spatial Structure of the DIG

If we indeed have a phase structure as it can be found in nature one would expect the coolest regions to be much denser than the hot regions. This is actually the case in our numerical model for the DIG. The density structure is visualised in Fig. 5.2. There we show the same cut through the computational domain as was used for the Fig. 5.1. Apparently the regions of highest density correspond to the coolest regions in Fig. 5.1 and vice versa.

These, however, cool often to such low temperatures that they do not remain in thermal pressure equilibrium. This can be seen from the pressure drops in some of the density enhancements in the pressure distribution depicted in Fig. 5.2. From this it is also obvious that we are not dealing with an ISM in thermal equilibrium, we rather observe a dynamical equilibrium. The assumption of a thermal equilibrium is, however, used quite often in models at least for the more quiet phases of the ISM. It is especially the WIM, which is thought to be quiet in this respect. Our results show that the assumption of thermal equilibrium should rather be substituted for one using a dynamic pressure equilibrium.

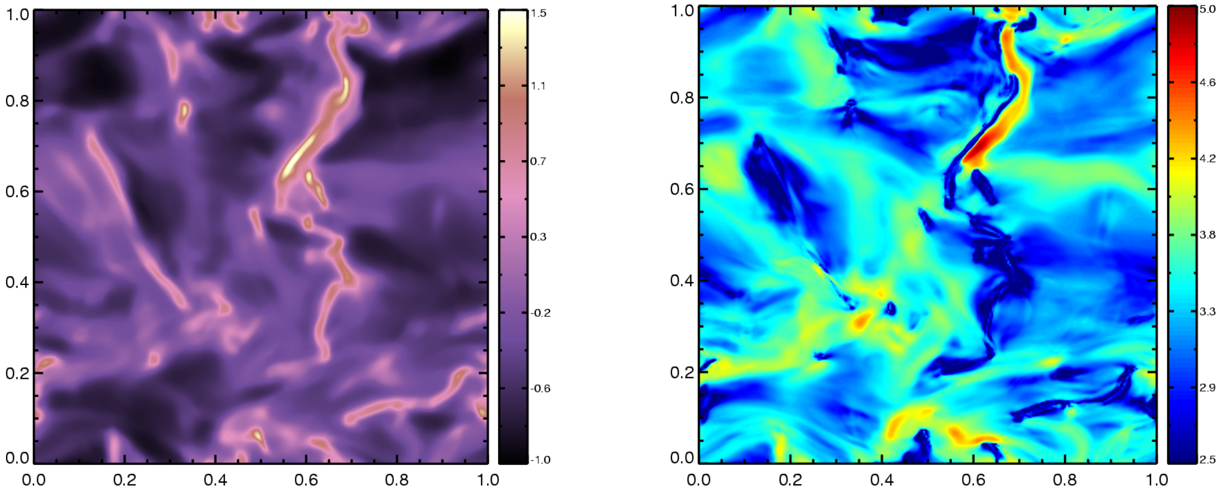

Fig. 5.2: Density (left) and thermal pressure (right) distribution in a cut of the computational domain. While the density is shown in linear normalised units we used a logarithmic scaling for the pressure.

Fig. 5.2 also illustrates the clear difference to the high Mach number turbulence found in molecular clouds. Here we find an average sound Mach number of $M_S \simeq 1.7$ and an Alfvén Mach number hardly in excess of $M_A = 0.5$ – again with the possibility of locally much higher values. While there are a lot of density enhancements visible in the density distribution, these are less frequent. The density structure is generally much smoother than in molecular clouds. Nonetheless, shocks are still present in the dilute gas, even though these essentially represent the cool phase dividing the regions of the quiet warm plasma. As will be seen in the next section this fact also has implications for the interpretation of observations of the magnetic field.

5.4 Faraday Effect

In the discussion concerning molecular clouds we already introduced the rotation measure resulting from the Faraday effect. This observable measure for the magnetic induction will now also be discussed for the case of the WIM. Naturally both the dispersion and the rotation measure are much lower for the same length to be traversed due to the lower mass density in warm ISM. Due to the higher strength of the magnetic field in relation to the turbulent fluctuations in this case the former can be expected to be more coherent than in the case of molecular clouds. This might also have some impact on the rotation measure.

The rotation measure for different directions in the numerical domain is given in Fig. 5.3. Here we compare the results for directions along and perpendicular to the initial magnetic field. The direction of the initial magnetic field can readily be recognised on the left of Fig. 5.3: whereas the rotation measure for a perpendicular direction is near zero on average, this average is different for the direction along the initial magnetic field due to the low plasma β. This shows that the magnetic field still coherently points in the initial direction. Due to this fact the rotation measure is also much higher than for a direction perpendicular to the field, thus leading to a stronger Faraday rotation everywhere. There is, in particular, no unperturbed polarisation vector for the direction along the magnetic field in contrast to the perpendicular direction. As for the molecular clouds, there are large regions, where the resulting polarisation is the same as the initial one.

Apart from that the basic structure of the rotation measure is almost the same for both directions. As for the molecular cloud simulations there are large regions of homogeneous rotation measure with quite sharp transitions from one region to the other. For the direction along the initial magnetic field the rotation measure appears to be a little bit more distorted. Furthermore, the polarisation vectors indicated

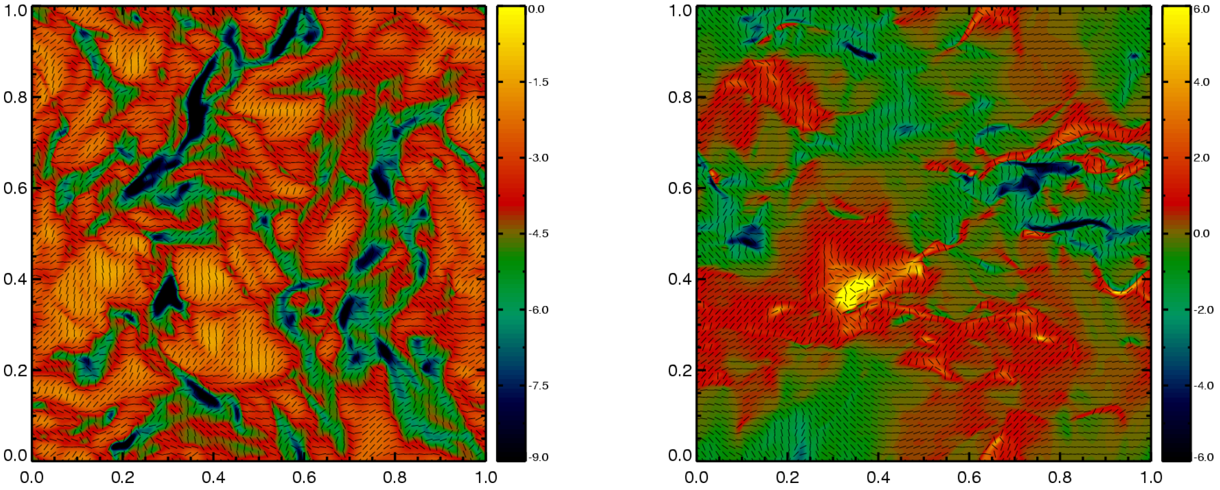

Fig. 5.3: Rotation measure given in units of rad m^{-2} together with the local polarisation of a homogeneously polarised background for a wavelength of $\lambda = 1$ m. On the left results are shown for the direction of the initially homogeneous magnetic field, whereas on the right results are given for a perpendicular direction.

in Fig. 5.3 show that the polarisation of a homogeneous background radiation is more disturbed for the direction along the initial magnetic field. This will become more evident by the following discussion of the polarisation canals.

Polarisation Canals

In radio maps there was found another interesting phenomenon – elongated structures with very little polarised intensity with a width near that of the telescope beam – being usually referred to as canals (see e.g. Fletcher and Shukurov 2006a), which are directly connected to the rotation measure. These canals are visible in observations of the polarised intensity, as is visible at the example observations depicted in Fig. 5.4. Physically they are thought to result at least partially from the finite resolution of the corresponding radio observations. Whenever the polarisation of the detected radiation changes over an area on the sky smaller than the beam of the telescope, these polarisation canals can occur. If the polarisation angles inside the beam are a mixture such that they cancel each other, the polarised intensity drops to zero in these regions. Whenever the rotation measure is homogeneous in large regions with extended gradients between these regions it is just at these boundaries that the polarisation canals can occur.

Presently there are two theories available for the formation of the canals (see Fletcher and Shukurov 2006b). One attributes the canals only to the above idea. This idea uses a foreground Faraday screen to account for these structures, i.e., it is assumed that the radiation is produced in a region behind a foreground medium, in which it is subject to Faraday rotation. Strong gradients in this foreground Faraday screen result also in strong gradients in the Faraday rotation for the background radiation. This then leads to the observed canals for a finite width of the telescope beam. The other model rather relies on line-of-sight effects. There it is assumed that the Faraday rotation and the actual emission of the radiation occur in the same region. In this case, with the radiation being emitted everywhere along the line-of-sight, even the radiation received at a single point will comprise a mixture of different polarisation angles. This process is also known as differential Faraday rotation. Therefore, depolarisation – that is mutual cancelling of the differently polarised radiation – can even occur for an infinitely small telescope beam.

Here we will only investigate depolarisation due to a foreground Faraday screen. Although the neglect of synchrotron radiation inside the medium itself is rather unphysical, it allows us to concentrate our study on the Faraday rotation caused by the medium itself as already presented in Fig. 5.3. Here we do not want to care about trying to disentangle the effects of emission and Faraday rotation. In the case

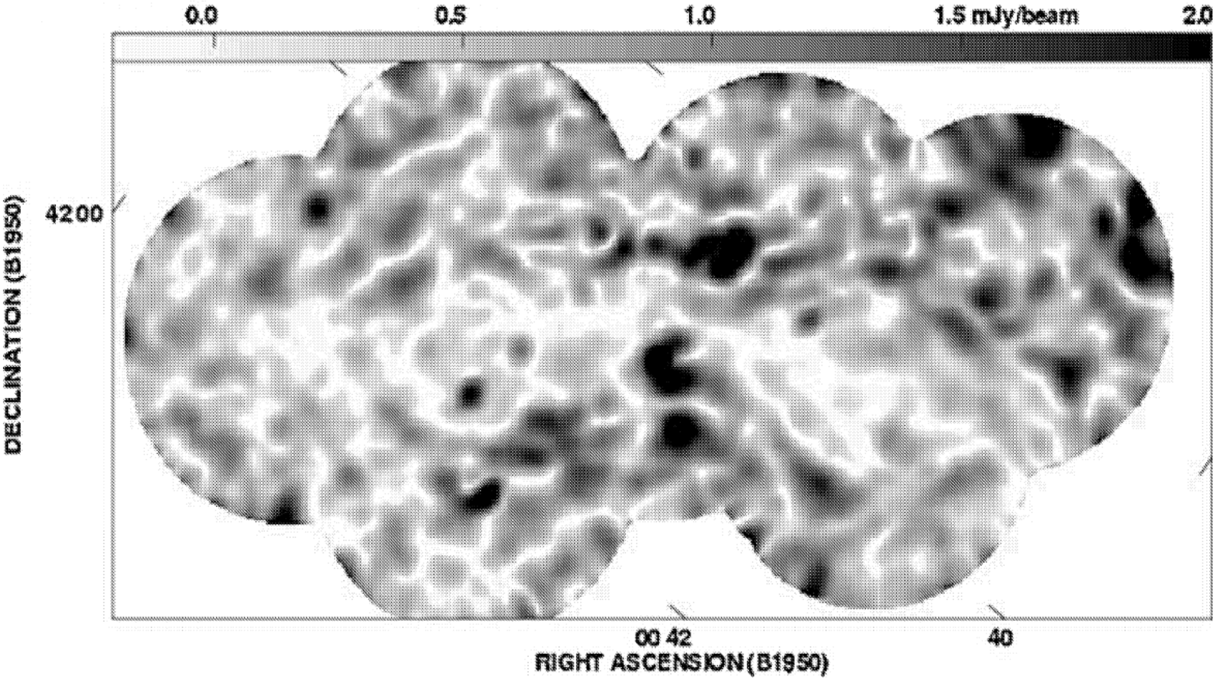

Fig. 5.4: Polarised intensity map for the field of the galaxy M31 taken at a wavelength of 0.205 m. The image is taken from Shukurov and Berkhuijsen (2003).

of a foreground Faraday screen the pattern of the observed canals strongly depends on the resolution of the telescope and also on the wavelength of the observed radiation. For the latter a too short wavelength means that the foreground Faraday rotation is too ineffective as to produce different polarisation angles. A too long wavelength in contrast to that causes complete depolarisation – even a slight difference in the rotation measure causes a huge difference in polarisation, so that the polarisation vectors become randomly distributed.

For the actual computation of the corresponding maps we use a similar procedure as introduced in Haverkorn and Heitsch (2004). From the rotation measure for the corresponding direction we first compute the local polarisation angle using Eq. (4.6) as it was also done for the production of Fig. 5.3. From the local polarisation angle $\delta\theta$ we then compute the stokes parameters Q and U, which are given as:

$$Q = \cos(2\delta\theta), \qquad U = \sin(2\delta\theta) \tag{5.1}$$

The maps of these parameters are smoothed using a Gaussian beam with a width of 2.5 grid cells, to mimic the limited telescope resolution. Finally we compute the resulting intensity according to:

$$I = \sqrt{Q^2 + U^2} \tag{5.2}$$

Be aware that the results shown here were computed for a medium in a box of a length of only 40 parsecs. Unlike Haverkorn and Heitsch we did not stack several of the simulation boxes atop of each other in the direction under consideration with a shift in a perpendicular direction. Here we rather intend to use a corresponding wavelength that yields canals in the polarised intensity. Whereas the wavelengths used might not correspond to those used for actual observations, an artificial extension of the numerical domain would just yield similar results for a shorter wavelength. We, however do not feel confident stacking shifted boxes atop of each other. This is because the shifts of the individual boxes against each other will lead to unphysical gradients at their intersections.

This polarised intensity found for our simulations is depicted in Fig. 5.5 for the same directions as they were used for Fig. 5.3. Here we compare the results for the effect of the foreground Faraday

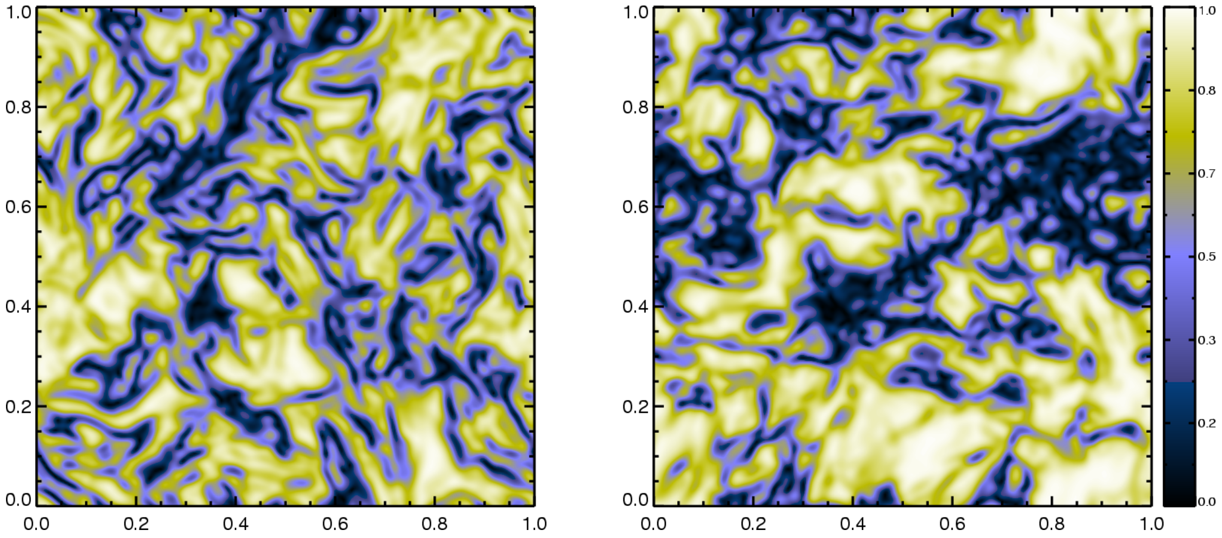

Fig. 5.5: Normalised polarised intensity computed assuming homogeneously polarised background radiation. The resulting intensity is computed with the plasma in the simulations being used as a foreground Faraday screen. The line-of-sight used on the left corresponds to the initial magnetic field direction, whereas on the right we show results for a direction perpendicular to this. On the left we show results for a wavelength, λ, of 1 m, whereas on the right it is chosen as $\lambda = 1.5$ m.

screen for a line-of-sight along the initial magnetic field direction and a direction perpendicular to this. For both cases we show the resulting intensity for a wavelength best suited to visualise the polarisation canals. Interestingly we had to choose different wavelengths for the two cases. Obviously the gradients of the rotation measure in the direction of the initial magnetic field are stronger than the ones in the perpendicular direction. Therefore, the wavelength for this case had to be chosen a little shorter than for the other one.

Nonetheless we can identify polarisation canals in both images, which have about the same width as the Gaussian telescope beam. Therefore, it is possible to explain the depolarisation canals visible in radio observations by a foreground Faraday screen. One has, however, to be careful with this statement. Here we found that these canals only become apparent in a very limited range of wavelengths. For actual observations it is highly improbable to observe just the appropriate wavelength range. Nonetheless, we see an encouraging similarity when we compare our results to the observations shown in Fig. 5.4.

Our results also look quite similar to those obtained by Haverkorn and Heitsch (2004). In contrast to their approach we used a physically correct representation of the warm phase of the ISM. Especially the Mach number chosen here is far more appropriate for the dilute plasma than the one used by Haverkorn and Heitsch. The authors' statement that the turbulence cascade is very similar for the high Mach number and the low Mach number regime has to be considered with caution. One important point is that the spatial density structure has a huge influence on the rotation measure as will become clear in the discussion on the average magnetic field. As was discussed in Kim and Ryu (2005) and as it was also seen in the previous section, the density structure is very different for different Mach numbers. Therefore, one has to be very careful when using high Mach number simulations for the dilute ISM.

This statement is supported by what is depicted in Fig. 5.6. There we compare the magnetic induction as it is inferred from the rotation and the dispersion measure with the average magnetic induction along the same direction. Clearly the estimate does not correspond at all to the actual values - this shows the strong difference between the mass-weighted and the unweighted average. What is additionally apparent in Fig. 5.6 is that the absolute value of the magnetic induction is generally overestimated as compared to the actual line-of-sight integral. This qualitative impression is confirmed by a quantitative analysis – on average the magnitude of the magnetic induction turns out to be overestimated by a factor of about

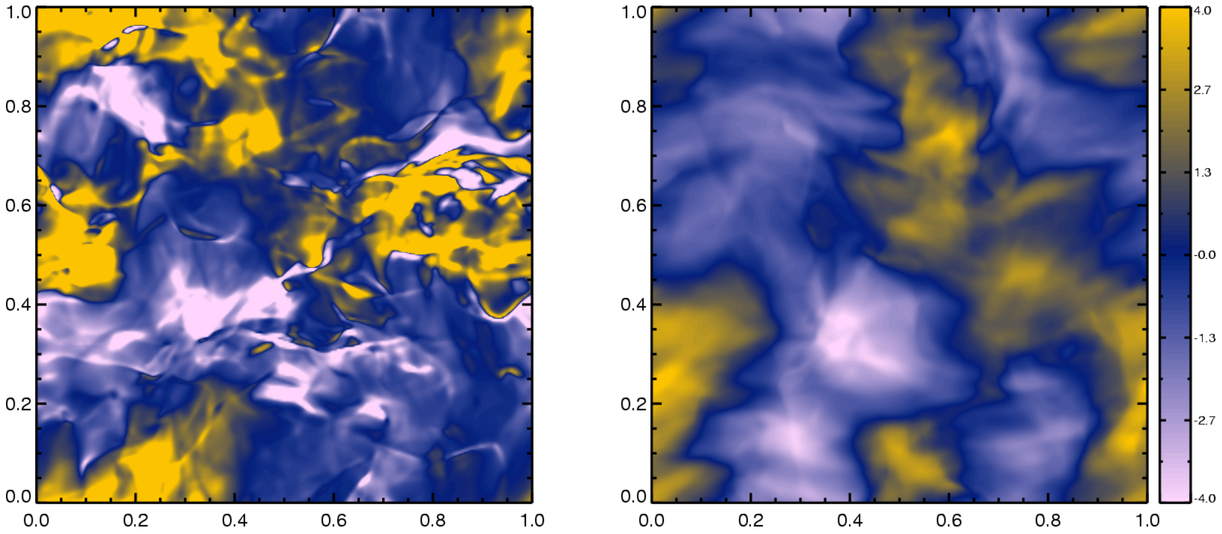

Fig. 5.6: Comparison of the density weighted average for the normalised parallel magnetic induction (left) to the actual line-of-sight integral (right).

1.5. This has to be taken into account, whenever an interpretation of any observations is desired. For a completely homogeneous medium the rotation measure directly yields the average magnetic induction. Obviously, the Mach number for the dilute phase of the ISM is still high enough to yield this strong discrepancy between the actual and the inferred magnetic field.

This result is another hint that one has to be careful to use the appropriate Mach numbers for the simulations of all the ISM phases. It also applies to the computation of the polarisation canals. Due to the fact that the rotation measure seem to depend strongly on the Mach number, one has to take care to use the appropriate simulations for the polarisation canals. It would be interesting to see how the deviation of the estimated magnetic field strength and also the structure of the canals depend on the average Mach number of the medium. This, again, is left as a task for the future.

5.5 Statistics

For the warm ISM we will briefly discuss the statistics of the turbulence. Due to the still quite low spatial resolution a discussion of the structure functions is not appropriate. Only for the lowest order structure function we can expect acceptable statistics - therefore, we will be content with a discussion of the spectrum. With the observations by Armstrong et al. (1995) and Deshpande et al. (2000) it is especially interesting to investigate the density fluctuation spectrum. With the simultaneous presence of a warm and a cool medium in the simulation box it can, unfortunately, be expected that the resulting density fluctuation spectrum will not correspond to any of those presented in the above publications. For this we have to remember that Armstrong et al. (1995) concentrate on the statistics of the WIM, whereas the spectrum shown in Deshpande et al. (2000) rather applies to molecular clouds.

In Fig. 5.7 we show the resulting density power spectrum on the left and the velocity power spectra on the right. The density fluctuation spectra are even flatter than the one for the molecular cloud simulations. At first it also seems to contradict the simulation results presented in Kim and Ryu (2005), where the low Mach number simulations yield a quite steep spectrum. These, however, are simulation results for hydrodynamical turbulence. When regarding the results presented in Padoan et al. (2004) instead our results are in accord with what is presented there. The authors find the density fluctuation spectrum to be nearly flat for a near equipartition of kinetic and magnetic pressures. With this being also the case in our simulations, we are confident to have found a suitable physical model for the description of the warm ISM.

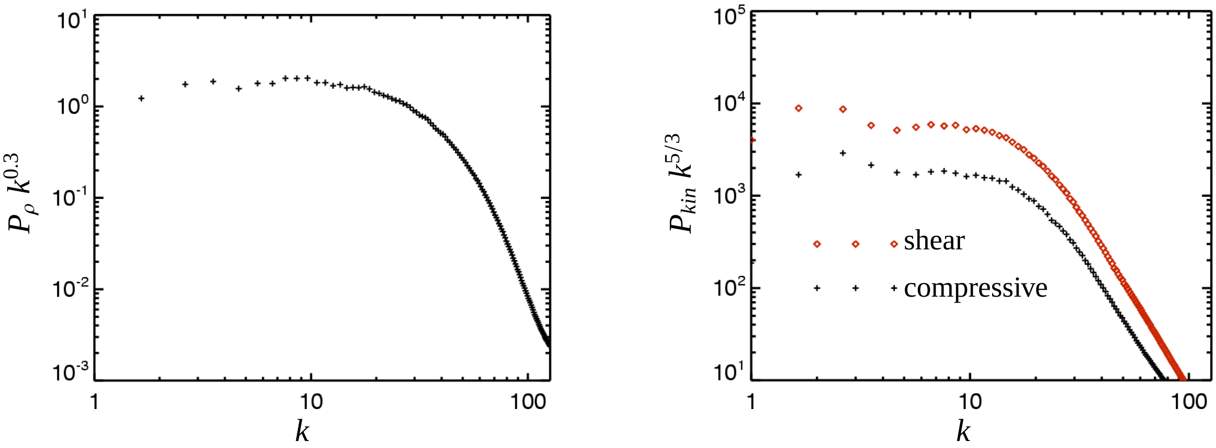

Fig. 5.7: Density (left) and velocity (power) spectrum for the simulations of the warm ISM. The latter is subdivided into the solenoidal and the compressible part. All spectra are given in normalised units.

Moreover, the results for the velocity spectrum depicted in Fig. 5.7 are in good agreement with the known turbulence models. The spectral slope for the compressive as well as the solenoidal part of the spectrum is very near to $5/3$ as is expected for compressible turbulence. As for the molecular cloud simulations the major part of the fluctuation energy is stored in incompressible modes; merely for the dissipation range compressibility starts to get more important.

5.6 Conclusions

In this chapter we presented the first results of our turbulence simulations for the warm phase of the ISM. We demonstrated that the model is appropriate for simulations of this phase. We found a density structure, which shows this phase to be much less compressive than the molecular cloud medium. Furthermore, the observed temperatures are in the range known for the WIM. The warm gas surrounds in these simulations dense filaments of a cold gas, which corresponds to the typical molecular cloud parameters. This two-phase medium was found, however, not to be in thermal pressure equilibrium. The ISM obviously has to be regarded as a very dynamic medium.

We also discussed the rotation measure obtained from the numerical simulations, where we could identify canals also seen in polarised intensity maps of the ISM found from radio observations. In this context we showed that it is important to use the correct Mach number in the simulations. Even for quite low Mach numbers for the WIM there is obviously a significant deviation of the estimate of the magnetic field inferred from the observation of the rotation measure as compared to the actual magnetic field.

Finally, we briefly discussed the turbulence statistics for these simulations. Although, due to the high computational costs, we could, so far, perform the simulations only with a spatial resolution of 256 cells in each spatial direction, the statistics looks quite good. The density power spectrum as well as the one for the velocity seem to be in good agreement either with theoretical models or with results from other, better resolved numerical simulations. Therefore, we can conclude that the model is also well suited for the simulation of the warm ISM.

Summary and Prospects

In this work we introduced basic turbulence theory into the framework of the interstellar medium. In many cases turbulence simulations are applied to the interstellar medium (ISM) merely because it is a medium, where extremely high Reynolds numbers are actually realised, and the parameters of the ISM are only taken into account as far as they are needed for the turbulence research. Here, however, we investigated the basic turbulence properties, while at the same time we modelled the properties of the ISM as thoroughly as possible. The important point is that there are many physical processes going on in the ISM, which should be incorporated in the corresponding simulations. These processes reach from external influences of the radiation field originating from hot stars to the internal interaction of the particles culminating in the intricate chemistry of the molecular cloud medium. Each of the different phases of the ISM has its own dominant processes to be taken into account for a realistic modelling. A suitable example to illustrate the problem can be seen in the rich variety of molecular clouds. It is not possible to investigate the *typical* molecular cloud medium, because there is no such thing. There is rather a variety of different plasma states present in all the giant molecular cloud complexes. This reaches from rather dilute atomic gas, surrounding the denser parts of a cloud, which is still fully exposed to the interstellar radiation field, to dense cores, where self-gravity is very important.

Therefore, we carefully took into account for each of the turbulence simulations, which medium we were investigating. Apart from that, we also tried to describe the physical processes of the plasma state under consideration as accurately as possible. For this we developed an intricate numerical solver that, beyond the necessity to describe the corresponding physics of the plasma in a closed, self-consistent form, had to meet several very fundamental requirements.

First of all turbulence simulations require a very high spatial resolution to allow for a reasonable study of the corresponding fluctuation spectra. This could only be achieved by a highly parallel numerical solver. Such a solver was developed especially for this purpose. The base scheme used in this numerical solver has to fulfil further requirements. Taking into account that in most phases of the ISM the energy content of the bulk motion exceeds the thermal one and sometimes even the magnetic energy, the occurrence of shock waves becomes likely. Therefore, the base scheme must be able to describe such discontinuities correctly without introducing spurious oscillations. This is particularly important in a highly turbulent medium where such artificial oscillations can hardly be distinguished from the turbulence itself. With a suite of numerical tests we not only established this characteristic of the base scheme, but also showed that it is independent of the propagation direction with respect to the coordinate axes. With a test used to verify the order of the numerical scheme we demonstrated that also this is independent of the propagation direction. This fact is especially important when considering that we found this property to be lacking in a higher order version of the scheme. Only with a scheme yielding the same order regardless of the propagation direction will homogeneous turbulence really be homogeneous.

In addition, the fact that we are dealing with a plasma complicates the correct description of the magnetic field. One important aspect for this is the necessity to keep the magnetic field solenoidal at all times. In this work we implemented and tested each of the basic available schemes to preserve the initial solenoidality of the field. We were able to show that only one of these methods, namely the constrained transport form of the numerical scheme, can produce satisfactory results for the purpose of ISM turbulence simulations. The others either failed to remove the unphysical magnetic monopoles or yielded unphysical results with regard to the turbulence spectra.

From the physical point of view, we also made sure to use the correct description for the interstellar plasma environment. For this we developed a two-fluid model for the molecular cloud medium. With the low degree of ionisation of the medium we felt the need to check whether it is necessary to describe the neutral and the charged particles individually and compared the results of the coupled set of evolution equations to the results obtained when using the MHD equations. By this we were able to show that a two-fluid description is not necessary for the phase of the molecular clouds investigated in this work and, thus, we applied the MHD equations to the modelling of molecular clouds. With this we performed a comparison of an isothermal molecular cloud medium to one where we used an adiabatic equation of state for the closure of the system of evolution equations. The conclusion that there is nearly no change in the turbulence statistics for the magnetic field and the velocity fluctuations nicely confirms recent models on compressible turbulence. For turbulence it does not seem to be important, how the dissipative shock structures actually look like. The statistics is rather determined by their dimensionality, which is the same for both equations of state.

For the more dilute ISM we also considered heating and cooling of the plasma. This phase was so far not in the focus of numerical turbulence research. Reasons for this apparent lack of interest are most probably connected to the fact that this phase can numerically be described only at very high computational costs and that appropriate heating and cooling functions have to be taken into account. The latter of those pose a problem in that they can not be given in a closed analytical form. The major drawback is that the degree of ionisation can not easily be included self-consistently in a numerical model. Here we investigated the evolution of the diffuse ISM by means of a combination of the MHD equations with an estimate of the corresponding cooling function for a fixed degree of ionisation. Due to the high computational costs we were not yet able to investigate the full statistics of the turbulence. Nonetheless, we could show the applicability of the model to the dilute ISM. Not only did we find a phase structure as it is known from observations, but we could in our simulation results even identify structures visible in actual radio maps. Moreover, the results for the turbulence statistics look very encouraging.

This work has to be regarded as the starting point of a thorough investigation of interstellar turbulence by means of a numerical model tuned to the description of the interstellar medium. With the models and methods in this work we will be able to perform complex simulations for the different phases of the ISM to investigate the turbulence statistics for these.

With this model at our disposal, a task for the future is to obtain a highly resolved simulation for the warm phase of the ISM in order to be able to perform a thorough investigation of the turbulence in this phase. This is of particular interest for theories on the propagation of energetic particles in the Galaxy, because this warm phase represents about half of the interstellar matter in our Galaxy. Nonetheless, we feel the need to further improve the physical model of the ISM. For this, the necessity to describe the dilute ISM by a multi-fluid model has to be checked. Most probably the inter-species collisions will not be sufficiently strong to couple the neutral and the charged particle fluid in a manner found for the molecular clouds. It is, however, possible that ionisation and recombination processes will facilitate a strong coupling of the different species. Apart from this we also see the need to find the correct cooling function for the highly ionised warm ISM.

Luckily, the classical cooling function is known in a closed analytical form for the colder phases of the ISM. Therefore, it is easily possible to apply the numerical model used to describe the dilute ISM also for the molecular cloud turbulence. We would like to supplement the study for these regions of the ISM by a simulation using the full evolution of the energy equation, thus, allowing for heating at shock waves in this regions. It will be very interesting to see if the plasma will actually be nearly isothermal due to the very high efficiency of the cooling in these dense regions. Finally there is still the possibility to improve the basic numerical scheme in a way better suited for high Mach number turbulence. This was already achieved for one-dimensional problems, but a multi-dimensional extension of this scheme needs further work. So, there exist a number of improvements and applications to which this work can be used as a starting point.

Appendix A

Derivation of the Single Species Pressure Equation

Each equation of the hierarchy of fluid equations is obtained from the corresponding moment of the Boltzmann equation. The resulting equation for the variable Q then reads:

$$\frac{\partial}{\partial t}(n_\alpha \langle Q\rangle_\alpha) - n_\alpha \left\langle \dot{Q} \right\rangle_\alpha + \nabla \cdot n_\alpha \langle Q\mathbf{v}\rangle_\alpha - n_\alpha \langle(\mathbf{v}\cdot\nabla)Q\rangle_\alpha - n_\alpha \langle(\boldsymbol{a}\cdot\nabla_{\mathbf{v}})Q\rangle_\alpha = \int_v Q\left(\frac{\delta f_\alpha(\boldsymbol{r},\mathbf{v})}{\delta t}\right)_{coll} d^3\mathrm{v} \quad \text{(A.1)}$$

Here we are interested in the derivation of the eqvolution equation for the pressure for the fluid species α. For this Q has to be chosen as:

$$Q = \frac{1}{2} m_\alpha (\mathbf{v} - \boldsymbol{u}_\alpha)\cdot(\mathbf{v} - \boldsymbol{u}_\alpha) \tag{A.2}$$

With this in mind we can discuss all the resulting terms of equation (A.1). The first of these becomes:

$$\frac{\partial}{\partial t}(n_\alpha \langle Q\rangle_\alpha) = \frac{\partial}{\partial t}\left(\frac{1}{2}\rho_\alpha \langle(\mathbf{v} - \boldsymbol{u}_\alpha)\cdot(\mathbf{v} - \boldsymbol{u}_\alpha)\rangle\right) = \frac{1}{\gamma - 1}\frac{\partial p_\alpha}{\partial t} \tag{A.3}$$

where we used the definition for the scalar pressure: $p_\alpha = \rho_\alpha \left\langle |\mathbf{v} - \boldsymbol{u}_\alpha|^2 \right\rangle$. The second term vanished, since t and $\mathbf{v}$ are independent variables. The third term, however, can also be transformed:

$$\begin{aligned}
\nabla \cdot n_\alpha \langle Q\mathbf{v}\rangle_\alpha &= \frac{1}{2}\nabla\cdot\rho_\alpha \langle(\mathbf{v} - \boldsymbol{u}_\alpha)\cdot(\mathbf{v} - \boldsymbol{u}_\alpha)\mathbf{v}\rangle \\
&= \frac{1}{2}\nabla\cdot\rho_\alpha \langle(\mathbf{v} - \boldsymbol{u}_\alpha)\cdot(\mathbf{v} - \boldsymbol{u}_\alpha)(\mathbf{v} - \boldsymbol{u}_\alpha)\rangle + \frac{1}{2}\nabla\cdot\rho_\alpha \langle(\mathbf{v} - \boldsymbol{u}_\alpha)\cdot(\mathbf{v} - \boldsymbol{u}_\alpha)\boldsymbol{u}_\alpha\rangle \\
&= \frac{1}{2}\nabla\cdot\rho_\alpha \left\langle |\mathbf{v} - \boldsymbol{u}_\alpha|^2(\mathbf{v} - \boldsymbol{u}_\alpha)\right\rangle + \frac{1}{2}\nabla\cdot\rho_\alpha\boldsymbol{u}_\alpha \left\langle |\mathbf{v} - \boldsymbol{u}_\alpha|^2\right\rangle \\
&= \nabla\cdot\boldsymbol{q}_\alpha + \frac{1}{\gamma - 1}\nabla\cdot p_\alpha\boldsymbol{u}_\alpha
\end{aligned} \tag{A.4}$$

The next term yields a tensorial contribution:

$$\begin{aligned}
n_\alpha \langle(\mathbf{v}\cdot\nabla)Q\rangle_\alpha &= \frac{1}{2}\rho_\alpha \langle(\mathbf{v}\cdot\nabla)(\mathbf{v}-\boldsymbol{u}_\alpha)\cdot(\mathbf{v}-\boldsymbol{u}_\alpha)\rangle_\alpha \\
&= \frac{1}{2}\rho_\alpha \sum_{i,j} \left\langle v_i \partial_{x_i}(v_k - u_{\alpha_k})^2 \right\rangle \\
&= \rho_\alpha \sum_{i,j} \left\langle v_i (v_k - u_{\alpha_k}) \partial_{x_i} u_{\alpha_k} \right\rangle \\
&= \rho_\alpha \sum_{i,j} \left(\left\langle (v_i - u_{\alpha_i})(v_k - u_{\alpha_k}) \partial_{x_i} u_{\alpha_k} \right\rangle + \left\langle (u_{\alpha_i})(v_k - u_{\alpha_k}) \partial_{x_i} u_{\alpha_k} \right\rangle \right) \\
&= \rho_\alpha \sum_{i,j} \left(\left\langle (v_i - u_{\alpha_i})(v_k - u_{\alpha_k}) \partial_{x_i} u_{\alpha_k} \right\rangle + u_{\alpha_i} \partial_{x_i} u_{\alpha_k} \underbrace{\left\langle (v_k - u_{\alpha_k}) \right\rangle}_{=0} \right) \\
&= (\mathsf{P}_\alpha \cdot \nabla) \cdot \boldsymbol{u}_\alpha
\end{aligned} \tag{A.5}$$

Finally for a force not depending on the volocity the fifth term is identical zero:

$$m_\alpha \langle(\boldsymbol{a}\cdot\nabla_{\mathbf{v}})Q\rangle_\alpha = \langle(\boldsymbol{a}\cdot 2(\mathbf{v}-\boldsymbol{u}_\alpha))\rangle = 2\boldsymbol{a}\langle(\mathbf{v}-\boldsymbol{u}_\alpha)\rangle = 0 \tag{A.6}$$

The same result also holds for magnetic part of the Lorentz force despite the fact that this does actually depend on the velocity. This is due to the presence of the outer product in the corresponding equation:

$$\begin{aligned}
\left\langle(\boldsymbol{F}_{mag}\cdot\nabla_{\mathbf{v}})Q\right\rangle_\alpha &= 2\left\langle \boldsymbol{F}_{mag}\cdot(\mathbf{v}-\boldsymbol{u}_\alpha)\right\rangle_\alpha \\
&= 2q_\alpha \langle(\mathbf{v}\times\boldsymbol{B})\cdot(\mathbf{v}-\boldsymbol{u}_\alpha)\rangle_\alpha \\
&= 2q_\alpha \underbrace{\left\langle((\mathbf{v}-\boldsymbol{u}_\alpha)\times\boldsymbol{B})\cdot(\mathbf{v}-\boldsymbol{u}_\alpha)\right\rangle_\alpha}_{=0} + 2q_\alpha \langle(\boldsymbol{u}_\alpha\times\boldsymbol{B})\cdot(\mathbf{v}-\boldsymbol{u}_\alpha)\rangle_\alpha \\
&= 2q_\alpha(\boldsymbol{u}_\alpha\times\boldsymbol{B})\cdot\langle\mathbf{v}-\boldsymbol{u}_\alpha\rangle_\alpha = 0
\end{aligned} \tag{A.7}$$

Taking all the above we find for the final form of the single species pressure equation:

$$\frac{1}{\gamma-1}\frac{\partial p_\alpha}{\partial t} + \frac{1}{\gamma-1}\nabla\cdot p_\alpha\boldsymbol{u}_\alpha + (\mathsf{P}_\alpha\cdot\nabla)\cdot\boldsymbol{u}_\alpha + \nabla\cdot\boldsymbol{q}_\alpha = \int_v |\mathbf{v}-\boldsymbol{u}_\alpha|^2 \left(\frac{\delta f_\alpha(\boldsymbol{r},\mathbf{v})}{\delta t}\right)_{coll} d^3\mathrm{v} \tag{A.8}$$

Appendix B

Derivation of the Macroscopic Fluid Equations

In this chapter we will demonstrate the derivation for the macroscopic momentum and energy equations stemming from the sum of the corresponding individual species equations. For this derivation we only take into account one ion species, which together with the electrons forms the macroscopic fluid for the charged particles.

B.1 Momentum Balance

We start by writing the momentum balance for electrons and ions individually, where we explicitly use the electromagnetic force as the only force present in the system. For ions we have according to Eq. (2.11):

$$\frac{\partial\left(\rho_i \boldsymbol{u}_i\right)}{\partial t} + \nabla\cdot\left(\rho_i \boldsymbol{u}_i \boldsymbol{u}_i\right) + \nabla\cdot\mathsf{P}_i - e n_i\left(\boldsymbol{E} + \boldsymbol{u}_i\times\boldsymbol{B}\right) = -\nu_{ie}\rho_i(\boldsymbol{u}_i - \boldsymbol{u}_e) - \nu_{in}\rho_i(\boldsymbol{u}_i - \boldsymbol{u}_n) \tag{B.1}$$

where we included collisions with electrons and neutral particles with the respective collision frequencies $\nu_{\alpha\beta}$. This equation is transformed using the identities (2.42) and (2.43):

$$\begin{aligned}\frac{\partial\left(\rho_i \boldsymbol{u}_i\right)}{\partial t} + \nabla\cdot\left(\rho_i \boldsymbol{u}_i \boldsymbol{u}_i\right) + \nabla\cdot\mathsf{P}_i - e n\left(\boldsymbol{E} + \boldsymbol{u}\times\boldsymbol{B}\right) - \frac{m_e}{m_i + m_e}\boldsymbol{J}\times\boldsymbol{B} \\ = -\left(\nu_{ie}\frac{m_i}{e} + \nu_{in}\frac{\mu}{e}\right)\boldsymbol{J} - \nu_{in}\rho_i(\boldsymbol{u} - \boldsymbol{u}_n)\end{aligned} \tag{B.2}$$

where we introduced the reduced mass of ions and electrons as:

$$\mu = \frac{m_i m_e}{m_i + m_e} \tag{B.3}$$

For electrons an equivalent equation can be computed:

$$\begin{aligned}\frac{\partial\left(\rho_e \boldsymbol{u}_e\right)}{\partial t} + \nabla\cdot\left(\rho_e \boldsymbol{u}_e \boldsymbol{u}_e\right) + \nabla\cdot\mathsf{P}_e + e n\left(\boldsymbol{E} + \boldsymbol{u}\times\boldsymbol{B}\right) - \frac{m_i}{m_i + m_e}\boldsymbol{J}\times\boldsymbol{B} \\ = \left(\nu_{ei}\frac{m_e}{e} + \nu_{en}\frac{\mu}{e}\right)\boldsymbol{J} - \nu_{en}\rho_e(\boldsymbol{u} - \boldsymbol{u}_n)\end{aligned} \tag{B.4}$$

As in the case of the continuity equation the sum of these two equations yields the evolution equation for the momentum of the plasma fluid:

$$\begin{aligned}\frac{\partial\left(\rho \boldsymbol{u}\right)}{\partial t} + \nabla\cdot\left(\rho_i \boldsymbol{u}_i \boldsymbol{u}_i + \rho_e \boldsymbol{u}_e \boldsymbol{u}_e\right) + \nabla\cdot\left(\mathsf{P}_i + \mathsf{P}_e\right) - \boldsymbol{J}\times\boldsymbol{B} \\ = -n\left(\nu_{en} m_e + \nu_{in} m_i\right)\left(\boldsymbol{u} - \boldsymbol{u}_n\right) - \frac{\mu}{e}\left(\nu_{in} - \nu_{en}\right)\boldsymbol{J}\end{aligned} \tag{B.5}$$

where we have used:

$$\nu_{ie}\rho_i = \nu_{ei}\rho_e \qquad \text{with} \qquad n_e = n_i = n \tag{B.6}$$

which is exactly fulfilled for charge exchange or elastic collisions.

Now we have to take care of the expressions still containing variables of the individual fluids. We will start by discussing the term:

$$\mathsf{A} = \rho_i \boldsymbol{u}_i \boldsymbol{u}_i + \rho_e \boldsymbol{u}_e \boldsymbol{u}_e \tag{B.7}$$

This is transformed using the following identity (with α as usual indicating either ions or electrons):

$$\boldsymbol{u}_\alpha = \boldsymbol{u} + (\boldsymbol{u}_\alpha - \boldsymbol{u}) = \boldsymbol{u} + \delta\boldsymbol{u}_\alpha \tag{B.8}$$

where $\delta\boldsymbol{u}_\alpha$ indicates the deviation of the single species fluid velocity from the average charged particle velocity. With this relation Eq. (B.7) is transformed into:

$$\begin{aligned}
\mathsf{A} &= \rho_p((\boldsymbol{u} + \delta\boldsymbol{u}_p)(\boldsymbol{u} + \delta\boldsymbol{u}_p)) + \rho_e((\boldsymbol{u} + \delta\boldsymbol{u}_e)(\boldsymbol{u} + \delta\boldsymbol{u}_e)) \\
&= \rho_p(\boldsymbol{u}\boldsymbol{u} + \boldsymbol{u}(\boldsymbol{u}_p - \boldsymbol{u}) + (\boldsymbol{u}_p - \boldsymbol{u})\boldsymbol{u} + \delta\boldsymbol{u}_p\delta\boldsymbol{u}_p) + \rho_e(\boldsymbol{u}\boldsymbol{u} + \boldsymbol{u}(\boldsymbol{u}_e - \boldsymbol{u}) + (\boldsymbol{u}_e - \boldsymbol{u})\boldsymbol{u} + \delta\boldsymbol{u}_e\delta\boldsymbol{u}_e) \\
&= \underbrace{(\rho_p + \rho_e)}_{\rho}\boldsymbol{u}\boldsymbol{u} + \boldsymbol{u}\underbrace{(\rho_p(\boldsymbol{u}_p - \boldsymbol{u}) + \rho_e(\boldsymbol{u}_e - \boldsymbol{u}))}_{\underbrace{\rho_p\boldsymbol{u}_p + \rho_e\boldsymbol{u}_e}_{\rho\boldsymbol{u}} - \rho\boldsymbol{u} = 0} + \underbrace{(\rho_p(\boldsymbol{u}_p - \boldsymbol{u}) + \rho_e(\boldsymbol{u}_e - \boldsymbol{u}))}_{=0}\boldsymbol{u} + \rho_p\delta\boldsymbol{u}_p\delta\boldsymbol{u}_p + \rho_e\delta\boldsymbol{u}_e\delta\boldsymbol{u}_e \\
&= \rho\boldsymbol{u}\boldsymbol{u} + \rho_p\delta\boldsymbol{u}_p\delta\boldsymbol{u}_p + \rho_e\delta\boldsymbol{u}_e\delta\boldsymbol{u}_e
\end{aligned} \tag{B.9}$$

Thus, we find:

$$\begin{aligned}
\frac{\partial(\rho\boldsymbol{u})}{\partial t} + \nabla\cdot(\rho\boldsymbol{u}\boldsymbol{u}) + \nabla\cdot\left(\rho_p\delta\boldsymbol{u}_p\delta\boldsymbol{u}_p + \rho_e\delta\boldsymbol{u}_e\delta\boldsymbol{u}_e\right) + \nabla\cdot(\mathsf{P}_p + \mathsf{P}_e) - \boldsymbol{J}\times\boldsymbol{B} \\
= -n\left(\nu_{en}m_e + \nu_{in}m_i\right)(\boldsymbol{u} - \boldsymbol{u}_n) - \frac{\mu}{e}\left(\nu_{in} - \nu_{en}\right)\boldsymbol{J}
\end{aligned} \tag{B.10}$$

Finally this is further abbreviation by the introduction of the *average pressure tensor*. Defining this – as suggested, e.g., in Bittencourt (2004) – as being caused by the random motions of the particles relative to the mean flow velocity $\boldsymbol{u}$ we find:

$$\mathsf{P} = \sum_\alpha \mathsf{P}_\alpha + \sum_\alpha \delta\boldsymbol{u}_\alpha\delta\boldsymbol{u}_\alpha \tag{B.11}$$

Thus, the third term on the left-hand side of Eq. (B.10) is absorbed into the pressure tensor:

$$\frac{\partial(\rho\boldsymbol{u})}{\partial t} + \nabla\cdot(\rho\boldsymbol{u}\boldsymbol{u}) + \nabla\cdot\mathsf{P} - \boldsymbol{J}\times\boldsymbol{B} = -n\left(\nu_{en}m_e + \nu_{in}m_i\right)(\boldsymbol{u} - \boldsymbol{u}_n) - \frac{\mu}{e}\left(\nu_{in} - \nu_{en}\right)\boldsymbol{J} \tag{B.12}$$

As mentioned above, P is the pressure dyad relative to the global mean velocity v of the charged particle fluid. With the introduction of the following abbreviation for the collision frequencies with neutral particles:

$$\nu_n \equiv \frac{m_i\nu_{in} + m_e\nu_{en}}{m_i + m_e} \tag{B.13}$$

the first of the collisional source terms can be abbreviated to read:

$$n\left(\nu_{en}m_e + \nu_{in}m_i\right)(\boldsymbol{u} - \boldsymbol{u}_n) = \left(m_e + m_i\right)n\left(\boldsymbol{u} - \boldsymbol{u}_n\right) = \rho\left(\boldsymbol{u} - \boldsymbol{u}_n\right) \tag{B.14}$$

Thus, the general form for the momentum equation of the charged particle fluid is:

$$\frac{\partial(\rho\boldsymbol{u})}{\partial t} + \nabla\cdot(\rho\boldsymbol{u}\boldsymbol{u}) + \nabla\cdot\mathsf{P} - \boldsymbol{J}\times\boldsymbol{B} = -\nu_n\rho(\boldsymbol{u} - \boldsymbol{u}_n) - \frac{\mu}{e}\left(\nu_{in} - \nu_{en}\right)\boldsymbol{J} \tag{B.15}$$

Finally, we would like to deal with the electromagnetic terms in this equation. First of all the assumption of quasi-neutrality is already included in Eq. (B.15). This assumption is justified for a plasma in interstellar space due to the fact that the spatial scales under consideration are much greater than the Debye length. Apart from that the current density can be expressed using Ampère's law. Neglecting the displacement current this reads:

$$\boldsymbol{J} = \frac{1}{\mu_0} \nabla \times \boldsymbol{B} \tag{B.16}$$

Including this into Eq. (B.15) we find:

$$\frac{\partial (\rho \boldsymbol{u})}{\partial t} + \nabla \cdot (\rho \boldsymbol{u}\boldsymbol{u}) + \nabla \cdot \mathsf{P} + \frac{1}{\mu_0} \boldsymbol{B} \times (\nabla \times \boldsymbol{B}) = -\nu_n \rho (\boldsymbol{u} - \boldsymbol{u}_n) - \frac{\mu}{e} (\nu_{in} - \nu_{en}) \boldsymbol{J} \tag{B.17}$$

Finally there is a tiny last modification to this equations, which will yield the conservative form of the above equations. This is desirable, because we are using a solver which only works for equations in conservative form. In order to avoid having to use another solver for the evolution of the magnetic induction, we transform the term containing the curl of the magnetic field into a conservative form:

$$\begin{aligned} \frac{1}{\mu_0} \boldsymbol{B} \times (\nabla \times \boldsymbol{B}) &= \nabla \left(\frac{1}{2\mu_0} B^2 \right) - \frac{1}{2\mu_0} (\boldsymbol{B} \cdot \nabla) \boldsymbol{B} \\ &= \nabla \cdot \left(\frac{1}{2\mu_0} B^2 \right) \mathbf{1} - \nabla \cdot \frac{1}{\mu_0} (\boldsymbol{B}\boldsymbol{B}) \end{aligned} \tag{B.18}$$

thus, ending up with:

$$\frac{\partial (\rho \boldsymbol{u})}{\partial t} + \nabla \cdot (\rho \boldsymbol{u}\boldsymbol{u}) + \nabla \cdot \mathsf{P} + \nabla \cdot \left(\frac{B^2}{2\mu_0} 1 - \frac{\boldsymbol{B}\boldsymbol{B}}{\mu_0} \right) = -\nu_n \rho (\boldsymbol{u} - \boldsymbol{u}_n) - \frac{\mu}{e} (\nu_{in} - \nu_{en}) \boldsymbol{J} \tag{B.19}$$

Based on the same ideas, we, also, can easily deduce an equation for the momentum balance of the neutral fluid:

$$\frac{\partial (\rho_n \boldsymbol{u}_n)}{\partial t} + \nabla \cdot (\rho_n \boldsymbol{u}_n \boldsymbol{u}_n) + \nabla \cdot \mathsf{P}_n = \nu_n \rho (\boldsymbol{u} - \boldsymbol{u}_n) + \frac{\mu}{e} (\nu_{in} - \nu_{en}) \boldsymbol{J} \tag{B.20}$$

Before we discuss the derivation of the energy equation we will first briefly discuss how Ohm's law can be abbreviated to the form used in this work.

B.2 Ohm's Law

To compute Ohm's law one usually multiplies Eqs. (B.2) and (B.4) by the appropriate charge-mass ratio and sums the resulting equations. Here, however, we will rather use the same strategy as illustrated in Song et al. (2001), i.e. we transform the equations in such a way as to get rid of the neutral velocity from the resulting equation. This can easily be acchieved by multiplying the ion-equation by the electron-neutral collision frequency and the electron-equation by the ion-neutral collision frequency and by the subsequent subtraction of the resulting equations.

The usual approach in the derivation for Ohm's law is to neglect the dynamic and the pressure terms in these equations as compared to the terms containing the electromagnetic quantities. Then the above procedure yields:

$$\begin{aligned} \nu_{en} m_e en (\boldsymbol{E} + \boldsymbol{u} \times \boldsymbol{B}) + \nu_{in} m_i en (\boldsymbol{E} + \boldsymbol{u} \times \boldsymbol{B}) + \frac{\nu_{en} m_e^2}{m_i + m_e} \boldsymbol{J} \times \boldsymbol{B} - \frac{\nu_{in} m_i^2}{m_i + m_e} \boldsymbol{J} \times \boldsymbol{B} \\ = \nu_{en} m_e \left(\nu_{ie} \frac{m_i}{e} + \nu_{in} \frac{\mu}{e} \right) \boldsymbol{J} + \nu_{in} m_i \left(\nu_{ei} \frac{m_e}{e} + \nu_{en} \frac{\mu}{e} \right) \boldsymbol{J} \end{aligned} \tag{B.21}$$

This can be cast in a more compact form:

$$\begin{aligned} en\left(m_e\nu_{en}+m_i\nu_{in}\right)(\boldsymbol{E}+\boldsymbol{u}\times\boldsymbol{B}) + \frac{1}{m_i+m_e}\left(m_e^2\nu_{en}-m_i^2\nu_{in}\right)\boldsymbol{J}\times\boldsymbol{B} \\ = \frac{m_e}{e}\left(m_i\nu_{en}\nu_{in}+m_e\nu_{en}\nu_{ei}+m_i\nu_{ei}\nu_{in}\right)\boldsymbol{J} \\ = \frac{m_e}{e}\left(m_e\nu_{en}\nu_{ei}+m_i\nu_{in}\left(\nu_{en}+\nu_{ei}\right)\right)\boldsymbol{J} \end{aligned} \tag{B.22}$$

From which we find:

$$e\rho\nu_n(\boldsymbol{E}+\boldsymbol{u}\times\boldsymbol{B}) + \frac{1}{m_i+m_e}\left(m_e^2\nu_{en}-m_i^2\nu_{in}\right)\boldsymbol{J}\times\boldsymbol{B} = \frac{m_e}{e}\left(m_e\nu_{en}\nu_{ei}+m_i\nu_{in}\left(\nu_{en}+\nu_{ei}\right)\right)\boldsymbol{J} \tag{B.23}$$

This can be cast into the convenient form:

$$(\boldsymbol{E}+\boldsymbol{u}\times\boldsymbol{B}) + \frac{1}{ne}\alpha_2\boldsymbol{J}\times\boldsymbol{B} = \tilde{\eta}\alpha_1\boldsymbol{J} \tag{B.24}$$

where we introduced the following quantities:

$$\begin{aligned} \tilde{\eta} &= \frac{m_e\nu_{ei}}{ne^2} \\ \alpha_1 &= \frac{m_e\nu_{en}\nu_{ei}+m_i\nu_{in}\left(\nu_{en}+\nu_{ei}\right)}{\nu_{ei}\nu_n(m_i+m_e)} \\ \alpha_2 &= \frac{m_e^2\nu_{en}-m_i^2\nu_{in}}{(m_i+m_e)^2\nu_n} \end{aligned} \tag{B.25}$$

Here $\tilde{\eta}$ is the longitudinal electrical conductivity. Also α_1 and α_2 are constants of order unity.

Eq. (B.24) is a general form of Ohm's law connecting the electromagnetic fields to the current density for a two-fluid description. Obviously the differences to the single-fluid Ohm's law only lie in the factors α_1 and α_2 each being of order unity: the second term is similar to the Hall-term in the Ohm's law for fully ionised plasmas. This form of Ohm's law allows us to apply the same approximations as for the one-fluid model. For single-fluid models usually for Ohm's law the conductivities are assumed to be infinite – in this case one refers to the equations as ideal / nonresistive MHD. To retain a finite current in this case we have, therefore, to require the LHS of Eq. (B.24) to vanish. The Hall term, however, is usually neglected for resistive MHD. Thus we have for a resistive representation:

$$\eta\boldsymbol{J} = \boldsymbol{E}+\boldsymbol{u}\times\boldsymbol{B} \tag{B.26}$$

where we defined $\eta = \tilde{\eta}\alpha_1$. From this we are finally able to deduce the usual induction equation.

B.3 The Energy Equation of the Ionised Fluid

For the closure of the system we finally need another equation. Since, we need to work with conserved quantities, the desired equation is an energy equation. Here one has to keep in mind that the pressure equation, though, in conservative form can not be used in this case. This is due to the fact that in contrast to the total energy density the thermal energy density is not conserved over a shock wave. This results in unphysical solutions when using a numercial scheme to compute the correponding shock-solution (see e.g. Kleimann 2005). The equation needed in this context will describe the evolution of the total energy density, total meaning under these circumstances, that we include internal, electromagnetic and kinetic energy density of the fluid. The kinetic energy density of the fluid motion is given by:

$$e_{fluid} = \frac{\rho|u|^2}{2} \tag{B.27}$$

Because of the electromagnetic quantities we only investigate the temporal evolution of the magnetic induction, we only have to take into account the magnetic energy density here:

$$e_{mag} = \frac{|B|^2}{2\mu_0} \tag{B.28}$$

When intending to use a definition for the internal energy in its most general form one has to keep in mind that the usual approach of giving the internal energy as:

$$e_{Int} = \frac{3}{2}nkT \tag{B.29}$$

is stricly only valid for a monoatomic ideal gas. Whereas we do not want to abandon the assumption of the ideal gas, we would still like to include the possibility of a polyatomic gas. Therefore, we consider the most general form for the internal energy for ν mols of gas, which is given by:

$$e_{Int} = \nu c_v T \tag{B.30}$$

where T is the temperature of the gas and c_v indicates the specific heat for constant volume. The latter depends on the structure of the molecules or atoms which the gas under consideration is comprised of. The most general form is:

$$c_V = \frac{3}{2}R + \frac{1}{2}RN_{Rot} + RN_{Vib} \tag{B.31}$$

where N_{Rot} and N_{Vib} indicate the number of rotational and vibrational degrees of freedom. Only the first term describing the kinetic degrees of freedom has to be taken into account for all kinds of gases. The others only occur for gases comprised of molecules, thus, causing a deviation from Eq. (B.29). When the user is not so much interested in the exact microscopic behaviour of the gas one can still find another suitable form for the specific heat:

$$\gamma = \frac{c_v + R}{c_v} \qquad \Longrightarrow \qquad c_v = \frac{R}{\gamma - 1} \tag{B.32}$$

By this the adiabatic exponent is connected to the specific heat. So, we finally find for the internal energy:

$$e_{Int} = \frac{1}{\gamma - 1}nk_BT \tag{B.33}$$

where we also used:

$$R = N_A k_B \qquad \text{and} \qquad \nu N_A = n \tag{B.34}$$

where N_A denotes Avogadro's number. When we addionally use the ideal gas law:

$$p = nk_BT \qquad \Longrightarrow \qquad e_{Int} = \frac{1}{\gamma - 1}p \tag{B.35}$$

we can give the final form for the total energy density to be used in this work:

$$e = \frac{\rho|u|^2}{2} + \frac{|B|^2}{2\mu_0} + \frac{p}{\gamma - 1} \tag{B.36}$$

What we have from the single species equations is the evolution equation for the internal energy for the individual species (see A). Therefore, the derivation of the energy equation is subdivided into several parts each of which considering one aspect of this equation. First we will begin by deriving an evolution equation for the energy contained in the magnetic field:

B.3.1 Magnetic Energy Evolution

With the magnetic energy density being defined as:

$$e_{mag} = \frac{|B|^2}{2\mu_0} \tag{B.37}$$

we can infer the evolution equation for this part of the overall energy density from the MHD form of the induction equation given in section 2.5. For this we find:

$$\frac{\partial e_{mag}}{\partial t} = \frac{\boldsymbol{B}}{\mu_0} \cdot \frac{\partial \boldsymbol{B}}{\partial t} \overset{2.5}{=} \frac{\boldsymbol{B}}{\mu_0} \cdot (\nabla \times (\boldsymbol{u} \times \boldsymbol{B}) - \nabla \times (\eta \boldsymbol{J}))$$

Usage of the vector identity:

$$\nabla \cdot (\boldsymbol{u} \cdot \boldsymbol{B})\boldsymbol{B} = (\boldsymbol{B} \cdot \nabla)(\boldsymbol{u} \cdot \boldsymbol{B}) + (\boldsymbol{u} \cdot \boldsymbol{B})\underbrace{\nabla \cdot \boldsymbol{B}}_{=0} = \boldsymbol{B} \cdot (\boldsymbol{B} \cdot \nabla)\boldsymbol{u} + \boldsymbol{B} \cdot (\boldsymbol{u} \cdot \nabla)\boldsymbol{B} + \boldsymbol{B} \cdot (\boldsymbol{u} \times (\nabla \times \boldsymbol{B})) \tag{B.38}$$

shows that we can write:

$$\begin{aligned}
\boldsymbol{B} \cdot \nabla \times (\boldsymbol{u} \times \boldsymbol{B}) &= \boldsymbol{B} \cdot (-\boldsymbol{B}(\nabla \cdot \boldsymbol{u}) + (\boldsymbol{B} \cdot \nabla)\boldsymbol{u} - (\boldsymbol{u} \cdot \nabla)\boldsymbol{B}) \\
&= -B^2(\nabla \cdot \boldsymbol{u}) - \underbrace{(\boldsymbol{u} \cdot \nabla)B^2 + (\boldsymbol{u} \cdot \nabla)B^2}_{=0} + \boldsymbol{B} \cdot (\boldsymbol{B} \cdot \nabla)\boldsymbol{u} - \boldsymbol{B} \cdot (\boldsymbol{u} \cdot \nabla)\boldsymbol{B} \\
&= -\nabla \cdot (B^2\boldsymbol{u}) + (\boldsymbol{u} \cdot \nabla)B^2 + \boldsymbol{B} \cdot (\boldsymbol{B} \cdot \nabla)\boldsymbol{u} - \boldsymbol{B} \cdot (\boldsymbol{u} \cdot \nabla)\boldsymbol{B} \\
&= -\nabla \cdot (B^2\boldsymbol{u}) + \boldsymbol{B} \cdot (\boldsymbol{B} \cdot \nabla)\boldsymbol{u} + \boldsymbol{B} \cdot (\boldsymbol{u} \cdot \nabla)\boldsymbol{b} \\
&\overset{(B.38)}{=} -\nabla \cdot (B^2\boldsymbol{u}) + \nabla \cdot (\boldsymbol{u} \cdot \boldsymbol{B})\boldsymbol{B} - \boldsymbol{B} \cdot (\boldsymbol{u} \times (\nabla \times \boldsymbol{B}))
\end{aligned} \tag{B.39}$$

Using this in the equation for the magnetic energy density leaves us with a conservative form for this equation:

$$\frac{\partial e_{mag}}{\partial t} = -\nabla \cdot \left(\frac{B^2}{\mu_0}\boldsymbol{u} - \frac{1}{\mu_0}(\boldsymbol{u} \cdot \boldsymbol{B})\boldsymbol{B}\right) - \boldsymbol{u} \cdot \left(\frac{\nabla \times \boldsymbol{B}}{\mu_0} \times \boldsymbol{B}\right) = -\frac{\boldsymbol{B}}{\mu_0} \cdot (\nabla \times (\eta \boldsymbol{J})) \tag{B.40}$$

The next term to discuss is the evolution equation for the internal energy. In this case we will soon find that the evolution equation equations for the kinetic energy density can easily be included here.

B.3.2 The Pressure Equation

The next thing to discuss is the pressure equation. For this we first have to clarify what the overall pressure really is. As already used in Eq. (B.11) for the pressure dyad the scalar pressure can be expressed as:

$$\begin{aligned}
p &= p_i + p_e + \frac{\gamma - 1}{2}\left(\rho_i(\boldsymbol{u}_i - \boldsymbol{u})^2 + \rho_e(\boldsymbol{u}_e - \boldsymbol{u})^2\right) \\
&= p_i + p_e + \frac{\gamma - 1}{2}\left(\rho_i \boldsymbol{u}_i^2 + \rho_e \boldsymbol{u}_e^2 - 2\underbrace{(\rho_i \boldsymbol{u}_i + \rho_e \boldsymbol{u}_e)}_{\rho\boldsymbol{u}} \cdot \boldsymbol{u} + \underbrace{(\rho_i + \rho_e)}_{\rho}\boldsymbol{u}^2\right) \\
&= p_i + p_e + \frac{\gamma - 1}{2}\left(\rho_i \boldsymbol{u}_i^2 + \rho_e \boldsymbol{u}_e^2 - \rho \boldsymbol{u}^2\right)
\end{aligned} \tag{B.41}$$

From this we easily find the connection between the different time derivatives to be:

$$\frac{1}{\gamma - 1}\frac{\partial p}{\partial t} = \frac{1}{\gamma - 1}\frac{\partial}{\partial t}(p_i + p_e) + \frac{1}{2}\frac{\partial}{\partial t}\left(\rho_i u_i^2 + \rho_e u_e^2 - \rho u^2\right) \tag{B.42}$$

Thus, we see, that the sum of thermal and kinetic energy is most easily computed together:

$$\frac{1}{\gamma-1}\frac{\partial p}{\partial t}+\frac{1}{2}\frac{\partial}{\partial t}\left(\rho u^2\right)=\frac{1}{\gamma-1}\frac{\partial}{\partial t}\left(p_i+p_e\right)+\frac{1}{2}\frac{\partial}{\partial t}\left(\rho_i u_i^2+\rho_e u_e^2\right) \tag{B.43}$$

Here we start out by computing the contribution by the single species pressure equations Eq. (2.12) for protons and electrons. This gives:

$$\frac{1}{\gamma-1}\left(\frac{\partial}{\partial t}\left(p_i+p_e\right)+\nabla\cdot\left(p_i\boldsymbol{u}_i+p_e\boldsymbol{u}_e\right)\right)+\left(\mathsf{P}_i\cdot\nabla\right)\cdot\boldsymbol{u}_i+\left(\mathsf{P}_e\cdot\nabla\right)\cdot\boldsymbol{u}_e+\nabla\cdot\left(\boldsymbol{q}_i+\boldsymbol{q}_e\right)=E_i+E_e \tag{B.44}$$

Now these terms will be evaluated one by one. We will begin at the end to spare the messy parts for later. The definition of the overall heat-flux vector according to Bittencourt (2004) yields:

$$\begin{aligned}\boldsymbol{q}=&\boldsymbol{q}_i+\boldsymbol{q}_e+\left(\boldsymbol{u}_i-\boldsymbol{u}\right)\cdot\mathsf{P}_i+\left(\boldsymbol{u}_e-\boldsymbol{u}\right)\cdot\mathsf{P}_e+\frac{1}{\gamma-1}\left(\left(\boldsymbol{u}_i-\boldsymbol{u}\right)p_i+\left(\boldsymbol{u}_e-\boldsymbol{u}\right)p_e\right)\\&+\frac{1}{2}\left(\rho_i\left(\boldsymbol{u}_i-\boldsymbol{u}\right)^2\left(\boldsymbol{u}_i-\boldsymbol{u}\right)+\rho_e\left(\boldsymbol{u}_e-\boldsymbol{u}\right)^2\left(\boldsymbol{u}_e-\boldsymbol{u}\right)\right)\end{aligned} \tag{B.45}$$

Additionally Eq. (B.41) can be used to reevaluate the divergence terms including the scalar pressure:

$$\begin{aligned}\frac{1}{\gamma-1}\nabla\cdot\left(p_i\boldsymbol{u}_i+p_e\boldsymbol{u}_e\right)=&\frac{1}{\gamma-1}\nabla\cdot\left(p_i((\boldsymbol{u}_i-\boldsymbol{u})+\boldsymbol{u})+p_e((\boldsymbol{u}_e-\boldsymbol{u})+\boldsymbol{u})\right)\\=&\frac{1}{\gamma-1}\nabla\cdot\left((p_i+p_e)\boldsymbol{u}+p_i(\boldsymbol{u}_i-\boldsymbol{u})+p_e(\boldsymbol{u}_e-\boldsymbol{u})\right)\\=&\frac{1}{\gamma-1}\nabla\cdot(p\boldsymbol{u})+\frac{1}{\gamma-1}\nabla\cdot\left(p_i(\boldsymbol{u}_i-\boldsymbol{u})+p_e(\boldsymbol{u}_e-\boldsymbol{u})\right)\\&-\frac{1}{2}\nabla\cdot\left(\rho_i(\boldsymbol{u}_i-\boldsymbol{u})^2+\rho_e(\boldsymbol{u}_e-\boldsymbol{u})^2\right)\boldsymbol{u}\end{aligned} \tag{B.46}$$

Putting both these things together we find:

$$\begin{aligned}&\frac{1}{\gamma-1}\nabla\cdot\left(p_i\boldsymbol{u}_i+p_e\boldsymbol{u}_e\right)+\nabla\cdot\left(\boldsymbol{q}_i+\boldsymbol{q}_e\right)\\&\quad=\frac{1}{\gamma-1}\left(\nabla\cdot(p\boldsymbol{u})+\nabla\cdot\left(p_i(\boldsymbol{u}_i-\boldsymbol{u})+p_e(\boldsymbol{u}_e-\boldsymbol{u})\right)\right)-\frac{1}{2}\nabla\cdot\left(\rho_i(\boldsymbol{u}_i-\boldsymbol{u})^2+\rho_e(\boldsymbol{u}_e-\boldsymbol{u})^2\right)\boldsymbol{u}\\&\qquad+\nabla\cdot\boldsymbol{q}-\nabla\cdot(\boldsymbol{u}_i-\boldsymbol{u})\cdot\mathsf{P}_i-\nabla\cdot(\boldsymbol{u}_e-\boldsymbol{u})\cdot\mathsf{P}_e-\frac{1}{\gamma-1}\nabla\cdot\left((\boldsymbol{u}_i-\boldsymbol{u})p_i+(\boldsymbol{u}_e-\boldsymbol{u})p_e\right)\\&\qquad-\frac{1}{2}\nabla\cdot\left(\rho_i\left(\boldsymbol{u}_i-\boldsymbol{u}\right)^2\left(\boldsymbol{u}_i-\boldsymbol{u}\right)+\rho_e\left(\boldsymbol{u}_e-\boldsymbol{u}\right)^2\left(\boldsymbol{u}_e-\boldsymbol{u}\right)\right) \qquad\qquad (B.47)\\&\quad=\frac{1}{\gamma-1}\nabla\cdot(p\boldsymbol{u})+\nabla\cdot\boldsymbol{q}-\nabla\cdot(\boldsymbol{u}_i-\boldsymbol{u})\cdot\mathsf{P}_i-\nabla\cdot(\boldsymbol{u}_e-\boldsymbol{u})\cdot\mathsf{P}_e-\frac{1}{2}\nabla\cdot\left(\rho_i(\boldsymbol{u}_i-\boldsymbol{u})^2(\boldsymbol{u}_i)+\rho_e(\boldsymbol{u}_e-\boldsymbol{u})^2(\boldsymbol{u}_e)\right)\end{aligned}$$

The next thing we will include is the term involving the pressure tensor. This is transformed in a way similar to the scalar pressure:

$$\begin{aligned}(\mathsf{P}_p\cdot\nabla)\cdot\boldsymbol{u}_p+(\mathsf{P}_e\cdot\nabla)\cdot\boldsymbol{u}_e&=(\mathsf{P}_p\cdot\nabla)\cdot\boldsymbol{u}+(\mathsf{P}_e\cdot\nabla)\cdot\boldsymbol{u}+(\mathsf{P}_p\cdot\nabla)\cdot(\boldsymbol{u}_p-\boldsymbol{u})+(\mathsf{P}_e\cdot\nabla)\cdot(\boldsymbol{u}_e-\boldsymbol{u})\\&=(\mathsf{P}\cdot\nabla)\cdot\boldsymbol{u}+(\mathsf{P}_p\cdot\nabla)\cdot(\boldsymbol{u}_p-\boldsymbol{u})+(\mathsf{P}_e\cdot\nabla)\cdot(\boldsymbol{u}_e-\boldsymbol{u})\\&\quad-\rho_p(\boldsymbol{u}_p-\boldsymbol{u})(\boldsymbol{u}_p-\boldsymbol{u})\cdot\nabla\cdot\boldsymbol{u}-\rho_e(\boldsymbol{u}_e-\boldsymbol{u})(\boldsymbol{u}_e-\boldsymbol{u})\cdot\nabla\cdot\boldsymbol{u}\end{aligned} \tag{B.48}$$

Thus, we have an expression for the sum of the pressure and heat flux terms, leading us to the intermediate result:

$$
\begin{aligned}
&\frac{1}{\gamma-1}\frac{\partial}{\partial t}(p_i+p_e) \\
&\quad = -\frac{1}{\gamma-1}\nabla\cdot\left(p_p\boldsymbol{u}_p+p_e\boldsymbol{u}_e\right)-(\mathsf{P}_p\cdot\nabla)\cdot\boldsymbol{u}_p-(\mathsf{P}_e\cdot\nabla)\cdot\boldsymbol{u}_e-\nabla\cdot\left(\boldsymbol{q}_p+\boldsymbol{q}_e\right)+E_i+E_e \\
&\quad = -\frac{1}{\gamma-1}\nabla\cdot(p\boldsymbol{u})-\nabla\cdot\boldsymbol{q}-(\mathsf{P}\cdot\nabla)\cdot\boldsymbol{u}+(\boldsymbol{u}_p-\boldsymbol{u})\cdot\nabla\cdot\mathsf{P}_p+(\boldsymbol{u}_e-\boldsymbol{u})\cdot\nabla\cdot\mathsf{P}_e+E_i+E_e \\
&\qquad +\frac{1}{2}\nabla\cdot\left(\rho_p(\boldsymbol{u}_p-\boldsymbol{u})^2(\boldsymbol{u}_p)+\rho_e(\boldsymbol{u}_e-\boldsymbol{u})^2(\boldsymbol{u}_e)\right)+\left(\rho_p(\boldsymbol{u}_p-\boldsymbol{u})(\boldsymbol{u}_p-\boldsymbol{u})+\rho_e(\boldsymbol{u}_e-\boldsymbol{u})(\boldsymbol{u}_e-\boldsymbol{u})\right)\cdot\nabla\cdot\boldsymbol{u}
\end{aligned}
\tag{B.49}
$$

Before discussing the source terms the next thing to worry about are the time derivatives of the single species kinetic energy density. These can be gained from a combination of the single species momentum equation and the corresponding equation of continuity. For this, we first insert the continuity equation for the ions into the corresponding momentum equation, leading to the equation:

$$
\rho_i\frac{\partial\boldsymbol{u}_i}{\partial t}+\rho_i(\boldsymbol{u}_i\cdot\nabla)\boldsymbol{u}_i+\nabla\cdot\mathsf{P}_i-en_i\left(\boldsymbol{E}+\boldsymbol{u}_i\times\boldsymbol{B}\right)=-\left(\nu_{ie}\frac{m_i}{e}+\nu_{in}\frac{\mu}{e}\right)\boldsymbol{J}-\nu_{in}\rho_i(\boldsymbol{u}-\boldsymbol{u}_n)
\tag{B.50}
$$

with an analogous relation for the electrons. Then we find for the time derivative of the corresponding kinetic energy – again using the example of the ions:

$$
\begin{aligned}
\frac{1}{2}\frac{\partial\left(\rho_i u_i^2\right)}{\partial t} &= \frac{1}{2}\left(\boldsymbol{u}_i\cdot\left(\rho_i\frac{\partial\boldsymbol{u}_i}{\partial t}+\frac{\partial\rho_i\boldsymbol{u}_i}{\partial t}\right)\right) \\
&= -\frac{1}{2}\rho_i\boldsymbol{u}_i\cdot(\boldsymbol{u}_i\cdot\nabla)\boldsymbol{u}_i-\frac{1}{2}\boldsymbol{u}_i\cdot\nabla\cdot\mathsf{P}_i+\frac{1}{2}en_i\boldsymbol{u}_i\cdot(\boldsymbol{E}+\boldsymbol{u}_i\times\boldsymbol{B}) \\
&\quad -\frac{1}{2}\boldsymbol{u}_i\cdot\left(\left(\nu_{ie}\frac{m_i}{e}+\nu_{in}\frac{\mu}{e}\right)\boldsymbol{J}-\nu_{in}\rho_i(\boldsymbol{u}-\boldsymbol{u}_n)\right) \\
&\quad -\frac{1}{2}\boldsymbol{u}_i\cdot(\nabla\cdot(\rho_i\boldsymbol{u}_i\boldsymbol{u}_i))-\frac{1}{2}\boldsymbol{u}_i\cdot\nabla\cdot\mathsf{P}_i+\frac{1}{2}en_i\boldsymbol{u}_i\cdot(\boldsymbol{E}+\boldsymbol{u}_i\times\boldsymbol{B}) \\
&\quad -\frac{1}{2}\boldsymbol{u}_i\cdot\left(\left(\nu_{ie}\frac{m_i}{e}+\nu_{in}\frac{\mu}{e}\right)\boldsymbol{J}-\nu_{in}\rho_i(\boldsymbol{u}-\boldsymbol{u}_n)\right) \\
&= -\frac{1}{2}\rho_i\boldsymbol{u}_i\cdot(\boldsymbol{u}_i\cdot\nabla)\boldsymbol{u}_i-\frac{1}{2}\boldsymbol{u}_i\cdot(\nabla\cdot(\rho_i\boldsymbol{u}_i\boldsymbol{u}_i))-\boldsymbol{u}_i\cdot\nabla\cdot\mathsf{P}_i \\
&\quad +en_i\boldsymbol{u}_i\cdot(\boldsymbol{E}+\boldsymbol{u}_i\times\boldsymbol{B})-\boldsymbol{u}_i\cdot\left(\left(\nu_{ie}\frac{m_i}{e}+\nu_{in}\frac{\mu}{e}\right)\boldsymbol{J}-\nu_{in}\rho_i(\boldsymbol{u}-\boldsymbol{u}_n)\right) \\
&= -\frac{1}{2}\nabla\cdot(\rho_i u_i^2\boldsymbol{u}_i)-\boldsymbol{u}_i\cdot\nabla\cdot\mathsf{P}_i+en_i\boldsymbol{u}_i\cdot\boldsymbol{E}-\boldsymbol{u}_i\cdot\left(\left(\nu_{ie}\frac{m_i}{e}+\nu_{in}\frac{\mu}{e}\right)\boldsymbol{J}+\nu_{in}\rho_i(\boldsymbol{u}-\boldsymbol{u}_n)\right)
\end{aligned}
\tag{B.51}
$$

For the electrons we find in an analogous approach:

$$
\frac{1}{2}\frac{\partial\left(\rho_e u_e^2\right)}{\partial t}=-\frac{1}{2}\nabla\cdot(\rho_e u_e^2\boldsymbol{u}_i)-\boldsymbol{u}_e\cdot\nabla\cdot\mathsf{P}_e-en_e\boldsymbol{u}_e\cdot\boldsymbol{E}+\boldsymbol{u}_e\cdot\left(\left(\nu_{ei}\frac{m_e}{e}+\nu_{en}\frac{\mu}{e}\right)\boldsymbol{J}-\nu_{en}\rho_e(\boldsymbol{u}-\boldsymbol{u}_n)\right)
\tag{B.52}
$$

Therefore, the sum of these two contributions is:

$$
\begin{aligned}
&\frac{1}{2}\frac{\partial}{\partial t}\left(\rho_i u_i^2+\rho_e u_e^2\right) \\
&\quad = -\frac{1}{2}\nabla\cdot(\rho_i u_i^2\boldsymbol{u}_i)-\frac{1}{2}\nabla\cdot(\rho_e u_e^2\boldsymbol{u}_i)-\boldsymbol{u}_i\cdot\nabla\cdot\mathsf{P}_i-\boldsymbol{u}_e\cdot\nabla\cdot\mathsf{P}_e+e\left(n_i\boldsymbol{u}_i-n_e\boldsymbol{u}_e\right)\cdot\boldsymbol{E} \\
&\qquad -\boldsymbol{u}_i\cdot\left(\left(\nu_{ie}\frac{m_i}{e}+\nu_{in}\frac{\mu}{e}\right)\boldsymbol{J}+\nu_{in}\rho_i(\boldsymbol{u}-\boldsymbol{u}_n)\right)+\boldsymbol{u}_e\cdot\left(\left(\nu_{ei}\frac{m_e}{e}+\nu_{en}\frac{\mu}{e}\right)\boldsymbol{J}-\nu_{en}\rho_e(\boldsymbol{u}-\boldsymbol{u}_n)\right)
\end{aligned}
\tag{B.53}
$$

Now we have to put all the stuff together. This leaves us with the somewhat messy result:

$$
\begin{aligned}
&\frac{1}{\gamma-1}\frac{\partial p}{\partial t}+\frac{1}{2}\frac{\partial}{\partial t}\left(\rho u^2\right)=-\frac{1}{\gamma-1}\nabla\cdot(p\boldsymbol{u})-\nabla\cdot\boldsymbol{q}\\
&\quad=-\left(\mathsf{P}\cdot\nabla\right)\cdot\boldsymbol{u}+(\boldsymbol{u}_i-\boldsymbol{u})\cdot\nabla\cdot\mathsf{P}_i+(\boldsymbol{u}_e-\boldsymbol{u})\cdot\nabla\cdot\mathsf{P}_e-\boldsymbol{u}_i\cdot\nabla\cdot\mathsf{P}_i-\boldsymbol{u}_e\cdot\nabla\cdot\mathsf{P}_e\\
&\qquad-\frac{1}{2}\nabla\cdot(\rho_i u_i^2\boldsymbol{u}_i)-\frac{1}{2}\nabla\cdot(\rho_e u_e^2\boldsymbol{u}_i)\\
&\qquad+\frac{1}{2}\nabla\cdot\left(\rho_i(\boldsymbol{u}_i-\boldsymbol{u})^2(\boldsymbol{u}_i)+\rho_e(\boldsymbol{u}_e-\boldsymbol{u})^2(\boldsymbol{u}_e)\right)+(\rho_i(\boldsymbol{u}_i-\boldsymbol{u})(\boldsymbol{u}_i-\boldsymbol{u})+\rho_e(\boldsymbol{u}_e-\boldsymbol{u})(\boldsymbol{u}_e-\boldsymbol{u}))\cdot\nabla\cdot\boldsymbol{u}\\
&\qquad+e\left(n_i\boldsymbol{u}_i-n_e\boldsymbol{u}_e\right)\cdot\boldsymbol{E}+E_i+E_e\\
&\qquad-\boldsymbol{u}_i\cdot\left(\left(\nu_{ie}\frac{m_i}{e}+\nu_{in}\frac{\mu}{e}\right)\boldsymbol{J}+\nu_{in}\rho_i(\boldsymbol{u}-\boldsymbol{u}_n)\right)+\boldsymbol{u}_e\cdot\left(\left(\nu_{ei}\frac{m_e}{e}+\nu_{en}\frac{\mu}{e}\right)\boldsymbol{J}-\nu_{en}\rho_e(\boldsymbol{u}-\boldsymbol{u}_n)\right)
\end{aligned}
\tag{B.54}
$$

There we can use the relation:

$$
(\boldsymbol{u}_i-\boldsymbol{u})\cdot\nabla\cdot\mathsf{P}_i+(\boldsymbol{u}_e-\boldsymbol{u})\cdot\nabla\cdot\mathsf{P}_e-\boldsymbol{u}_i\cdot\nabla\cdot\mathsf{P}_i-\boldsymbol{u}_e\cdot\nabla\cdot\mathsf{P}_e=-\boldsymbol{u}\cdot\nabla\cdot(\mathsf{P}_i+\mathsf{P}_e)
\tag{B.55}
$$

Using Eq. (B.11) this becomes:

$$
-\boldsymbol{u}\cdot\nabla\cdot(\mathsf{P}_i+\mathsf{P}_e)=-\boldsymbol{u}\cdot\nabla\cdot\mathsf{P}+\boldsymbol{u}\cdot\nabla\cdot((\boldsymbol{u}_i-\boldsymbol{u})(\boldsymbol{u}_i-\boldsymbol{u})+(\boldsymbol{u}_e-\boldsymbol{u})(\boldsymbol{u}_e-\boldsymbol{u}))
\tag{B.56}
$$

By additional usage of $\nabla\cdot(\mathsf{P}\cdot\boldsymbol{u})=(\mathsf{P}\cdot\nabla)\cdot\boldsymbol{u}+\boldsymbol{u}\cdot(\nabla\cdot\mathsf{P})$ we find for the kinetic part of the energy evolution equation:

$$
\begin{aligned}
&\frac{1}{\gamma-1}\frac{\partial p}{\partial t}+\frac{1}{2}\frac{\partial}{\partial t}\left(\rho u^2\right)=-\frac{1}{\gamma-1}\nabla\cdot(p\boldsymbol{u})-\nabla\cdot\boldsymbol{q}-\nabla\cdot(\mathsf{P}\cdot\boldsymbol{u})\\
&\quad=+\boldsymbol{u}\cdot\nabla\cdot((\boldsymbol{u}_i-\boldsymbol{u})(\boldsymbol{u}_i-\boldsymbol{u})+(\boldsymbol{u}_e-\boldsymbol{u})(\boldsymbol{u}_e-\boldsymbol{u}))-\frac{1}{2}\nabla\cdot(\rho_i u_i^2\boldsymbol{u}_i)-\frac{1}{2}\nabla\cdot(\rho_e u_e^2\boldsymbol{u}_i)\\
&\qquad+\frac{1}{2}\nabla\cdot\left(\rho_i(\boldsymbol{u}_i-\boldsymbol{u})^2(\boldsymbol{u}_i)+\rho_e(\boldsymbol{u}_e-\boldsymbol{u})^2(\boldsymbol{u}_e)\right)+(\rho_i(\boldsymbol{u}_i-\boldsymbol{u})(\boldsymbol{u}_i-\boldsymbol{u})+\rho_e(\boldsymbol{u}_e-\boldsymbol{u})(\boldsymbol{u}_e-\boldsymbol{u}))\cdot\nabla\cdot\boldsymbol{u}\\
&\qquad+e\left(n_i\boldsymbol{u}_i-n_e\boldsymbol{u}_e\right)\cdot\boldsymbol{E}+E_i+E_e\\
&\qquad-\boldsymbol{u}_i\cdot\left(\left(\nu_{ie}\frac{m_i}{e}+\nu_{in}\frac{\mu}{e}\right)\boldsymbol{J}+\nu_{in}\rho_i(\boldsymbol{u}-\boldsymbol{u}_n)\right)+\boldsymbol{u}_e\cdot\left(\left(\nu_{ei}\frac{m_e}{e}+\nu_{en}\frac{\mu}{e}\right)\boldsymbol{J}-\nu_{en}\rho_e(\boldsymbol{u}-\boldsymbol{u}_n)\right)
\end{aligned}
\tag{B.57}
$$

The next thing we will discuss are the terms containing only velocities and densities. For this we find:

$$
\begin{aligned}
&\boldsymbol{u}\cdot\nabla\cdot(\rho_i(\boldsymbol{u}_i-\boldsymbol{u})(\boldsymbol{u}_i-\boldsymbol{u})+\rho_e(\boldsymbol{u}_e-\boldsymbol{u})(\boldsymbol{u}_e-\boldsymbol{u}))+(\rho_i(\boldsymbol{u}_i-\boldsymbol{u})(\boldsymbol{u}_i-\boldsymbol{u})+\rho_e(\boldsymbol{u}_e-\boldsymbol{u})(\boldsymbol{u}_e-\boldsymbol{u}))\cdot\nabla\cdot\boldsymbol{u}\\
&\quad=\nabla\cdot((\rho_i(\boldsymbol{u}_i-\boldsymbol{u})(\boldsymbol{u}_i-\boldsymbol{u})+\rho_e(\boldsymbol{u}_e-\boldsymbol{u})(\boldsymbol{u}_e-\boldsymbol{u}))\cdot\boldsymbol{u})\\
&\quad=\nabla\cdot\left((\rho_i(\boldsymbol{u}_i\cdot\boldsymbol{u}-u^2))\boldsymbol{u_i}+(\rho_e(\boldsymbol{u}_e\cdot\boldsymbol{u}-u^2))\boldsymbol{u}_e-(\underbrace{\rho_i(\boldsymbol{u}_i\cdot\boldsymbol{u}-u^2)+\rho_e(\boldsymbol{u}_e\cdot\boldsymbol{u}-u^2)}_{=0})\boldsymbol{u}\right)
\end{aligned}
\tag{B.58}
$$

The remaining such terms can be merged in the following way:

$$
\begin{aligned}
&\frac{1}{2}\nabla\cdot\left(\rho_i(\boldsymbol{u}_i-\boldsymbol{u})^2(\boldsymbol{u}_i)+\rho_e(\boldsymbol{u}_e-\boldsymbol{u})^2(\boldsymbol{u}_e)\right)-\frac{1}{2}\nabla\cdot(\rho_i u_i^2\boldsymbol{u}_i)-\frac{1}{2}\nabla\cdot(\rho_e u_e^2\boldsymbol{u}_e)\\
&\quad=\frac{1}{2}\nabla\cdot\left(\left(\rho_i(u_i^2-2\boldsymbol{u}_i\cdot\boldsymbol{u}+u^2)\boldsymbol{u_i}-\rho_i u_i^2\boldsymbol{u}_i\right)+\left(\rho_e(u_e^2-2\boldsymbol{u}_e\cdot\boldsymbol{u}+u^2)\boldsymbol{u_e}-\rho_e u_e^2\boldsymbol{u}_e\right)\right)\\
&\quad=-\nabla\cdot\left(\rho_i(\boldsymbol{u}_i\cdot\boldsymbol{u}-\frac{1}{2}u^2)\boldsymbol{u_i}+\rho_e(\boldsymbol{u}_e\cdot\boldsymbol{u}-\frac{1}{2}u^2)\boldsymbol{u_e}\right)
\end{aligned}
\tag{B.59}
$$

Equations (B.58) and (B.59) together are, therefore, just:

$$
\begin{aligned}
&\boldsymbol{u}\cdot\nabla\cdot((\boldsymbol{u}_i-\boldsymbol{u})(\boldsymbol{u}_i-\boldsymbol{u})+(\boldsymbol{u}_e-\boldsymbol{u})(\boldsymbol{u}_e-\boldsymbol{u}))-\frac{1}{2}\nabla\cdot(\rho_i u_i^2\boldsymbol{u}_i)-\frac{1}{2}\nabla\cdot(\rho_e u_e^2\boldsymbol{u}_i)\\
&\quad+\frac{1}{2}\nabla\cdot\left(\rho_i(\boldsymbol{u}_i-\boldsymbol{u})^2(\boldsymbol{u}_i)+\rho_e(\boldsymbol{u}_e-\boldsymbol{u})^2(\boldsymbol{u}_e)\right)+(\rho_i(\boldsymbol{u}_i-\boldsymbol{u})(\boldsymbol{u}_i-\boldsymbol{u})+\rho_e(\boldsymbol{u}_e-\boldsymbol{u})(\boldsymbol{u}_e-\boldsymbol{u}))\cdot\nabla\cdot\boldsymbol{u}\\
&=-\frac{1}{2}\nabla\cdot\left((\rho_i\boldsymbol{u}_i+\rho_e\boldsymbol{u}_e)u^2\right)=-\frac{1}{2}\nabla\cdot\left(\rho u^2\boldsymbol{u}\right)
\end{aligned}
\tag{B.60}
$$

With all this in mind Eq. (B.57) can nicely abbreviated. Here we shift all the conservative terms to the left-hand side and the source terms to the right-hand side. Additionally we used Eq. (2.34) for the current density. By this we obtain:

$$\begin{aligned}
&\frac{1}{\gamma-1}\frac{\partial p}{\partial t}+\frac{1}{2}\frac{\partial}{\partial t}\left(\rho u^2\right)+\nabla\cdot\left(\left(\frac{1}{\gamma-1}p+\frac{1}{2}\rho u^2+\mathsf{P}\right)\boldsymbol{u}\right)+\nabla\cdot\boldsymbol{q}\\
&\quad=-\boldsymbol{u}_i\cdot\left(\left(\nu_{ie}\frac{m_i}{e}+\nu_{in}\frac{\mu}{e}\right)\boldsymbol{J}+\nu_{in}\rho_i(\boldsymbol{u}-\boldsymbol{u}_n)\right)+\boldsymbol{u}_e\cdot\left(\left(\nu_{ei}\frac{m_e}{e}+\nu_{en}\frac{\mu}{e}\right)\boldsymbol{J}-\nu_{en}\rho_e(\boldsymbol{u}-\boldsymbol{u}_n)\right)\\
&\quad+\boldsymbol{J}\cdot\boldsymbol{E}+E_i+E_e
\end{aligned}\tag{B.61}$$

Before we include the magnetic energy to obtain an equation for the overall energy density we will strive to find a more explicit form for the above source terms. Starting from the source terms for the single species momentum equations we find:

$$\begin{aligned}
&\boldsymbol{u}_i\cdot\left(\left(\nu_{ie}\frac{m_i}{e}+\nu_{in}\frac{\mu}{e}\right)\boldsymbol{J}+\nu_{in}\rho_i(\boldsymbol{u}-\boldsymbol{u}_n)\right)-\boldsymbol{u}_e\cdot\left(\left(\nu_{ei}\frac{m_e}{e}+\nu_{en}\frac{\mu}{e}\right)\boldsymbol{J}-\nu_{en}\rho_e(\boldsymbol{u}-\boldsymbol{u}_n)\right)\\
&=\ \nu_{ei}\frac{m_e}{e^2n}\boldsymbol{J}^2+\frac{\mu}{e}\left(\nu_{in}-\nu_{en}\right)\boldsymbol{J}\cdot\boldsymbol{u}+\left(\frac{\mu^2}{e^2n}\left(\frac{\nu_{in}}{m_i}+\frac{\nu_{en}}{m_e}\right)\right)J^2+\nu_n\rho\boldsymbol{u}\cdot(\boldsymbol{u}-\boldsymbol{u}_n)+\frac{\mu}{e}\left(\nu_{in}-\nu_{en}\right)\boldsymbol{J}\cdot(\boldsymbol{u}-\boldsymbol{u}_n)\\
&=\ \eta\boldsymbol{J}^2+\nu_n\rho\boldsymbol{u}\cdot(\boldsymbol{u}-\boldsymbol{u}_n)+\frac{\mu}{e}\left(\nu_{in}-\nu_{en}\right)\boldsymbol{J}\cdot(2\boldsymbol{u}-\boldsymbol{u}_n)+\left(\frac{\mu}{e^2n}\left(\frac{\nu_{in}}{m_i}+\frac{\nu_{en}}{m_e}\right)\right)J^2
\end{aligned}\tag{B.62}$$

This finally provides us with the possibility to give a quite brief form for Eq. (B.57):

$$\begin{aligned}
&\frac{1}{\gamma-1}\frac{\partial p}{\partial t}+\frac{1}{2}\frac{\partial}{\partial t}\left(\rho u^2\right)+\nabla\cdot\left(\left(\frac{1}{\gamma-1}p+\frac{1}{2}\rho u^2+\mathsf{P}\right)\boldsymbol{u}\right)+\nabla\cdot\boldsymbol{q}\\
&\quad=-\eta\boldsymbol{J}^2-\nu_n\rho\boldsymbol{u}\cdot(\boldsymbol{u}-\boldsymbol{u}_n)-\frac{\mu}{e}\left(\nu_{in}-\nu_{en}\right)\boldsymbol{J}\cdot(2\boldsymbol{u}-\boldsymbol{u}_n)-\left(\frac{\mu^2}{e^2n}\left(\frac{\nu_{in}}{m_i}+\frac{\nu_{en}}{m_e}\right)\right)J^2+\boldsymbol{J}\cdot\boldsymbol{E}+E_i+E_e
\end{aligned}\tag{B.63}$$

Here the term $\eta\boldsymbol{J}^2$ describes Ohmic heating. So far, however, we did not specify the individual source terms for the single species internal energy equations. This will be treated in the following paragraph:

The Source Terms

For the source terms of the single species energy equation we know:

$$E_\alpha=\sum_\beta\left(-2\frac{k_B}{\gamma_\alpha-1}\nu_{\alpha\beta}n_\alpha\frac{m_\alpha}{m_\alpha+m_\beta}(T_\alpha-T_\beta)+\nu_{\alpha\beta}n_\alpha m_\alpha\frac{m_\beta}{m_\alpha+m_\beta}(\boldsymbol{u}_\alpha-\boldsymbol{u}_\beta)^2\right)\tag{B.64}$$

where the sum is over all species apart from α. With this and using the same γ for all species the term E_p+E_e yields:

$$\begin{aligned}
E_i+E_e=&-2\frac{k_B}{\gamma-1}\nu_{ie}\rho_i\frac{1}{m_i+m_e}(T_i-T_e)+\nu_{ie}\rho_i\frac{m_e}{m_i+m_e}(\boldsymbol{u}_i-\boldsymbol{u}_e)^2\\
&-2\frac{k_B}{\gamma-1}\nu_{ei}\rho_e\frac{1}{m_i+m_e}(T_e-T_i)+\nu_{ei}\rho_e\frac{m_i}{m_i+m_e}(\boldsymbol{u}_e-\boldsymbol{u}_i)^2\\
&-2\frac{k_B}{\gamma-1}\nu_{in}\rho_i\frac{1}{m_i+m_n}(T_i-T_n)+\nu_{in}\rho_i\frac{m_n}{m_i+m_n}(\boldsymbol{u}_i-\boldsymbol{u}_n)^2\\
&-2\frac{k_B}{\gamma-1}\nu_{en}\rho_e\frac{1}{m_e+m_n}(T_e-T_n)+\nu_{en}\rho_e\frac{m_n}{m_e+m_n}(\boldsymbol{u}_e-\boldsymbol{u}_n)^2
\end{aligned}\tag{B.65}$$

Using the conservation of momentum for the electron-proton collisions, which results in:

$$\nu_{ie}\rho_i=\nu_{ei}\rho_e\tag{B.66}$$

the first two temperature terms cancel identically:

$$\begin{aligned}E_i + E_e =&\nu_{ie}\rho_i \frac{m_e}{m_i + m_e}(\boldsymbol{u}_i - \boldsymbol{u}_e)^2 + \nu_{ei}\rho_e \frac{m_i}{m_i + m_e}(\boldsymbol{u}_e - \boldsymbol{u}_i)^2 \\ &- 2\frac{k_B}{\gamma - 1}\nu_{in}\rho_i \frac{1}{m_i + m_n}(T_i - T_n) + \nu_{in}\rho_i \frac{m_n}{m_i + m_n}(\boldsymbol{u}_i - \boldsymbol{u}_n)^2 \\ &- 2\frac{k_B}{\gamma - 1}\nu_{en}\rho_e \frac{1}{m_e + m_n}(T_e - T_n) + \nu_{en}\rho_e \frac{m_n}{m_e + m_n}(\boldsymbol{u}_e - \boldsymbol{u}_n)^2 \end{aligned} \tag{B.67}$$

Apart from that we can also use the representation of the current density given in Eq. (2.39) to simplify the above results even further:

$$\begin{aligned}E_i + E_e = \eta \boldsymbol{J}^2 &- 2\frac{k_B}{\gamma - 1}\nu_{in}\rho_i \frac{1}{m_i + m_n}(T_i - T_n) + \nu_{in}\rho_i \frac{m_n}{m_i + m_n}(\boldsymbol{u}_i - \boldsymbol{u}_n)^2 \\ &- 2\frac{k_B}{\gamma - 1}\nu_{en}\rho_e \frac{1}{m_e + m_n}(T_e - T_n) + \nu_{en}\rho_e \frac{m_n}{m_e + m_n}(\boldsymbol{u}_e - \boldsymbol{u}_n)^2 \end{aligned} \tag{B.68}$$

Being finished, with the charged particle source terms we have to consider the collisional terms for neutral-charged particle interaction. For the temperature terms we have to use some assumption on how the electron and ion temperatures are related. For the velocities, however, we have to go from electron and ion velocities over to average charged particle velocities and current density using the relations (2.42) and (2.43). This yield:

$$\begin{aligned}&\nu_{in}\rho_i \frac{m_n}{m_i + m_n}(\boldsymbol{u}_i - \boldsymbol{u}_n)^2 + \nu_{en}\rho_e \frac{m_n}{m_e + m_n}(\boldsymbol{u}_e - \boldsymbol{u}_n)^2 \\ &=(\nu_{in}\mu_{in} + \nu_{en}\mu_{en})n(\boldsymbol{u} - \boldsymbol{u}_n)^2 + 2\frac{\mu}{e}\left(\frac{\nu_{in}m_n}{m_i + m_n} - \frac{\nu_{en}m_n}{m_e + m_n}\right)\boldsymbol{J}\cdot(\boldsymbol{u} - \boldsymbol{u}_n) \\ &+ \frac{\mu^2}{e^2 n}\left(\frac{\nu_{in}m_n}{m_i(m_i + m_n)} + \frac{\nu_{en}m_n}{m_e(m_e + m_n)}\right)\boldsymbol{J}^2 \end{aligned} \tag{B.69}$$

where we introduced the reduced masses:

$$\mu_{in} = \frac{m_i m_n}{m_i + m_n} \qquad \text{and} \qquad \mu_{en} = \frac{m_e m_n}{m_e + m_n}$$

To Eq. (B.69) we now add some of the other source terms containing the velocities:

$$\begin{aligned}&\nu_{in}\rho_i \frac{m_n}{m_i + m_n}(\boldsymbol{u}_i - \boldsymbol{u}_n)^2 + \nu_{en}\rho_e \frac{m_n}{m_e + m_n}(\boldsymbol{u}_e - \boldsymbol{u}_n)^2 - \nu_n\rho(\boldsymbol{u} - \boldsymbol{u}_n)^2 \\ &\quad - 2\frac{\mu}{e}\left(\nu_{in} - \nu_{en}\right)\boldsymbol{J}\cdot(\boldsymbol{u} - \boldsymbol{u}_n) - \frac{\mu^2}{e^2 n}\left(\frac{\nu_{in}}{m_i} + \frac{\nu_{en}}{m_e}\right)\boldsymbol{J}^2 \\ &= -\left(\frac{\nu_{in}m_i^2}{m_i + m_n} + \frac{\nu_{en}m_e^2}{m_e + m_n}\right)n(\boldsymbol{u} - \boldsymbol{u}_n)^2 - 2\frac{\mu}{e}\left(\frac{\nu_{in}m_i}{m_i + m_n} - \frac{\nu_{en}m_e}{m_e + m_n}\right)(\boldsymbol{u} - \boldsymbol{u}_n)\cdot\boldsymbol{J} \\ &\quad - \frac{\mu^2}{e^2 n}\left(\frac{\nu_{in}}{(m_i + m_n)} + \frac{\nu_{en}}{(m_e + m_n)}\right)\boldsymbol{J}^2 \end{aligned} \tag{B.70}$$

The collision terms connencting neutral and charged particles can still be simplified a little further. This, however, is not important at this point since these are exactly the terms also emerging in the evolution equation for the internal energy of the neutral fluid. Alse the discussion of the source term containing the electric field will be deferred to the point, when the magnetic energy is also included. So far we have the evolution equation:

$$
\begin{aligned}
&\frac{1}{\gamma-1}\frac{\partial p}{\partial t}+\frac{1}{2}\frac{\partial}{\partial t}\left(\rho u^2\right)+\nabla\cdot\left(\left(\frac{1}{\gamma-1}p+\frac{1}{2}\rho u^2+\mathsf{P}\right)\boldsymbol{u}\right)+\nabla\cdot\boldsymbol{q}\\
&\quad=-\nu_n\rho\boldsymbol{u}_n\cdot(\boldsymbol{u}-\boldsymbol{u}_n)-\frac{\mu}{e}\left(\nu_{in}-\nu_{en}\right)\boldsymbol{J}\cdot\boldsymbol{u}_n+\boldsymbol{J}\cdot\boldsymbol{E}\\
&\quad-2\frac{k_B}{\gamma-1}\rho_i\frac{\nu_{in}}{m_i+m_n}(T_i-T_n)-2\frac{k_B}{\gamma-1}\rho_e\frac{\nu_{en}}{m_e+m_n}(T_e-T_n)\\
&\quad-\left(\frac{\nu_{in}m_i^2}{m_i+m_n}+\frac{\nu_{en}m_e^2}{m_e+m_n}\right)n(\boldsymbol{u}-\boldsymbol{u}_n)^2-2\frac{\mu}{e}\left(\frac{\nu_{in}m_i}{m_i+m_n}-\frac{\nu_{en}m_e}{m_e+m_n}\right)(\boldsymbol{u}-\boldsymbol{u}_n)\cdot\boldsymbol{J}\\
&\quad-\frac{\mu^2}{e^2n}\left(\frac{\nu_{in}}{m_i+m_n}+\frac{\nu_{en}}{m_e+m_n}\right)\boldsymbol{J}^2
\end{aligned}
\tag{B.71}
$$

Now we are finally ready to put all results together into one evolution equation for the overall energy density.

B.3.3 Evolution Equation for the Energy Density

The evolution equation for the energy density of the ionised fluid can finally be found by putting the dynamic and the magnetic energy equations together. This sum leads to:

$$
\begin{aligned}
&\frac{\partial}{\partial t}\left(\frac{p}{\gamma-1}+\frac{1}{2}\rho u^2+\frac{B^2}{2\mu_0}\right)+\nabla\cdot\left(\left(\frac{p}{\gamma-1}+\frac{1}{2}\rho u^2+\frac{B^2}{\mu_0}+\mathsf{P}\right)\boldsymbol{u}\right)+\nabla\cdot\boldsymbol{q}-\frac{1}{\mu_0}(\boldsymbol{u}\cdot\boldsymbol{B})\boldsymbol{B}\\
&=-\nu_n\rho\boldsymbol{u}_n\cdot(\boldsymbol{u}-\boldsymbol{u}_n)-\frac{\mu}{e}\left(\nu_{in}-\nu_{en}\right)\boldsymbol{J}\cdot\boldsymbol{u}_n+\boldsymbol{J}\cdot(\boldsymbol{E}+\boldsymbol{u}\times\boldsymbol{B})-\frac{\boldsymbol{B}}{\mu_0}\cdot(\nabla\times\eta\boldsymbol{J})\\
&\quad-2\frac{k_B}{\gamma-1}\rho_i\frac{\nu_{in}}{m_i+m_n}(T_i-T_n)-2\frac{k_B}{\gamma-1}\rho_e\frac{\nu_{en}}{m_e+m_n}(T_e-T_n)\\
&\quad-\left(\frac{\nu_{in}m_i^2}{m_i+m_n}+\frac{\nu_{en}m_e^2}{m_e+m_n}\right)n(\boldsymbol{u}-\boldsymbol{u}_n)^2-2\frac{\mu}{e}\left(\frac{\nu_{in}m_i}{m_i+m_n}-\frac{\nu_{en}m_e}{m_e+m_n}\right)(\boldsymbol{u}-\boldsymbol{u}_n)\cdot\boldsymbol{J}\\
&\quad-\frac{\mu^2}{e^2n}\left(\frac{\nu_{in}}{m_i+m_n}+\frac{\nu_{en}}{m_e+m_n}\right)\boldsymbol{J}^2
\end{aligned}
\tag{B.72}
$$

By the application of Ohm's law to this equation we can get rid of some of the source terms. For this we can write:

$$
\boldsymbol{J}\cdot(\boldsymbol{E}+\boldsymbol{u}\times\boldsymbol{B})=\boldsymbol{J}\cdot(\eta\boldsymbol{J})=\eta\boldsymbol{J}\cdot\nabla\times\frac{\boldsymbol{B}}{\mu_0}=\nabla\cdot(\frac{\boldsymbol{B}}{\mu_0}\times\eta\boldsymbol{J})+\frac{\boldsymbol{B}}{\mu_0}\cdot(\nabla\times\eta\boldsymbol{J})
\tag{B.73}
$$

Taking this into account we are led to the resulting evolution equation for the overall energy density:

$$
\begin{aligned}
&\frac{\partial e}{\partial t}+\nabla\cdot\left(\left(e+\frac{B^2}{2\mu_0}+\mathsf{P}\cdot\right)\boldsymbol{u}+\boldsymbol{q}-\frac{1}{\mu_0}(\boldsymbol{u}\cdot\boldsymbol{B})\boldsymbol{B}+\eta\boldsymbol{J}\times\frac{\boldsymbol{B}}{\mu_0}\right)\\
&=-\nu_n\rho\boldsymbol{u}_n\cdot(\boldsymbol{u}-\boldsymbol{u}_n)-\frac{\mu}{e}\left(\nu_{in}-\nu_{en}\right)\boldsymbol{J}\cdot\boldsymbol{u}_n\\
&\quad-2\frac{k_B}{\gamma-1}\rho_i\frac{\nu_{in}}{m_i+m_n}(T_i-T_n)-2\frac{k_B}{\gamma-1}\rho_e\frac{\nu_{en}}{m_e+m_n}(T_e-T_n)\\
&\quad-\left(\frac{\nu_{in}}{m_i+m_n}\right)\frac{1}{n}\left(\rho_i(\boldsymbol{u}-\boldsymbol{u}_n)-\frac{\mu}{e}\boldsymbol{J}\right)^2-\left(\frac{\nu_{en}}{m_e+m_n}\right)\frac{1}{n}\left(\rho_e(\boldsymbol{u}-\boldsymbol{u}_n)+\frac{\mu}{e}\boldsymbol{J}\right)^2
\end{aligned}
\tag{B.74}
$$

Now we are left with the task to show that this is consistent with the energy equation for the neutral fluid, i.e. that the source terms are consistent to each other.

B.4 The Energy Equation for the Neutral Fluid

For the neutral fluid we luckily just have one momentum equation to consider. Apart from this we only have to take the internal energy into account, since the magnetic energy is already accounted for in the energy equation for the ionised species. Therefore, what we are looking for is an evolution equation for the quantity:

$$e_n = \frac{1}{2}\rho_n u_n^2 + \frac{p_n}{\gamma - 1} \tag{B.75}$$

Naturally the equation for the thermal energy of the neutral fluid is:

$$\frac{1}{\gamma-1}\frac{\partial p_n}{\partial t} = -\frac{1}{\gamma-1}\nabla\cdot(p_n\boldsymbol{u_n}) - (\mathsf{P}_n\cdot\nabla)\cdot\boldsymbol{u}_n - \nabla\cdot\boldsymbol{q}_n + E_n \tag{B.76}$$

A short derivation also yields the equation for the kinetic energy:

$$\frac{1}{2}\frac{\partial(\rho_n u_n^2)}{\partial t} = -\frac{1}{2}\nabla\cdot(\rho_n u_n^2\boldsymbol{u}_n) - \boldsymbol{u}_n\cdot\nabla\cdot\mathsf{P}_n + \nu_n\rho\boldsymbol{u}_n\cdot(\boldsymbol{u}-\boldsymbol{u}_n) + \frac{\mu}{e}(\nu_{in} - \nu en)\boldsymbol{u}_n\cdot\boldsymbol{J} \tag{B.77}$$

The sum of these two equations results in:

$$\frac{\partial e_n}{\partial t} + \nabla\cdot(e_n + \mathsf{P}\cdot)\boldsymbol{u}_n + \nabla\cdot\boldsymbol{q_n} = E_n + \nu_n\rho\boldsymbol{u}_n\cdot(\boldsymbol{u}-\boldsymbol{u}_n) + \frac{\mu}{e}(\nu_{in} - \nu en)\boldsymbol{u}_n\cdot\boldsymbol{J} \tag{B.78}$$

where the source term E_n is given consistently to the ones used in the energy equation for the ionised fluid above as:

$$\begin{aligned} E_n = &-2\frac{k_B}{\gamma-1}\nu_{ni}\rho_n\frac{1}{m_n+m_i}(T_n - T_i) + \nu_{ni}\rho_n\frac{m_i}{m_n+m_i}(\boldsymbol{u}_n - \boldsymbol{u}_i)^2 \\ &-2\frac{k_B}{\gamma-1}\nu_{ne}\rho_n\frac{1}{m_n+m_e}(T_n - T_e) + \nu_{ne}\rho_n\frac{m_e}{m_n+m_e}(\boldsymbol{u}_n - \boldsymbol{u}_e)^2 \end{aligned} \tag{B.79}$$

By usage of $\nu_{in}\rho_i = \nu_{ni}\rho_n$ and the corresponding relation for the electrons it is easy to show that the temperature terms exactly correspond to the one given in the energy equation for the ionised species. The velocity-terms, however, become a little more difficult:

$$\begin{aligned} E_n = &\quad 2\frac{k_B}{\gamma-1}\nu_{in}\rho_i\frac{1}{m_i+m_n}(T_i - T_n) + \nu_{in}\rho_i\frac{m_i}{m_n+m_i}(\boldsymbol{u}_i - \boldsymbol{u}_n)^2 \\ &+2\frac{k_B}{\gamma-1}\nu_{en}\rho_e\frac{1}{m_e+m_n}(T_e - T_n) + \nu_{en}\rho_e\frac{m_e}{m_n+m_e}(\boldsymbol{u}_e - \boldsymbol{u}_n)^2 \end{aligned} \tag{B.80}$$

Because things become quity messy for the velocity terms, we will dedicate the next paragraph just to this problem:

The Collision Terms

What we are looking at are the terms:

$$\nu_{in}\rho_i\frac{m_i}{m_n+m_i}(\boldsymbol{u}_i - \boldsymbol{u}_n)^2 + \nu_{en}\rho_e\frac{m_e}{m_n+m_e}(\boldsymbol{u}_e - \boldsymbol{u}_n)^2 \tag{B.81}$$

These are now transformed in a way as to get rid of the electron and proton velocities. Namely, we find:

$$\begin{aligned} &\nu_{in}\rho_i\frac{m_i}{m_n+m_i}(\boldsymbol{u}_i - \boldsymbol{u}_n)^2 + \nu_{en}\rho_e\frac{m_e}{m_n+m_e}(\boldsymbol{u}_e - \boldsymbol{u}_n)^2 \\ &= \left(\nu_{in}\rho_i\frac{m_i}{m_n+m_i} + \nu_{en}\rho_e\frac{m_e}{m_n+m_e}\right)(\boldsymbol{u} - \boldsymbol{u}_n)^2 + 2\left(\frac{\nu_{in}m_i}{m_n+m_i} - \frac{\nu_{en}m_e}{m_n+m_e}\right)\mu\boldsymbol{J}\cdot(\boldsymbol{u} - \boldsymbol{u}_n) \\ &\quad + \frac{\mu^2}{e^2 n}\left(\frac{\nu_{in}}{m_n+m_i} + \frac{\nu_{en}}{m_n+m_e}\right)\boldsymbol{J}^2 \end{aligned} \tag{B.82}$$

This term is clearly identical to the one found in the energy equation for the ionised fluid. Therefore, we are now able to give the system of equations applicable to a partly ionised fluid:

B.5 The MHD Equations for a Partly Ionised Fluid

Summarising what was computed above, the system of MHD-equations for a partly ionised fluid, where only elastic collisions are taken into account, reads:

For the continuity equation:

$$\frac{\partial \rho}{\partial t} + \nabla \cdot (\rho \boldsymbol{u}) = 0 \qquad \text{(ionised fluid)} \tag{B.83}$$

$$\frac{\partial \rho_n}{\partial t} + \nabla \cdot (\rho_n \boldsymbol{u}_n) = 0 \qquad \text{(neutral fluid)} \tag{B.84}$$

For the momentum equation:

$$\frac{\partial (\rho \boldsymbol{u})}{\partial t} + \nabla \cdot (\rho \boldsymbol{u}\boldsymbol{u}) + \nabla \cdot \mathsf{P} + \nabla \cdot \left(\frac{B^2}{2\mu_0}\mathsf{1} - \frac{\boldsymbol{B}\boldsymbol{B}}{\mu_0} \right) = -\, \nu_n \rho (\boldsymbol{u} - \boldsymbol{u}_n) - \frac{\mu}{e} \left(\nu_{in} - \nu_{en} \right) \boldsymbol{J} \qquad \text{(ionised fluid)} \tag{B.85}$$

$$\frac{\partial (\rho_n \boldsymbol{u}_n)}{\partial t} + \nabla \cdot (\rho_n \boldsymbol{u}_n \boldsymbol{u}_n) + \nabla \cdot \mathsf{P}_n = \ \nu_n \rho (\boldsymbol{u} - \boldsymbol{u}_n) + \frac{\mu}{e} \left(\nu_{in} - \nu_{en} \right) \boldsymbol{J} \qquad \text{(neutral fluid)} \tag{B.86}$$

For the energy equation:

$$\frac{\partial e}{\partial t} + \nabla \cdot \left(\left(e + \frac{B^2}{2\mu_0} + \mathsf{P}\cdot \right) \boldsymbol{u} + \boldsymbol{q} - \frac{1}{\mu_0} (\boldsymbol{u} \cdot \boldsymbol{B}) \boldsymbol{B} + \eta \boldsymbol{J} \times \frac{\boldsymbol{B}}{\mu_0} \right) = -S_{ien} \qquad \text{(ionised fluid)} \tag{B.87}$$

$$\frac{\partial e_n}{\partial t} + \nabla \cdot (e_n + \mathsf{P}\cdot) \boldsymbol{u}_n + \nabla \cdot \boldsymbol{q}_n = \ S_{ien} \qquad \text{(neutral fluid)} \tag{B.88}$$

with the correponding source terms:

$$\begin{aligned} S_{ien} =& \nu_n \rho \boldsymbol{u}_n \cdot (\boldsymbol{u} - \boldsymbol{u}_n) + \frac{\mu}{e} \left(\nu_{in} - \nu_{en} \right) \boldsymbol{J} \cdot \boldsymbol{u}_n \\ &+ 2 \frac{k_B}{\gamma - 1} \rho_i \frac{\nu_{in}}{m_i + m_n} (T_i - T_n) + 2 \frac{k_B}{\gamma - 1} \rho_e \frac{\nu_{en}}{m_e + m_n} (T_e - T_n) \\ &+ \left(\frac{\nu_{in}}{m_i + m_n} \right) \frac{1}{n} \left(\rho_i (\boldsymbol{u} - \boldsymbol{u}_n) - \frac{\mu}{e} \boldsymbol{J} \right)^2 + \left(\frac{\nu_{en}}{m_e + m_n} \right) \frac{1}{n} \left(\rho_e (\boldsymbol{u} - \boldsymbol{u}_n) + \frac{\mu}{e} \boldsymbol{J} \right)^2 \end{aligned} \tag{B.89}$$

This system is supplemented by an equation describing the evolution of the magnetic induction:

$$\frac{\partial \boldsymbol{B}}{\partial t} = \nabla \times (\boldsymbol{u} \times \boldsymbol{B}) + \frac{1}{\mu_0} \left(\eta \nabla^2 \boldsymbol{B} - (\nabla \eta) \times (\nabla \times \boldsymbol{B}) \right) \tag{B.90}$$

$$= -\nabla \cdot (\boldsymbol{u}\boldsymbol{B} - \boldsymbol{B}\boldsymbol{u}) + \frac{1}{\mu_0} \left(\eta \nabla^2 \boldsymbol{B} - (\nabla \eta) \times (\nabla \times \boldsymbol{B}) \right) \tag{B.91}$$

With this summary we conclude the derivation of the evolution equation for the partly ionised plasma.

Appendix C

Normalisation of the Charged Particle Fluid Equations

In this paragraph we will show how to normalise the individual evolution equations at the example of the charged particle fluid. For the neutral fluid exactly the same procedure has to be followed. Here we will discuss the corresponding equations one by one.

C.1 Equation of Continuity

The equation of continuity is rewritten using the normalisation given in table 2.8.1 as:

$$\frac{\rho_0}{\tau_0}\frac{\partial\tilde{\rho}}{\partial\tilde{t}} = -\frac{\rho_0 u_0}{L}\tilde{\nabla}\cdot\tilde{\boldsymbol{s}} \tag{C.1}$$

where we introduced the normalised mass-flux:

$$\tilde{\boldsymbol{s}} = \tilde{\rho}\tilde{\boldsymbol{u}} \tag{C.2}$$

With the above definitions the continuity-equation can be reduced to:

$$\frac{\partial\tilde{\rho}}{\partial\tilde{t}} = -\tilde{\nabla}\cdot\tilde{\boldsymbol{s}} \tag{C.3}$$

The next equation we attend to is the induction equation.

C.2 Induction Equation

The induction equation reads using the normalised quantities:

$$\frac{B_0}{\tau_0}\frac{\partial\tilde{\boldsymbol{B}}}{\partial\tilde{t}} = -\frac{B_0\rho_0 u_0}{\rho_0 L}\tilde{\nabla}\cdot\left(\frac{\tilde{\boldsymbol{s}}\tilde{\boldsymbol{B}}-\tilde{\boldsymbol{B}}\tilde{\boldsymbol{s}}}{\tilde{\rho}}\right) \tag{C.4}$$

which can be abbreviated to give:

$$\frac{\partial\tilde{\boldsymbol{B}}}{\partial\tilde{t}} = -\tilde{\nabla}\cdot\left(\frac{\tilde{\boldsymbol{s}}\tilde{\boldsymbol{B}}-\tilde{\boldsymbol{B}}\tilde{\boldsymbol{s}}}{\tilde{\rho}}\right) \tag{C.5}$$

In the next subsection we will discuss the momentum equation, before finally transforming the evolution equation for the total energy density.

C.3 Momentum Equation

The momentum equation translates into the form:

$$\frac{\rho_0 u_0}{\tau_0}\frac{\partial \tilde{\mathbf{s}}}{\partial \tilde{t}} = -\tilde{\nabla}\cdot\left(\frac{\rho_0^2 u_0^2}{\rho_0 L}\frac{\tilde{\mathbf{s}}\tilde{\mathbf{s}}}{\tilde{\rho}} + \left(\frac{P_0}{L}\tilde{P} + \frac{B_0^2}{L}\frac{\tilde{B}^2}{2\mu_0}\right)\mathbf{1} - \frac{B_0^2}{L}\frac{\tilde{\boldsymbol{B}}\tilde{\boldsymbol{B}}}{\mu_0}\right) + \boldsymbol{A}_{ien} \tag{C.6}$$

This yields:

$$\frac{\partial \tilde{\mathbf{s}}}{\partial \tilde{t}} = -\tilde{\nabla}\cdot\left(\frac{\tilde{\mathbf{s}}\tilde{\mathbf{s}}}{\tilde{\rho}} + \left(\frac{P_0}{\rho_0 u_0^2}\tilde{P} + \frac{B_0^2}{\mu_0\rho_0 u_0^2}\frac{\tilde{B}^2}{2}\right)\mathbf{1} - \frac{B_0^2}{\mu_0\rho_0 u_0^2}\tilde{\boldsymbol{B}}\tilde{\boldsymbol{B}}\right) + \tilde{\boldsymbol{A}}_{ien} \tag{C.7}$$

At first sight it looks like this result strongly depends on the choice for the velocity normalisation. However, in both cases discussed here we have:

$$p_0 = \rho_0 u_0^2 \qquad \text{and} \qquad B_0 = \sqrt{\mu_0\rho_0 u_0^2} \tag{C.8}$$

Therefore we find for the normalised momentum equation:

$$\frac{\partial \tilde{\mathbf{s}}}{\partial \tilde{t}} = -\tilde{\nabla}\cdot\left(\frac{\tilde{\mathbf{s}}\tilde{\mathbf{s}}}{\tilde{\rho}} + \left(\tilde{P} + \frac{\tilde{B}^2}{2}\right)\mathbf{1} - \tilde{\boldsymbol{B}}\tilde{\boldsymbol{B}}\right) + \tilde{\boldsymbol{A}}_{ien} \tag{C.9}$$

The final equation to be discussed is the equation for the evolution of the energy density.

C.4 Evolution of the Energy Density

As already given in tables 2.8.1 and the normalisation for the total energy density is naturally given by dimensional analysis as:

$$e_0 = \rho_0 u_0^2 \tag{C.10}$$

This can also be seen directly from the equation for the total energy density:

$$\begin{aligned} e = e_0\tilde{e} = \frac{\rho u^2}{2} + \frac{B^2}{2\mu_0} + \frac{p}{\gamma-1} &= \rho_0 u_0^2\frac{\tilde{\rho}\,\tilde{u}^2}{2} + \frac{B_0^2}{\mu}\frac{\tilde{B}^2}{2} + p_0\frac{\tilde{p}}{\gamma-1} \\ &= \rho_0 u_0^2\left(\frac{\tilde{\rho}\,\tilde{u}^2}{2} + \frac{\tilde{B}^2}{2} + \frac{\tilde{p}}{\gamma-1}\right) \end{aligned} \tag{C.11}$$

Thus, we find for the normalised total energy density:

$$\tilde{e} = \frac{\tilde{\rho}\,\tilde{u}^2}{2} + \frac{\tilde{B}^2}{2} + \frac{\tilde{p}}{\gamma-1} \tag{C.12}$$

Now we proceed to the normalisation for the evolution equation itself:

$$\frac{e_0}{\tau_0}\frac{\partial \tilde{e}}{\partial t} = -\nabla\cdot\left(\left(\frac{u_0 p_0}{L}\tilde{e} + \frac{u_0 p_0}{L}\tilde{\mathsf{P}}\cdot + \frac{u_0 B_0^2}{L}\frac{\tilde{B}^2}{2\mu_0}\right)\tilde{\mathbf{s}} - \frac{u_0 B_0^2}{\mu_0}(\tilde{\mathbf{s}}\cdot\tilde{\boldsymbol{B}})\tilde{\boldsymbol{B}}\right)\frac{1}{\tilde{\rho}} + S_e \tag{C.13}$$

In the same way as it was done for the momentum equation his can be recast into the form:

$$\frac{\partial \tilde{e}}{\partial t} = -\nabla\cdot\left(\left(\tilde{e} + \tilde{\mathsf{P}}\cdot + \frac{\tilde{B}^2}{2}\right)\tilde{\mathbf{s}} - (\tilde{\mathbf{s}}\cdot\tilde{\boldsymbol{B}})\tilde{\boldsymbol{B}}\right)\frac{1}{\tilde{\rho}} + \tilde{S}_e \tag{C.14}$$

This concludes the derivation of the normalised form of the evoltion equations.

Appendix D

Characteristic Velocities

For the derivation of the characteristic velocities we will intensely investigate the hydrodynamic equations. These read in conservative form:

$$\partial_t \boldsymbol{U} = \partial_t \begin{pmatrix} \rho \\ \rho u_x \\ \rho u_y \\ \rho u_z \end{pmatrix} = -\nabla \cdot \begin{pmatrix} \rho \boldsymbol{u} \\ \left(\frac{\rho u_x \rho \boldsymbol{u}}{\rho} + p\boldsymbol{e}_x\right) \\ \left(\frac{\rho u_y \rho \boldsymbol{u}}{\rho} + p\boldsymbol{e}_y\right) \\ \left(\frac{\rho u_z \rho \boldsymbol{u}}{\rho} + p\boldsymbol{e}_z\right) \end{pmatrix} \tag{D.1}$$

where we closed the system via the adiabatic equation of state since source terms are not of interest here. The characteristic velocities of the flow are obtained using the quasi-linear form of the evolution equations. This is obtained via differentiation of the corresponding flux functions. For the above three-dimensional system this yields:

$$\partial_t \boldsymbol{U} = - \begin{pmatrix} \partial_x(\rho u_x) + \partial_y(\rho u_y) + \partial_z(\rho u_z) \\ u_x \nabla \cdot (\rho \boldsymbol{u}) + u_x \partial_x(\rho u_x) - u_x^2 \partial_x \rho + u_y \partial_y(\rho u_x) - u_x u_y \partial_y \rho + u_z \partial_z(\rho u_x) - u_x u_z \partial_z \rho + \gamma \frac{p}{\rho} \partial_x \rho \\ u_y \nabla \cdot (\rho \boldsymbol{u}) + u_x \partial_x(\rho u_y) - u_x u_y \partial_x \rho + u_y \partial_y(\rho u_y) - u_y^2 \partial_y \rho + u_z \partial_z(\rho u_y) - u_y u_z \partial_z \rho + \gamma \frac{p}{\rho} \partial_y \rho \\ u_z \nabla \cdot (\rho \boldsymbol{u}) + u_x \partial_x(\rho u_z) - u_x u_z \partial_x \rho + u_y \partial_y(\rho u_z) - u_z u_y \partial_y \rho + u_z \partial_z(\rho u_z) - u_z^2 \partial_z \rho + \gamma \frac{p}{\rho} \partial_z \rho \end{pmatrix} \tag{D.2}$$

From this one easily finds the general form:

$$\frac{\partial \boldsymbol{U}}{\partial t} = -\mathsf{J}_x(\boldsymbol{U}) \cdot \frac{\partial \boldsymbol{U}}{\partial x} - \mathsf{J}_y(\boldsymbol{U}) \cdot \frac{\partial \boldsymbol{U}}{\partial y} - \mathsf{J}_z(\boldsymbol{U}) \cdot \frac{\partial \boldsymbol{U}}{\partial z} \tag{D.3}$$

with the corresponding Jacobians for each direction:

$$\mathsf{J}_x = \begin{pmatrix} 0 & 1 & 0 & 0 \\ -u_x^2 + \gamma p/\rho & 2u_x & 0 & 0 \\ -u_x u_y & u_y & u_x & 0 \\ -u_x u_z & u_z & 0 & u_x \end{pmatrix} \qquad \mathsf{J}_y = \begin{pmatrix} 0 & 0 & 1 & 0 \\ -u_x u_y & u_y & u_y & 0 \\ -u_y^2 + \gamma p/\rho & 0 & 2u_y & 0 \\ -u_y u_z & 0 & u_z & u_y \end{pmatrix}$$
$$\mathsf{J}_z = \begin{pmatrix} 0 & 0 & 0 & 1 \\ -u_x u_z & u_z & 0 & u_x \\ -u_y u_z & 0 & u_z & u_y \\ -u_z^2 + \gamma p/\rho & 0 & 0 & 2u_z \end{pmatrix} \tag{D.4}$$

Now, whenever $\frac{\partial \boldsymbol{U}}{\partial x}$ is an eigenvector of J_x the system of equations holds the possibility of wave propagation along the x-direction – with the corresponding statement for the other directions. This picture originates from the analysis of linear systems, where such a result means, that the structures propagate with unchanged form in the whole domain of interest. Therefore, the corresponding possible wave speeds in the x-direction are naturally given by the eigenvalues of J_x. For this the characteristic polynomial of J_x can with very little algebra be found to be:

$$P_x = -(\lambda - u_x)^2(\lambda^2 - 2u_x\lambda + u_x^2 - \gamma p/\rho) \tag{D.5}$$

With the identification of the speed of sound c_s as:

$$c_s = \sqrt{\gamma p/\rho} \tag{D.6}$$

the eigenvalues are most easily identified to be:

$$\lambda_{1,2} = u_x \tag{D.7}$$

$$\lambda_{3,4} = u_x \pm c_s \tag{D.8}$$

Here the eigenspace corresponding to $\lambda_{1,2} = u_x$ is two-dimensional since these eigenvalues represent shear waves being propagated in either the y- or the z-direction. For the MHD equation the algebra gets a little more messy, but the results are obtained in a similar way as for the hydrodynamical equations.

Velocities for MHD

The characteristic velocities for the normalised MHD equations are obtained in a very similar way as they are for the hydrodynamic system. With a similar transformation of the system of equations as in the preceding chapter we find for the Jacobian for the x-direction:

$$\mathsf{J}_x = \begin{pmatrix} 0 & 1 & 0 & 0 & 0 & 0 & 0 \\ -u_x^2 + \gamma p/\rho & 2u_x & 0 & 0 & -B_x & B_y & B_z \\ -u_x u_y & u_y & u_x & 0 & -B_y & -B_x & 0 \\ -u_x u_z & u_z & 0 & u_x & -B_z & 0 & -B_x \\ 0 & 0 & 0 & 0 & u_x & 0 & 0 \\ (u_x B_x - u_x B_y)/\rho & B_y/\rho & -B_x/\rho & 0 & 0 & u_x & 0 \\ (u_z B_x - u_x B_z)/\rho & B_z/\rho & 0 & -B_x/\rho & 0 & 0 & u_x \end{pmatrix} \tag{D.9}$$

From this the characteristic velocities can, again, be found as the eigenvalues. Thus, we find for these for the x-direction:

$$\lambda_1 = u_x \tag{D.10}$$

$$\lambda_{2,3} = u_x \pm \mathrm{v}_{A_x} \tag{D.11}$$

$$\lambda_{4,5} = u_x \pm \mathrm{v}_{f_x} \tag{D.12}$$

$$\lambda_{6,7} = u_x \pm \mathrm{v}_{s_x} \tag{D.13}$$

together with the definitions:

$$c_s := \sqrt{\frac{\mathrm{d}p}{\mathrm{d}\rho}} = \sqrt{\gamma \frac{p}{\rho}} \qquad \text{speed of sound} \tag{D.14}$$

$$\mathrm{v}_A := \frac{B}{\sqrt{\rho}} \qquad \left(\mathrm{v}_{A_x} := \frac{B_x}{\sqrt{\rho}}\right) \qquad \text{Alfvén speed (in } x\text{-direction)} \tag{D.15}$$

$$\mathrm{v}_{f_x} := \frac{1}{\sqrt{2}} \sqrt{c_s^2 + \mathrm{v}_A^2 + \sqrt{(c_s^2 + \mathrm{v}_A^2)^2 - (2c_s \mathrm{v}_{A_x})^2}} \qquad \text{fast magnetosonic speed in } x\text{-direction} \tag{D.16}$$

$$\mathrm{v}_{s_x} := \frac{1}{\sqrt{2}} \sqrt{c_s^2 + \mathrm{v}_A^2 - \sqrt{(c_s^2 + \mathrm{v}_A^2)^2 - (2c_s \mathrm{v}_{A_x})^2}} \qquad \text{slow magnetosonic speed in } x\text{-direction} \tag{D.17}$$

Thus, we see, that also the system of the MHD equations is strictly hyperbolic. A matter unaccounted for so far, however, is the fact that different ways to present the Jacobian also leads to different values for the characteristic velocities. The Jacobian can easily be transformed to the the shape given in Kleimann (2005). This is done by using:

$$\nabla \cdot \boldsymbol{B} = 0 \tag{D.18}$$

Even though, the system described by the resulting equations is identical to the one under consideration here, the resulting characteristic velocities differ. Whereas it is just λ_1 being different – namely one arrives at $\lambda_1 = 0$ in that case (see Kleimann 2005) – this result seems to be unphysical as compared to the result given here: Waves propagating with $-u_x$ against the background flow u_x are not expected for possibly supersonic fluid flow.

Bibliography

Armstrong, J. W., Rickett, B. J. and Spangler, S. R. Electron density power spectrum in the local interstellar medium. *ApJ*, **443**, 209, 1995

Assous, F., Degond, P., Heintze, E., Raviart, P. A. and Segre, J. On a finite-element method for solving the three-dimensional Maxwell equations. *J. Comput. Phys.*, **109**(2), 222, 1993

Bakes, E. L. O. and Tielens, A. G. G. M. The photoelectric heating mechanism for very small graphitic grains and polycyclic aromatic hydrocarbons. *ApJ*, **427**, 822, 1994

Balsara, D. S. and Kim, J. A Comparison between Divergence-Cleaning and Staggered-Mesh Formulations for Numerical Magnetohydrodynamics. *ApJ*, **602**, 1079, 2004

Balsara, D. S. and Spicer, D. S. A staggered mesh algorithm using high order Godunov fluxes to ensure solenodial magnetic fields in magnetohydrodynamic simulations. *J. Comput. Phys.*, **149**(2), 270, 1999

Benzi, R., Ciliberto, S., Tripiccione, R., Baudet, C., Massaioli, F. and Succi, S. Extended self-similarity in turbulent flows. *Phys. Rev. E*, **48**(1), R29, 1993

Bittencourt, J. A. *Fundamentals of Plasma Physics*. Fundamentals of Plasma Physics, Third Edition by J.A. Bittencourt. Published by Springer-Verlag, New York, Inc.; 2004. ISBN 0-387-20975-1., 2004

Blevins, R. D. *Applied fluid dynamics handbook*. New York, Van Nostrand Reinhold Co., 1984, 568 p., 1984

Boldyrev, S., Nordlund, Å. and Padoan, P. Scaling Relations of Supersonic Turbulence in Star-forming Molecular Clouds. *ApJ*, **573**, 678, 2002

Brackbill, J. U. and Barnes, D. C. The effect of nonzero product of magnetic gradient and B on the numerical solution of the magnetohydrodynamic equations. *J. Comp. Phys.*, **35**, 426, 1980

Breitschwerdt, D. and de Avillez, M. A. The history and future of the Local and Loop I bubbles. *A&A*, **452**, L1, 2006

Brio, M. and Wu, C. C. An upwind differencing scheme for the equations of ideal magnetohydrodynamics. *Journal of Computational Physics*, **75**, 400, 1988

Bronstein, N., I., Semendjajew, A., K., Musiol, G. and Mühlig, H. *Taschenbuch der Mathematik*. Verlag Harri Deutsch, 3 edition, 1997

Burgers, M. A mathematical model illustrating the theory of turbulence. *Adv. Appl. Math.*, **1**, 1, 1948

Chorin, A. J. A numerical method for solving incompressible viscous flow problems. *J. Comput. Phys.*, **2**(1), 12, 1967

Chorin, A. J. Numerical solution of the Navier-Stokes equations. *Math. Comp.*, **22**(104), 745, 1968

Chorin, A. J. On the Convergence of Discrete Approximations to the Navier-Stokes Equations. *Math. Comp.*, **23**(106), 341, 1969

Christensson, M., Hindmarsh, M. and Brandenburg, A. Inverse cascade in decaying three-dimensional magnetohydrodynamic turbulence. *Phys. Rev. E*, **64**(5), 056405, 2001

Courant, R., Friedrichs, K. and Lewy, H. Über die partiellen Differenzengleichungen der mathematischen Physik. *Math. Ann.*, **100**, 32, 1928

Cox, D. P. The Three-Phase Interstellar Medium Revisited. *ARA&A*, **43**, 337, 2005

Cox, D. P. and Tucker, W. H. Ionization Equilibrium and Radiative Cooling of a Low-Density Plasma. *ApJ*, **157**, 1157, 1969

Dalgarno, A. and McCray, R. A. Heating and Ionization of HI Regions. *ARA&A*, **10**, 375, 1972

de Avillez, M. and Breitschwerdt, D. MHD Simulations of the ISM: The Importance of the Galactic Magnetic Field on the ISM "Phases". *Ap&SS*, **292**, 207, 2004

de Avillez, M. A. Disc-halo interaction - I. Three-dimensional evolution of the Galactic disc. *MNRAS*, **315**, 479, 2000

de Sterck, H., Low, B. C. and Poedts, S. Characteristic analysis of a complex two-dimensional magnetohydrodynamic bow shock flow with steady compound shocks. *Physics of Plasmas*, **6**, 954, 1999

Dedner, A., Kemm, F., Kröner, D., Munz, C.-D., Schnitzer, T. and Wesenberg, M. Hyperbolic divergence cleaning for the MHD equations. *J. Comput. Phys.*, **175**(2), 645, 2002

Deshpande, A. A., Dwarakanath, K. S. and Goss, W. M. Power Spectrum of the Density of Cold Atomic Gas in the Galaxy toward Cassiopeia A and Cygnus A. *ApJ*, **543**, 227, 2000

Dobler, W., Haugen, N. E., Yousef, T. A. and Brandenburg, A. Bottleneck effect in three-dimensional turbulence simulations. *Phys. Rev. E*, **68**(2), 026304, 2003

Dubrulle, B. Intermittency in fully developed turbulence: Log-Poisson statistics and generalized scale covariance. *Phys. Rev. Lett.*, **73**(7), 959, 1994

Dyson, J. E. and Williams, D. A. *The physics of the interstellar medium*. The physics of the interstellar medium. Edition: 2nd ed. Publisher: Bristol: Institute of Physics Publishing, 1997. Edited by J. E. Dyson and D. A. Williams. Series: The graduate series in astronomy. ISBN: 0750303069, 1997

Elmegreen, B. G. The Origin and Evolution of Giant Molecular Clouds. In: C. J. Lada and N. D. Kylafis (Editors), *NATO ASIC Proc. 342: The Physics of Star Formation and Early Stellar Evolution*, 35–+. 1991

Elmegreen, B. G. and Scalo, J. Interstellar Turbulence I: Observations and Processes. *ARA&A*, **42**, 211, 2004

Evans, C. R. and Hawley, J. F. Simulation of magnetohydrodynamic flows - A constrained transport method. *ApJ*, **332**, 659, 1988

Field, G. B. Thermal Instability. *ApJ*, **142**, 531, 1965

Field, G. B., Goldsmith, D. W. and Habing, H. J. Cosmic-Ray Heating of the Interstellar Gas. *ApJ*, **155**, L149+, 1969

Fletcher, A. and Shukurov, A. Canals in Milky Way radio polarization maps. *MNRAS*, **371**, L21, 2006a

Fletcher, A. and Shukurov, A. Depolarization canals and interstellar turbulence. *ArXiv Astrophysics e-prints*, 2006b

Frigo, M. A fast Fourier transform compiler. *SIGPLAN Not.*, **39**(4), 642, 2004

Frisch, U. *Turbulence. The legacy of A.N. Kolmogorov*. Cambridge: Cambridge University Press, —c1995, 1995

Frisch, U., Sulem, P.-L. and Nelkin, M. A simple dynamical model of intermittent fully developed turbulence. *Journal of Fluid Mechanics*, **87**, 719, 1978

Gerritsen, J. P. E. and Icke, V. Star formation in N-body simulations. I. The impact of the stellar ultraviolet radiation on star formation. *A&A*, **325**, 972, 1997

Glassgold, A. E., Krstić, P. S. and Schultz, D. R. H^++H Scattering and Ambipolar Diffusion Heating. *ApJ*, **621**, 808, 2005

Godunov, S. K. Finite difference method for numerical computation of discontinuous solution of the equations of fluid dynamics. *Mat. Sb.*, **47**, 271, 1959

Habing, H. J. The interstellar radiation density between 912 A and 2400 A. *Bull. Astron. Inst. Netherlands*, **19**, 421, 1968

Haverkorn, M. and Heitsch, F. Canals beyond Mars: Beam depolarization in radio continuum maps of the warm ISM. *A&A*, **421**, 1011, 2004

Herweijer, J. and van de Water, W. Universal Shape of Scaling Functions in Turbulence. *Phys. Rev. Lett.*, **74**(23), 4651, 1995

Hosking, J. G. and Whitworth, A. P. Modelling ambipolar diffusion with two-fluid smoothed particle hydrodynamics. *MNRAS*, **347**, 994, 2004

Jiang, G.-S. and Shu, C.-W. Efficient Implementation of Weighted ENO Schemes. *J. Comp. Phys.*, **126**, 202, 1996

Kalikhman, L. E. *Elements of Magnetogasdynamics*. W. B. Saunders Company (Philadelphia and London), 1967

Kim, J. and Ryu, D. Density Power Spectrum of Compressible Hydrodynamic Turbulent Flows. *ApJ*, **630**, L45, 2005

Kissmann, R. and Grauer, R. A low dissipation essentially non-oscillatory central scheme. *Comp. Phys. Comm.*, in press, 2006

Kleimann, J. *MHD-Modellierung der Dydnamik der solaren Korona*. Ph.D. thesis, Ruhr-Universität Bochum, 2005

Kleimann, J., Kopp, A., Fichtner, H., Grauer, R. and Germaschewski, K. Three-dimensional MHD high-resolution computations with CWENO employing adaptive mesh refinement. *Comp. Phys. Comm.*, **158**, 47, 2004

Kolmogorov, A. N. Dissipation of energy in locally isotropic turbulence (in Russian). *Dokl. Akad. Nauk. SSSR.*, **32**, 16, 1941a

Kolmogorov, A. N. Local structure of turbulence in an incompressible fluid at very high Reynolds numbers (in Russian). *Dokl. Akad. Nauk. SSSR.*, **30**, 299, 1941b

Kolmogorov, A. N. A refinement of previous hypotheses concerning the local structure of turbulence in a viscous incompressible fluid at high Reynolds number. *J. Fluid Mech*, **13**, 82, 1962

Kurganov, A. and Levy, D. A Third-Order Semidiscrete Central Scheme for Conservation Laws and Convection-Diffusion Equations. *SIAM J. Sci. Comput.*, **22**, 1461, 2000

Kurganov, A., Noelle, S. and Petrova, G. Semidiscrete Central-Upwind Schemes for Hyperbolic Conservation Laws and Hamilton–Jacobi Equations. *SIAM J. Sci. Comput.*, **23**(3), 707, 2001

Landau, L. D. and Lifshitz, E. M. *Fluid mechanics (Course of Theoretical Physics)*. Butterworth-Heinemann Ltd (31 Jul 1987), 1987

Leveque, J., Randall. *Numerical Methods for Conservation Laws*. Birkhäuser Verlag, Basel, 1992

Lizano, S. and Shu, F. H. Molecular cloud cores and bimodal star formation. *ApJ*, **342**, 834, 1989

Longair, M. S. *High energy astrophysics. Vol.2: Stars, the galaxy and the interstellar medium*. Cambridge: Cambridge University Press, —c1994, 2nd ed., 1994

Merrifield, J. A., Müller, W.-C., Chapman, S. C. and Dendy, R. O. The scaling properties of dissipation in incompressible isotropic three-dimensional magnetohydrodynamic turbulence. *Phys. of Plasmas*, **12**, 1, 2005

Minter, A. H. and Spangler, S. R. Heating of the Interstellar Diffuse Ionized Gas via the Dissipation of Turbulence. *ApJ*, **485**, 182, 1997

Nessyahu, H. and Tadmor, E. Non-oscillatory central differencing for hyperbolic conservation laws. *J. Comp. Phys.*, **87**, 408, 1990

Padoan, P., Jimenez, R., Juvela, M. and Nordlund, Å. The Average Magnetic Field Strength in Molecular Clouds: New Evidence of Super-Alfvénic Turbulence. *ApJ*, **604**, L49, 2004

Pareschi, L., Puppo, G. and Russo, G. Central Runge–Kutta Schemes for Conservation Laws. *SIAM Journal on Scientific Computing*, **26**(3), 979, 2005

Penston, M. V. Cooling Mechanisms in the Interstellar Gas. *ApJ*, **162**, 771, 1970

Qiu, J. and Shu, C.-W. On The Construction, Comparison, and Local Characteristic Decomposition for High-Order Central WENO Schemes. *J. Comp. Phys.*, **183**, 187, 2002

Reynolds, R. J. Diffuse Optical Emission Lines as Probes of the Interstellar and Intergalactic Ionizing Radiation. In: A. Ferrara, C. F. McKee, C. Heiles and P. R. Shapiro (Editors), *ASP Conf. Ser. 80: The Physics of the Interstellar Medium and Intergalactic Medium*, 388–+. 1995

Reynolds, R. J., Haffner, L. M. and Tufte, S. L. Evidence for an Additional Heat Source in the Warm Ionized Medium of Galaxies. *ApJ*, **525**, L21, 1999

Ryu, D. and Jones, T. W. Numerical magetohydrodynamics in astrophysics: Algorithm and tests for one-dimensional flow‘. *ApJ*, **442**, 228, 1995

Ryu, D., Jones, T. W. and Frank, A. Numerical Magnetohydrodynamics in Astrophysics: Algorithm and Tests for Multidimensional Flow. *ApJ*, **452**, 785, 1995

Schlickeiser, R. On the interplanetary transport of solar cosmic rays. *J. Geophys. Res.*, **93**, 2725, 1988

Schlickeiser, R. Cosmic-ray transport and acceleration. I - Derivation of the kinetic equation and application to cosmic rays in static cold media. II - Cosmic rays in moving cold media with application to diffusive shock wave acceleration. *ApJ*, **336**, 243, 1989

Schröer, A., Birk, G. T. and Kopp, A. DENISIS - A three-dimensional partially ionized dusty magnetoplasma code. *Computer Physics Communications*, **112**, 7, 1998

Sedov, L. I. *Similarity and Dimensional Methods in Mechanics*. Academic Press, New York, 1959

She, Z.-S. and Leveque, E. Universal scaling laws in fully developed turbulence. *Phys. Rev. Lett.*, **72**(3), 336, 1994

Shukurov, A. and Berkhuijsen, E. M. Faraday ghosts: depolarization canals in the Galactic radio emission. *MNRAS*, **342**, 496, 2003

Snow, T. P. and McCall, B. J. Diffuse Atomic and Molecular Clouds. *ARA&A*, **44**, 367, 2006

Sod, G. A survey of several finite difference methods for systems of nonlinear hyperbolic conservation laws. *J. Comput. Phys.*, **27**, 1, 1978

Song, P., Gombosi, T. I. and Ridley, A. J. Three-fluid Ohm's law. *J. Geophys. Res.*, **106**, 8149, 2001

Spangler, S. R. The dissipation of magnetohydrodynamic turbulence responsible for interstellar scintillation and the heating of the interstellar medium. *ApJ*, **376**, 540, 1991

Spanier, F. and Schlickeiser, R. Damping and wave energy dissipation in the interstellar medium. II. Fast magnetosonic waves. *A&A*, **436**, 9, 2005

Stone, J. M., Hawley, J. F., Evans, C. R. and Norman, M. L. A test suite for magnetohydrodynamical simulations. *ApJ*, **388**, 415, 1992

Stone, J. M., Ostriker, E. C. and Gammie, C. F. Dissipation in Compressible Magnetohydrodynamic Turbulence. *ApJ*, **508**, L99, 1998

Strang, G. On the Construction and Comparison of Difference Schemes. *SIAM Journal on Numerical Analysis*, **5**(3), 506, 1968

Thornton, K., Gaudlitz, M., Janka, H.-T. and Steinmetz, M. Energy Input and Mass Redistribution by Supernovae in the Interstellar Medium. *ApJ*, **500**, 95, 1998

Toro, E. F. *Riemann Solvers and Numerical Methods for Fluid Dynamics*. Springer-Verlag, 1997

Tóth, G. Numerical study of two-fluid C-type shock waves. *ApJ*, **425**, 171, 1994

van Dyke, M. *An album of fluid motion*. Stanford, CA: Parabolic Press, 1982, 1982

van Leer, B. Towards the Ultimate Conservative Difference Scheme. *J. Comp. Phys.*, **32**, 101, 1979

Vestuto, J. G., Ostriker, E. C. and Stone, J. M. Spectral Properties of Compressible Magnetohydrodynamic Turbulence from Numerical Simulations. *ApJ*, **590**, 858, 2003

von Weizsäcker, C. F. The Evolution of Galaxies and Stars. *ApJ*, **114**, 165, 1951

Wolfire, M. G., Hollenbach, D., McKee, C. F., Tielens, A. G. G. M. and Bakes, E. L. O. The neutral atomic phases of the interstellar medium. *ApJ*, **443**, 152, 1995

Wolleben, M. and Reich, W. Faraday screens associated with local molecular clouds. *A&A*, **427**, 537, 2004

Ziegler, U. A central-constrained transport scheme for ideal magnetohydrodynamics. *J. Comp. Phys.*, **196**, 393 , 2004

Index

Danksagung

Im Zusammenhang mit dieser Arbeit haben mir viele Menschen hilfreich zur Seite gestanden. All diesen möchte ich an dieser Stelle herzlich danken. Im besonderen danke ich:

- Herrn PD Dr. Horst Fichtner. Ich danke ihm für die Themenstellung und seine vorbildliche Betreuung. Besonders durch seine Herangehensweise an die Physik habe ich viel lernen können.
- Ich danke Herrn Prof. Dr. Reinhard Schlickeiser, der mich schon während meines Studiums gefördert und unterstützt hat und mir einen Platz an seinem Lehrstuhl zur Verfügung stellte.
- Herrn Prof. Dr. Ralf-Jürgen Dettmar danke ich für seine finanzielle und fachliche Unterstützung.
- Herrn Prof. Dr. Rainer Grauer gebührt mein Dank für seine intensive Betreuung und gute Zusammenarbeit.
- Andreas Kopp danke ich für das wohl beeindruckendste Korrekturlesen. Ich hätte niemals gedacht, daß jemand all diese Gleichungen kontrollieren würde.
- Auch Jens Ruppel danke ich für seinen Anteil am Korrekturlesen. Besonders aber wird mir die schöne Zeit in unserem Büro in Erinnerung bleiben.
- Ich danke Jens Kleimann und Felix Spanier für viele hilfreiche Kommentare und Anregungen.
- Überhaupt möchte ich mich bei allen Mitglieder des TP4-Lehrstuhls bedanken, die für ein so gutes Arbeitsklima sorgen.

Mein besonderer Dank gilt natürlich meinen Eltern, ohne die ich niemals so weit gekommen wäre. Und ich danke Dir, Doro. Ohne Dich hätte ich nicht bis hier durchgehalten. Vielen Dank für Deine unendliche Geduld.

Physical Constants

Avogadro’s Number	N_A	=	$6.0221364 \cdot 10^{23}$
Boltzmann Constant	k_B	=	$1.380658 \cdot 10^{-23}$ F m^{-1}
Electron Mass	m_e	=	$9.109690 \cdot 10^{-31}$ kg
Electron Charge	e	=	$1.6021773 \cdot 10^{-19}$ C
Gas Constant	R	=	8.31451 J K^{-1} mol^{-1}
Parsec	1pc	=	$3.0856776 \cdot 10^{16}$ m
Permittivity of Free Space	ε_0	=	$8.854188 \cdot 10^{-12}$ A s V^{-1} m^{-1}
Permeability of Free Space	μ_0	=	$4\pi 10^{-7} = 1.256637 \cdot 10^{-6}$ V s A^{-1} m^{-1}
Proton Mass	m_p	=	$1.6426231 \cdot 10^{-27}$ kg
Speed of Light	c	=	$2.99792458 \cdot 10^{8}$ m s^{-1}

Fundamental Plasma Parameters

Thermal Velocity	v_{Ti}	=	$\sqrt{k_B T/m_i}$
Thermal Pressure	P	=	$n k_B T$
Alfvén Speed	v_A	=	$B_0/\sqrt{\mu_0 \rho}$
Speed of Sound	c_s	=	$\sqrt{\gamma k_B T/m}$
Gyrofrequency	ω_{ci}	=	eB/m_i
Gyroradius	r_i	=	$\mathrm{v}_{Ti}/\omega_{ci} = \sqrt{m\beta/2\mu_0 e^2 n}$
Debye Length	λ_D	=	$\sqrt{\varepsilon_0 k_B/n_e e^2}$
Plasma Frequency	ω_{pi}	=	$\sqrt{n_i Z_i^2 e^2/\varepsilon_0 m_i}$
Plasma β	β	=	$2\mu_0 p/B^2$